FZR-401



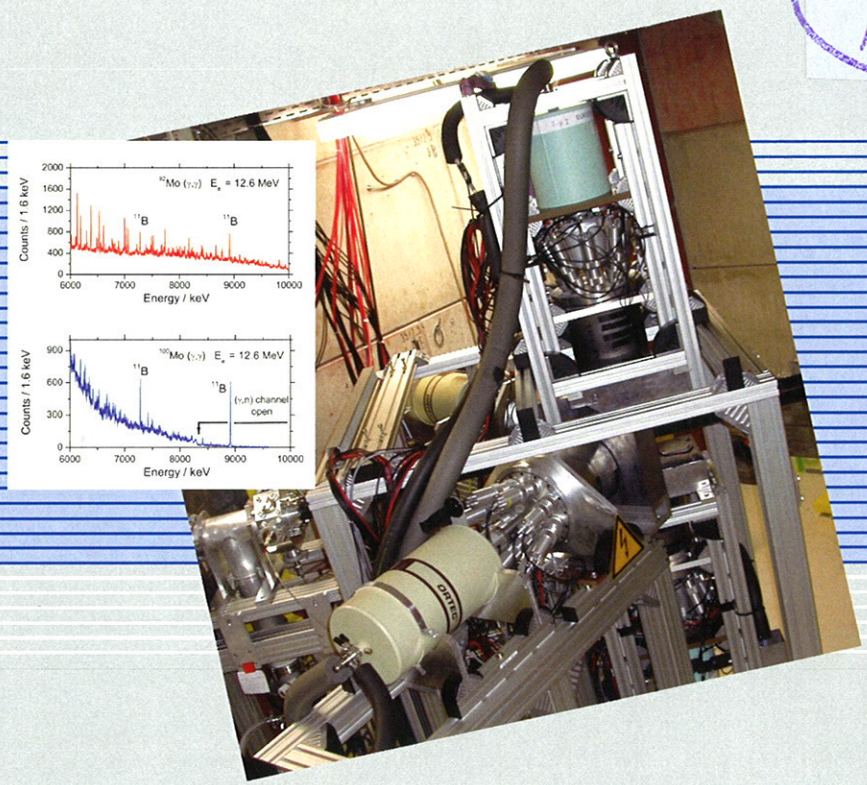


Wissenschaftlich-Technische Berichte
FZR-401 2004 · ISSN 1437-322X

# Annual Report 2003

## Institute of Nuclear and Hadron Physics

Forschungszentrum
Rossendorf

Wissenschaftlich-Technische Berichte
**FZR-401**
2004

# Annual Report 2003

## Institute of Nuclear and Hadron Physics

**Editors:**

**W. Enghardt, K. Fahmy, E. Grosse,**

**B. Kämpfer, C. Schneidereit, A. Wagner**

Forschungszentrum
Rossendorf

# Contents

# Life Sciences:
## Biostructures and Radiation 45

# Preface

*The Forschungszentrum Rossendorf (FZR) at Dresden is a multidisciplinary research centre within the Leibniz-Gemeinschaft (WGL), one of the German national institutions for extra-university research. Using various kinds of radiation the centre is active in research on the structure of matter as well as in life sciences and environmental research. The Institute of Nuclear and Hadron Physics (IKH) within the FZR avails for its research the coupling of radiation to matter in subatomic dimensions as well as to tissue, to cells, and to their components. Its investigations in the field of Subatomic Physics are part of the FZR-program Structure of Matter and its research concerning the interaction of Biostructures and Radiation contributes to the Life Science program of the FZR. This combination forms a good basis for IKH's endeavour to heavily exploit the possibilities for transfer and introduction of experimental and theoretical techniques from particle and nuclear physics to life science projects. A remarkable example of interdisciplinary transfer is the institute's work on the Radiation Source ELBE at the FZR. This large installation provides photons in the wide wavelength range from fm to mm - i.e. bremsstrahlung for the excitation of nuclei in laboratory studies related to cosmic processes and infrared light for investigations on the structural dynamics of biomolecules. The compact bunches of relativistic electrons and secondary beams derived from them - like X-rays and neutrons - are employed as well in the Institute's studies in the life sciences and on the subatomic structure of matter.*

*In this Scientific Report the research projects of the Institute of Nuclear and Hadron Physics are presented by several articles each. Other contributions describe the progress made in the production of the different kinds of secondary radiation at ELBE, and on the experimental equipment dedicated for their use. The conceptual design studies for the infrared free electron laser (FEL) at ELBE and the detailed work on a magnetic undulator constitute a very important contribution to this FELBE project, which very likely will be attractive to many outside users. Similarly, the numerical simulations and tests performed for the optimization of the production stations for bremsstrahlung, channeling X-rays and MeV-neutrons indicate that ELBE is apt to allow experiments with high sensitivity and favourable background conditions.*

*The coupling of radiation to matter not only dominates the projects in nuclear physics and astrophysics as pursued at ELBE, it also is a central theme of the experimental and theoretical research performed by the IKH in close interrelation with the experimental program at the heavy ion synchrotron SIS at GSI Darmstadt. At ELBE electron beams became available regularly during the year 2003. Parallel to intensive attempts to optimize the experimental conditions with respect to resolution, luminosity and background conditions first investigations on dipole strength distributions in various nuclei were performed. Special emphasis was put on several isotopes of Molybdenum, which were selected such that the full range in neutron to proton ratio available as target material is covered; nuclides participating in the three different (r-, s- and p-) processes for cosmic element production could be studied. The experimental conditions achieved at ELBE proved to be very favourable for such studies as they allowed to cover the excitation energy range up to well beyond particle separation energies. In future studies photon or electron induced fission will be of use as the source of neutron rich nuclei whose properties are of special importance for the detailed understanding of the stellar element cooking. For such questions neutron beams in the MeV range later available at ELBE may play a role as well; the first neutron beams at ELBE will very likely serve for the measurement of cross sections for processes of anticipated use for the transmutation of radioactive waste.*

*Hadron physics at the IKH - as described in the second section of this report - deals with the strong (nuclear) interaction and its variation within the hadronic medium. Experiments related to such questions are performed at high energy heavy-ion accelerators; the IKH is heavily involved in research within the international HADES collaboration performed with SIS at GSI. Theoretical studies refer to these experiments and to data obtained at even higher energies, where a phase transition to a quark gluon plasma has been predicted to occur. Understanding the high density*

*phases of hadronic matter is an important step towards understanding the Big Bang and the evolution of the universe.*

*In its second chapter this Report comprises research in the life sciences, partly performed by using nuclear technology. In the past IKH contributed considerably to the field of tumour-conform radiotherapy employing positron emission tomography (PET): The outstanding achievement here is the successful operation of a PET scanner simultaneously to the irradiation of tumors with heavy ion beams. During the last years a significant number of patients has been treated with carbon ions at GSI and the reliability and reproducibility of such radiation therapy could be improved considerably by in-situ PET as developed at IKH. Recent efforts at the Institute focused on the feasibility of this method for the control of irradiations performed with lighter ions or even with photons and very promising results were obtained.*

*In the coming years interesting biomedical investigations will be performed with beams from ELBE: Quasi-monochromatic X-rays of easily variable energy as produced in electron channeling have been observed at several energies with intensities as predicted. They will be used as a probe for the elementary processes responsible for radiation induced cell damage and for first experiments related to photon activation therapy (PAT). For such studies a laboratory with a conventional X-ray tube for reference irradiations and a cell laboratory are installed at ELBE, which may also be used for investigating the interactions of cells and tissue with tunable FEL-radiation in the infrared - as becoming available soon at ELBE.*

*Biophysical and biochemical research will profit as well from the IR-radiation generated by ELBE, which allows to study biomolecular dynamics under non-destructive and native-like conditions. Fundamental aspects of the structure and conformational changes of rhodopsin-like G-protein-coupled receptors play a key role in these investigations – up to now performed with IR from other, less favourable sources. Protein-metal interactions have become another field of interest. Here, IR-absorption studies have demonstrated for the first time the relation between protein metallization, protein structure, and stability of bacterial surface proteins that are of biotechnological interest for heavy metal absorption.*

*The interaction between the different areas of research at IKH has led to considerable synergy effects with respect to soft- and hardware for running and analyzing the experimental investigations; here the transfer of information from the large international particle and nuclear physics community to the life sciences is especially important. Thus there are ample interconnections between the various research projects of the institute -reaching from laboratory studies on processes of importance for cosmic nucleosynthesis or radioactive waste transmutation all the way to the interactions of various types of radiation with bio-molecules and cells.*

*In 2003 the institute's work was especially acknowledged: The research prize of FZR was awarded to members of the Nuclears Physic Division for their long-lasting, internationally recognized research on rotation-like nuclear modes. Another award was given to the detector-lab's crew for their outstanding success in the development and fabrication of large area, high precision particle detectors.*

*The scientific activities of the IKH have benefited from generous support from various sources. First of all, we gratefully acknowledge the close and fruitful collaboration with the Technical University (TU) Dresden and with GSI Darmstadt. Contacts to them and many other scientific institutions in Germany and abroad are of vital importance for the institute. Specific projects were subsidized by the Federal Ministry for Education and Research (BMBF), the Saxon State Ministry for Science and Art (SMWK), GSI Darmstadt and Forschungszentrum Jülich. We express our gratitude to all these as well as to the Deutsche Forschungsgemeinschaft (DFG) and to the European Union (EU) for the support of several research projects initiated by the Institute.*

# Structure of Matter:

## Nuclear and Hadron Physics

*In 2003, the nuclear physics research at the Forschungszentrum Rossendorf focused primarily on experiments with the new ELBE facility. The available beamtime was still scarce; while it was devoted to systematic studies of electric and magnetic dipole strength distributions, mainly in medium-mass nuclei. During the experiments changes of the Bremsstrahlung-production and detection setup have been made resulting in significant improvements of the detection efficiency and the reduction of unwanted background. In a series of experiments the stable Molybdenum isotopes Mo-92 (the most neutron-deficient), Mo-98, and Mo-100 (the most neutron-rich) have been studied and dipole strength distributions have been derived. The results are compared to theoretical investigations which have been performed using a model based on a random-phase approximation from many particle theory - here applied to nuclei without spherical symmetry. The aim is to understand the properties of collective excitations of nuclei close to the particle separation energies. Furthermore, the dipole response of Sr-88 has been investigated extending previous studies at the S-Dalinac accelerator at TU Darmstadt to higher excitation energies.*

*With the possibility to use photon beam energies beyond the particle separation energy experiments of astrophysical interest have been done. Here, a first measurement on the photo-activation of a p-process nucleus has been carried out, and a dedicated setup has been installed for further systematic studies.*

*The development of a novel time-of-flight spectrometer for the detection and identification of fission fragments from photon-induced fission has progressed and a first prototype of the detector has been built. The fission-fragment studies aim towards the detailed understanding of the nucleosynthesis of neutron-rich nuclei in the rapid-neutron capture process which takes place in explosive scenarios in the universe.*

*As a future project, neutron-induced reactions will be investigated at the new neutron time-of-flight facility which is under construction at ELBE. Within a collaboration between IKH, the FZR-institutes for safety research and radiochemistry and TU Dresden various research areas from the cosmic element synthesis in neutron-rich environments to nuclear transmutation will become accessible. The nuclear physics department plays a key role in the detector development, the design and the setup of the experiments at this new facility.*

*While nuclear physics investigates the structure and reactions of nuclei, hadron physics research uses the atomic nucleus as laboratory where properties of hadrons are explored in the environment of nuclear matter. Experimentally this is accomplished with the High Acceptance Di- Electron Spectrometer HADES installed at the heavy-ion synchrotron SIS at GSI Darmstadt. The particular focus will be the detection of di-electrons stemming from decays of vector mesons in the nuclear medium created in the course of nucleus-nucleus collisions. From previous experiments the first di-electron spectra are obtained; to obtain detailed information on the production of vector mesons, an improved analysis technique is presently developed.*
*Due to the complexity of the strong interaction the individual reaction channels between hadrons outside of the medium also need more detailed studies. In fact, the first of a series of experiments on the p+p system has been performed at HADES, and special emphasis was put on channels important for vector mesons and for their production strengths. The experimental activities at HADES (and other experiments previously performed from IKH scientists) are complemented by theoretical research; various aspects of importance for HADES are thus covered in a sufficiently wide context.*

*The hadron physics results described in this report are obtained in the following international collaborations:*

*HADES: Univ. Frankfurt, TU München, Univ. Giessen, GSI Darmstadt, FZ Rossendorf, Institute of Physics Bratislava (Slovakia), LNS Catania (Italy), LPC and Univ. Blaise Pascal Clermont (France), Jagellonian Univ. Cracow (Poland), JINR Dubna (Russia), Univ. degli Studi di Milano (Italy), ITEP Moscow (Russia), INR Moscow (Russia), MEPhI Moscow (Russia), Univ. of Cyprus (Cyprus), Institute de Physique Nucleaire d'Orsay (France), Nuclear Physics Institute Rez (Tschechia), Univ. of Santiago de Compostela (Spain), Univ. of Valencia (Spain),*

*KaoS: TU Darmstadt, Univ. Frankfurt, Univ. Marburg, GSI Darmstadt, Jagellonian Univ. Cracow (Poland), FZ Rossendorf.*

*Some data mentioned in this report stem from the FOPI set-up at GSI, from E91916 at Jefferson Labaratory and from ANKE at FZR.*

*The research in nuclear physics has profited from collaboratoring with groups in the following institutions: Tech. Univ. Dresden, Univ. of Stuttgart, Univ. of Cologne, Tech. Univ. Darmstadt, GSI Darmstadt, INRE, Bulgaria, Univ. of Sofia, Bulgaria, Univ. of Notre Dame, USA, and JINR, Dubna, Russia, Inst. for Safety Research, and Inst. for Radiochemistry, FZR*

# Improvements of the Bremsstrahlung Facility at ELBE

K.D. Schilling, F. Dönau, M. Erhard, E. Grosse, A. Hartmann, K. Heidel, A.R. Junghans, K. Kosev, M. Langer, T. Riedel[1], G. Rusev, W. Schulze, R. Schwengner, A. Wagner, U. Wolf, B. Wustmann[1]

According to experiences of the first photon-scattering experiments at ELBE, the bremsstrahlung facility has been optimized in order to reduce the influence of undesired background radiation and, thus, to improve the sensitivity of the experimental set-up. The present detector set-up is shown on the title page of this report. The layout of the present facility is displayed in Fig. 1. The modifications of several components are described in the following:

• A new radiator holder of the same construction as described in [1], but with five positions for different radiator foils was manufactured and will be used in future. It will enable the use of a larger variety of radiator materials with different thicknesses and a convenient change of them without the disturbance of the vacuum status during an accelerator session.

• The graphite (C) absorber for the beam hardening [2] was replaced by a modified Al absorber composed of a TRIAMET case (composite material containing 95% W) with a cylindrical hole (9 mm diameter) filled with high-purity aluminium (Al99.5) as the actual hardener directly in front of the collimator entrance aperture of 5 mm diameter. The aim was to get a more efficient bremsstrahlung collimation and shielding of the HPGe, silicon and scintillation detectors in the experimental cave from the non-axial radiation components produced in the radiator.

• For the same reason, the last segment of the bremsstrahlung collimator [3] in beam direction with the largest conical aperture (exit opening of 24 mm diameter) originally made from Al99.5 was substituted by a TRIAMET cylinder of identical design.

• In addition to the 10 cm thick lead wall established earlier between the electron beam dump and the concrete wall in the accelerator hall [4], two further Pb walls were assembled in the experimental cave (cf. Fig. 1). The large one (20 cm thick, with a 180 mm aperture tilted by 45°) stands parallel to the concrete wall. It shields from all radiation components penetrating the concrete wall outside the collimator from the accelerator cave, i.e. from the electron beam dump and from those components of the spatial bremsstrahlung distribution that pass through the concrete wall outside the collimator tube. The second Pb wall (also 20 cm thick) is perpendicular to the beam direction and has an inner aperture of only 46 mm, thus shielding from the attenuated radiation components which have passed through the hardener and the collimator materials (Al and W). A photograph of the two lead walls in the experimental cave is shown in Fig. 3 of report [5].

• The photon-beam tube in the experimental cave originally made of aluminium was partially replaced by a polyethylene (PE) tube. The choice of this lower-$Z$ material reduces the background generated by pair production and by Compton scattered $\gamma$-quanta into the HPGe and NaI(Tl) detectors and the photo-neutron production as well.

• The lead collimators for the HPGe detectors and the BGO escape-suppression shields [6] were substituted by new ones with different geometry. The new collimators are larger in thickness (10 cm instead of 7 cm [6]) and also in area such that they protect now the complete front and side of the BGO shields from direct $\gamma$-radiation produced mainly by pair production and Compton scattering in the target and in the PE beam tube downstream the target. The new collimators as well as the new PE tube described above can be viewed on the title page of this report and on the first page and in Fig. 3 of report [5].

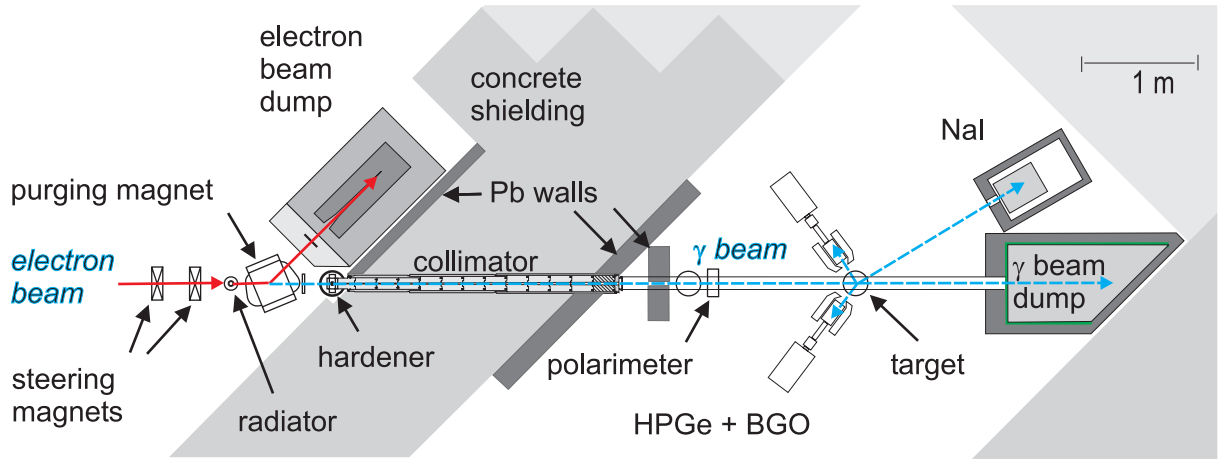


**Fig. 1** *Layout of the bremsstrahlung facility for nuclear and astrophysics experiments at ELBE.*

[1] *FZ Rossendorf, FWF*

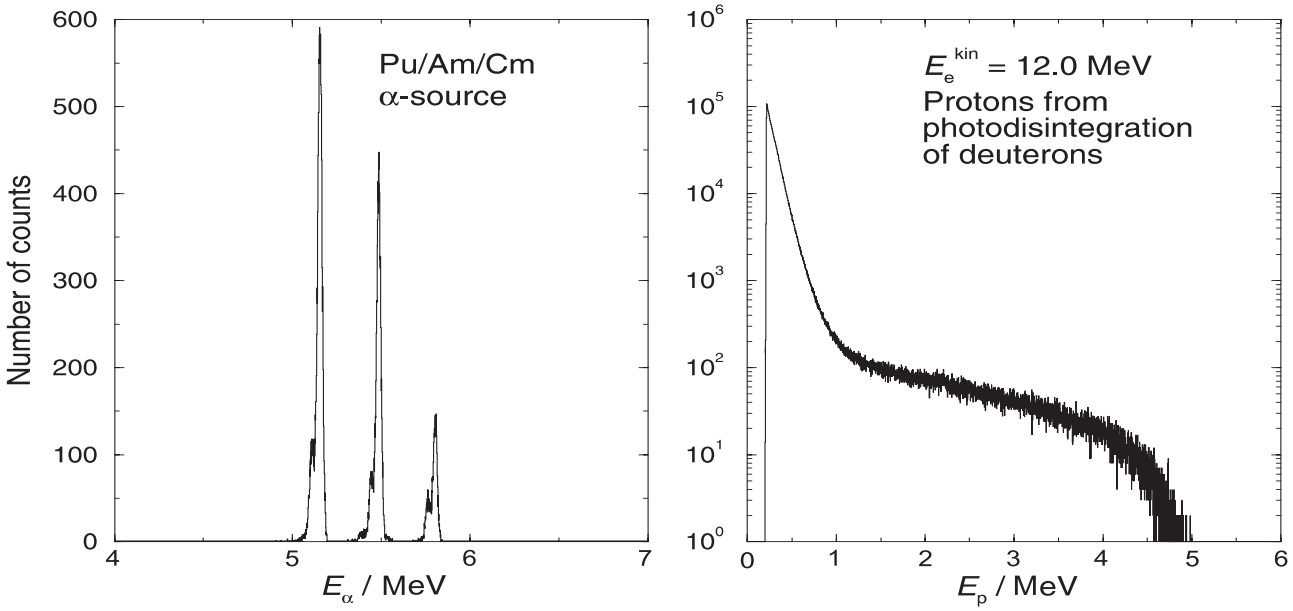


**Fig. 2** *Spectra of a silicon detector of the polarimeter for a mixed $\alpha$-source (left panel) and for protons measured during the irradiation of a 40 $\mu$m thick deuterated polyethylene ($CD_2$) film with 12 MeV bremsstrahlung (right panel). The peak below 1 MeV is mainly due to contributions from $\gamma$-ray background. Note the different scales on the left and the right panels.*

• The horizontal frames of the detector set-up [7] were changed in such a way that the two horizontal HPGe detectors can be moved between 90° and 127° relative to the beam direction as indicated in Fig. 1 in order to measure angular distributions of $\gamma$-rays emitted from the target and, thus, to deduce the spins of the excited nuclear states.

• The polarization monitor [8] (polarimeter) was moved downstream to a position behind the second Pb wall in the experimental cave (Fig. 1) and was equipped with four new silicon detectors. The latter have a 600 mm$^2$ sensitive area (28 mm diameter) and a thickness of 300 $\mu$m each - corresponding to the maximum range of 6 MeV protons which are generated by 14 MeV photons in the deuterated PE target [8]. Absorbers in front of the detectors can be used in case of even higher photon energies. The proton spectra will be used to deduce the degree of polarization in measurements with polarized bremsstrahlung [4]. The new detectors are about 10 times thinner than those presented in [8] resulting in a considerably reduced efficiency (sensitivity) for photon and electron detection. The simple kinematics of the photodisintegration of the deuteron is used to determine the electron beam energy of ELBE from the end-point energy of the proton spectra with an accuracy of better than 150 keV. Examples of measured proton- as well as $\alpha$-spectra are shown in Fig. 2.

• A new isolation transformer for a symmetrical voltage power supply was installed separating the ground termination of the experimental electronics and data acquisition system from the accelerator grounding. In this way, parasitic noise on the cables originating from outside could be minimized and the energy resolution of the HPGe detectors could be improved to 2.8 keV for the 1.3 MeV $\gamma$-ray transition of $^{60}$Co with a binning of 1.3 keV/channel.

• With a refined coincidence scheme, as the substitution of constant-fraction discriminators by leading-edge triggers and subsequent reduction of the electronic transit times, the efficiency of the anti-Compton (escape-suppression) shields of the HPGe detectors could be improved up to a factor of 5 to 6 for $\gamma$-ray energies as high as 9 MeV.

• For on-line and off-line monitoring purposes of slow-control parameters (beam energy, beam current, beamline settings, etc.), a data exchange path based on an OPC (open connectivity) client-server model has been installed. Data from the accelerator control are inserted into the data stream with a frequency of 1 Hz.

To summarize: All of the above described upgrades and refinements have led to substantial, qualitative improvements of the $\gamma$-spectra obtained in the nuclear-physics experiments at ELBE.

[1,4] K.D. Schilling et al., Wiss.-Tech. Ber. FZR-372 (2003) 30, 31
[2,3] K.D. Schilling et al., Wiss.-Tech. Ber. FZR-341 (2002) 41, 37
[5] R. Schwengner, Wiss.-Tech. Berichte FZR-398 (2004) 24
[6] G. Rusev et al., Wiss.-Tech. Berichte FZR-372 (2003) 29
[7] R. Schwengner et al., Wiss.-Tech. Ber. FZR-372 (2003) 27
[8] R. Schwengner et al., Wiss.-Tech. Ber. FZR-341 (2002) 39

# Photon Scattering from $^{92}$Mo, $^{98}$Mo and $^{100}$Mo up to the Neutron Separation Energy [D]

G. Rusev, R. Schwengner, A. Wagner, K.D. Schilling, F. Dönau, M. Erhard, A.R. Junghans, K. Kosev, S. Frauendorf, E. Grosse

The bremsstrahlung facility at the ELBE accelerator allows the investigation of dipole-strength distributions in the energy range below the giant-dipole resonance. The properties of the dipole-strength distribution provide an interesting test ground for the influence of the proton-neutron interaction on the nuclear structure. An example for a systematic investigation of the dipole-strength distribution and a study of the influence of collectivity on the dipole excitations is the chain of stable Mo isotopes, which starts with the spherical nucleus $^{92}$Mo ($N = 50$) and ends with the slightly deformed $^{100}$Mo ($N = 58$).

$^{98}$Mo and $^{100}$Mo had previously been investigated in photon-scattering experiments up to 3.8 MeV [1, 2] at the bremsstrahlung facility of the Stuttgart Dynamitron accelerator. In order to extend our study of dipole excitations in Mo isotopes to higher energies we performed photon-scattering experiments on $^{92}$Mo, $^{98}$Mo and $^{100}$Mo at the ELBE accelerator at electron energies of 12 MeV and 9 MeV close to the neutron separation energies of $^{92}$Mo ($S_n$ = 12.7 MeV), $^{98}$Mo ($S_n$ = 8.7 MeV) and $^{100}$Mo ($S_n$ = 8.3 MeV). Samples of 2035.7 mg $^{92}$Mo, 2952.5 mg $^{98}$Mo and 2916.8 mg $^{100}$Mo were used as targets in the three experiments. The targets were combined with elementary $^{11}$B for photon flux calibration. Four 100 % HPGe detectors were used in the measurements, two of them placed at 127° and the other two at 90° relative to the incident beam in order to deduce the angular distributions of resonantly scattered $\gamma$-rays. Parts of the spectra measured at 127° for the three isotopes are shown in Fig. 1. The closed-shell nucleus $^{92}$Mo shows prominent peaks up to 11 MeV while the heavier isotopes $^{98}$Mo and $^{100}$Mo have weak transitions up to 6.5 MeV. The peaks above 4 MeV in $^{98}$Mo and $^{100}$Mo were observed for the first time in photon-scattering experiments, while $^{92}$Mo was previously investigated at the former linac at Ghent at an electron energy of 10 MeV [3].

The multipolarity of the observed transitions were obtained by comparing the ratios of the $\gamma$-ray intensities observed at 90° and 127° with the expected values for dipole and quadrupole transitions [4], 0.73 and 2.28, respectively. Most of the transitions show dipole character.

The reduced level widths of the observed transitions, which are proportional to the reduced transition strengths, were deduced for the three isotopes. A comparison of the dipole-strength distributions for $^{92}$Mo, $^{98}$Mo and $^{100}$Mo is shown in Fig. 2. $^{92}$Mo and $^{98}$Mo display broad distributions up to 10.5 and 8.5 MeV, respectively. In contrast, the distribution in $^{100}$Mo fades already at about 7 MeV. The three distributions show a concentration of dipole strength separated in two energy ranges below and above 5 MeV. The low-energy dipole-strength concentration coincides with the range where M1 mixed-symmetry states were observed in the neighboring nuclei $^{94}$Mo [5] and $^{96}$Mo [6]. In other nuclei the concentration of dipole strengths around 7 MeV was interpreted as E1 and pygmy resonances [7].

Random-Phase-Approximation (RPA) calculations for E1 transitions were performed to understand the nature of the dipole-strength distributions in $^{98}$Mo and $^{100}$Mo. Only particle-hole configurations were included in the calculations. Fig. 3 shows the $B$(E1) strength distributions for $^{98}$Mo and $^{100}$Mo predicted from RPA. The calculations predict E1 strength only above 5 MeV. The comparison with the RPA calculations shows that the dipole strength above 5 MeV may be mainly E1 strength while the strength below 5 MeV may be dominated by M1 transitions.

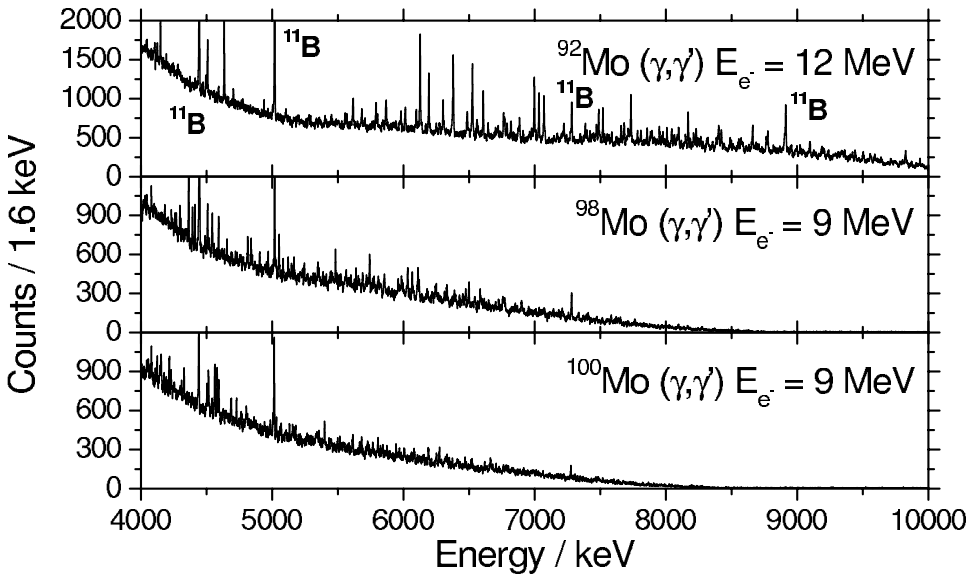


**Fig. 1** *Partial photon-scattering spectra from $^{92}$Mo, $^{98}$Mo and $^{100}$Mo measured at 127° relative to the beam axis.*

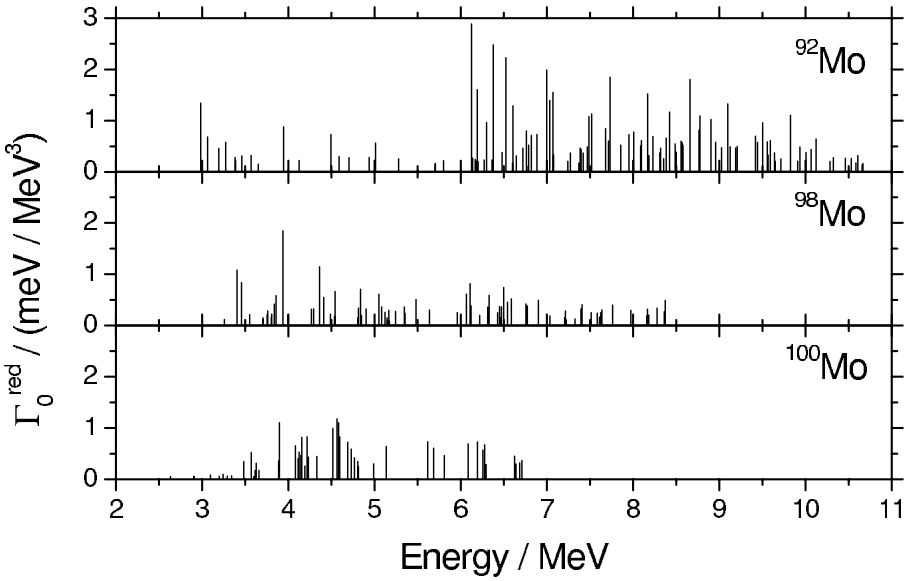


**Fig. 2** *Distribution of reduced level widths for the dipole transitions in $^{92}$Mo, $^{98}$Mo and $^{100}$Mo, respectively.*

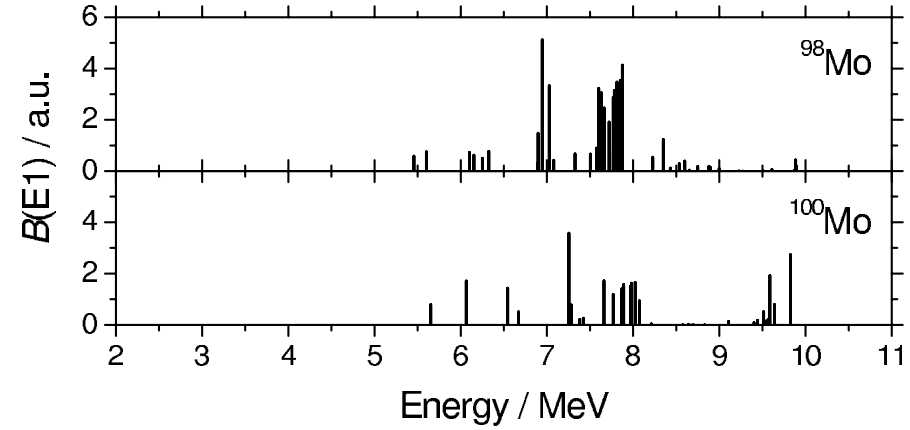


**Fig. 3** *RPA calculations for the reduced transition strengths for E1 transitions in $^{98}$Mo and $^{100}$Mo.*

This systematic investigation of the three Mo isotopes allows us to study the dependence of the dipole-strength distribution on the proton-to-neutron ratio. The energy-weighted sum of the E1 strength is calculated under the assumption that all transitions above 5 MeV are E1 transitions. The sum was calculated over all transitions with an energy above 5 MeV or with energy in the range between 5 and 8.3 MeV (the neutron separation energy for $^{100}$Mo), respectively. Fig. 4 shows the dependence of the energy-weighted $B$(E1) strength for the three isotopes. The summed E1 strength drops by a factor of 5 or more with the number of neutrons changing from 50 to 58. Such a dependence is in contrast to the understanding of pygmy resonances being due to the vibration of the excessive neutrons against an inert proton-neutron core. The interpretation of the observed behavior requires further experimental and theoretical investigations.

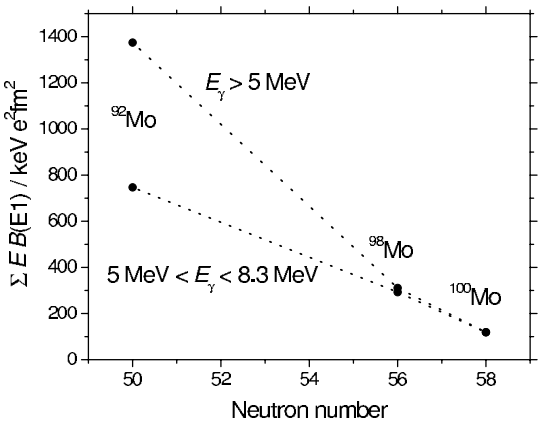


**Fig. 4** *Energy-weighted sums of E1 strength for all transitions with an energy above 5 MeV or with an energy in the range between 5 and 8.3 MeV, respectively.*


[1] G. Rusev et al., Wiss.-Tech. Ber. FZR-372 (2003) 34
[2] G. Rusev et al., Wiss.-Tech. Ber. FZR-372 (2003) 35
[3] F. Bauwens, Ph. D. thesis, University of Ghent, 2000
[4] U. Kneissl, H.H. Pitz and A. Zilges. Prog. Part. Nucl. Phys. 37 (1996) 349
[5] N. Pietralla et al., Phys. Rev. Lett. 83 (1999) 1303
[6] V. Werner et al., IfS Annual Report 1999, p. 18
[7] A. Zilges et al., Phys. Lett. B 542 (2002) 43

# Photon Scattering from $^{88}$Sr up to the Neutron-Separation Energy [D]

R. Schwengner, G. Rusev, A. Wagner, K.D. Schilling, F. Dönau, M. Erhard, A.R. Junghans, K. Kosev, E. Grosse[1]

The response of atomic nuclei to photons has attracted increasing interest in recent years. In particular, the structure of dipole excitations close to the neutron-separation energy is expected to reveal information on new types of collective excitation modes posing a challenge to the theoretical description of the nuclear many-body system [1,2]. Besides, the distribution of the dipole strength around the neutron-separation energy influences reaction rates in specific processes of the nucleosynthesis and is therefore of importance for astrophysical problems [3].

Dipole-strength distributions close to the neutron-separation energies could be studied for only few nuclides until now. The new bremsstrahlung facility at the ELBE accelerator of the FZR opens up the possibility to investigate dipole excitations with a sensitive detector setup at energies above 10 MeV.

In the course of a systematic study of dipole-strength distributions in nuclei around $A = 90$ we initiated the investigation of the $N = 50$ nuclide $^{88}$Sr. We had studied this nuclide before in a photon-scattering experiment at the S-Dalinac with an electron energy of 6.7 MeV [4]. The present photon-scattering experiment at ELBE was carried out with bremsstrahlung produced with an electron beam hitting a niobium radiator of 4 $\mu$m thickness. The energy of the electrons was 12 MeV which is slightly above the neutron-separation energy of $^{88}$Sr of $S_n = 11.1$ MeV. The average electron current was 500 $\mu$A. A 10 cm thick aluminium absorber was placed behind the radiator in order to suppress the low-energy part of the bremsstrahlung spectrum. The target consisted of 2731.8 mg of $^{88}SrCO_3$ with an enrichment of 99.9 %, combined with 311.5 mg of $^{11}$B used for the calibration of the photon flux. $\gamma$ rays were measured with four high-purity germanium detectors of 100 % efficiency relative to a 3"$\times$3" NaI detector. All detectors were surrounded by escape-suppression shields of bismuth germanate scintillation detectors. Two detectors were placed at 90° relative to the photon-beam direction while the other two were positioned at 127° to deduce angular distributions of the $\gamma$ rays.

Part of a $\gamma$-ray spectrum measured at 127° during the irradiation of about 98 hours is shown in Fig. 1. About 100 $\gamma$ transitions in the energy range from 6.7 to 11.0 MeV were observed for the first time. The analysis of the $\gamma$-ray spectra is in progress. The dipole-strength distribution to be deduced from the $\gamma$-ray intensities will be compared with the dipole-strength distribution of the $N = 50$ isotone $^{92}$Mo [5] to evaluate the behaviour with varying proton number. Besides, it will be useful to test theoretical predictions as done for dipole excitations observed in studies of neighbouring nuclides [5].

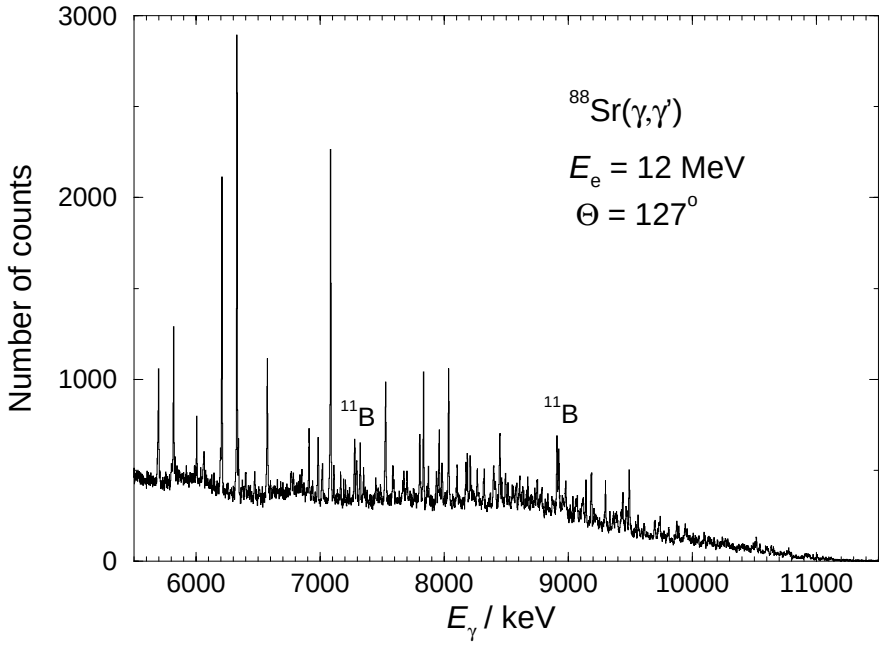


**Fig. 1** *Partial spectrum of photons scattered from $^{88}$Sr, measured at 127° with respect to the incident beam.*

[1] A. Zilges et al., Phys. Lett. B 542 (2002) 43
[2] N. Ryezayeva et al., Phys. Rev. Lett. 89 (2002) 272502
[3] S. Goriely, Phys. Lett. B 436 (1998) 10
[4] L. Käubler et al., Eur. Phys. J. A 7 (2000) 15, and to be published
[5] G. Rusev et al., This Report p. 7

[1] *also Technische Universität Dresden*

# Deconvolution of Bremsstrahlung Spectra Measured by Means of a NaI Detector [D]

G. Rusev, A.R. Junghans, A. Wagner, R. Beyer

At the bremsstrahlung facility of the ELBE accelerator a large NaI detector is used for beam-flux monitoring. The NaI crystal has a size of 10"×10" and an efficiency of 1100 %. The detector is placed at 25° relative to the beam and shielded with 10 cm thick lead housing with a collimator hole of 4 cm in diameter. We have analyzed a spectrum measured with the NaI detector in order to unfold the spectral distribution of the incident photon beam using simulations for the response of the detector. Monte Carlo simulations including the experimental setup of the photon-scattering experiment on $^{98}$Mo [1] were performed for a photon beam with uniform energy distribution. The beam energy range from 0 to 10 MeV was divided to 40 bins with a width of 250 keV, each. The simulations were performed for $10^9$ photons/bin using the program code GEANT3 [2]. A response spectrum $S_i$ of the deposited energy in the NaI crystal includes the probability for $\gamma$-scattering from the target [3] and the response of the detector. Fig. 1 shows an example response spectrum of the detector from a quasi-monoenergetic photon beam with energies between 9.75 and 10 MeV. The measured NaI-spectrum $S_{exp}$ can be approximated with a linear combination of such simulated response spectra $S_i$:

$$S_{exp} = \sum_i a_i S_i, \qquad (1)$$

where the coefficients $a_i$ are free positive definite parameters of the fit, they correspond to the intensity of the incident photon beam in the energy range of bin $i$.

Applying the method, we use a NaI spectrum measured for 2 hours from the photon-scattering experiment on $^{98}$Mo at an electron energy of about 9 MeV. The reconstructed initial bremsstrahlung spectrum from the measured NaI spectrum is shown in Fig. 2. It is compared with GEANT simulations of the photon flux including the radiator and the beam hardener. Fig. 2 shows that the unfolded spectrum reproduces well the slope of the beam-intensity distribution. In order to obtain the end-point energy of the bremsstrahlung spectrum more precisely we used the presented simulations in the inverse way. We simulated NaI spectra corresponding to different electron-beam energies and compared them with the measured NaI spectrum. The spectra were normalised in the energy range from 1 to 2 MeV. The squared difference between measured and predicted spectra for the NaI detector is plotted in Fig. 3. The minimum in Fig. 3 gives the end-point energy located at about 8.2 MeV. Of crucial importance for precise end-point energy determination is the energy calibration of the NaI detector and the knowledge of the position angle of the detector relative to the beam.

The presented method reproduces rather well the spectral distribution of the incident beam spectrum. The end-point energy of the bremsstrahlung distribution can be determined. The method can be applied for on-line monitoring of the incident beam using a highly efficient NaI detector and spectra measured for short time.

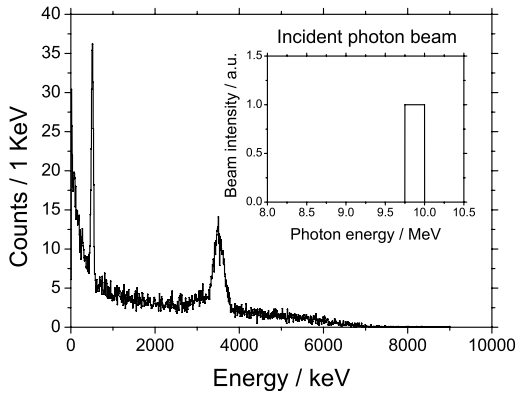


**Fig. 1** *Simulated spectrum of a NaI detector for a photon beam energy from 9.75 to 10 MeV.*

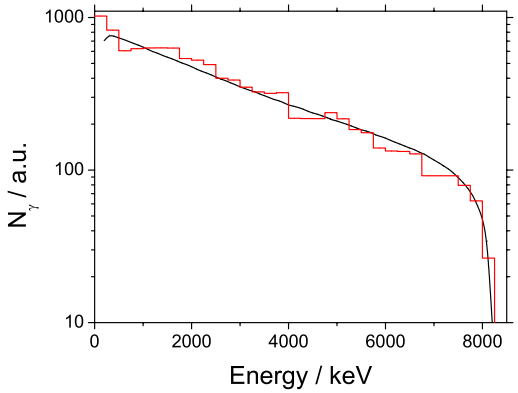


**Fig. 2** *Unfolded bremsstrahlung spectrum (the histogram) compared with simulated bremsstrahlung spectrum for an electron energy of 8.2 MeV.*

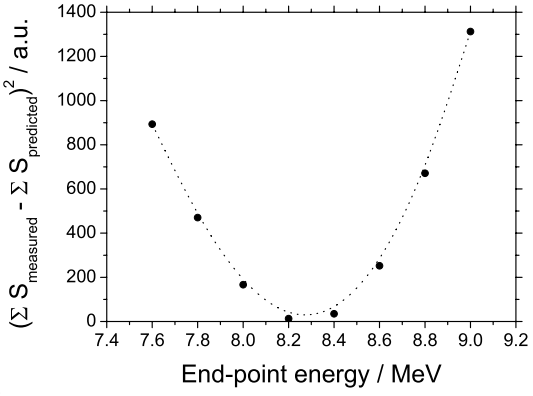


**Fig. 3** *Square difference between measured spectrum and predicted spectra for different end-point energies. The line is to guide the eye.*

[1] G. Rusev et al., This Report, p. 7
[2] CERN Program Library Long Writeup Q121, CERN, Geneva (CH), 1994
[3] A. Wagner et al., Wiss.-Tech. Ber. FZR-341 (2002) 38

# The E1-Strength of $^{208}$Pb in 1p-1h Continuum Shell-Model Approximation

E. Grosse, A. Wagner, R. Wünsch

We performed a continuum shell-model (CSM) calculation [1] in 1p-1h approximation for the closed-shell nucleus $^{208}$Pb. 27 proton and neutron shells defined by an average Woods-Saxon potential have been taken into account. Among them are four quasi-bound single-particle resonances which are subject to the cut-off technique [2]. Within the configuration space consisting of one nucleon above and one hole below the Fermi level 30 $1^-$ states can be formed. The residual nucleon-nucleon interaction mixes this configurations. Above a threshold, which is determined by the energy of the lowest decay channel, the Hamiltonian of the CSM has a continuous spectrum of eigenstates $\Psi_E^f$ and describes decaying states. In 1p-1h approximation of $^{208}$Pb the decay channels $f$ are restricted to the emission of a nucleon with a residual nucleus $^{207}$Pb or $^{207}$Tl described by a 1h-configuration. Other decay channels are not taken into account within this approximation. At certain energies $E_\rho$ the excitation probability of a state $\Psi_E^f$ exhibits a resonant behavior.

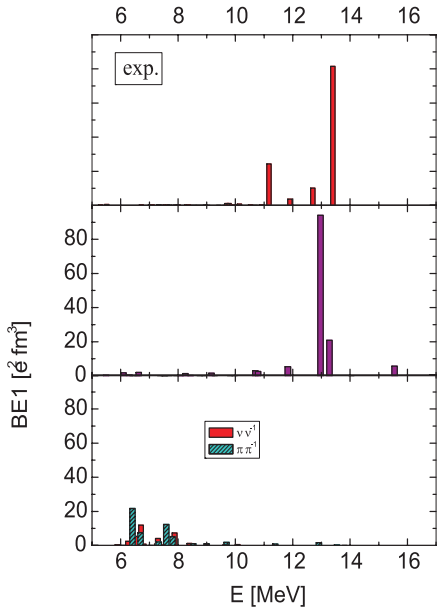


**Fig. 1** *$B(E1)$ strengths of the 1p-1h states of $^{208}$Pb calculated in continuum shell-model approximation without (lower panel) and with residual nucleon-nucleon interaction (central panel). The upper panel shows the measured strengths.*

Fig. 1 shows the calculated energies of the $1^-$ resonance states of $^{208}$Pb and their electromagnetic excitation probability $B(E1)$. The figure demonstrates the importance of the configuration mixing for the formation of the giant dipole resonance. Without residual interaction the E1-strength is distributed over many 1p-1h configurations at excitation energies between 6 and 10 MeV. Switching on the residual interaction leads to a concentration of the strength into a single state at 13 MeV.
The calculation in CSM approach yields a continuous excitation spectrum consisting of the coherent superposition of resonance contributions resulting from the various 1p-1h configurations and a quasi-elastic contribution with a smooth energy dependence. Since the momentum transfer is small in $\gamma$-excitation the latter is negligible in this reaction. Fig. 2 shows the calculated distribution of the $B(E1)$ strength in comparison to the incoherent superposition of the single resonance contribution. The figure demonstrates the influence of interference effects on the shape of the excitation spectrum and their importance for the visual size of the parameters of the observed resonances.

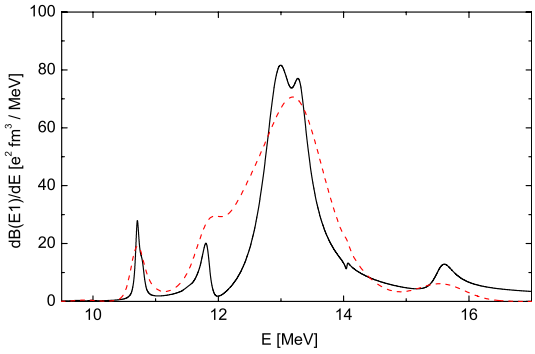


**Fig. 2** *Continuous $B(E1)$ distribution of $^{208}$Pb (full line) as a function of the excitation energy $E$ calculated in 1p-1h CSM approximation. The dashed line shows the incoherent superposition of the single resonance contributions assuming a Breit-Wigner shape with the calculated widths and excitation strengths.*

[1] C. Mahaux, H.A. Weidenmüller, Shell-model approach to nuclear reactions (North-Holland, Amsterdam, 1969); H.W. Barz, I. Rotter, J. Höhn, Nucl. Phys. A 275 (1977) 111
[2] W.L. Wang, C.M. Shakin, Phys. Lett. 32 B (1970) 421

# Identification of Isomers in the $N = Z + 1$ Nucleus $^{95}$Ag [G]

J. Döring[1] H. Grawe[1], K. Schmidt[1], R. Borcea[1], S. Galanopoulos[2], M. Gorska[1], S. Harissopulos[2], M. Hellström[1], Z. Janas[1,3], R. Kirchner[1], M. La Commara[1,4], C. Mazzocchi[1,5], E. Roeckl[1], R. Schwengner

For decades, spin-gap isomers have been predicted by shell-model studies for nuclei close to $^{100}$Sn [1]. These isomers are based on the attractive $g_{9/2}$ proton $g_{9/2}$ neutron residual interaction for holes in the upper part of the $g_{9/2}$ subshell lowering the excitation energy of certain stretched high-spin configurations such that the depopulation of these levels via $\beta$ decay can compete with the slow electromagnetic decay via a high-multipole $\gamma$ transition. Such a spin-gap isomer has been identified, for example, in $^{95}$Pd via $\beta$-delayed protons and $\gamma$ rays [2,3]. Applying this scenario to other nuclei in this mass region, high-spin isomers such as a $23/2^+$ $M3$ isomer in $^{95}$Ag or a $16^+$ $E6$ isomer in $^{96}$Cd were predicted [1] but not yet identified experimentally. Previous attempts to identify the decay of the predicted isomer in $^{95}$Ag concentrated on the measurement of $\beta$-delayed protons and $\beta$-delayed $\gamma$ rays [4], but without success. The electromagnetic decay was also searched for, but hampered by the low detection efficiency for $\gamma$ rays. We have carried out a new search for an isomeric $\gamma$ decay in $^{95}$Ag by using a composite Ge-detector array with high granularity.

The $^{95}$Ag nuclei were produced via the $^{58}$Ni($^{40}$Ca, $p2n$) reaction using a $^{40}$Ca beam of $3.94 \cdot A$MeV and 80 particle-nA provided by the GSI UNILAC accelerator. The beam impinged on a 2.8 mg/cm$^2$ thick $^{58}$Ni foil. The reaction products were stopped in a hot carbon catcher inside a FEBIAD-B2C ion source. The $A = 95$ recoils were separated from the other reaction products by the GSI on-line mass separator. A beam intensity of about 28 ions/s was obtained. For the detection of $\gamma$ rays, an array of 13 Ge crystals was used in close geometry around the deposition point of the mass-separated beam on a tape inside a plastic beam pipe. Positrons were measured with a plastic scintillator having an efficiency of about 85%. The decay of the activity was measured during deposition (grow-in method) for about 7.5 h, i.e., 5645 cycles with 4.8 s. In the off-line analysis, $\beta$-$\gamma$-$\gamma$ matrices with different dispersion were sorted, and the known $\beta$-delayed $\gamma$ rays from the $^{95}$Ag $\rightarrow$ $^{95}$Pd decay [4], such as the 1262 keV line, were observed. The high $\beta$-detection efficiency allowed also the sorting of $\gamma$-$\gamma$ coincidence events in anti-coincidence with positrons. In this matrix, three distinct $\gamma$-ray sequences have been found and assigned to the decay of three isomers in $^{95}$Ag, as shown in Fig. 1. The assignment of $\gamma$ rays depopulating the $23/2^+$ isomer at 2531 keV in $^{95}$Ag is supported also by a recent publication [5] where three $\gamma$ rays (164, 937 and 1117 keV) in $^{95}$Ag were observed in-beam for the first time.

Spin and parity assignments to the states in $^{95}$Ag are based on predictions by the shell model such as $9/2^+$, $1/2^-$ and $23/2^+$ for the ground state, the 344 keV and the 2531 keV isomers, respectively, on experimental level-energy systematics of $N = 48$ isotones and on the observed decay patterns.

Shell-model calculations have been performed in the minimum model space $(p_{1/2}, g_{9/2})$ for both protons and neutron using an empirical interaction. In this way, the level energies of the $1/2^-$ and $23/2^+$ isomers are well reproduced, and a $37/2^+$ state is predicted as a candidate for a high-lying $E4$ spin-gap isomer, as can be seen on the right side of Fig. 1. The wave function of the $37/2^+$ state reveals a close relation to isomers in neighbouring nuclei, namely the coupling of a $g_{9/2}$ proton to the $14^+$ isomer of $^{94}$Pd.

In summary, the long-standing search for the predicted $23/2^+$ spin-gap isomer in $^{95}$Ag has been successfully carried out at the GSI on-line mass separator. Sufficient yield and stable experimental conditions were obtained to perform detailed spectroscopic investigations. The results have been published recently [6].

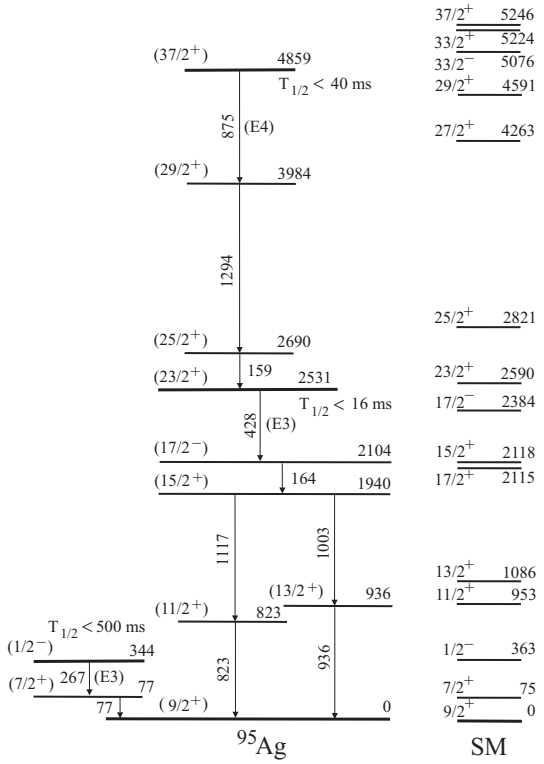


**Fig. 1** *Experimental decay scheme of isomers in $^{95}$Ag compared to empirical shell-model calculations.*

[1] K. Ogawa, Phys. Rev. C 28 (1983) 958
[2] E. Nolte and H. Hicks, Phys. Lett. 97B (1980) 55
[3] E. Nolte and H. Hicks, Z. Phys. A 305 (1982) 289
[4] K. Schmidt et al., Nucl. Phys. A 624 (1997) 185
[5] K. Lagergren et al., Eur. Phys. J. A 14 (2002) 393
[6] J. Döring et al., Phys. Rev. C 68 (2003) 034306

[1] *GSI Darmstadt;* [2] *NCSR Demokritos, Greece;* [3] *Warsaw University, Poland;* [4] *University of Naples and INFN, Italy;* [5] *University of Milan, Italy*

# Setup for a Photoactivation Experiment of Astrophysical Interest at ELBE

M. Erhard, A. Wagner, A.R. Junghans, K.D. Schilling, R. Schwengner, E. Grosse, B. Fertala[1]

The nucleosynthesis of heavy elements proceeds mainly via rapid and slow neutron-capture processes during supernova explosions or in red giant stars (AGB, asymptotic giant branch stars). 35 proton-rich (p-)nuclides, which cannot be reached by either of these processes are called p-process nuclei, and they are thought to be created in a sequence of proton-captures and/or photodisintegrations. Up to now most of the $(\gamma, \mathrm{n})$-, $(\gamma, \mathrm{p})$-, $(\gamma, \alpha)$-reaction rates of the p-nuclei averaged over a thermal spectrum have only been determined from theoretical models, although they are a decisive input to nucleosynthesis network calculations.

A powerful tool to deliver these urgently needed data is photoactivation: The bremsstrahlung spectrum can be used to mimic the Planck-distribution of $\gamma$-quanta present in stellar nucleosynthesis [1]. This simulated stellar photon bath is then used for activation experiments to be performed at different endpoint energies. The astrophysical reaction rates can then be deduced from the proper superposition of several bremsstrahlung spectra.

A first photoactivation experiment was performed with bremsstrahlung delivered from ELBE. To produce bremsstrahlung, a 4 $\mu$m thick Nb radiator was irradiated with electrons at currents of typically 500 $\mu$A. A photon flux of $\approx 10^8/(\mathrm{s} \cdot \mathrm{cm}^2 \cdot \mathrm{MeV})$ with endpoint energies between 5 and 20 MeV can be achieved inside the low-background environment of the nuclear physics cave. Parallel to photoactivation, a precise determination of the spectral shape and the integrated flux using calibration targets ($^{11}$B, $^{12}$C, $^{27}$Al) and HPGe detectors is possible. Half-lives for activation measurements are limited to $T_{1/2} \geq 10$ min due to access time constraints.

The measurement of $\gamma$- and/or X-rays from the radioactive decay of the reaction products has been realized in a low-level counting setup at VKTA[1], where a Germanium detector is shielded with ultra-low level lead to suppress background radiation. Based on this experience, a low-level measurement site was installed at ELBE which will be used for future activation experiments.

For the first test experiment, an enriched (97.31%) $^{92}$Mo target (of mass 2.0 g) was chosen. $^{92}$Mo has the highest isotopic abundance (14.84 %) and the second highest solar abundance (0.378 relative to $10^6$ Si atoms) of all p-nuclei. Its neutron (proton) separation energy is $S_n = 12.672$ MeV ($S_p = 7.456$ MeV). The tunneling probability $P$ for protons is estimated to be $\approx$10% at a photon energy of $E_\gamma = 12.6$ MeV which is slightly below the neutron threshold. A $\gamma$-ray spectrum measured after the irradiation is shown in Fig. 1.

In the $(\gamma, \mathrm{p})$-process, only the population of the isomeric state in $^{91}$Nb can be observed by $\gamma$-decay (see Fig. 2). The population of the 680 y ground state of $^{91}$Nb is suppressed by the large ground state spin of 9/2.

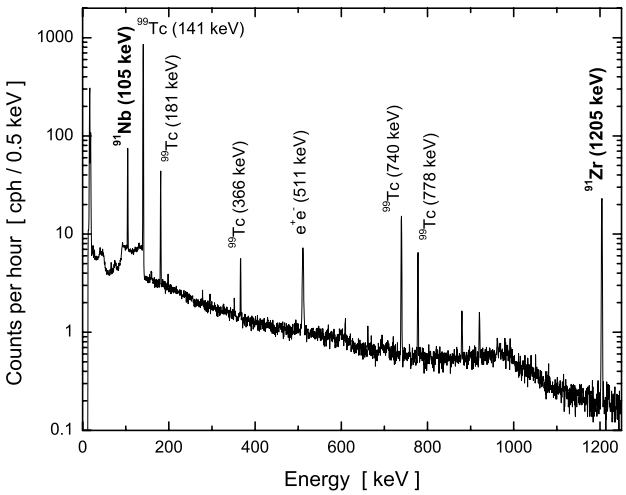


**Fig. 1** *$\gamma$-ray-spectrum of activated, enriched $^{92}$Mo (cf. text; electron energy: $E_{e^-} = 12.6$ MeV, electron current: $I_{e^-} \approx 500\ \mu$A, activation time: $t_{act.} \approx 118$ h).*

The 104.6 keV transition deexciting the $1/2^-$-isomer in $^{91}$Nb and the 1204.8 keV $\gamma$-ray following the electron capture from $^{91m}$Nb to $^{91}$Zr$^*$ are clearly visible in a spectrum measured after the photoactivation of $^{92}$Mo (Fig. 1). The 1204.8 keV line had a count rate of $\approx$1 Bq which corresponds to a total activity produced of $^{91m}$Nb of 50 Bq. This means that in a reasonable activation measurement period sufficient statistics can be accumulated.

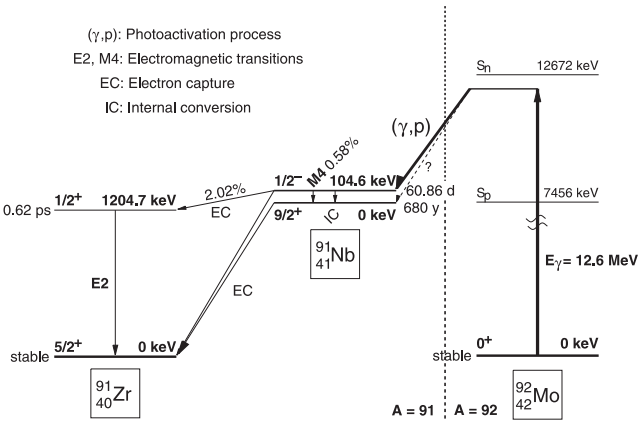


**Fig. 2** *Photoactivation of $^{92}$Mo via $(\gamma, \mathrm{p})$-process and successive radioactive decay channels [2]. (Not to scale.)*

Traces of $^{100}$Mo (0.37 %) yield five strong transitions from decays of $^{99}$Tc (Fig. 1), which may have been produced by $^{100}\mathrm{Mo}(\gamma, \mathrm{n})^{99}\mathrm{Mo}(\beta^-)^{99}\mathrm{Tc}$.

[1] P. Mohr et al., Phys. Lett. B 488 (2000) 127

[2] C.M. Baglin, Nuclear Data Sheets 86 (1999) 1

[1] *VKTA (Verein für Kernverfahrenstechnik und Analytik Rossendorf e.V.), Rossendorf*

# Pycnonuclear Reactions

A.V. Afanasjev[1] , L.R. Gasques[1], S. Frauendorf, and M. Wiescher[1]

Fusion reactions inside compact astrophysical objects can be divided into thermonuclear fusion and pycnonuclear processes. While thermonuclear fusion takes place in relatively hot and dilute plasmas inside stars with only the high-energetic components of the velocity distribution being important, pycnonuclear fusion happens at rather high densities where mostly low-energetic nuclei contribute to the fusion process. Pycno-nuclear reactions in neutron stars are considered as a possible energy source for $\gamma$-ray bursts. Neutron-rich nuclei are arranged on a lattice, the spacing of which is shrinking under the gravitational pressure of accreting material. At a critical distance nuclear fusion of lattice nuclei sets in. The detailed knowledge of the nuclear matter distribution is crucial for the determination of the pyconuclear fusion rates and their dependence on the densities inside the neutron star's crust. The Relativistic Hartree-Bogoliubov approach is used for calculating the density profiles for protons and neutrons in the nuclei involved in pycno-nuclear reactions. They are necessary nuclear structure inputs for estimating this critical lattice constant and the rates of these reactions. The rates are calculated within the optical model where the Pauli nonlocality of nuclear interaction is taken into account [1]. The figure illustrates the accuracy of the description of the S-factors obtained within such hybrid approach by comparing with reactions that are accessible in the laboratory. The agreement promises reliable predictions for the reactions in the neutron star. The work is progress and the final results will be reported later. [2].

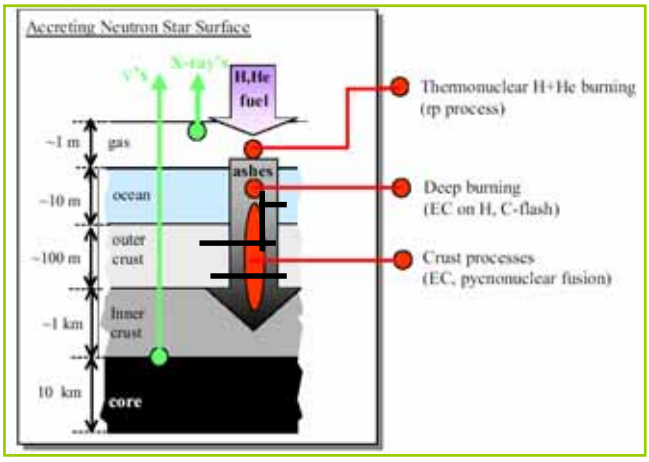


**Fig. 1** *Schematic illustration of pycno nuclear reactions is the crust of neutron stars*

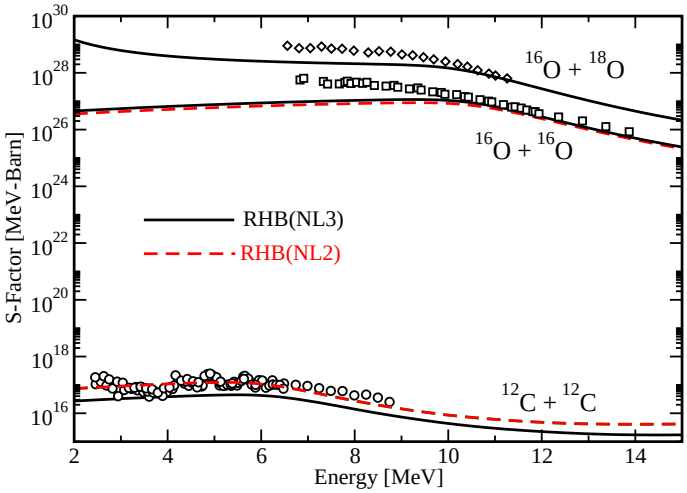


**Fig. 2**
*Calculated and experimental S-factors of indicated reactions. The calculations are based on the RHB densities obtained with the NL3 and NL2 parametrizations of the RMF Lagrangian.*

[1] L. C. Chamon, B. V. Carlson, L. R. Gasques, D. Pereira, C. De Conti, M. A. Alvarez, M. S. Hussein, M. A. Candino Ribeiro, E. S. Rossi, Jr, and C. P. Silva, Phys. Rev. C 66 (2002) 014610

[2] L. R. Gasques et al., in preparation

[1] *University of Notre-Dame, IN 46556, USA*

# Comparison of $S_{17}(E)$ Deduced from Direct Experiments and Coulomb Dissociation

A.R. Junghans, K.A. Snover[1], E.C. Mohrmann[1],

Precise predictions of the *production rate* of $^8$B solar neutrinos are important for limiting the allowed neutrino mixing parameters including possible contributions of sterile species and also for testing solar models. The predicted $^8$B production rate in the sun is based on solar model calculations that depend on measured reaction rates for the solar burning steps following the initial p+p fusion, the most uncertain of which has been the $^7$Be(p,$\gamma$)$^8$B rate. The currently recommended value for $S_{17}(0)$, the astrophysical S-factor for this reaction, is 21.4 $\pm$ 0.5(*expt*) $\pm$ 0.6(*theor*) eV b [1, 2]. It is based on recent *direct* measurements of $^7$Be(p,$\gamma$)$^8$B only. Coulomb dissociation of $^8$B and peripheral heavy-ion transfer reactions allow to deduce $S_{17}(0)$ by the theorem of detailed balance. A comparison of data of Coulomb dissociation experiments and direct measurements shows a systematic difference in the slope of $S_{17}(0)$, which lead to the conclusion that there is a so far not understood technique dependence of the astrophysical S-factor from both kinds of measurements [1].

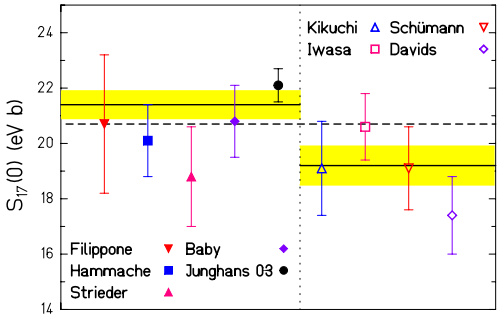


**Fig. 1** *$S_{17}(0)$ values and 1$\sigma$ experimental uncertainties from Descouvemont and Baye fits to data with $\bar{E}_{\rm c.m.} \leq 425$ keV as given in ref. [1]. The dashed line is the 20.7 eV b mean value from a fit to the full data set. The solid lines and shaded bands show the 21.4 $\pm$ 0.5 eV b and 19.2 $\pm$ 0.7 eV b mean values from the fits to direct and to CD data, respectively.*

Coulomb dissociation (CD) experiments, in which a secondary radioactive beam of $^8$B nuclei is dissociated into $^7$Be + p in the field of a heavy nucleus such as Au or Pb, have now been performed by several groups, ref. given in ref. [1]

The relative weighting of E1, M1 and E2 multipolarities in the virtual-photon spectrum responsible for the Coulomb breakup is very different than the weighting in the direct photon-emission spectrum.

In the virtual-photon spectrum, the E2 cross section, which is negligible in the direct process, is enhanced relative to E1 by several orders of magnitude and may not be negligible in the breakup cross section. E2 contributions estimated from measured breakup momentum distributions range from small but significant [3] to negligible [4], and are not given reliably by theory. The effect of the 630 keV $1^+$ M1 resonance is taken into account, while weaker M1 strength located at higher energies is not treated explicitly.

The $S_{17}(0)$ values deduced from CD data fall systematically below the direct values, as shown in Fig. 1 The theoretical uncertainty involved in extrapolating to $S_{17}(0)$ given through the choice of the model does not enter here as the same model was used in every case. The Descouvemont and Baye cluster model was chosen because it fits the the slope of the direct $S_{17}$(E) data very well.

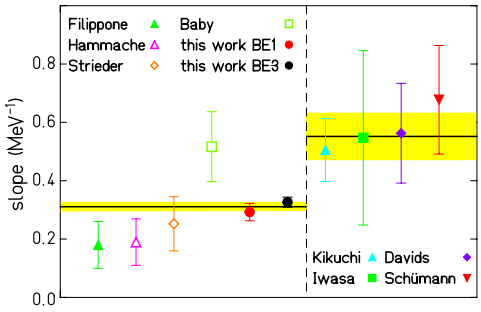


**Fig. 2** *Slope parameters determined from linear fits to direct and CD data The horizontal lines and shaded bands correspond to the mean values and uncertainties from direct and CD data, respectively.*

We have quantified the difference in energy dependence between direct and CD experiments by fitting a straight line of the form $S_{17}(\bar{E}_{\rm c.m.}) = a(1+b\bar{E}_{\rm c.m.})$ to data in the range $\bar{E}_{\rm c.m.} \leq 425$ keV and 830 keV $\leq \bar{E}_{\rm c.m.} \leq 1300$ keV. Fig. 2 displays $b$, the fitted slope, for each experiment. For the direct data, $S_{17}(\bar{E}_{\rm c.m.})$ values near the $1^+$ resonance were excluded, and the high-energy tail of the $1^+$ resonance was subtracted from $S_{17}(\bar{E}_{\rm c.m.})$ values above the resonance before fitting, based on the M1/DB ratio determined from our data. Since the CD $S_{17}(\bar{E}_{\rm c.m.})$ values do not include the $1^+$ resonance contribution, they were fitted directly. All of the fits had $\chi^2/\nu < 1.3$, indicating that the straight line fit is a good approximation. The results, shown in Fig. 2, demonstrate a systematic difference in slope between the 2 types of experiments. From the direct experiments the mean slope is 0.311 $\pm$ 0.014 MeV$^{-1}$, with $\chi^2/\nu = 1.9$, and the mean slope determined from the CD data is 0.552 $\pm$ 0.079 MeV$^{-1}$, with $\chi^2/\nu = 0.2$. Increasing the uncertainty on the direct mean by the factor $(1.9)^{1/2}$ to account for the fit $\chi^2/\nu$, we find the probability that these 2 results arise from the same parent distribution is $P(\chi^2, \nu) = 0.003$. Because of the not understood different energy dependences observed in CD and direct experiments, it is difficult to know how to make a meaningful quantitative $S_{17}(0)$ comparison and the recommended value should based on direct measurements only.

[1] A.R. Junghans et al., Phys. Rev. C68 (2003) 065803
[2] J. Bahcall et al., Phys. Rev. Lett. 92 (2004) 121301
[3] B. Davids et al., Phys. Rev. Lett. 86 (2001) 2750
[4] F. Schümann et al., Phys. Rev. Lett. 90 (2003) 232501

[1] *CENPA, University of Washington, Seattle, U.S.A.*

# Nuclear Tidal Waves

S. Frauendorf

In nuclear structure textbooks, two types of collective excitations are distinguished: rotations and vibrations. Rotation corresponds to a fixed deformed surface that rotates, i. e. the $B(E2)$ values do not change strongly with the angular momentum $I$. The transition energy between the levels of a rotational band is given by $E(I+2)-E(I) \approx (I-j)/\mathcal{J}$, where the alignment $j \geq 0$. The angular frequency is $\omega(E(I+2)-E(I))/2)$. In a plot $I(\omega)$, a rotational bands appears as a nearly straight line that intercepts the $I$ axis, as for example $N = 90$ in Fig. 1 and AMR in Fig. 2. In contrast, a quadrupole vibration corresponds to an oscillating surface. The distance between the vibrational multiplets is the vibrational frequency $\Omega$. The yrast state in each multiplet is a wave traveling over the nuclear surface like a tidal wave travels the surface of the ocean. Its angular frequency is constant $\omega = \Omega/2$. The angular momentum increases with the square root of the amplitude of the wave, which means $B(E2) \propto I$. The vibrational band of these tidal waves would appear as a vertical line in Figs. 1 and 2. As a rule, vibrations in real nuclei are substantially anharmonic. In a $I(\omega)$ plot, anharmonic tidal waves will have finite slope and intercept the $\omega$ axis. The $B(E2)$ values will grow more slowly than $\propto I$. Fig. 2, demonstrates, how the anharmonic tidal waves develop into a a rotation as $N$ increases from 84 (spherical nucleus) to 92 (deformed nucleus).

In the reference frame rotating with $\omega$, the tidal wave corresponds to a statically deformed shape, which permits us to employ the Cranking Model for a microscopic description. Marshalek [1] demonstrated that in the harmonic limit of small deformation the self-consistent equations of the Cranking model become the RPA equations for quadrupole vibrations. Fig. 2 shows a calculation by means of the Tilted Axis Cranking model with a QQ-interaction [2]. The high-spin part (AMR) is an antimagnetic rotational band (see [3]). The low spin part is the tidal wave. Its frequency is well reproduced (no fit of the QQ-coupling constant). The experimental $B(E2)$ values, which are compared in Tab. 1 with the calculations, show the expected roughly linear increase with $I$. Note that the deformation of the tidal wave becomes larger than the one of the antimagnetic rotor.

In the case of the low-spin states of even-even nuclei, the tidal waves correspond to an axial or triaxial shape turning about a principal axis. In general, the rotational axis does not need to coincide with a principal axis of the shape and may also change with $I$. Such a case is realized in $^{182}$Os, as discussed in [4]. Tidal waves are a quite common phenomenon in weakly deformed nuclei. A more systematic analysis is planned. An alternative theoretical description based on angular momentum projection techniques is being tested.

| tidal wave | | | antimagnetic rotor | | |
|---|---|---|---|---|---|
| I | exp | calc | I | exp | calc |
| 2 | 23.0 (15) | 18 | 12 | 39 (2) | 25 |
| 4 | 46 (6) | 43 | 14 | 29 (3) | 25 |
| 6 | 62 (20) | 56 | 16 | 25 | 25 |

**Tab. 1** *$B(E2, I \rightarrow I-2)$ values in Weisskopf units.*

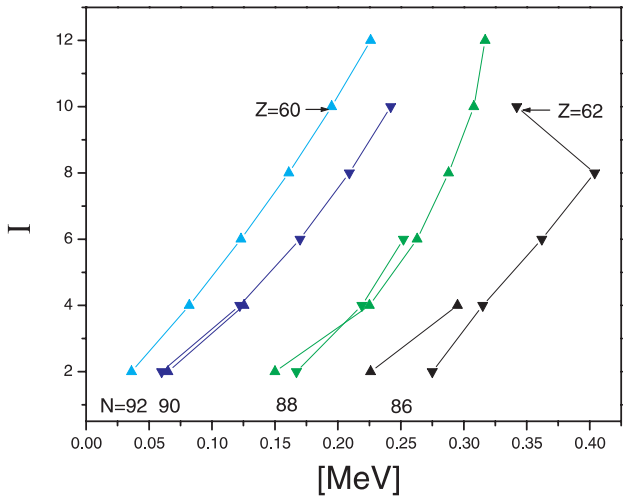


**Fig. 1** *Angular momentum as function of the angular frequency for the yrast levels of the even-A Nd and Sm isotopes. Lines are drawn to guide the eye.*

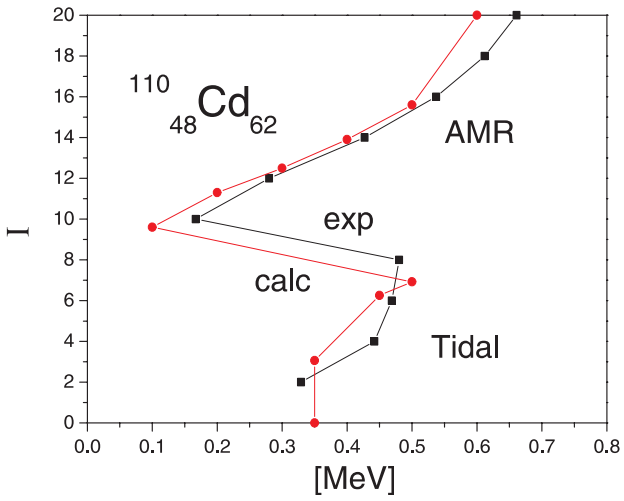


**Fig. 2** *Angular momentum as function of the angular frequency for the yrast levels in $^{110}$Cd.*

[1] E. Marshalek, Phys. Rev. C 54 (1996) 159
[2] S. Frauendorf Nucl. Phys. A 677 (2000) 115
[3] A.J. Simons et al., This Report p. 20
[4] L.K. Pattison et al., This Report p. 18

# Neutron-Proton Pairing in Rotating $N \sim Z$ Nuclei: Dominance of the Isovector Component

A. V. Afanasjev[1] and S. Frauendorf

The rotational features of the $N \approx Z$ $A \sim 60-80$ nuclei were systematically studied within the cranked relativistic mean field (CRMF), the cranked relativistic Hartree-Bogoliubov theories, and the cranked Nilsson-Strutinsky (CNS) approach. Good agreement (comparable with the one seen away from the N = Z line) between experiment and CRMF and CRHB theories is shown in figure. Our analysis suggests that **(i)** the pairing is very weak at high spin in these systems, **(ii)** available experimental high-spin data do not require the introduction of the $t = 0$ $np$-pairing into the models, and, thus, do not provide any evidence for this type of pairing. In addition, the low-spin data and band crossing regions are reasonably well described by the CRHB theory [2, 3, 4].

The physical picture emerging from the present systematic analysis of rotating $N \approx Z$ nuclei is consistent with that suggested in Ref. [1]: there is no isoscalar $t = 0$ $np$-pair field but a strong isovector $np$-pair field at low spin, the strength of which is defined by the isospin symmetry. At high spin, the isovector pair field is destroyed and the data are well described by the calculations assuming zero pairing.

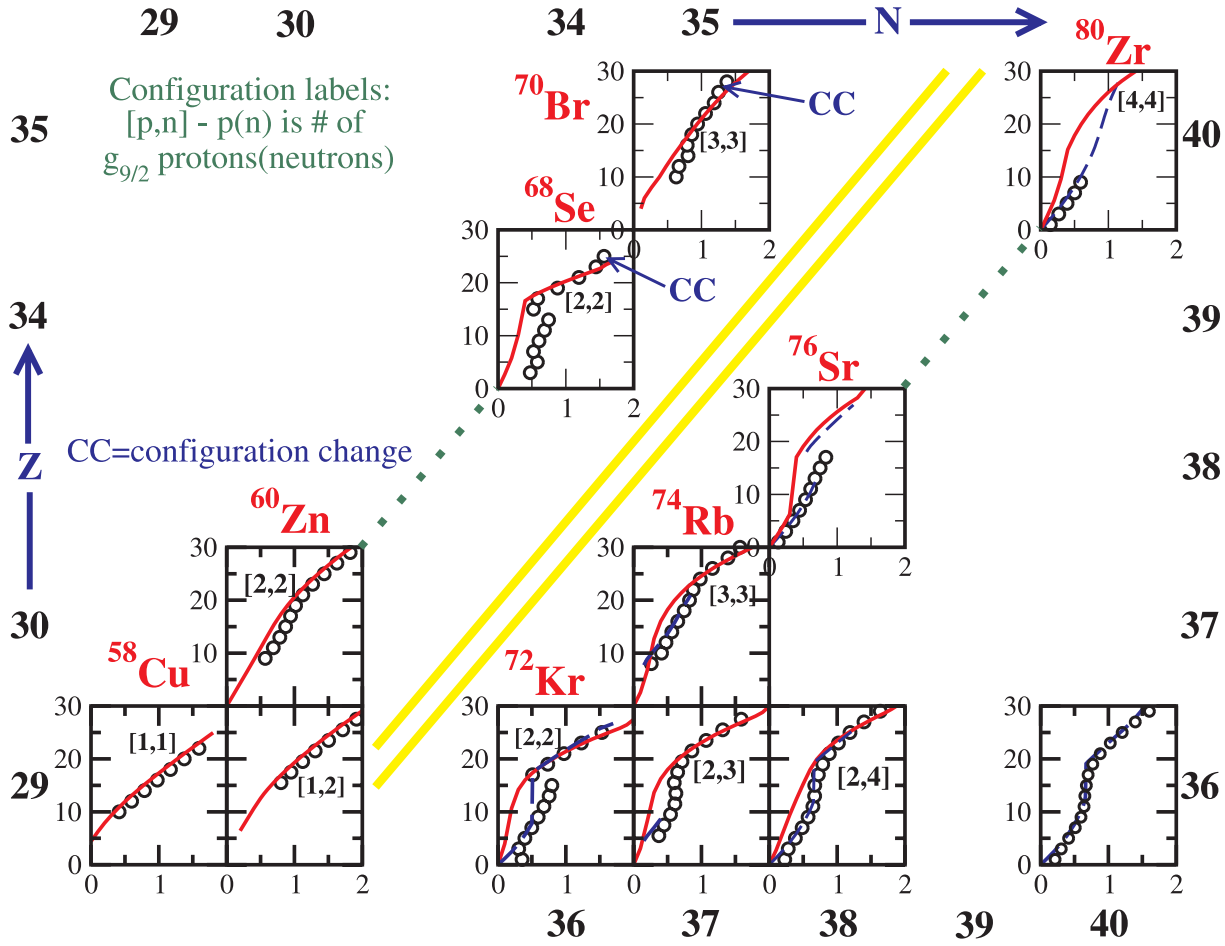


**Fig. 1** *Angular momentum of the deformed structures (shown as open circles) in the $N \approx Z$ nuclei compared with the results of the CRMF (solid lines) and CRHB (dashed lines) calculations.*

[1] S.G. Frauendorf and J.A. Sheikh, Nucl. Phys. A 645 (1999) 509
[2] A.V. Afanasjev and S. Frauendorf, Nucl. Phys. A, in press; and in preparation
[3] N.S. Kelsall et al., Phys. Rev. C 65 (2002) 024309, and EuroPhysical Journal A, in press
[4] C.D. O'Leary et al., Phys. Rev. C 67 (2003) 021301(R)

[1] *University of Notre-Dame, IN 46556, USA*

# Multi-Phonon Vibrations at High Angular Momentum in $^{182}$Os

L.K. Pattison[1], D.M. Cullen [1], J.F. Smith[1], P.M. Walker[2], H.M. El-Masri[2], Zs. Podolyák[2], R.J. Wood[2], C. Wheldon[2], C. Scholey[3] G. Mukherjee[4], D. Balabanski[5], M. Djongolov [6], Th. Dalsgaard [7], H. Thisgaard[7], G. Sletten[7], F. Kondev[8], D. Jenkins[8], G.D. Dracoulis[9], G.J. Lane[9], I.-Y. Lee[10], A.O. Macchiavelli[10], D. Almehed[11], and S. Frauendorf

In well deformed nuclei, high-K isomers appear if the angular momentum projections on the symmetry axis of the excited quasiparticles add up to large values. The collective excitations on such isomers are regular rotational bands. In contrast, we observed a structure built on the $K^\pi = 25^+$ six-quasiparticle isomeric state, which consists of two slightly irregular sequences of interlinked $E2$ transitions with approximately the same transition energies (see Fig. 1). Normally one would observe gradually increasing transition energies which would span a much larger energy range, like those in the g- and t-bands in Fig. 1. The sequence is interpreted as a multi-phonon excitation. The observation of the twelve-phonon excitation is a surprise for nuclear physics. It is the consequence that the vibrational band forms the yrast line, which prevents fragmentation over more complex excitations. Using the possibility to describe the yrast sequence of multi-phonon bands by means of the Tilted Axis Cranking method (SCTAC, see [2]), we were able to theoretically describe the new structure (see Fig. 2). The vibrational mode is a combination of a non-axial deformation with an change of the orientation of the shape relative to the angular momentum vector. Work hass been published in [3].

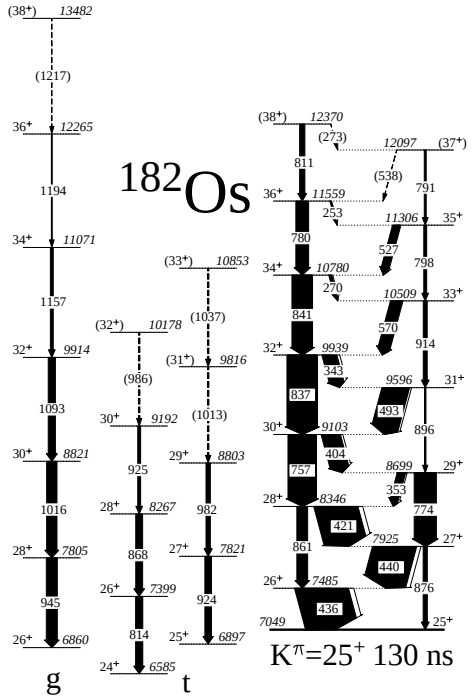


**Fig. 1** *Partial level scheme for $^{182}$Os showing the new structure above the 130 ns isomeric state. The extensions to the $K \approx 0$ ground-state band (g) and the $K \approx 8$ band (t) are also shown.*

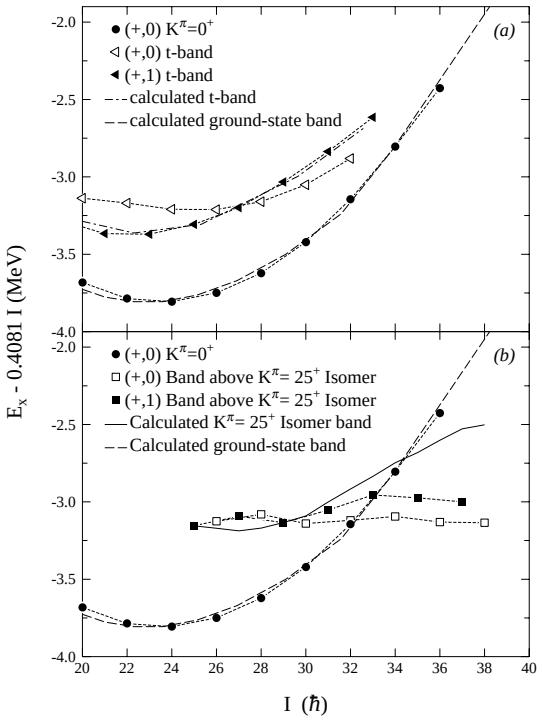


**Fig. 2** *Comparison of the experimental excitation energies of the states with those predicted by the SCTAC calculation for $^{182}$Os.* **(a)** *The $K^\pi = 0^+$ ground-state and t bands, and* **(b)** *the $K^\pi = 0^+$ ground-state band and the structure above the $K^\pi = 25^+$ isomer.*

[1] L.K. Pattison et al., Phys. Rev. Lett. 91 (2003) 182501
[2] S. Frauendorf, Tidal Waves, This Report p. 16

[1] *Schuster Lab., University of Manchester, Manchester, M13 9PL, U.K.*
[2] *Department of Physics, University of Surrey, Guildford, GU2 7XH, U.K.*
[3] *Oliver Lodge Laboratory, University of Liverpool, Liverpool, L69 7ZE, U.K.*
[4] *Department of Physics, University of Massachusetts, Lowell, Massachusetts 01854, USA*
[5] *Faculty of Physics, University of Sofia, BG-1164 Sofia, Bulgaria.*
[6] *Department of Physics and Astronomy, University of Tennessee, Knoxville, Tennessee 37996, USA*
[7] *Niels Bohr Institute, Blegdamsvej 17, DK-2100, Copenhagen, Denmark*
[8] *Physics Division, Argonne National Laboratory, Argonne, Illinois 60439, USA*
[9] *Department of Nuclear Physics, RSPhysSE, Australian National University, Canberra, ACT 0200, Australia*
[10] *Lawrence Berkeley National Laboratory, Berkeley, California 94720, USA*
[11] *Department of Physics, UMIST, P.O. Box 88, Manchester, M60 1QD, U.K*

# Evidence for Composite Chiral Bands

S. Frauendorf, U. Garg[1] , S. Zhu[1], J. Timár[2]

The rotational motion of triaxial nuclei attains a chiral character if the angular momentum has substantial projections on all three principal axes of the triaxial density distribution [1]. Fig. 1 illustrates how chirality emerges from the combination of the triaxial geometry with an axis of rotation that lies out of the three symmetry planes of the ellipsoid. The three components of the angular momentum vector form either a left-handed or a right-handed system, which manifest themselves as two degenerate rotational bands—the chiral doublet. This argument, which is based only on the symmetry of the rotating triaxial nucleus, is independent of how the three components of the angular momentum are composed. If one proton aligns its angular momentum with the short axis, one neutron hole aligns its angular momentum with the long axis, and the collective angular momentum generated by all other nucleons aligns with the intermediate axis, one has the simplest possibility of a chiral configuration, which was studied both theoretically and experimentally in a number of odd-odd nuclei in the mass 134 and 105 regions. If the geometrical concept of chirality is correct it must also appear for more complex configurations that have substantial angular momentum components along the three principal axes. We report the first observation of a pair of chiral bands in an odd-A nucleus $^{135}$Nd (see Fig. 2). In this case, the angular momentum of *two* $h_{11/2}$ protons is aligned with the short axis and of one $h_{11/2}$ neutron hole is aligned with the long axis. The observation is consistent with Tilted Axis Cranking (TAC) calculations. The resulting chiral configuration is illustrated in Fig. 1. A second composite pair of chiral bands, which is composed of two $h_{11/2}$ neutrons and one $g_{9/2}$ proton hole, may have been found in $^{105}$Rh. TAC calculations are on the way. Our results represent an important confirmation of the geometrical interpretation in terms of broken chiral symmetry [1], which claims that pairs of nearly degenerate ΔI=1 bands with the same parity appear whenever there is a chiral geometry of the angular momentum components, irrespective of how they are composed. The work on $^{135}$Nd is published in [3]. Due to limited space, the full list of collaborators could not be included.

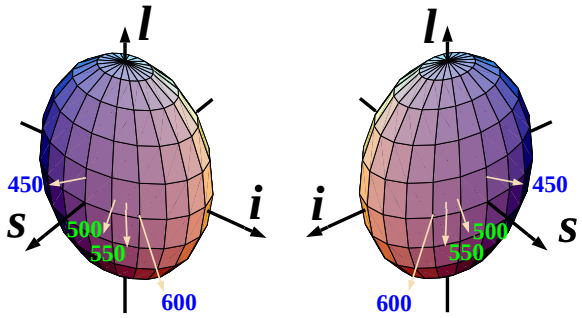


**Fig. 1** *The orientation of the total angular momentum vector, I, with respect to the axes of the triaxially deformed density distribution in $^{135}$Nd (light arrows) for different rotational frequencies from the TAC calculations. The numbers show the rotational frequency in keV. The labels l, s and i stand for long-, short- and intermediate-axis, respectively. In the order s-i-l, these axes form a "right-handed" system (left part of the figure) and a "left-handed" system (right part of the figure)—a chiral doublet.*

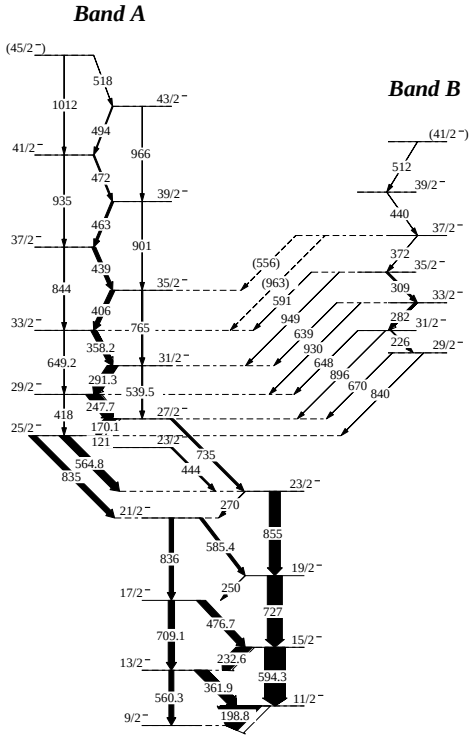


**Fig. 2** *Partial level scheme showing the $\pi h_{11/2}^2 \nu h_{11/2}^{-1}$ band and the newly observed sideband of $^{135}$Nd. Bands A and B are interpreted as the chiral pair.*

[1] S. Frauendorf, Rev. Mod. Phys. 73 (2001) 463
[2] S. Zhu et al., Phys. Rev. Lett. 91 (2003) 132502

[1] *Physics Department, University of Notre Dame, Notre Dame, IN 46556, USA*
[2] *Institute of Nuclear Research, Pf. 51, 4001 Debrecen, Hungary*

# Evidence for Antimagnetic Rotation in $^{106}$Cd

A.J. Simons[1], R. Wadsworth[1], D.G. Jenkins[1], R.M. Clark[2], M. Cromaz[2], M.A. Deleplanque[2], R.M. Diamond[2], P. Fallon[2], G.J. Lane[2], I.Y. Lee[2], A.O. Macchiavelli[2], F.S. Stephens[2], C.E. Svensson[2], K. Vetter[2], D. Ward[2], and S. Frauendorf

Recently a new type of rotational band consisting of magnetic dipole (M1) transitions in nearly spherical nuclei has been discovered in various mass regions (see [1]). The orientation of these rotors is specified by the current distribution of the high-j nucleons involved in the configurations rather than by their overall nuclear density distribution. This has been verified through lifetime measurements, which indicate that these structures have very small quadrupole deformations. For these nuclei, the current loops of the valence nucleons break the isotropy as illustrated in Fig. 1a. These loops generate a magnetic dipole vector that rotates and produces the strong M1 transitions. The name "magnetic rotation" alludes to the fact that it is the current loops and the magnetic dipole that are rotating in space. Fig. 1b shows an alternative arrangement of high-j proton-hole and neutron-particle current loops which also breaks the axial symmetry about the total angular momentum vector. This coupling can lead to a new kind of rotational band in near-spherical nuclei that has been termed "antimagnetic rotation" [1]. This is because the configuration can also be considered as being composed of two "shears-like" sub-systems (each consisting of one proton-hole and and one neutron particle in the example shown) of the magnetic type, the magnetic moments of which add such that the total transverse moment is zero. The angular momentum vectors of the valence proton holes are antiparallel at the band head. The angular momentum increases by gradually alignment of these two vectors. "Antimagnetic bands" should consist of regular sequences of energy levels differing in spin by $2\hbar$ and that they should decay by weak electric quadrupole (E2) transitions, the B(E2) values of which should decrease with increasing spin. Recent work in the light Pd isotopes [2] has provided the first tentative evidence for such structures; however, the decrease of the B(E2) values remained to be proven. We have studied the lifetimes of states in the lowest lying positive parity band in $^{106}$Cd by means of the DSAM technique. The B(E2) values derived show the expected small values and rapid decrease with increasing spin. Tilded Axis Cranking calculations (see [1]) have been carried out, which predict that following the initial alignment of the $h_{\frac{11}{2}}$, $g_{\frac{7}{2}}$ neutrons at spin 16, the $g_{\frac{9}{2}}$ proton hole vectors are almost antiparallel. As the spin increases these vectors gradually close on the aligned neutron vectors and the spherical symmetry is restored. The measured B(E2) values are in remarkable agreement with the calculations. These results provide the first firm evidence for the antimagnetic rotation form of the shears mechanism. The work is published in [3].

[1] S. Frauendorf, Rev. Mod. Phys. 73 (2001) 463
[2] S. Zhu et al., Phys. Rev. C 64 (2001) 041302
[3] A.J. Simons et al., Phys. Rev. Lett. 91 (2003) 162501

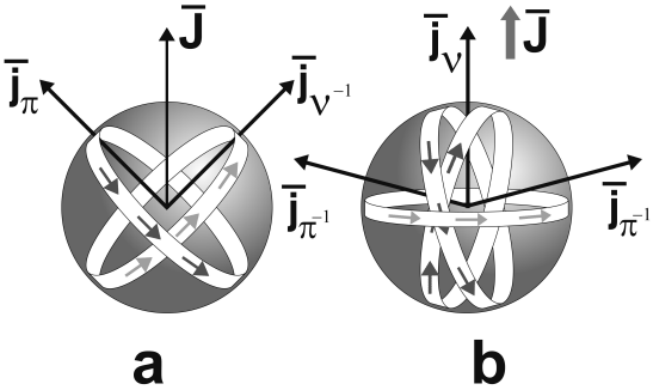


**Fig. 1** *Illustration of the shears mechanism for (a) magnetic and (b) antimagnetic cases.* $\overline{\mathbf{J}}$ *is the total intrinsic angular momentum vector and* $\overline{\mathbf{j}}_\pi$ *and* $\overline{\mathbf{j}}_\nu$ *are the proton and neutron components respectively. The vectors are not to scale. Both figures show the near-bandhead configuration for each mechanism.*

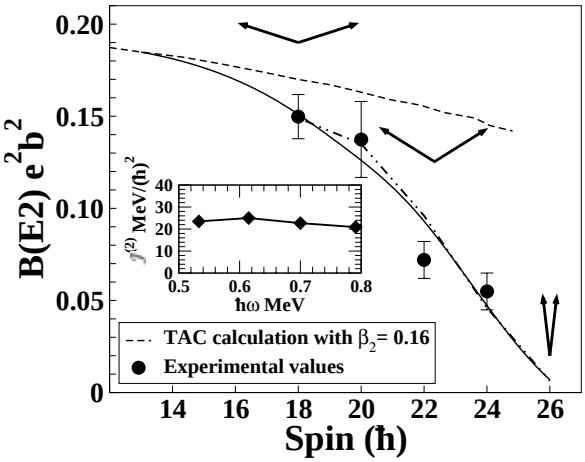


**Fig. 2** *Plot of B(E2) values against spin for band 1 in* $^{106}$*Cd. The solid line represents the B(E2) values obtained from TAC calculations through minimizing the energy in the rotating frame for a range of* $\beta_2$ *and* $\gamma$ *values. The arrows show the relative positions of the* $g_{\frac{9}{2}}$ *proton hole vectors at various spins. The insert shows the experimental dynamic moment of inertia as a function of rotational frequency.*

[1] *Department of Physics, University of York, Heslington, York Y010 5DD, U.K.*
[2] *Nuclear Science Division, Lawrence Berkeley National Laboratory, Berkeley, California 94720*

# Test Measurements of Position-Sensitive Micro-Channel-Plate Detectors

K. Kosev, A. Wagner, N. Nankov[1], K.D. Schilling, H. Sharma[2]

For the detection of ions at medium and low kinetic energies, a time-of-flight (TOF) spectrometer is under construction using position-sensitive TOF detectors. In order to study the performance of these detectors, experimental investigations and data analysis have been carried out. The characterisation of the resolving capabilities of these detectors is an important issue for the TOF spectrometer [1].

An intense, broad beam of alpha particles bombarded a metal plate with holes called a mask (Fig. 1). Only those particles which penetrated the holes could reach the position-sensitive detector and form the mask image. The detector consisted of a pair of selected rimless micro-channel-plate (MCP) detectors in chevron configuration supported by a pair of partially metallized ceramic rings and a two-dimensional delay-line anode. The operation of the system required two DC voltages for the MCP front and back contacts and three voltages for the support plate (holder) and the wires of the delay line. The position of the detected particle was derived from the time difference signal at both ends of the delay lines. The detector setup was operated inside a vacuum chamber set at about $3.4 \times 10^{-8}$ mbar.

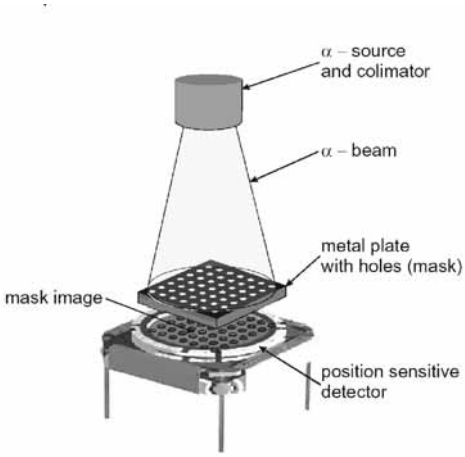


**Fig. 1** *Test setup of the position-sensitive MCP detector.*

A dedicated electronics setup was used for these measurements. The DLA-TR6 block from the company "RoentDek" combined up to six differential amplifiers and constant-fraction discriminators [2]. The four wire pairs from both delay-line ends of each dimension were connected to vacuum feedthroughs by a twisted-pair wire configuration. The single-path signal propagation time on the delay-line anode was about 0.71 ns/mm corresponding to 1.42 ns/mm in the 2D image. The difference between the signal arrival times at both ends of each delay-line was proportional to the position on the MCP in the respective dimension. The timing signals were measured by CAEN V775 TDC VME modules and recorded by the GSI MBS data acquisition system [3].

As time reference (start of the TDC) either MCP back or front signals were taken. As one could expect the time sum of these arrival times was nearly constant (Fig. 2).

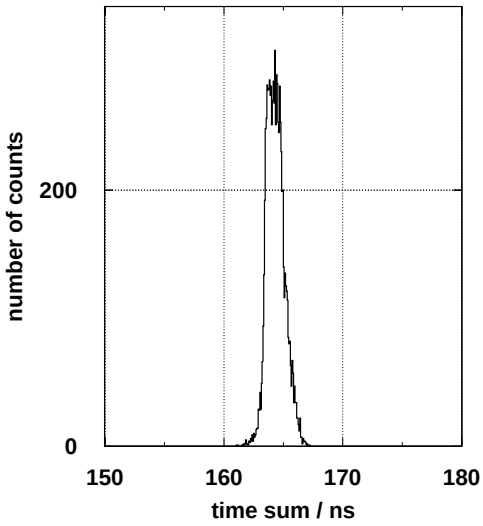


**Fig. 2** *Distribution of the time sum.*

The inaccuracy in the time sum spectrum determines the position resolution of the system which was found to be around 1mm. From the single wire spectra the 2D mask image was obtained as shown in Fig. 3.

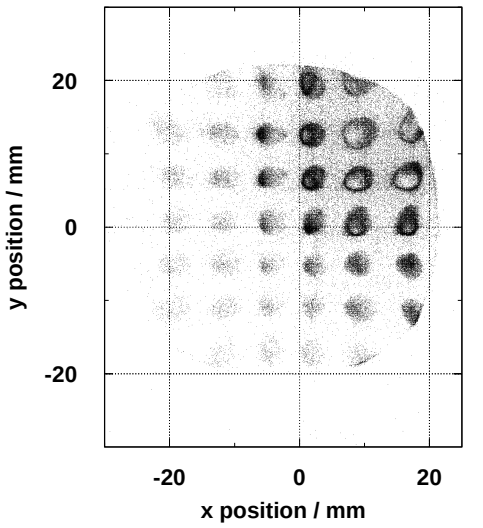


**Fig. 3** *Image of the two-dimensional position distribution.*

[1] H. Sharma et al., Wiss.-Tech. Ber. FZR-372 (2003) 36
[2] RoentDek GmbH: http://www.roentdek.com
[3] Multi-Branch-System: http://daq.gsi.de

[1] *Institute for Nuclear Research and Nuclear Energy, Sofia, Bulgaria*
[2] *now at: Saha Institute of Nuclear Physics, Calcutta-700 064, India*

# ELBE-n-ToF: Status of the Project and Expected Neutron Beam Properties

A.R. Junghans, E. Grosse, K. Möller, and A. Wagner for the n-ToF collaboration

The ELBE-n-ToF facility will be used for measurements of the energy dependence of neutron interaction cross sections in the keV to MeV range. For the production of neutrons at ELBE a radiator, which is hit by the accelerated electrons, simultaneously serves to convert these into bremsstrahlung photons and to generate neutrons with them. For both purposes a high atomic number is advantageous for the radiator, which also has to sustain the power introduced by the ELBE-beam into a rather small volume. For these purposes a liquid Pb radiator flowing in a square Mo pipe was found to be the best choice and – using a test stand installed at the MHD division of the ISF at the FZR – the practicability of such a device was proven. The actual radiator set-up is presently in the final design phase and its construction and installation will be finished within a year [1].
Fig. 1 shows the floor plan of the neutron-cave with the ELBE-n-ToF target and beam dump. The planned experimental set-up is behind a collimator with a minimal flight path of 3.6 m.

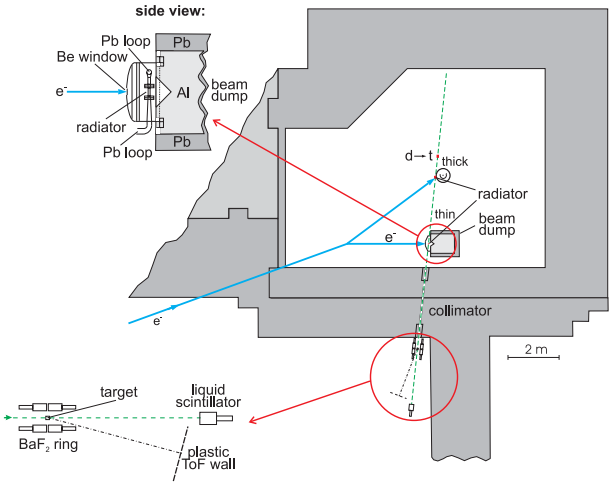


**Fig. 1** *Floorplan of the ELBE-n-ToF setup in the neutron cave. Inserts show a cut through the neutron radiator and the planned experimental site.*

A 3D rendering of the proposed design is shown in Fig. 2. The target and beam-dump assembly is located on a spindle lift platform and for radiation protection it can be lowered into a lead house when not in use. This mechanism also allows the operation of the Tungsten neutron target and the DT neutron generator sharing the same cave. The electron beam enters the Pb-Mo radiator housing through a Beryllium window, especially designed for good thermal stability and low scattering [2] After passing through the radiator the beam is stopped in a water-cooled aluminum beam dump.
Extensive numerical simulations were performed to optimize the radiator geometry and to predict the expected neutron beam properties. A compromise had to be found between the neutron intensity and the neutron energy resolution to be obtained from the measurement of their time of flight (tof) in a rather short flight path allowing a large solid angle for a given size of the target to be hit by the neutrons. Optimum values are a radiator cross section of 11 mm × 11 mm and a neutron emission perpendicular to the e-beam into a collimator imbedded into the 2.8 m thick shielding wall. The intensity peak of the neutrons produced by 30 - 40 MeV electrons in Pb lies at about 2 MeV and it allows to well cover the range of 0.2 to 8 MeV, when an absorber containing $^{6}$Li is used to suppress all slower neutrons. The repetition rate matched to these energies and to the total neutron flight path of 3.6 m is 1.6 MHz, the 3rd subharmonic of the ELBE 'standard' of 13 MHz.

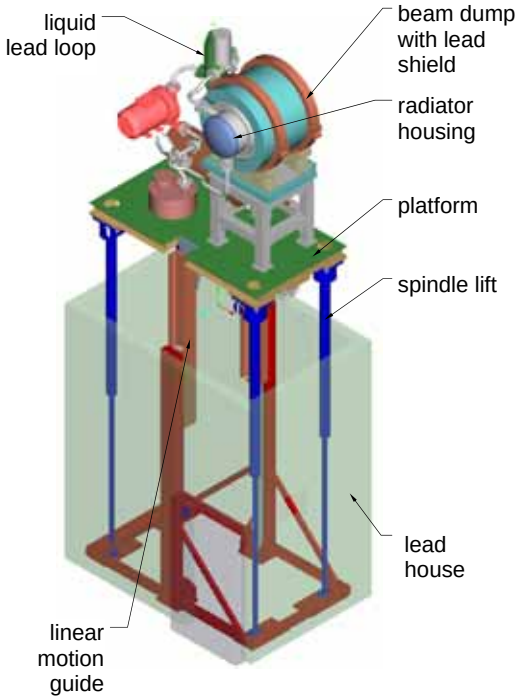


**Fig. 2** *3D rendering of the ELBE-n-ToF facility.*

Neutrons of these energies are of special interest for the transmutation of the even Pu isotopes and other minor actinides produced from Pu in fission reactors. These nuclides make up a large fraction of the long lived activity of the burnt down fuel rods, especially when they originally contained $^{239}$Pu. The cross sections of reactions allowing their transmutation to shorter lived fission products are of particular interest, such that efforts especially suited for their determination are planned in several countries; within the 6th framework program the European Union has formulated especially urgent 'nuclear data needs' to be met within its Integrated Project EUROTRANS.
As can be seen in the table below, ELBE is especially suited to do measurements in this energy range; it clearly surpasses all existing high resolution neutron beams in its luminosity - including nToF at the CERN-PS. The proton accelerator based neutron sources at Los Alamos

and the planned Oak Ridge Neutron Spallation Source loose a big portion of their intensity advantage over ELBE, when they increase their flight path such that they match the energy resolution of $< 1$ % expected for ELBE-n-ToF. The neutron beam properties predicted on the basis of the present e-beams at ELBE are listed in the first of the three columns dealing with ELBE. The next one shows the improvements expected when the planned laser driven photo-cathode electron injector allows to increase the number of electrons in each bunch to drive the accelerator to its design beam power at the above-mentioned 1.6 MHz.
The last column lists the expected performance of ELBE-n-ToF when the repetition rate is reduced by another factor of 8 to allow an undisturbed tof-spectroscopy with even slower neutrons of 3 keV up to 200 keV. These energies are of major interest for the understanding of the cosmic creation of the heavy elements by the successive accumulation of neutrons. Theoretical arguments based on rather low statistics laboratory data predict several scenarios for this accumulation: Slow s-processes at stellar temperatures equivalent to 15 - 30 keV follow the 'valley of stability' in the isotopic landscape. Laboratory experiments to determine the crucial nuclear data have been performed largely at the installations labelled ORNL-Orela and especially at FZK-VdG at Karlsruhe. From the comparison of their n-beam properties the potential for improved data from ELBE is obvious; preparations for a scheme of partial thermalisation of the faster neutrons emitted from the Pb radiator are under way. For many neutron rich nuclides a much higher neutron flux than obtainable in stars is needed; it is expected to exist during short periods of a supernova event or during the close encounter of a neutron star with another star. Here temperatures are expected to reach 300 keV and cross-section measurements of importance for the understanding of such processes may profit from both the neutron tof alternatives described above.

**Tab. 1**
*Parameters of operational and planned neutron time of flight facilities.*

| n-ToF-facility | CERN nTOF | LANL NSC | ORNL SNS | FZK VdG | ORNL Orela | IRMM Gelina | ELBE | ELBE with photo-gun |
|---|---|---|---|---|---|---|---|---|
| bunch charge /nC | | | | | | | 0.1 | 0.7 |
| power /kW | 45 | 64 | 2000 | 0.2 | 8 | 7 | 6 | 40 |
| rate /$s^{-1}$ | 0.4 | 20 | 60 | $25 * 10^4$ | 525 | 800 | $16 * 10^5$ | $16 * 10^5$ |
| fligh path /m | 183 | 20 | 20 | 0.8 | 40 | 20 | 4 | 4 |
| n-bunch length /ns | $> 7$ | 125 | 350 | 2 | 8 | $> 1$ | $\approx 1$ | $\approx 1$ |
| $E_{min}$ /eV | 1 | 1 | 1 | $3 * 10^3$ | 10 | 10 | $2 * 10^5$ | $2 * 10^5$ |
| $E_{max}$ /eV | $5 * 10^8$ | $5 * 10^8$ | $10^8$ | $2 * 10^5$ | $5 * 10^6$ | $4 * 10^6$ | $8 * 10^6$ | $8 * 10^6$ |
| $\Delta E_n/E_n(\%)$ | 0.3 | 5 | 13 | 3 | 0.2 | 0.2 | $\leq 1$ | $\leq 1$ |
| n-flux /$s^{-1}cm^{-2}$ | $\approx 10^5$ | $5 * 10^6$ | $10^8$ | $10^4$ | $4 * 10^4$ | $2 * 10^5$ | $2 * 10^6$ | $15 * 10^6$ |


[1] E. Altstadt et al., FZ Rossendorf, Wiss.-Tech. Ber. FZR-369 (2003) und Abschlussbericht in Vorbereitung
[2] P. Michel and R. Schlenk, priv. comm.

# First Physics Measurements with HADES [B,G]

F. Dohrmann, E. Grosse, B. Kämpfer, K. Kanaki, R. Kotte, L. Naumann, A. Sadovsky and the HADES collaboration

The High Acceptance Di-Electron Spectrometer (HADES) aims at measuring in-medium modifications of light vector mesons ($\rho$, $\omega$, $\phi$) in nuclear matter. Such modifications of hadron properties are predicted by various models based on fundamental principles like chiral symmetry and QCD.

In summer 2003 all components of the HADES spectrometer were installed at the heavy-ion synchrotron SIS in GSI/Darmstadt except for two of the 24 Multiwire Drift Chambers (MDC) which will be delivered in 2004/2005. In this configuration the tracking system of HADES is completed in four out of six HADES sectors and ready to perform high-resolution measurements with an anticipated $\Delta M/M = 1.5\,\%$ mass resolution. All six large-area drift chamber modules of MDC-III produced at FZ Rossendorf for the outer tracking planes were installed. A series of pp scattering experiments has been scheduled in fall of 2003 and beginning of 2004. The goal of these experiments is to establish high resolution tracking and to measure calibration reactions like *pp* elastic scattering, as well exclusive meson production channels i.e. $\pi^0$, $\eta$ at 1.5 and 2.2 GeV beam energy. The latter ones are important for the full understanding of the HADES dielectron reconstruction efficiency and second level trigger (LVL2) performance.

In September 2003 we installed for the first time the liquid hydrogen target for proton and pion beam experiments. The target, first trigger settings and background situation were commissioned in October 2003. A maximum beam intensity of $2 \times 10^7$ protons/sec and trigger rates of $5kHz$ have been achieved. Careful beam handling and design of the target area allowed to obtain a ratio of full/empty target trigger rates of 10 : 1.

In parallel to the recent experiments the data obtained for the C + C collision at 2 A·GeV have been extensively studied. The two experimental runs in 2001 and 2002 with a total collected statistics of around $5 \times 10^7$ (LVL1) and $20 \times 10^7$ (56 % LVL1 + 44 % LVL2) events have been analyzed. The LVL1 trigger selects the 10 % most central events. In the second run we used for the first time a LVL2 trigger to select LVL1 trigger events with electron candidate tracks. Preliminary results from these experiments are presented below.

Particle identification in the HADES detector starts with track reconstruction in the MDC [1]. For a preliminary data analysis the inner MDC track segments are correlated with hits in the Time-of-Flight (TOF) wall and the Pre-Shower placed behind the magnetic field to form particle trajectories. No MDCIII/IV information was used. Particle momenta are derived from the measured by the deflection in the magnetic field. A preliminary analysis is based on the hypothesis that the reconstructed track belongs to a certain type of particle (e.g., proton, charged pion, electron etc.). Hadron identification is performed on the basis of momentum as measured by the deflection in the magnetic field, the velocity and energy loss as measured by the TOF detector. For the lepton identification, data from the RICH (Ring Imaging Cherenkov) and the Pre-Shower detectors are used in addition. The principle of the particle identification is illustrated in Fig. 1. Particles with different mass fill different region in the velocity vs momentum distribution. The pronounced maxima in the left side correspond to charged pions and protons. The analysis shows that positive charged pions can be separated from protons up to momenta of $p_{lab} < 1000 MeV/c$ with purity better then 80%. Electron identification can be improved if the RICH electron condition is switched on, as shown on the right side of Fig. 1. Detailed investigations of measured electron distributions and dedicated Monte Carlo simulations using the URQMD event generator reveal that the residual contamination of hadronic background is less than 2% and the purity of electron reconstruction is around 90%. The remaining 10% is electron misidentification that can be attributed, in addition to the mentioned hadron contribution, to fake combinations of inner MDC track segments with the hits in the TOF/Shower detectors.

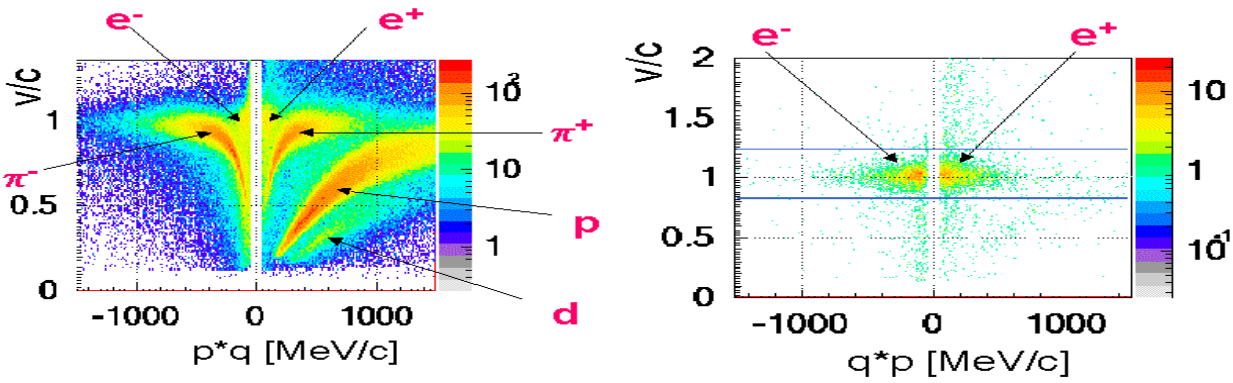


***Fig. 1*** *Correlation between velocity and momentum for all reconstructed tracks from C + C collisions at 2 A·GeV. The parameter q defines the charge.* **Left***: Pion and proton branches are clearly resolved.* **Right***: Additional condition that the particle was identified with the RICH, thus selecting* $e^{\pm}$.

This fake contribution is expected to be significantly reduced once the MDCIII/IV information is included in the analysis of the November 2002 data. Absolute proton and pion yields were extracted from the data. The correction factors accounting for the geometrical acceptance and the efficiency of detectors and the tracking method were obtained via simulations. As an example of our hadron analysis results we show in Fig. 2 the transverse mass distribution of positively charged pions measured at midrapidity. Similar results can also be derived from the analysis of negative charged pions, in agreement with previous data on pion production for the same system and similar energy [2]. The average number of participants in the events selected by the LVL1 trigger was estimated to be $A_{part} = 8.6$. The average of the yields of positively and negatively charged pions per participant extrapolated to $4\pi$ is $N_\pi/A_{part} = 0.148 \pm 0.015$. This value is in a good agreement with the previous result measured by the TAPS detector for neutral pions as $0.138 \pm 0.014$ [3].

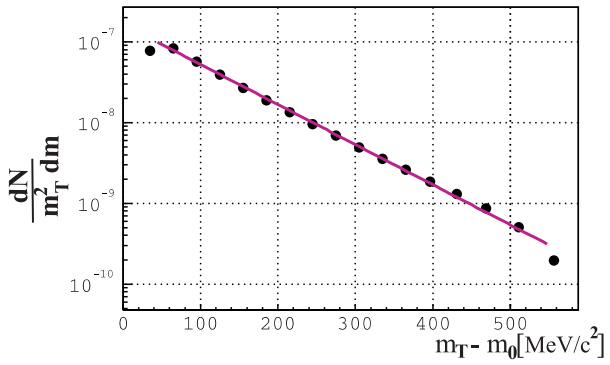


***Fig. 2*** *Transverse mass distribution of positively charged pions in C+C collisions at 2 A·GeV. The solid line is a thermal fit with the two slope parameters 41 and 84 MeV.*

The yields and shapes of the momentum spectra of electrons and positrons are very similar with average multiplicities of $2 \times 10^{-2}$ per LVL1 trigger event. The measured spectra agree in shape with the ones obtained from simulation but their integral is by $\sim 25\,\%$ lower. This finding and studies of single electron identification capabilities indicate that with the current analysis procedure the detection inefficiency amounts to $20\,\%$. The total dilepton statistics, after subtraction of combinatorial background amounts to $\sim 2500$. Dielectron invariant mass distributions for data and simulation normalized to the average number of charged pions, $0.5(N_{\pi^+} + N_{\pi^-})$, determined from the same data set show that in the low mass region ($\pi^0$ Dalitz) simulations overestimate the data by a factor of $\sim 2$, but in higher mass region the simulation and the data agree rather well. In order to disentangle the different sources of the discrepancy (uncertainties of elementary cross sections and electron identification efficiency) a dedicated calibration measurement of exclusive $\pi^0$ and $\eta$ production in $pp$ scattering was scheduled for February 2004. The HADES second level trigger was fully operational during the beam-time of November 2002 where C + C reaction were measured at 2 AGeV. Events which contain at least one electron candidate, i.e. a correlation between a RICH ring and a hit in the Pre-Shower or TOF within a broad azimuthal window, were positively triggered with an event candidate reduction by a factor 12. It has been estimated that higher reductions, up to a factor 20, are achievable without further loss of dilepton detection efficiency. A preliminary analysis of the collected data allows an estimation of the LVL2 trigger performance. Due to a more restrictive implementation of the ring recognition algorithm, a single electron detection efficiency of $62\,\%$ was calculated, while $84\,\%$ was estimated for dielectrons with opening angle larger than $4°$, and $92\,\%$ for larger than $8°$. No physical bias was introduced in the data, since an agreement between electron and dielectron spectra for triggered and untriggered events is observed. In the triggered events an enhancement by a factor 7.5 is found in the lepton yield, and by a factor 11 in the dilepton yield, with respect to the untriggered ones.

In Fig. 3 the dilepton distributions after the combinatorial background subtraction are plotted for C + C collision data. Both distribution are normalized to the number of LVL1 and LVL2 trigger events, respectively. The analysis procedures were the same as explained above and a lepton pair opening angle cut of $\Theta < 4°$. The higher statistics (factor of 10) achieved due to the second LVL2 trigger allows investigations of dielectron production over a wider invariant mass range.

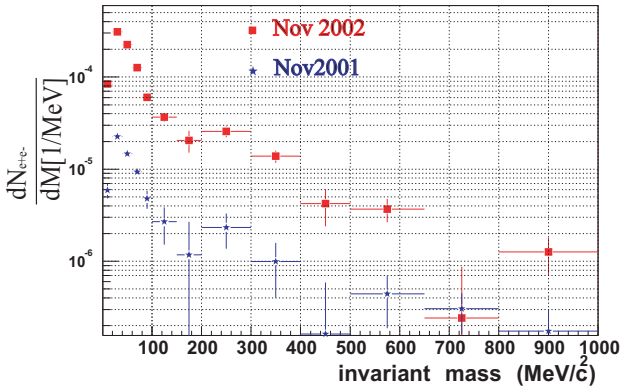


***Fig. 3*** *Comparison of dielectron invariant mass distributions normalized to the number of LVL1 trigger events (November 2001 data) and the LVL2 trigger events (November 2002 data).*


[1] H. Bokemeyer et al., Nucl. Instr. Meth. A 477 (2002) 397
[2] A. Kugler et al. (HADES collaboration), Nucl. Phys. A 734 (2004) 78c
[3] R. Averbeck et al., Phys. Rev. C 68 (2003) 024903
[4] J. Bielcik, PhD thesis, TU Darmstadt (2003);
T. Eberl, PhD thesis, TU München (2003);
J. Otwinowski, PhD thesis, Univ. Cracow (2003)

# Search for $K^+$ Mesons in the Reaction $^{12}$C(2 AGeV) + C with HADES [B,G]

A. Sadovsky, R. Kotte, F. Dohrmann, E. Grosse, B. Kämpfer, L. Naumann and the HADES collaboration

The HADES spectrometer took data on C + C in November 2001 (NOV2001) and November 2002 (NOV2002). In this study, NOV2001 data were analysed to explore the possibility of positive kaon detection. During NOV2002 data were taken using multiplicity trigger asking for four charged particles in forward direction. The detector setup is described elsewhere [1]. In NOV2001 the setup included two multiwire drift chamber (MDC) planes between the target and the toroidal magnet, TOF (time of flight) detectors were located behind the magnetic field and used there also for coordinate information. The corresponding tracking method is described in [2]. Data summary tapes (DST) were produced for both the experimental data as well as for the corresponding simulation data. Although the setup did not allow for high-resolution tracking, it should explore the feasibility of $K^+$ identification in NOV2002 data and future experiments.

At first, simulation data based on the UrQMD event generator were analyzed to optimize track selection cuts for $K^+$. The analysis was done using the outer TOF detector region ($45° < \theta < 79°$). For NOV2001 data one obtains $K^+$ and $p$ mass resolution of $\Delta m/m \approx 10 \ldots 12\,\%$ in this angular range. This value is expected to improve up to an order of magnitude for NOV2002 data and future analyses. For selecting kaons we required: *i*) tracks coming from the target, *ii*) TOF-MDC track matching required, in addition each MDC track has only one hit in TOF, *iii*) track bending in the magnetic field indicates positively charged particles, *iv*) energy loss in the TOF detector is in agreement with charge 1 particles, *v*) particle velocity is within $0.45 < \beta < 0.80$ to avoid the contamination of decays from slow kaons and insufficient momentum reconstruction of fast ones. The analysis of simulation data allowed to optimize these cuts.

Fig. 1 shows simulation data, for which we expect good separation of $K^+$. Inside the region of 410 MeV $< m <$ 575 MeV (two-sigma around $K^+$ mass) the signal-to-background ratio is $\sim 1.7$.

The analysis of NOV2001 experimental data indicates a $K^+$ mass peak (Fig. 2), but it is smeared out by current alignment accuracy limitations and long term calibration stability. The estimated number of $K^+$ is $\sim$ 3400 out of $3.4 \cdot 10^6$ events analysed from NOV2001 data within the selected kinematical region. Using this result we estimate the number of $K^+$ in NOV2002 data to be about 5200 $K^+$ mesons per sector (1/6-th of azimuthal acceptance), using all four MDC planes with high resolution tracking. We expect a much better tracking quality from analysis of November 2002 experiment.

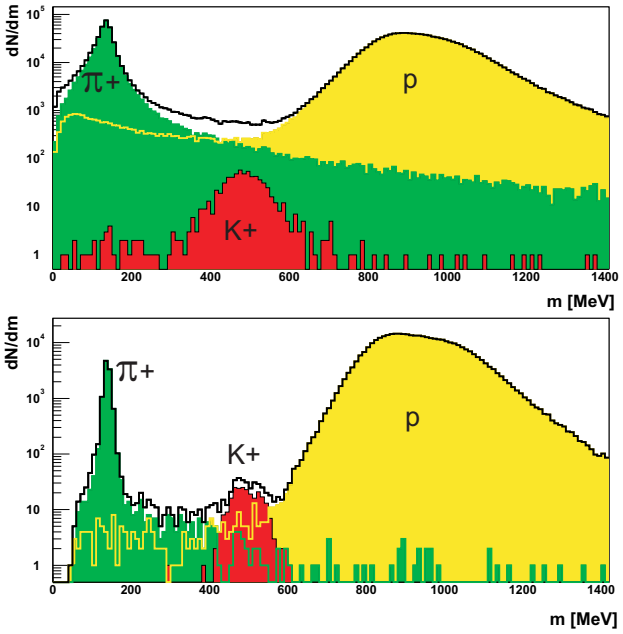


**Fig. 1** *Results for simulation data. Upper part: Mass distribution of positively charged particles within the TOF acceptance. Kaons are shown in dark, pions in gray and protons in light gray. Lower part: The same, but after kaon-selection cuts.*

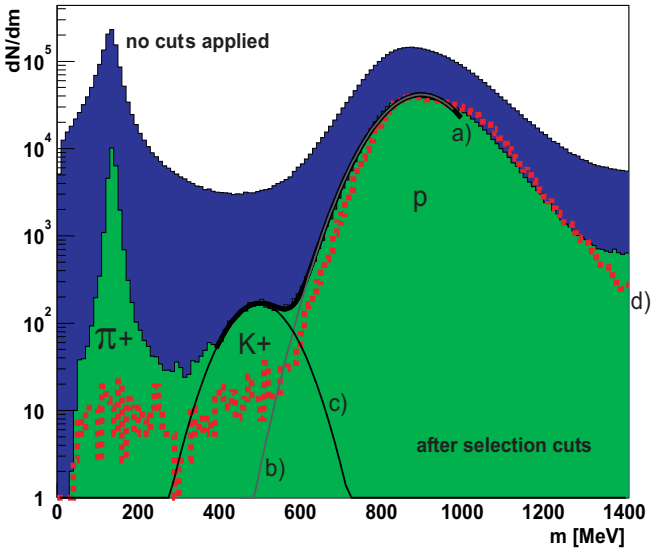


**Fig. 2** *Analysis results for experimental data. The upper histogram gives the mass distribution for reconstructed tracks in the TOF region before applying any cuts. Lower (gray) histogram is the same, but after $K^+$ selection cuts. The thick curve a) represents a fit of two Gaussians to the $K^+$ and $p$ mass peaks, using the mass range between 400 and 1000 MeV. The corresponding single Gaussian components are shown: b) for protons and c) for $K^+$ mesons. In addition, the dashed line d) represents the scaled proton-mass distribution from simulation.*

[1] http://www.fz-rossendorf.de/pls/rois/Cms?pOid=11197
[2] Manuel Sànchez Garcia, Momentum reconstruction and Pion Production Analysis in the HADES Spectrometer at GSI, Ph.D. thesis, Universidade de Santiago de Compostela (2003)

# Investigation of Filament Growth in the HADES Drift Chambers [B,G]

K. Kanaki, F. Dohrmann, W. Enghardt, J. Hutsch, A. Kondyurin[1], R. Kotte, L. Naumann, M. Sobiella

The third plane of the HADES Multiwire Drift Chambers (MDC-III) has been completed and installed at GSI, Darmstadt. Of specific interest in this report are observations of filament growth in one of the chambers that has been used in-beam [1]. The chamber had successfully worked during the previous beam times, as well as during the later spring beam time but signs of malfunction made its repair necessary.

A detailed investigation of the open chamber lead to the observation of white-coloured filaments spread over the surface of the first anode layer. Their diameter varied from 2 $\mu$m - 100 $\mu$m and their length could be as large as 12 cm, growing across 20 wires. An Energy Dispersive X-Ray (EDX) spectroscopy investigation gave information about their chemical composition. The identified elements were Na, Al, Si, S, Cl, K and Ca (see Fig. 1). The C and O peaks at the lower energies are significantly contaminated from background, making the method unreliable for identification of organic material. Among the remaining elements, Si and Ca require special attention; the first one has strong adhesion capability and the latter one points to organic material.

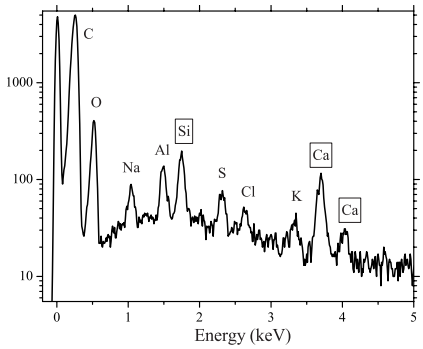


**Fig. 1** *EDX spectrum of filaments (not normalized).*

The EDX method allows us to identify the atomic composition of a sample. However, to learn about molecular structure though, infrared beams are the appropriate tool. Further information about the composition of the filaments was obtained using Fourier Transform InfraRed spectroscopy (FTIR) [2]. FTIR is a standard method in cases where there is need for high resolution of weak signals. The reflection spectra presented in Fig. 2 were recorded by a FTIR spectrometer with an infrared microscope. Spectra of wool, cotton, hair and two sorts of tissue were recorded for comparison (see Fig. 2).

The largest similarity is observed between the spectra of the filaments and the two samples of tissue used for cleaning purposes during the production process. These are depicted separately in Fig. 3. Note that the structure of the filaments was most probably altered while operating the MDC with high voltage, as a consequence of plasma discharge close to the wire surface.

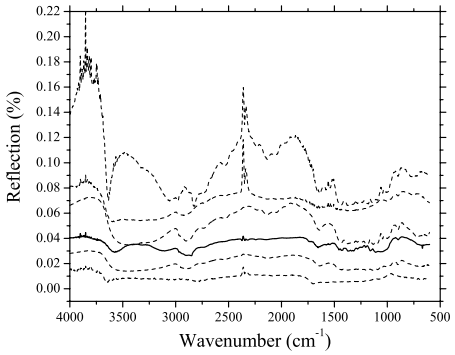


**Fig. 2** *Infrared spectra for various organic materials (not normalized). The sequence of the spectra from bottom to top is: hair, tissue 1, filaments (solid line), wool, tissue 2 and cotton. The lines are shifted for display reasons.*

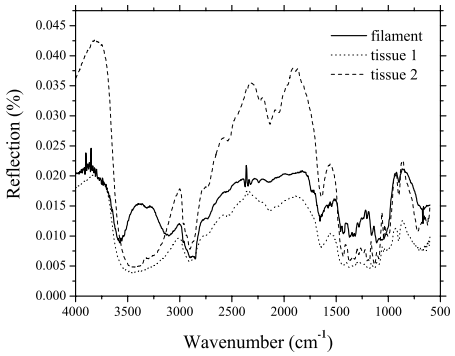


**Fig. 3** *Infrared spectra for filaments and tissue.*

One possible source of the filaments could be cellulose containing tissue material used in the production process, although the spectra do not fully match. In particular, Si traces are problematic to explain. Silicon is a component of the frame material, as well as of the glue used to hold the wires. A possible scenario could be that leftovers of the tissue were contaminated with silicon of either source and slipped into the active area of the chamber. Such a mixture has low conductivity but while operating the chamber, it may be modified by local discharges. The process of carbonization can increase the surface conductivity of organic substances in plasma and arc which could partially explain the difference between the filament and the tissue spectra. It is very unlikely though, that these structures are dose related aging phenomena. The aging tests performed, as well as the absence of such filaments in several other chambers that had to be opened, supports this claim.

After the removal of the filaments and the careful cleaning of the detector components, the chamber was normally operated under beam conditions and regular operation of the HADES experiment resumed.

[1] NSS-MIC 2003 Conference Proceedings, Portland, USA (to be published)

[2] D.J. O'Connor, B. A. Saxton, R.St.C. Smart, "Surface analysis methods in materials science", Springer Verlag Berlin Heidelberg, 1992

[1] Institut für Polymerforschung, Technische Universität Dresden.

# Near-Threshold Production of $\omega$ Mesons in the $pn \to d\omega$ Reaction [B, J]

I. Lehmann for the ANKE Collaboration

The comparison of cross sections for meson production in $pp$ and $pn$ collisions tests theoretical models describing the production mechanisms. For $\eta$ production the observed ratio $R = \sigma_{\rm tot}(pn \to pn\eta)/\sigma_{\rm tot}(pp \to pp\eta) \approx 6.5$ [1] is generally attributed to isovector dominance in model calculations based on meson exchange [2]. It is therefore interesting to investigate whether a similar isospin dependence is found also for the $\omega$ meson. Relatively few experiments were performed for the reaction $pp \to pp\omega$ [3,4], and no data are available in $pn$ collisions. The $pn \to d\omega$ reaction was studied in the $pd \to p_{\rm sp}d\omega$ reaction at four proton beam momenta at ANKE (Fig. 1). A deuterium cluster-jet target was used as an effective neutron target, detecting the recoil protons ($p_{\rm sp}$), which have momenta of about 80 MeV/c, in a silicon telescope placed close to the target [5]. These recoil protons can be treated as "spectators" that influence the reaction only through their modification of the kinematics. By varying the angle and momentum of the spectator protons, a certain range in excess energy $Q$ is selected experimentally. This range is used to extract results in $pn$ collisions for the corresponding $Q$ values. The deuterons emitted at angles below 8° with momenta around 2 GeV/c were detected in the forward system of the ANKE spectrometer. Inclined Čerenkov counters in combination with two layers of scintillation counters enabled us to identify these deuterons despite a two orders of magnitude higher proton background [5]. Their momenta were reconstructed using the information from two multi-wire proportional chambers. The $pn \to d\omega$ reaction was then identified *via* the missing mass technique. In order to normalize the data, the absolute luminosity was determined by $pd$ elastic scattering.

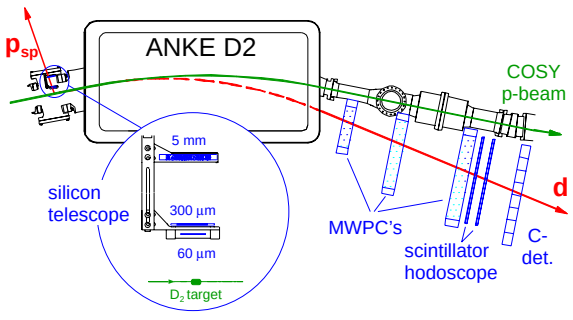


**Fig. 1** *Top view of the detector set-up at ANKE used for the detection of the slow recoil proton "$p_{\rm sp}$" and a fast deuteron "d" from the reaction $pd \to p_{\rm sp}d\omega$. Magnified is the silicon telescope used for the spectator detection.*

Measurements of $pp \to pp\omega$ at SATURNE [3] show there to be a strong contribution from multi-pion production below the $\omega$ peak in the missing mass spectrum. This can only be reliably estimated by comparing data above and below the $\omega$ threshold. We used experimental data at 2.6, 2.7, 2.8 and 2.9 GeV/c beam momentum, which correspond to mean $Q$ values in $pn \to d\omega$ of -40, -5, 28 and 57 MeV respectively. At the highest energy, there is clear evidence for an $\omega$ peak, whereas at 2.8 GeV/c the residual $\omega$ signal depends much more sensitively upon the background description. The cross sections $\sigma$ for $pn \to d\omega$ are extracted to be $(2.6 \pm 1.6 \pm 2.3)\,\mu$b at $Q = (28^{+16}_{-20})$ MeV and $(9.0 \pm 3.2^{+3.6}_{-2.5})\,\mu$b at $Q = (57^{+21}_{-15})$ MeV (Fig. 2), where the uncertainty in $Q$ reflects the total width of the bin. The first error in $\sigma$ is statistical and the second systematic. The fact, that the cross sections are significantly smaller than theoretical predictions, suggests that the reaction mechanism for $\omega$ production differs from that for the $\eta$, possibly implying a relatively larger contribution from isoscalar meson exchange.

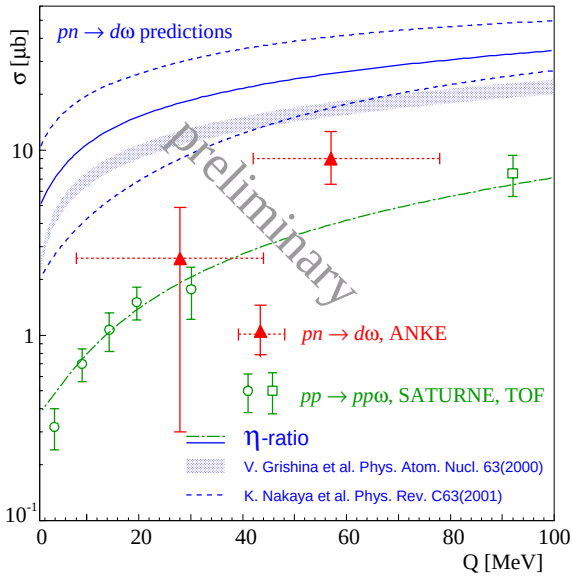


**Fig. 2** *Total cross sections for $\omega$ production. The $pp \to pp\omega$ data are taken from SATURNE [3] (open circles) and COSY-TOF [4] (open square), whereas our two $pn \to d\omega$ points are given by the closed triangles. Only systematic errors are shown as the statistical errors are smaller. The horizontal bars indicate the width of the Q ranges. The dot-dashed curve is the semi-phenomenological fit given in [3] to the $pp \to pp\omega$ results. If the ratio for $d\omega$ to $pp\omega$ were similar to that for $\eta$ production [1], one would then obtain the solid curve, which predicts a $pn \to d\omega$ cross section of over 25 $\mu$b at 57 MeV. The predictions of the Jülich group depend upon the relative contributions of exchange and production current terms and lie between the two dashed curves [6]. The only other published estimate [7] is shown by the shaded area.*

[1] H. Calén et al., Phys. Rev. C 58 (1998) 2667 and refs. therein
[2] G. Fäldt, T. Johansson, C. Wilkin, Phys. Scr. T99 (2002) 146
[3] F. Hibou et al., Phys. Rev. Lett. 83 (1999) 492
[4] S. Abd El-Samad et al., Phys. Lett. B 522 (2001) 16
[5] I. Lehmann, PhD thesis, University of Cologne, 2003
[6] K. Nakayama et al., Phys. Rev. C 63 (2001) 015201
[7] V. Grishina et al., Phys. Atom. Nucl. 63 (2000) 1824

# Evidence for a Penta-Quark Strangeness S = +1 Baryon

K. Möller for the COSY-TOF Collaboration

Recently in an exclusive measurement [1] of the reaction $pp \rightarrow pK^0\Sigma^+$ at COSY-TOF a resonance was found in the invariant mass spectrum of the corresponding $K^0p$ subsystem at an invariant mass value of $m_{res} = (1530 \pm 5)MeV/c^2$ with a width of $\Delta m_{res} = (22 \pm 3)MeV/c^2$. The total cross section was estimated to be $(0.4 \pm 0.1(\text{statistic}) \pm 0.1(\text{systematic}))\mu$b. The resonance exists with a significance of 4 - 6 $\sigma$. The final missing mass spectrum after kinematical fits and other reduction procedures is shown in Fig. 1. The observed resonance is interpreted as evidence for the penta-quark strangeness S = +1 exotic $Z^+$ baryon (now denoted by $\Theta^+$ baryon) the possible existence of which has already been suggested as early as 1977 by Jaffe (first ref. in [2]). The results of the measurement are very close to the theoretical predictions of ref.[3] ($E_{res} = 1530\ MeV$, $\Gamma = 15\ MeV$) obtained on the basis of a soliton model. The structure of this state is exotic in the sense that it contains a $q\bar{q}$ - pair in addition to the usual three valence quarks of normal baryons, or to put it in terms of theory: The Fock-space of the corresponding theoretical description for baryon states usually spanned by three quarks qqq is extended to also include an additional $q\bar{q}$ sea quark pair. Thus a quark content of uudd$\bar{s}$ is attributed to the resonance found in the measurement resulting in a strangeness S = +1 state. The strangeness of the baryons known up to now ranges from S = -3 to S = 0. In terms of $SU(3)$ symmetry the $\Theta^+$ baryon belongs to an anti-decuplet with a spin value of $J = (1/2)^+$, where the $\Theta^+$ baryon is an isospin $T = 0$ state.

The theoretical predictions for the position and the width of the $\Theta^+$ baryon were derived from symmetry considerations and by using the fact that the well known $N(1710)$ baryon resonance belongs to the same multiplet as the $\Theta^+$ resonance [3]. Experimentally the evidence of the resonance found in the COSY-TOF experiment is corroborated by the findings of other groups who also report on the existence of the $\Theta^+$ state (refs. [4] - [9]). In these measurements the $\Theta^+$ resonance has been observed in either the $pK^0$ ([5, 8, 9]) channel or the $nK^+$ channel ([4, 6, 7]). In an upcoming run COSY-TOF will measure the reaction $pn \rightarrow pK^0\Lambda$, which will provide an independent check of the present results. The detection of $\Lambda$-particles in this reaction is more favourable than detecting $\Sigma$-particles as in the present experiment because by its design COSY-TOF is optimized for the detection of $\Lambda$-particles. But on the other hand as a trade-off the use of a deuteron target as neutron target introduces uncertainties connected with the spectral function of the neutron distribution in the deuteron which only partly can be removed by using proton spectator tagging.

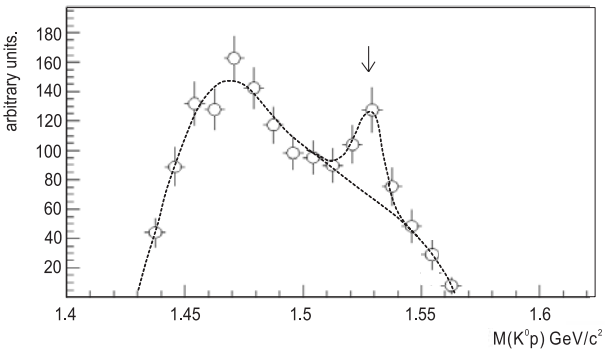


**Fig. 1** *Reduced missing mass spectrum of the $K^0p$ - subsystem.*

[1] The COSY-TOF Collaboration, Phys. Lett. B (2004) in print
[2] M.V. Polyakov et al., Eur. Phys. J. A 9 (2000) 115
[3] D. Diakonov et al., Z. Phys. A 359 (1997) 305
[4] T. Nakano et al., SPring8 Collaboration, Phys. Rev. Lett. 91 (2003) 12
[5] V.V. Barnim et al., DIANA Collaboration, hep-ex/0304040
[6] S. Stepanyan et al., CLAS Collaboration, hep-ex/0307018
[7] J. Barth et al., SAPHIR Collaboration, Phys. Lett. B 572 (2003) 127
[8] A. Airapetian et al., HERMES Collaboration, hep-ex/0312044
[9] A. Aleev et al., SVD Collaboration, hep-ex/0401024

# Inclusive $K^{\pm}$ Production in Proton-Nucleus Collisions near Threshold [B]

W. Scheinast, F. Dohrmann, L. Naumann, E. Grosse, B. Kämpfer and the KaoS Collaboration

The reaction $pA \rightarrow K^{\pm}X$ has been measured by the KaoS collaboration [1, 2] to provide a competitive data base which fills the gap of $K^{\pm}$ production between $pp$ and $AA$ collisions. The data can be systematized by a fit with the function

$$E\frac{d^3\sigma}{dp^3} = \sigma^{\rm fit}\frac{\hat{E}}{4\pi m_K^2 K_2(m_k/T)}\exp\left(-\frac{\hat{E}}{T}\right) \qquad (1)$$

with the parameters $\sigma^{\rm fit}$, $v$, and $T$; $\hat{E} = (E - vp\cos\Theta)/\sqrt{1-v^2}$ and $E = \sqrt{m_K^2 + p^2}$. $E$ and $p$ are the corresponding energy and momentum of $K^{\pm}$ in the laboratory system. The experimental data and the resulting fits are displayed in fig. 1. One observes a fairly well reproduction of the data with eq. (1) for $K^-$, while for $K^+$ the fit is less convincing.

The meaning of eq. (1) is to allow an estimate of the total cross section by $\sigma^{\rm fit}$. By using the geometrical cross sections for the systems $pp$, CC, AuAu, respectively, one can convert the estimated cross section in multiplicities, $M_K = \sigma^{\rm fit}/\sigma_{\rm geo}$. The comparison of these multiplicities, scaled by the estimated number of participants $A_{\rm part}$, is exhibited in fig. 2. One observes that the multiplicities for the reactions $p$C (left panels) and $p$Au (right panels) are closer to the multiplicities in $pp$ reactions at the same beam energies than to the ones of the heavy-ion reactions. That means, at higher beam energies the $K^{\pm}$ reaction resemble more the elementary nucleon-nucleon reaction, while at lower beam energies cooperative effects become significant. The multiplicities for $K^{\pm}$ production increase by a factor of about 50 when going from CC to AuAu collisions. In contrast, the $K^-$ ($K^+$) multiplicity increases only by factor of about 1.3 (2.0) when replacing the C target by the Au target at given proton beam energy.

A subset of the presented data has been analysed within a transport code of BUU type [4]. These calculations reveal the necessity of a weakly repulsive $K^+$ potential and a stronger attractive $K^-$ potential. In addition, the strangeness transfer channels $YX \rightarrow K^-X'$ is found to be important. While the role of the $K^{\pm}$ potentials is in line with previous findings for subthreshold $K^{\pm}$ production in heavy-ion reactions [5], the strangeness transfer channel is isolated in [4], with such clearness for the first time, by the analysis of our $pA$ data.

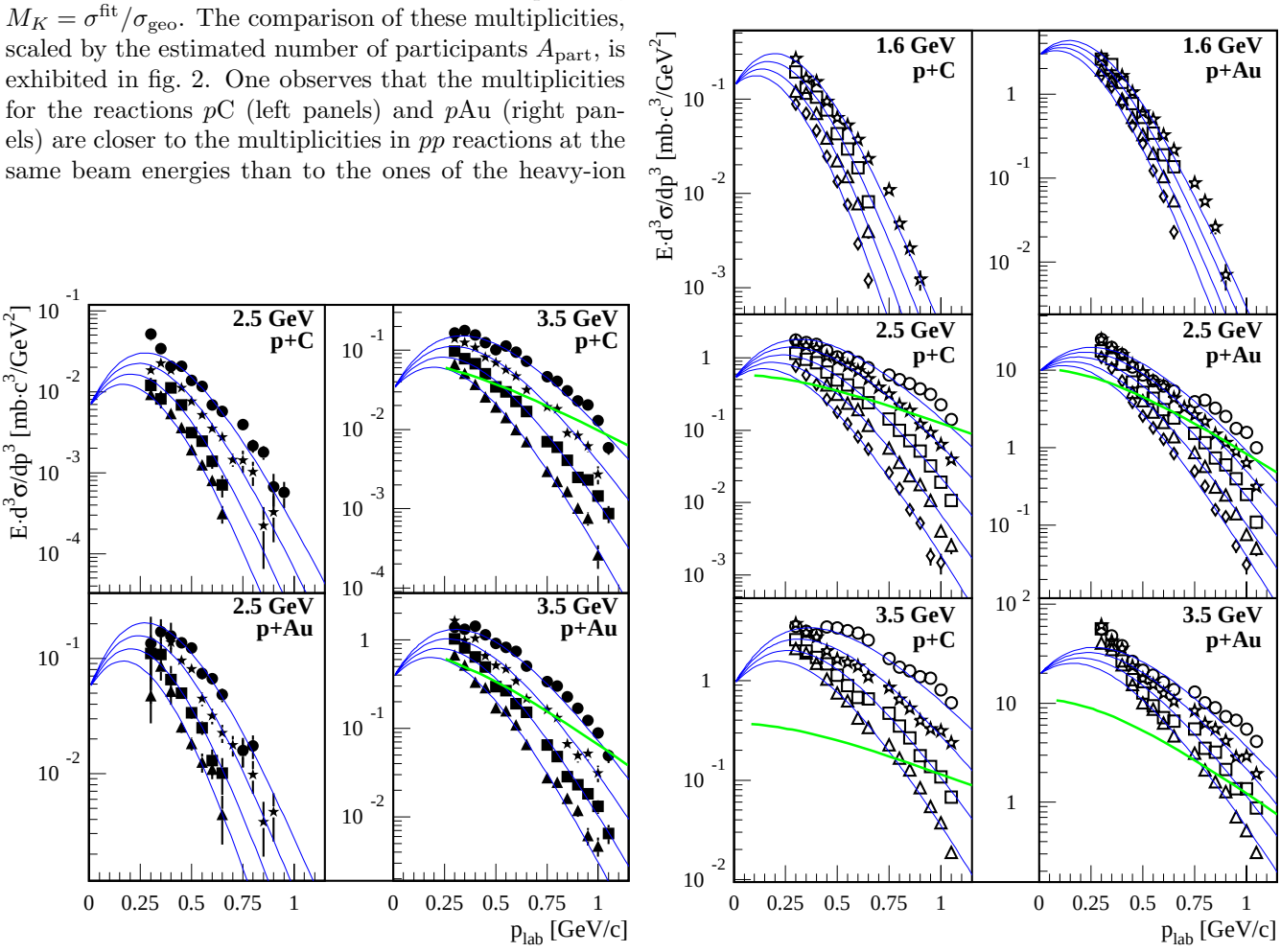


**Fig. 1** *Comparison of our data with the fits by eq. (1). The grey curves separate subthreshold from above-threshold kinematical regions. Parameters are summarized in [2]. Left (right): $K^-$ ($K^+$). The symbols circles, stars, squares, triangles, and diamonds refer to the scattering angles of 32°, 40°, 48°, 56°, and 64°, respectively.*

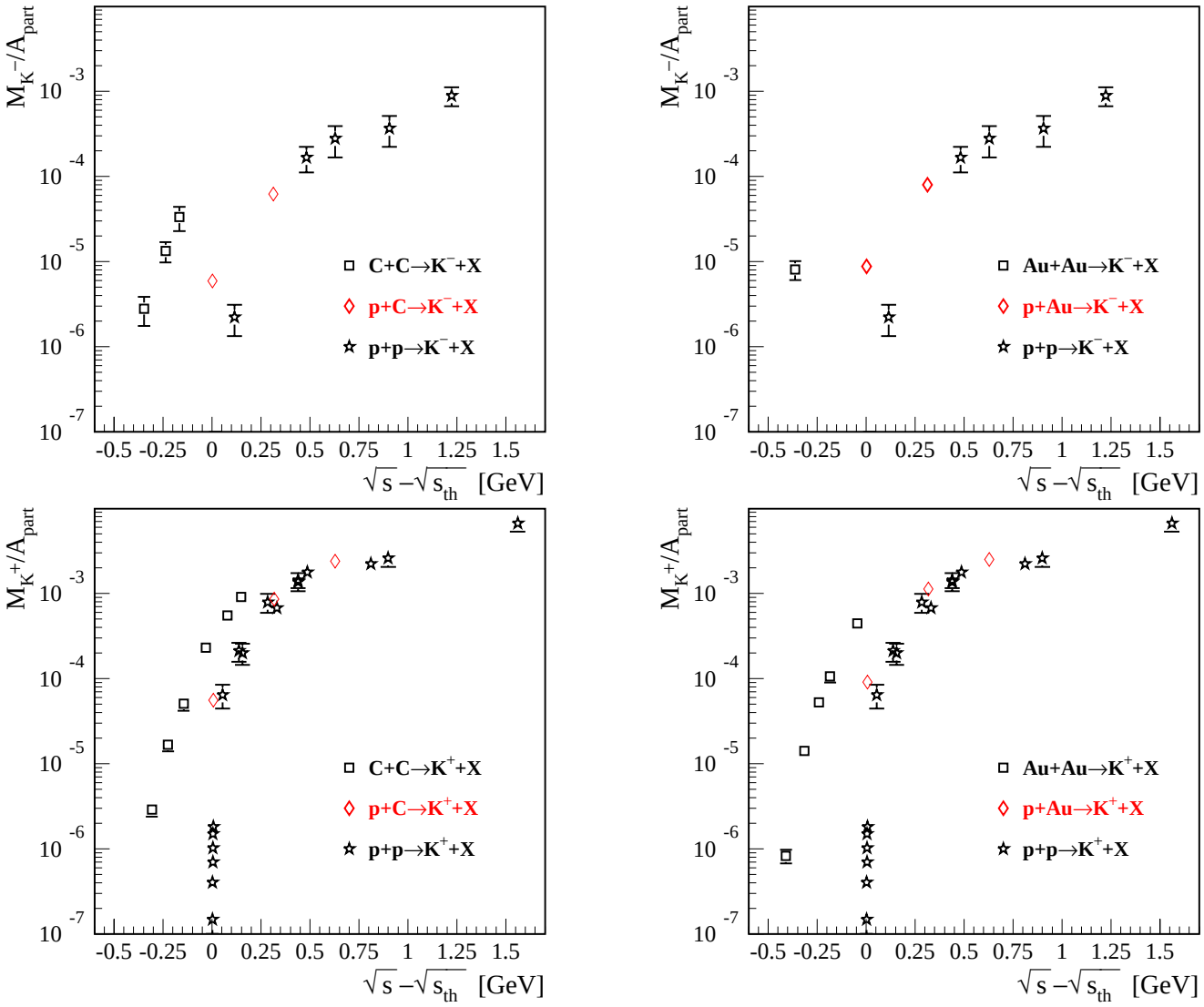


**Fig. 2** *Comparison of multiplicities determined by eq. (1) for pA reactions with multiplicities in pp and AA reactions (data from [3]).*


[1] W. Scheinast et al., Acta Phys. Pol. B, Meson 2002 Workshop Proc (2003) 493
[2] W. Scheinast, Ph. D. thesis, TU Dresden (2004)
[3] P. Senger, Habilitation thesis, Johann Wolfgang Goethe Universität Frankfurt (2000)
A. Förster at al., Phys. Rev. Lett. 91 (2003) 152301
[4] H.W. Barz, L. Naumann, Phys. Rev. C 68 (2003) 041901
[5] Ch. Hartnack, H. Oeschler, J. Aichelin, Phys. Rev. Lett. 90 (2003) 102302

# Electroproduction of Strangeness on $^{3,4}$He

F. Dohrmann for the Jefferson Lab E91016 Collaboration

The electroproduction of strangeness is a complementary approach to experiments with pion and kaon beams [1]. Jefferson Lab experiment E91016 measured $A(e,e'K^+)X$ for Helium targets, using high intensity CW electron beams. Angular distributions of kaons were measured at forward angles with respect to the virtual photon, $\gamma^*$. During the experiment the spectrometer angle for detecting the $e'$ was kept fixed; the $K^+$ arm was varied. Three angle settings between the virtual photon $\gamma^*$ and the ejected kaon were studied, $\theta^{lab}_{\gamma^*K} \simeq 1.7^o$, $\simeq 6^o$, and $\simeq 12^o$. Special high density cryogenic targets were used. The background, consisting of random coincidences and contributions from the aluminum walls of the targets cells were subtracted to obtain charge normalized yields. The two spectrometer coincidence acceptance as well as radiative processes are computed by Monte Carlo simulations. A parametrization of the $\gamma^*N$ cross section has been derived by fitting the kinematic dependences of the $^1$H$(e,e'K^+)Y$ cross section over the acceptance [3]; the same parametrization has been used for our data on $^{3,4}$He. We do not resolve separated $\Sigma^0, \Sigma^-$ hyperon peaks, produced off the proton and the neutron, respectively. Using the impulse approximation, we obtain momentum and in-medium energy of the struck nucleon in the $^{3,4}$He nucleus from full spectral functions [5]. Excess yields close to the respective $\Lambda n$ and $\Sigma N$ thresholds are attributed to FSI which we model by using an effective range model. The agreement comparison between simulation and data is shown in [2]. Near the quasifree $\Lambda$-thresholds for $A = 3$ and 4, we find relatively narrow enhancements that we attribute to ${}^3_\Lambda$H and ${}^4_\Lambda$H bound states. The structure is evident at all angles and is centered, within the resolution of the experiment, at the correct binding energy [2, 6]. Fig. 1 shows the resulting angular distribution for the reaction $^3$He$(e,e'K^+)^3_\Lambda$H and $^4$He$(e,e'K^+)^4_\Lambda$H. In addition, we show theoretical calculations for both reactions [4]. For ${}^3_\Lambda$H only one bound state (the hypertriton) is known ($B \sim 150\,$keV). For ${}^4_\Lambda$H the ground state ($B \sim 2.04\,$MeV) as well as the excited state ($B \sim 1.00\,$MeV) exist. The resolution of the experiment does not allow for a separation of the ground and first excited states of ${}^4_\Lambda$H. Data taken at forward angles should strongly favor the excited state, as supported by the theoretical curves. The preliminary analysis yields a cross section for the ${}^3_\Lambda$H state of less than 5 nb/sr and roughly 25 nb/sr for the ${}^4_\Lambda$H state. Our measurements of the angular distributions for $^{3,4}$He$(e,e'K^+)^{3,4}_\Lambda$H are very important for precise studies on the hypernuclear wave function [4]. It is the first time, the ${}^{3,4}_\Lambda$H bound states have been measured in electroproduction.

F. Dohrmann acknowledges the support by the the A. v. Humboldt Foundation through a Feodor Lynen Research Fellowship and the support by Argonne National Laboratory as the host institution for this research.

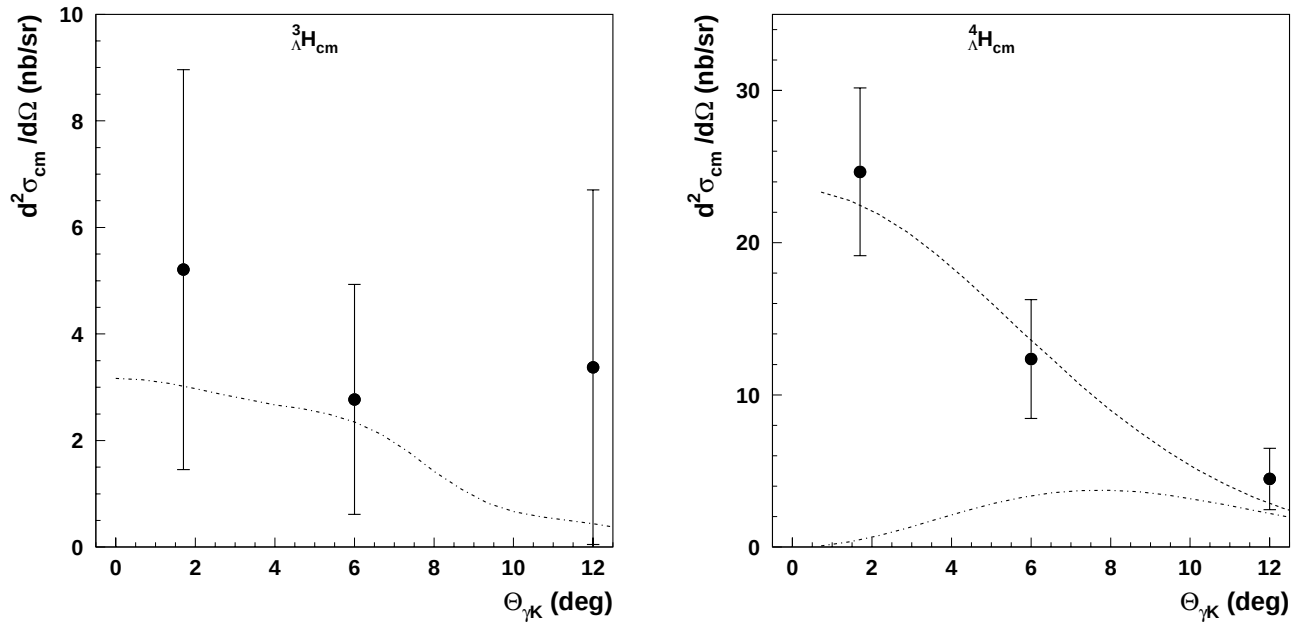


**Fig. 1** *Differential cross section in the center of mass for electroproduction of ${}^3_\Lambda H$ (left) and ${}^4_\Lambda H$ (right) as a function of the angle between the virtual photon and the emitted kaon in the laboratory. The curves show theoretical calculations for the excited state (dashed) and ground state (dashed-dotted), which have been renormalized to fit the data [4].*

[1] J.-M. Laget, Nucl. Phys. A 691 (2001) 11c
[2] F. Dohrmann [Jefferson Laboratory E91-016 Collaboration], Prog. Part. Nucl. Phys. 50 (2003) 587
[3] R. M. Mohring et al., Phys. Rev. C 67 (2003) 055205
[4] T. Mart et al., Nucl. Phys. A 640 (1998) 235, and private communication 2003
[5] O. Benhar et al., Nucl. Phys. A 579 (1994) 493
[6] B. F. Gibson and E. V. Hungerford, Phys. Rept. 257 (1995) 349

# Testing Novel TOF Detectors at ELBE [E]

F. Dohrmann, R. Kotte, L. Naumann, B. Kämpfer, E. Grosse

At GSI Darmstadt an international accelerator facility of the next generation is planned. It builds on the experience and technological developments already made at the existing GSI facility, and incorporates new technological concepts [1]. The new facility will cover a broad range of research concerning the structure of matter and the evolution of the universe. Among the fascinating questions about the evolution of the universe are whether it is possible to use nuclear reactions to recreate and study the transition from nuclear matter to quark-gluon matter as well as what the state of matter under extreme temperatures and pressures will be [1]. To address these questions a new generation of physics experiments will be built. These experiments require novel detector techniques, fast, efficient, but low cost since typically large areas have to be covered. One example are fast time-of-flight (TOF) detectors [2, 3]. The FZR participates in the planned Compressed Baryonic Matter (CBM) experiment [4], as a natural expansion of its research on heavy-ion and hadronic physics at GSI within the KaoS, FOPI and HADES collaborations. Currently fast TOF detectors are developed for the CBM and other current and future GSI experiments [2, 3]. Prototypes have to be tested with respect to rate capability and time resolution.

An ideal testing opportunity at FZR is provided by the ELBE electron beam. Using the ps pulse structure of the electron beam we will use e-beams up to 20 MeV in order to test the time resolution of fast detectors. Due to the excellent time resolution of the electron beam no reference detectors should be necessary. The electrons will mimic the behavior of minimum ionizing particles like pions and kaons. Such tests will take place at ELBE in the radiation cave, possibly parasitic to experiments of the radiation physics group. A sketch of the experimental cave is shown in Fig. 1. Ideally one would like to use very low intensity primary electron beam ($\lesssim 10^3\,\mathrm{s}^{-1}$) to be sent directly on the detectors. However, currently beam diagnostics limits the controllable beam current to $\gtrsim 1\,\mu$A. Hence a scattering experiment will be used to control the intensity of the electrons impinging onto the prototypes. Tests are planned using a $1-10\,\mu A$ electron beam scattering off a thin target foil. The scattered $e^-$ will leave the scattering chamber under $\theta \simeq 45^o$ through a thin ultra high vacuum window ($\leq 160\,\mu$m Beryllium) with small solid angle and through the chamber walls ($\approx 4\,$mm stainless steel) with large solid angle. Fig. 2 shows the energy distribution for electrons scattered off a $10\,\mu$m Aluminum foil, calculated by FLUKA [5].

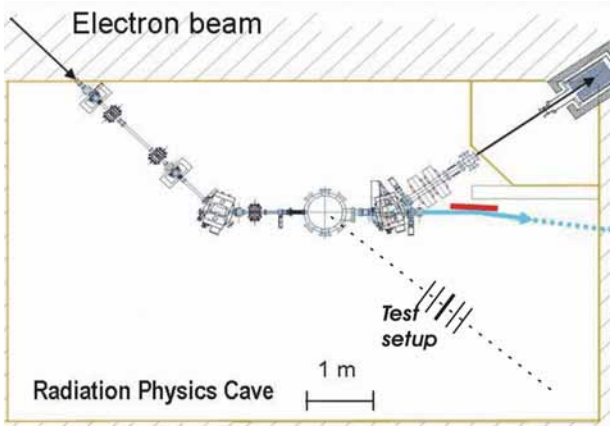


**Fig. 1** *Sketch of the radiation physics cave (courtesy of J. Pawelke FZR-FWKS). The location for first tests on background and rate conditions is depicted.*

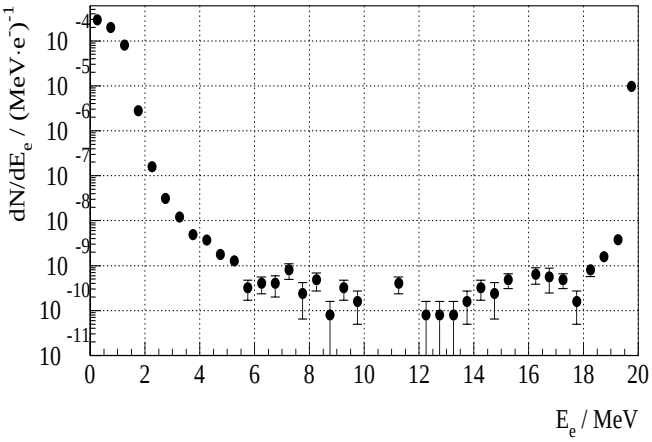


**Fig. 2** *Differential energy distribution of scattered $e^-$ covering $\theta_{\mathrm{lab}} \simeq 40^o - 50^o$ for incident electrons of* 20 MeV *kinetic energy. The energy binning is* 0.5 MeV*. The $e^-$ production threshold is* 100 keV*. Target and beam spot are assumed pointlike (calculation and figure by B. Naumann FZR-FVTS).*

[1] http://www.gsi.de/zukunftsprojekt/forschung_e.html
[2] M. Petrovici et al, Nucl. Instrum. Meth. A 508 (2003) 75
[3] A. Blanco et al, Nucl. Instrum. Meth. A 508 (2003) 70
[4] http://www.gsi.de/documents/DOC-2004-Jan-116-1.pdf
[5] A. Fasso, A. Ferrari and P. Sala, Proc. of the MC 2000 Conference, Lisbon, October 23–26, 2000, A. Kling, F. Barao, M. Nakagawa, L. Tavora, P. Vaz eds., Springer-Verlag Berlin, (2001) 159

# Finite-Width QCD Sum Rules for $\rho$ and $\omega$ Mesons [B,G]

S. Zschocke, O.P. Pavlenko[1], B. Kämpfer

Modifications of vector meson properties in dense nuclear medium are subject of intensive studies both theoretically and experimentally.

Among the theoretical approaches are QCD sum rules. These interconnect hadronic observables with largely non-perturbative QCD quantities like condensates. First evaluations within the QCD sum rule approach in zero-width approximation supported a mass dropping of vector mesons like $\rho$ and $\omega$ with same strength in agreement with Brown-Rho scaling hypothesis [1]. Later, it was realized that the impact of Landau damping as well as finite width effects, which arise from rather strong inelastic scatterings of mesons with surrounding nucleons, change the unique scaling scenario predicted before. Especially, the global characteristics of vector mesons in matter like mass shift and width broadening turn out to be correlated in nuclear matter.

To account for finite width effects we apply the general ansatz for vector mesons spectral function [1]:

$$S^V = \frac{-\Im\,\Sigma_V(s,n)}{(s-\overset{\circ}{m}{}^2_V\,(n) - \Re\,\Sigma_V(s,n))^2 + (\Im\,\Sigma_V(s,n))^2}\ . \quad (1)$$

The forward off-shell meson-nucleon scattering amplitude $T_{VN}$ is associated with the in-medium self-energy via $\Sigma_V(s,n) = \Sigma_V(s,0) - n\,T_{VN}$. Inserting this ansatz, instead of the often employed zero-width approximation $S^V \sim \delta(s - m_V^2)$, in the QCD sum rule equation one gets the parameter $\overset{\circ}{m}_V\,(n)$ which density dependence is driven by condensates, the Landau damping term and self-energy.

To account for uncertainties regarding the density dependence of poorly known scalar four-quark condensate we have introduced a parameter $\kappa_N$ [2]:

$$\langle(\overline{q}\gamma_\mu\lambda^a q)^2\rangle_n = \frac{16}{9}\langle\overline{q}q\rangle_0^2\,\kappa_0\left[1 + \frac{\kappa_N}{\kappa_0}\frac{\sigma_N}{m_q\langle\overline{q}q\rangle_0}\right]\ . \quad (2)$$

To study consistently the in-medium broadening of light vector mesons we have employed $\rho N$ and $\omega N$ scattering amplitudes derived recently from a covariant unitary channel approach adjusted to pion-and photon-induced reactions [4]. To determine the in-medium modification of $\rho$ and $\omega$ on a common footing is the main objective of our investigation. The results are exhibited in Fig.1.

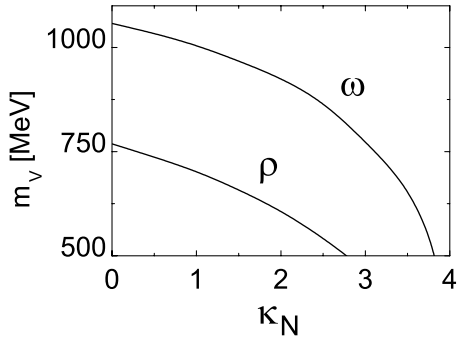


**Fig. 1** *Mass shifts of $\rho$ and $\omega$ mesons as a function of the parameter $\kappa_N$ at saturation density $n = 0.15$ fm$^{-3}$.*

Our evaluation elucidates that properties of $\rho$ and $\omega$ depend on the common four-quark condensate. Once one of this vector mesons is identified in medium, the other one is constrained or even partially determined. With respect to preliminary results of the CB-TAPS collaboration at ELSA [6], a very useful constraint of the density dependence of four-quark condensate is at reach: Supposed the $\omega$ meson does not suffer a positive mass shift, which appears for small values of $\kappa_N$ (see Fig.1), $\kappa_N$ is constrained to larger values. This in turn leads to the prediction of a strong down shift of the $\rho$ meson, as evidenced in Fig.1.

The described framework is well defined, supposed scattering amplitude $T_{VN}$ is reliably known. Unfortunately, the determination of $T_{VN}$ is hampered by uncertainties (cf. results in [4, 7]). To account for this source of uncertainty we have scaled $T_{VN}$ by a factor $\gamma$ and studied the dependence $m_V(\kappa_N, \gamma)$ [5]. Despite that our chosen range of $\gamma$ covered an enormous range of the width the tendency of a down-shift of the $\rho$ mass and a related up-shift of the $\omega$ mass remains robust. In addition, it turned out that the sensitivity against variation of $\kappa_N$ is larger than that of $\gamma$. Accordingly, the uncertainty of scattering amplitude are not so important than uncertanties of the four-quark condensate.

In summary, in contrast to the universal Brown-Rho scaling hypothesis [1] there is no unique in-medium behaviour of $\rho$ and $\omega$ mesons. If an up-shift of $\omega$ meson can be experimentally excluded [6], the present QCD sum rule analysis points to a strong down-shift of $\rho$ meson already at nuclear saturation density.

[1] G.E. Brown, M. Rho, Phys. Rev. Lett. 66 (1991) 2720
[2] S. Zschocke, O.P. Pavlenko, B. Kämpfer, hep-ph/0308070
[3] S. Zschocke, O.P. Pavlenko, B. Kämpfer, Eur. Phys. J. A 15 (2002) 529
[4] M.F. Lutz, Gy. Wolf, B. Friman, Nucl. Phys. A 706 (2002) 431
[5] B. Kämpfer, S. Zschocke, Prog. Part. Nucl. Phys. 52 (2004), in print
[6] D. Trnka et al. (CB-TAPS collaboration), to be published
[7] F. Klingl, N. Kaiser, W. Weise, Nucl. Phys. A 624 (1997) 527; Nucl. Phys. 650 (1999) 299

[1] *Institute for Theoretical Physics, 03143 Kiev - 143, Ukraine*

# Transport Model Study of Di-Electron Production in Intermediate-Energy Heavy-Ion Collisions [B]

Gy. Wolf[1], B. Kämpfer, O.P. Pavlenko[2]

One of the main goals of the experiments with the HADES detector is the search for a direct evidence of in-medium modifications of hadrons in the di-electron ($e^+e^-$) channel. The chiral quark condensate $\langle\bar{q}q\rangle$ as order parameter of the chiral symmetry breaking decreases with increasing baryon density. Since $\langle\bar{q}q\rangle$ is coupled to the vector meson spectral densities one can expect considerable in-medium effects of light vector mesons. Since a pronounced vector meson mass shift is expected for large baryon density, there is the hope to verify the effect in heavy-ion collisions at SIS18 energies. However, for heavy-ion collisions such measurements face problems related to the collective expansion, i.e., the baryon density $n$ depends on time so that a time average of the mass shift is to be expected and the mass shift is distributed over an interval related to the change of $n$. This can make the identification of the expected mass shift, in particular for the $\rho$ meson, rather difficult.

In [1] we have proposed an extension of the usual analysis of the invariant mass spectrum $dN/dM^2$ to the double-differential spectrum $dN/dM^2\,dM_\perp^2$, where $M_\perp = (M^2 + \vec{Q}_\perp^2)^{1/2}$ is the transverse mass of the pair with transverse two-momentum $\vec{Q}_\perp$. Such an extension with suitable kinematical cuts allows to avoid the majority of the above mentioned difficulties in extracting information on the in-medium vector meson spectral function. Here we present results of our calculations [2] of double-differential di-electron spectra in heavy-ion collisions within a BUU transport model.

In fig. 1 various contributions to the invariant mass spectrum are exhibited. We assume schematically a constant in-medium broadening of $\rho$ and $\omega$ mesons and a constant mass shift of the $\rho$ meson. While in the full invariant mass spectrum (bottom panel) the $\rho$ peak disappears, a suitable $M_\perp$ cut evidences clearly the shifted $\rho$ peak (top panel). The $\omega$ meson anyway sticks out.

The prospects to identify a density dependent in-medium shift of the $\omega$ meson are less convincing. The reason is that a density dependent in-medium broadening pulls down the strength of the $\omega$ peak. Results of a calculation with optimistically tuned parameters are exhibited in fig. 2. Here the distributed $\omega$ in-medium strength mimics a $\rho$ peak. Triggering on low-$Q_\perp$ pairs enhances the in-medium $\omega$ decay contribution. For more realistic parameters, however, the in-medium $\omega$ strength is below the $\rho$ contribution [2].

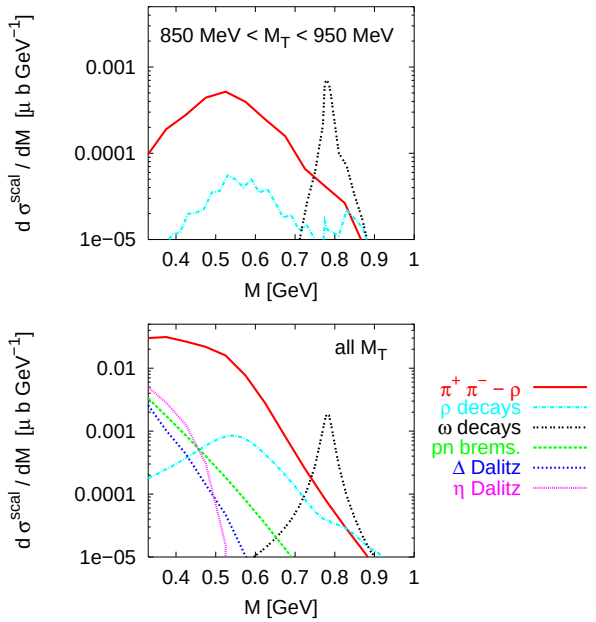


**Fig. 1** *Contributions to the di-electron spectrum $d\sigma^{\rm scal}/dM$ for central collisions Au(1 AGeV) + Au. A resonance broadening by a factor 3 is assumed for both $\rho$ and $\omega$, and a $\rho$ mass shift of 150 MeV. In the calculation the $\rho$ contributions are split in $\pi^+\pi^-$ annihilation and so-called direct $\rho$ mesons stemming from resonance decays. pn bremsstrahlung and $\Delta$ and $\eta$ Dalitz decays are also shown.*

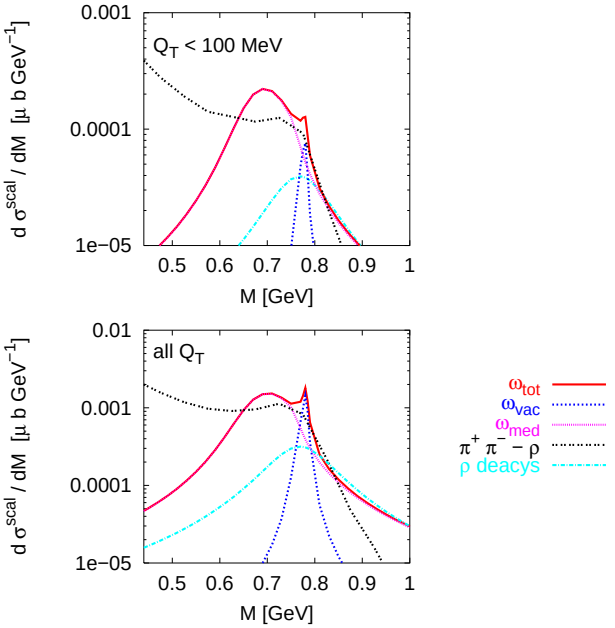


**Fig. 2** *Invariant mass spectra from $\omega$ decays for the following density dependent in-medium effects: $m_\omega(n) = m_\omega(1 - \delta m_\omega n/n_0)$, $\Gamma_\omega(n) = \Gamma_\omega + \delta\Gamma_\omega n/n_0$ with $\delta m_\omega = 50$ MeV and $\delta\Gamma_\omega = 50$ MeV. As reference the $\rho$ contribution for vacuum parameters is shown. In this calculation it is assumed that both the total and the electromagnetic width of $\omega$ scale in the same manner.*

[1] B. Kämpfer, O.P. Pavlenko, Eur. Phys. J. A 10 (2001) 101
[2] Gy. Wolf, O.P. Pavlenko, B. Kämpfer, nucl-th/0306029

[1] *RKMI, KFKI, Budapest, Hungary*
[2] *Institute for Theoretical Physics, Kiev, Ukraine*

# Describing Di-Electron Spectra in Relativistic Heavy-Ion Collisions at CERN-SPS Energies [B,E]

K. Gallmeister[1], B. Kämpfer

Intermediate-mass di-electrons are considered as a useful probe of phenomena related to chiral symmetry restoration in hot and dense nuclear matter [1]. Indeed, we found a consistent description of NA38, HELIOS-3, NA50 and CERES-NA45 data for di-electrons and di-muons by assuming that the emissivity of matter is not longer a superposition of individual hadron channels but resembles a smooth continuum which we call thermal radiation [2]. In fact, our rate is parameterized as a $\bar{q}q$ annihilation spectrum pointing to a drastic reshaping of the hadronic excitation spectrum. Even more, also the WA98 photon data are compatible with such an ansatz [3].

By now, new data are at our disposal which can be used to test further our model ansatz and to arrive at a consolidated understanding of the di-electron emission in heavy-ion collisions at CERN-SPS energies. The CERES-NA45 collaboration has shown first preliminary data from a high-statistics run in 2000 [4]. As exhibited in fig. 1 our model [2] also describes this new data set fairly well. The data sample is for a stronger centrality selection than previous CERES data. As a consequence the weight of the thermal source is correspondingly larger. The data do not require a larger space-time averaged temperature than in collisions which do not obey such a sharp centrality selection.

Also two new photon data points of the WA98 collaboration at very low $k_\perp$ [5] are qualitatively described by our model [2, 3] without changing any parameter, see fig. 2. (Note, however, that we have up-scaled our old model [3] by a correction factor accounting for the complete leading order photon emission rate [6].) The particular point here is that the new data [5] are in a region where the hardly controllable semi-hard QCD processes are of subdominant order and the thermal radiation dominates.

The previous and new data together point to thermal radiation of a source with space-time averaged temperature of 170 MeV. Having in mind a picture of an expanding and cooling fireball, our conclusion is that in hot spots and at early stages the fire ball must have had a temperature larger than 170 MeV, i.e., above the deconfinement temperature $T_{decon} \approx 170$ MeV. This is in distinct contrast to the di-electron data in the reaction $Pb(40AGeV) + Au \to e^+e^-X$, where we found a space-time averaged temperature of the thermal source of 145 MeV [7], well below the deconfinement temperature.

It is interesting to note that the found space-time averaged temperatures, which are the main characteristic quantities of our model, agree with the chemical freeze-out temperatures deduced from hadron multiplicities.

A crucial further test of our model ansatz will be given by the forthcoming di-muon data from NA60.

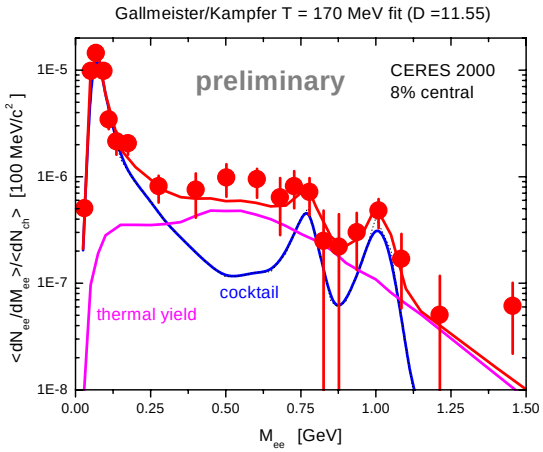


**Fig. 1** *Comparison of preliminary di-electron data from CERES-NA45 [4] for the reaction* $Pb(158AGeV) + Au \to e^+e^-X$ *with our model [2]. The acceptance is described by* $\Theta_{e^+e^-} > 35$ *mrad,* $p_\perp^{e^\pm} > 200$ *MeV, and* $2.1 < \eta < 2.65$. *The centrality is characterized by* $\sigma_{\rm trigger}/\sigma_{\rm tot} = 8\%$.

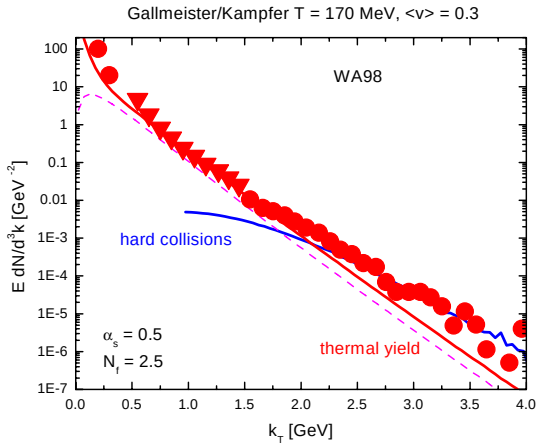


**Fig. 2** *Comparison of the photon data [5] (points: data, triangles: upper limits, error bars are discarded) for the reaction* $Pb(158AGeV) + Pb \to \gamma X$ *with our model [3] (dashed curve) and the up-scaled yield (solid curve). The hard perturbative QCD contribution is correspondingly labeled.*

[1] R. Rapp, J. Wambach, Adv. Nucl. Phys. 25 (2000) 1
[2] K. Gallmeister et al., Phys. Lett. B473 (2000) 20, Nucl. Phys. A688 (2001) 939
[3] K. Gallmeister et al., Phys. Rev. C62 (2000) 057901
[4] A. Marin (for the CERES collaboration), talk at QM2004, Oakland, USA, Jan. 11 - 16, 2004
[5] M.M. Aggarwal et al. (WA98 collaboration), nucl-ex/0310022, Phys. Rev. Lett. 85 (2000) 3595
[6] P. Arnold, G.D. Moore, L.G. Yaffe, JHEP 0111 (2001) 057
[7] K. Gallmeister et al., Nucl. Phys. A698 (2002) 424c

[1] *Institut für Theoretische Physik, Universität Giessen*

# Spread of Mass Distribution of $\phi$ Mesons Observed by $K^+K^-$ and $e^+e^-$ Pairs [S,B]

H.W. Barz, M. Zétényi[1]

The study of in-medium properties of hadrons in nuclear matter is an important subject of contemporary strong interaction physics. Over the last decade a dropping in-medium mass has been considered a precursor phenomenon of chiral symmetry restoration. Especially a strong reduction of the $K^-$ mass is expected with the consequence that the width of a $\phi$ meson in matter could reach values of 45 MeV leading to a dramatical decrease of its life time. Thus most of slow $\phi$ mesons would decay inside the nucleus mainly into kaon pairs. However for kaon pairs created inside the reaction zone there is a great chance that at least one particle of the pair is scattered or absorbed, such that they cannot anymore signal their original invariant mass. This effect will strongly depend on the size of the nuclear system and will lead to a characteristic dependence of the $\phi$ meson yield on the target-mass number $A$.

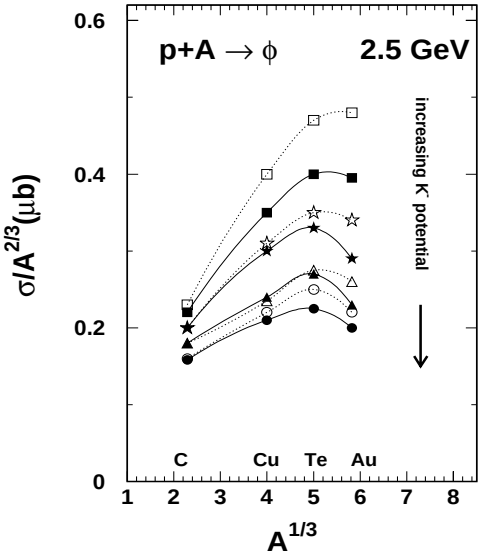


**Fig. 1** *Rescaled cross sections for $\phi$ meson production as a function of the target mass for different kaon potentials. The cross sections are reconstructed from electron pairs (open symbols) and from kaon pairs (full symbols), respectively. Squares: without $K^-$ potential, stars: with a moderate $K^-$ potential, triangles: with momentum dependent potential, circles: strong momentum independent potential.*

In Fig. 1 we present the cross sections for $\phi$ mesons calculated [1] for different attractive potentials of the $K^-$ mesons where the $\phi$ mesons are identified either by kaon pairs or by electron pairs with invariant masses of $m_\phi^{\rm vacuum} \pm 50$ MeV. It is clearly seen that an increasing $K^-$ potential diminishes the production rates. It was assumed that the $\phi$ mass is not altered in the nuclear medium. However the invariant mass of the $K^+K^-$ pairs can considerably deviate from the vacuum $\phi$ mass due to the action of the time dependent kaon potentials. Since the strong attractive $K^-$ potential has the dominant influence, the invariant mass will mostly exceed the vacuum mass. The effect is demonstrated in Fig. 2 for two different target nuclei and two different potentials. Similar results are reported in [2]. In the case of the gold nucleus with a strong $K^-$ potential about 50% of the kaon pairs are created inside the nucleus and their spread is of the same order as the strength of the $K^-$ potential. This has the consequences that these widely spread kaon pairs can hardly be used to identify $\phi$ mesons.

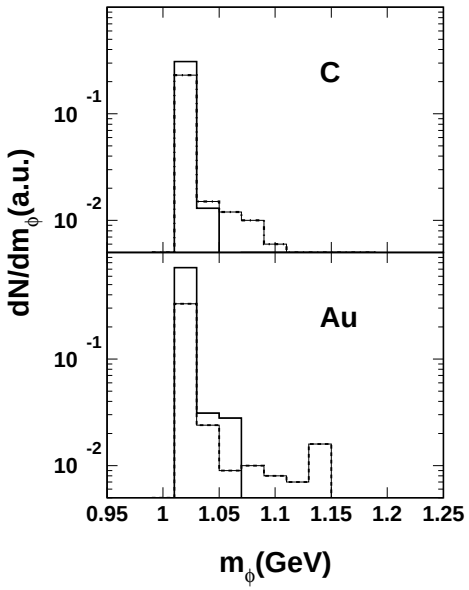


**Fig. 2** *Distribution of the invariant mass of the kaon pairs produced in pC and pAu reaction for two different depths of $K^-$ potential of 70 MeV (smooth histogram) and 120 MeV (dashed histogram).*

The long range Coulomb force of the target nucleus causes much smaller shifts and spreads of the invariant mass distributions. The effect scales with the charge number of the target. For the heavy nucleus Au the mass shift of a $\phi$ meson depends on the momentum and angle and amounts up to +5 MeV and a maximum spread of 15 MeV. Here we have assumed that the life time is only 5 fm/c. If the $\phi$ meson decays mostly outside of the nucleus the values reduce by about a factor of two. If the $\phi$ mesons are reconstructed from electron pairs the corresponding shift is less than 1 MeV, while the maximum spread due to the Coulomb force amounts to 10 MeV if the $\phi$ decays inside the nucleus and half that value if it decays outside the gold nucleus.

[1] H.W. Barz, M. Zétényi, Phys. Rev. C 69 (2004) 024605
[2] P. Mühlich, T. Falter, C. Greiner, J. Lehr, M. Post, and U. Mosel, Phys. Rev. C 67 (2003) 024605

[1] *KFKI Budapest, Hungary*

# $\rho$ - $\omega$ Splitting and Mixing at Finite Density [B,G]

S. Zschocke, B. Kämpfer

In vacuum the mass splitting between $\rho$ and $\omega$ amounts to $\Delta m = m_\omega - m_\rho = 13$ MeV. By means of the QCD sum rule approach we have investigated how pronounced this splitting in matter is, i.e. $\Delta m(n)$. The corresponding mass equation for both vector mesons reads [1]

$$\frac{m_V^2}{M^2} = \left\{ C_0 \left( 1 - [1 + \frac{s_0^V}{M^2}] \mathrm{e}^{-s_0^V/M^2} \right) - \frac{C_2}{M^4} - \frac{C_3}{M^6} \right\} \left\{ C_0 \left( 1 - \mathrm{e}^{-s_0^V/M^2} \right) + \frac{C_1 - \rho_{\mathrm{scatt}}^{VN}}{M^2} + \frac{C_2}{M^4} + \frac{C_3}{2M^6} \right\}^{-1} . \quad (1)$$

The parameter $s_0^V(n) \approx 1.0 \ldots 2.0$ GeV characterizes the continuum threshold. The real coefficients $C_n$ denote Wilson coefficients including density dependent condensates; $\rho_{\mathrm{scatt}}^{\rho,N} = n/(4M_N)$, $\rho_{\mathrm{scatt}}^{\omega,N} = 9n/(4M_N)$ are the Landau damping terms, and $M_{\min}(n) \le M \le M_{\max}(n)$ stands for the Borel mass parameter. The results, after averaging over dynamical Borel window, are shown in Fig.1. In vacuum there is only one condensate (the so-called flavour mixed scalar four-quark condensate) which governs the mass splitting but turns out to play a subdominant rule in matter. Instead, the Landau damping term $\rho_{\mathrm{scatt}}^{V,N}$ is mainly responsible for the strong mass splitting of $\rho$ and $\omega$ at finite densities, while the scalar flavour unmixed four-quark condensate governs the strength of individual mass shifts.

Another effect seen in vacuum concerns the experimental observation of the decays $\rho \to \pi^+\pi^-\pi^0$ and $\omega \to \pi^+\pi^-$. Accordingly, the physical mesons are not pure isospin eigenstates but mixed with each other in the form

$$\begin{pmatrix} \rho \\ \omega \end{pmatrix} = \begin{pmatrix} 1 & -\epsilon \\ \epsilon & 1 \end{pmatrix} \begin{pmatrix} \rho^I \\ \omega^I \end{pmatrix} . \quad (2)$$

The complex mixing angle $\epsilon$ enters the pion form factor

$$F_\pi = 1 - \frac{q^2}{q^2 - m_\rho^2 - i\,\Im(\Sigma_\rho)} - \frac{\epsilon\, q^2}{q^2 - m_\omega^2 - i\Im(\Sigma_\omega)} . \quad (3)$$

Using the QCD sum rule we have investigated the strength of the mixing at finite density, i.e. $\epsilon(n)$ when taking into account the individual mass shifts of vector mesons. The results for the pion form factor are shown in the left panel of Fig. 2, while the corresponding di-electron production rate $R = dN^{\mathrm{e+e-}}/d^4x$ has been plotted in the right panel. A disappearance of the $\rho$ - $\omega$ mixing at finite density is seen in contradiction to earlier predictions made without taking care about mass shifts of $\rho$ and $\omega$.

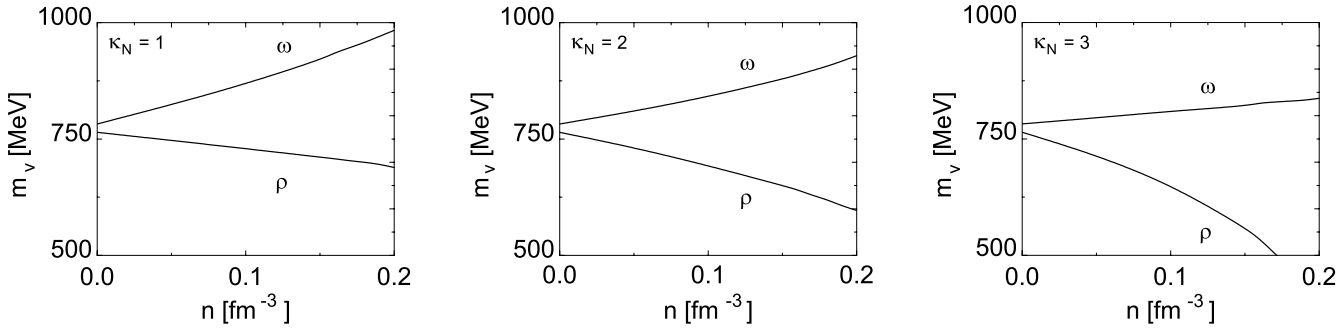


**Fig. 1** *The $\rho$ and $\omega$ meson mass splitting as a function of the density. The parameter $\kappa_N$ governs the strength of density dependence of the poorly known scalar flavour-unmixed four-quark condensate.*

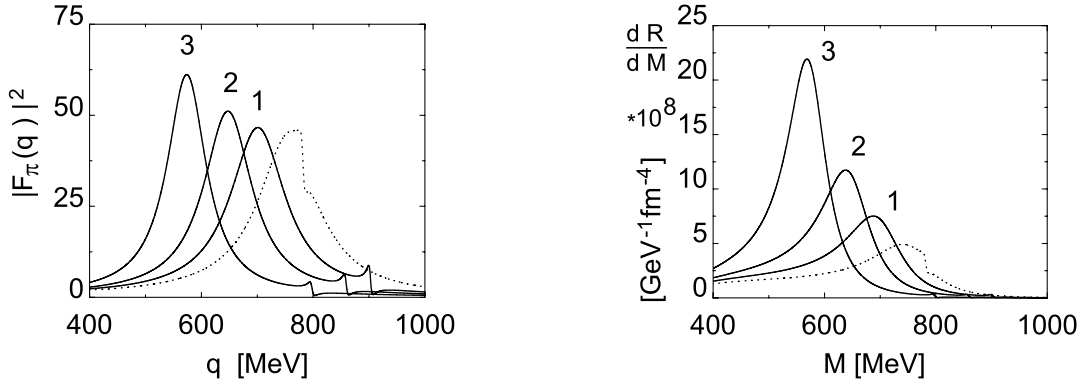


**Fig. 2** *The pion-formfactor (left panel) and the the di-electron production rate (right panel) for different baryonic densities for $T = 100$ MeV. The individual mass shifts of $\rho$ and $\omega$ have been taken into account. The dashed-dotted line indicates for reference $n = 0$ (i.e. hot pion gas), solid line depicts $n = n_0$, and dashed line is for $n = 2\,n_0$.*

[1] S. Zschocke, O.P. Pavlenko, B. Kämpfer, Eur. Phys. J. A 15 (2002) 529
[2] B. Kämpfer, S. Zschocke, Prog. Part. Nucl. Phys. 52 (2004), in print

# $\omega$ Production in Nucleon-Nucleon Reactions [B]

L.P. Kaptari[1 2], B. Kämpfer, A.I. Titov[2 3]

The understanding of vector meson production in elementary hadronic reactions is a prerequisite for the comprehensive study of in-medium effects with direct probes like the channel $e^+e^-$. The physics programme of HADES has correspondingly, besides the study of heavy-ion and hadron-nucleus collisions, also the goal to measure particulary channels in $\pi N$ and $pN$ reactions.
Within an effective Lagrangian tree-level approach we have recently studied the $\rho - \omega$ quantum interference in the reaction $\pi N \to e^+e^- N$ [1], $\omega$ and $\phi$ production in $\pi N$ reactions [2] and the $\phi$ production in $\pi N$, $NN$ and $pd$ collisions [3] as well. (For a survey cf. [4].) Here we report on our treatment of the reaction $pN \to \omega pN$ near threshold. Using $s$, $u$ and $t$ channel diagrams with one-boson exchange and form factors and coupling strengths similar to [3] we find an appropriate parameterization of available data as shown in fig. 1. We emphasize that even without the inclusion of baryon resonances a fairly well description of the data is accomplished, in contrast to [5].

Further work will be devoted to fold the found parameterization of the cross section for $pn \to \omega pn$ with the deuteron wave function to study the quasi-free tagged reaction $pd \to d\omega p_{\rm spec}$ for which first data are available from COSY-ANKE.

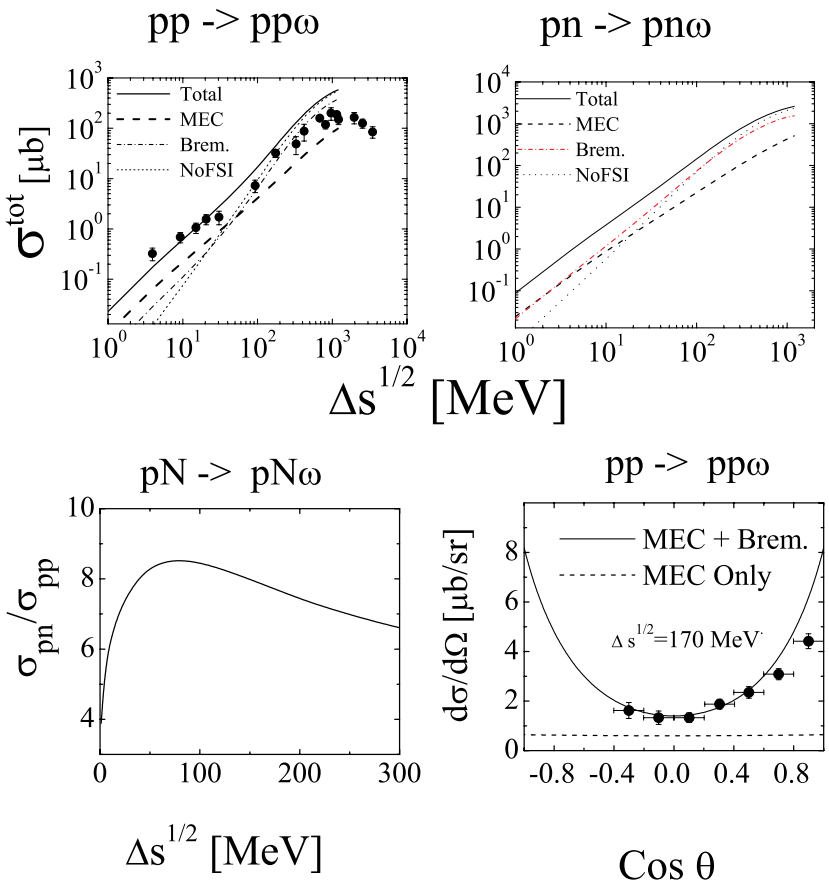


**Fig. 1** *Energy dependence of the total cross section for the reactions $pp \to \omega pp$ and $pn \to \omega pn$ (top, data compilation from [5]) and their ratio (left bottom). The parameters are adjusted to the angular distribution at excess energy of 173 MeV (right bottom, data from [6]). "MEC" denotes the contribution from the meson current (t channel), while "Brem." depicts the contribution from s and u channels. Final state interaction (FSI) among the nucleons is included along the lines of [2,3]. For more details cf. [4].*

[1] A.I. Titov, B. Kämpfer, Eur. Phys. J. A 12 (2001) 217
[2] A.I. Titov, B. Kämpfer, B.L. Reznik, Phys. Rev. C 65 (2002) 065202
[3] A.I. Titov, B. Kämpfer, B.L. Reznik, Eur. Phys. J. A 7 (2000) 543
L.P. Kaptari, B. Kämpfer, Eur. Phys. J. A 14 (2002) 211
[4] B. Kämpfer, L.P. Kaptari, A.I. Titov, nucl-th/0402044
[5] K. Tsushima, K. Nakayama, Phys. Rev. C 68 (2003) 034612
[6] S. Abd El-Samad et al., Phys. Lett. B 522 (2001) 16

[1] *Department of Physics, University of Perugia, and INFN Sezione di Perugia, via A. Pascoli, I-06100, Italy*
[2] *permanent address: Bogolyubov Laboratory of Theoretical Physics, JINR Dubna, 141980, Russia*
[3] *Advanced Science Research Center, Japan Atomic Energy Research Institute, Tokai, Ibaraki, 319-1195, Japan*

# Contribution of the Nucleon-Hyperon Reaction Channels to $K^-$ Production in Proton-Nucleus Collisions [B]

H.W. Barz, L. Naumann

To study the properties of kaons and antikaons in nuclear matter the measurements of their production rates in heavy-ion collisions at energies near or below the production threshold of nucleon-nucleon collisions is a very appropriate tool. However, to extract the potentials of kaons the knowledge of their production mechanism is a necessary condition. $K^-$ mesons are mainly produced in reactions of nucleons and pions with hyperons $Y$ ($\Lambda$, $\Sigma$) which are created in first collisions. To get insight of the role of the different reaction channels it is useful to study besides heavy-ion collisions also nucleon-nucleus collisions as a further source of information. Especially, in $pA$ collisions $NY$ processes are important as pions must be produced in further collisions.

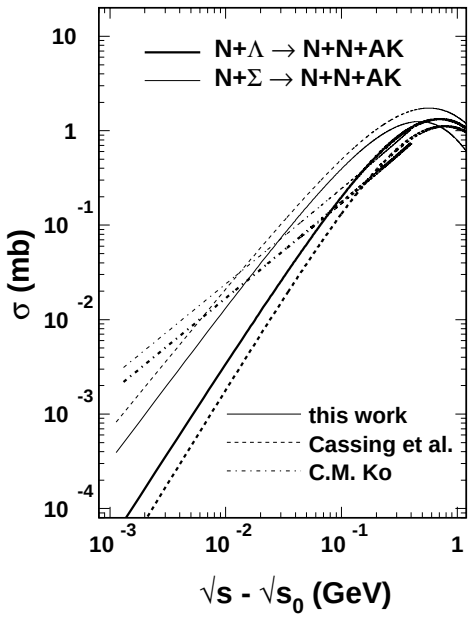


**Fig. 1** *Comparison of isospin averaged production cross sections for antikaon(AK) production versus excess energy obtained by various models [1-3].*

Here, we draw our attention to the nucleon-hyperon channel $NY \to NNK^-$ cross section. This cross section which is not measurable was already calculated early in the one-pion exchange model [1] and later in one-boson exchange approximation [2,3] and was found to be negligible for heavy-ion collisions. Avoiding the uncertainties arising from the badly known formfactors we reevaluated the cross section exploiting the pion exchange mechanism and using the experimentally known $\pi N$ cross sections. In Fig. 1 we show the cross sections obtained using the different approaches. In the relevant region of kinetic energies of about 100 MeV the magnitudes of the cross sections do not differ very much and show the dominance of the N$\Sigma$ channel.

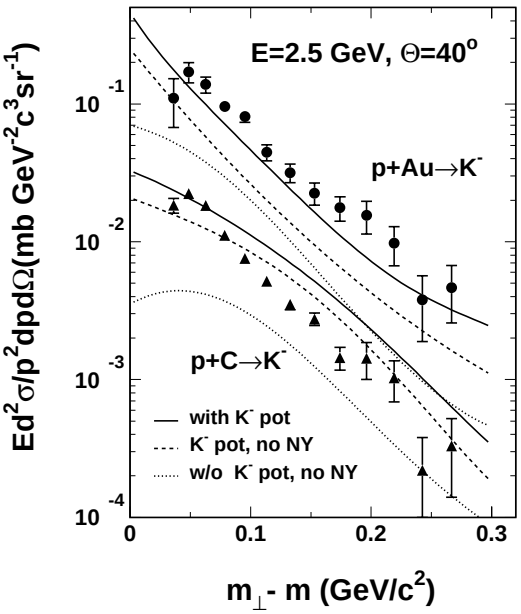


**Fig. 2** *Comparison of measured invariant $K^-$ meson cross sections (symbols) as a function of the transverse mass with calculations for $pC$ and $pAu$ collisions. See text for details.*

To probe the relevance of the $NY \to NNK^-$ we compare BUU calculations with recent data [4] from the KaoS collaboration for the $p$C and $p$Au collisions at a bombarding energy of 2.5 GeV at a laboratory angle of 40°. In Fig. 2 we present the invariant $K^-$ cross sections calculated without using potentials for the kaons and antikaons (dotted lines). These calculations underestimate clearly the measured data, and even an attractive antikaon potential of 120 MeV $n/n_0$ gives too small a cross section (dashed lines). Including the $NY$ channel in addition clearly improves the agreement with experiment. For the light C target the influence is much smaller as the hyperons have a smaller chance to collide with further nucleons before leaving the reaction zone.
We conclude that the $NY \to NNK^-$ channels which are usually neglected have to be included in realistic calculations, especially for heavy targets, in order to study the properties of strange mesons in nuclear matter at normal nuclear density.

[1] C.M. Ko, Phys. Rev. C 29 (1984) 2169
[2] W. Cassing and E.L. Bratkovskaya, Phys. Rep. 308 (1999) 65
[3] H.W. Barz, L. Naumann, Phys. Rev. C 68 (2003) 041901
[4] W. Scheinast (KaoS collaboration), Meson 2002, World Scientific Publ. (Singapore) (2003) 493

# Equation of State of Dense Quark Matter [B,E]

M. Bluhm[1], B. Kämpfer, A. Peshier[2], G. Soff[1]

With respect to the planned Compressed Baryon Matter (CBM) project at the Future Accelerator Complex at GSI [1] a determination of the phase border line from confined to deconfined matter and the equation of state as well are important. We report here results for the equation of state of deconfined matter obtained within our quasi-particle model [2].

Our model is based on dynamically excited quark and gluon modes near the light cone. The quasi-particle excitations determine the entropy density, which delivers the pressure and energy density in a thermodynamically self-consistent manner. A crucial ingredient is the effective coupling to be adjusted at lattice QCD data. The recent lattice QCD data [3] deliver the equation of state in the form

$$\frac{\Delta p(T,\mu)}{T^4} \equiv \frac{1}{T^4}\left(p(T,\mu)-p(T,\mu=0)\right) \quad (1)$$

$$= c_2(T)\left(\frac{\mu}{T}\right)^2 + c_4(T)\left(\frac{\mu}{T}\right)^4 + \cdots, \quad (2)$$

where $p$ denotes the pressure, $T$ means the temperature, and $\mu$ is the quark-chemical potential. The expansion coefficients $c_{2,4}(T)$ are directly calculable with established numerical simulations at $\mu = 0$. Our quasi-particle model in turn allows to adjust the effective coupling $G(T)$ to these coefficients, e.g., for $c_2$ by

$$c_2 = \frac{N_f d_q}{2\pi^2 T^3}\int_0^\infty dk\, k^2\, \frac{e^{E_q/T}}{(e^{E_q/T}+1)^2}, \quad (3)$$

where $E_q^2 = k^2 + m_q^2$ and $m_q^2 = \frac{1}{3}T^2\, G^2(T)$ is a dynamically generated quasi-quark mass; $N_f$ is the number of active flavors, and $d_q$ stands for the degeneracy factor of quarks. Fig. 1 exhibits an example of such an adjustment with the parameterization

$$G^2(T) = \begin{cases} G^2_{2-\mathrm{loop}}(T), & T \geq T_c \\ G^2_{2-\mathrm{loop}}(T_c)\,\dfrac{1-\alpha T/T_c}{1-\alpha}, & T < T_c \end{cases} \quad (4)$$

with $G^2_{2-\mathrm{loop}}$ as two-loop running QCD coupling with the *log* argument $\lambda(T - T_s)/T_c$ and the parameters $T_s = 0.93T_c$, $\lambda = 21.3$; below the pseudo-critical temperature $T_c$ the linear behavior of $G^2$ is appropriate with $\alpha = 0.9457$. The extrapolation to finite baryon density is based on a thermodynamic self-consistency condition and a extremum property of the pressure as thermodynamical potential [2]. The key is the solution of a partial differential equation which maps the coupling $G(T)$ to non-vanishing values of $\mu$. Knowing this new effective coupling $G(T,\mu)$ the calculation of thermodynamical quantities like pressure, entropy density, quark density, susceptibility etc. is straightforward. Fig. 2 exhibits an example of the normalized quark density, $n_q/T^3 = \partial(\Delta p(T,\mu)/T^4)/\partial\mu$.

The remarkable agreement with the data let us argue that the quasi-particle model catches the relevant propagating modes with momenta $k \sim T, \mu$ in deconfined matter. Thus a suitable equation of state is at our disposal which is needed, e.g., to describe the baryon-dense states of highly compressed nuclear matter envisaged in the CBM project.

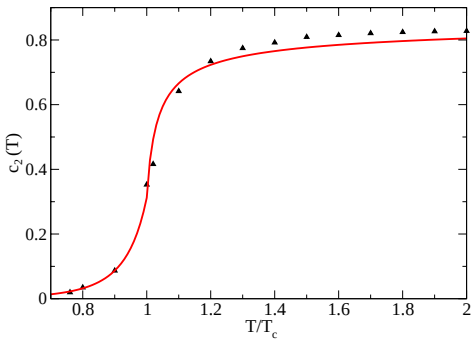


**Fig. 1** *The coefficient $c_2$ as a function of the temperature (in units of the pseudo-critical temperature). Symbols: lattice QCD results [3], curve: use of eqs. (3, 4) with adjusted $G(T)$.*

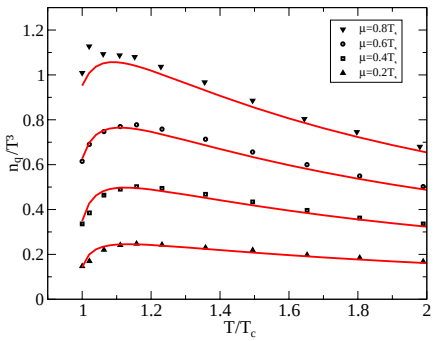


**Fig. 2** *Normalized quark number density as a function of the temperature for various values of the chemical potential. Data from [3]; curves represent results of our model. For more details cf. [4].*

[1] CBM Letter of Indend: http://www.gsi.de/documents/DOC-2004-jan-116.pdf
[2] A. Peshier, B. Kämpfer, O. P. Pavlenko, G. Soff, Phys. Rev. D 54 (1996) 2399;
A. Peshier, B. Kämpfer, G. Soff, Phys. Rev. C 61 (2000) 045203; Phys. Rev. D 66 (2002) 094003
[3] C.R. Allton et al., Phys. Rev. D 68 (2003) 014507
[4] M. Bluhm, B. Kämpfer, G. Soff, hep-ph/0402252

[1] *Institut für Theoretische Physik, TU Dresden*
[2] *Institut für Theoretische Physik, Universität Giessen*

# Energy Loss of Heavy Quarks by Gluon Radiation [B]

R. Thomas[1], B. Kämpfer, G. Soff[1]

One of the striking results of the heavy-ion experiments at the relativistic heavy-ion collider RHIC in Brookhaven is the circumstantial evidence of a substantial partonic energy loss of light quarks which is interpreted as unique signature of the transient creation of the long wanted quark gluon plasma. Experimentally the effect is seen as attenuation of the transverse momentum spectra of light mesons and baryons.

Puzzling, however, is the lack of a similar attenuation of the transverse momentum spectrum of charmed mesons [1]. A possible explanation is the dead cone effect, i.e., the radiation pattern of high-energetic particles is modified if the particles have a non-negligible mass. Since the energy loss, which causes the transverse momentum attenuation, is mainly due to induced gluon emission during the passage of the quark through deconfined matter, a detailed understanding of the emission processes is a necessary prerequisite for deriving global energy loss formulae. The energy loss of charmed mesons has consequences for the di-electron spectrum [2]. Also details of partially balanced di-jets depend on the energy loss mechanism [3].

Similar to [4] we begin to analyse the one-gluon emission by a single scattering process off a screened potential described by the following diagrams

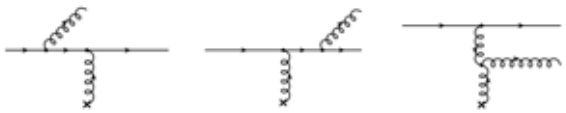

named pre-emission, post-emission and three-gluon. The found radiation pattern then serves as the basis for generalizing to multiple scattering processes. The aim of this study is an exact treatment of the emission process. We employ a C++ code [5] which takes into account the complete kinematics, full spinor algebra with all spin effects, color algebra and gluon polarization. Fig. 1 exhibits contributions to the radiation amplitude for a light quark and the emission of a soft gluon. $\Theta_0 \equiv m/E$ (where $m$ is quark mass and $E$ the incidence energy) is a dimensionless scale defined by the mass of the radiating particle. At fixed energy of the emitted gluon and for fixed momentum transfer $q_\perp$, the radiation is suppressed for emission angles $\Theta < \Theta_0$. This is the famous dead cone effect. For the selected kinematics the three-gluon diagram is negligible. In the chosen $A^+ = 0$ gauge the contribution of the post-emission diagram dominates at $\Theta < \Theta_c \equiv m^2/(q_\perp E)$. In the region $\Theta > \Theta_q \equiv q_\perp/E$ the pre-emission and post-emission interfere destructively to change the radiation amplitude $\propto 1/(\omega^2\Theta^4)$.

Fig. 2 depicts a kinematical situation, where the factorization and the neglect of the non-Abelian diagram do not longer hold. Here, a hard gluon is emitted by a massive quark. At $\Theta < \Theta_{3\mathrm{glu}} \equiv q_\perp/\omega$ the three-gluon diagram dominates. This causes the striking difference of the radiation pattern in Abelian and non-Abelian gauge theories. The dead cone effect happens only for Abelian radiation below $\Theta_0$ and is visible as decreasing amplitude towards $\Theta_q$ where again the post-emission diagram dominates. A comprehend study of the radiation pattern for various kinematical situations can be found in [5], where also the scattering at a potential with screening length $1/\mu$ (this sets the scale $\Theta_\mu = \mu/E$) is compared with dynamical quark-quark scattering.

As an important step towards the formulation of a radiation energy loss formula the calculation of the one-gluon emission in double scattering processes is needed. Here the isolation of a divergence is required to allow for our numerical treatment. Calculations are in progress.

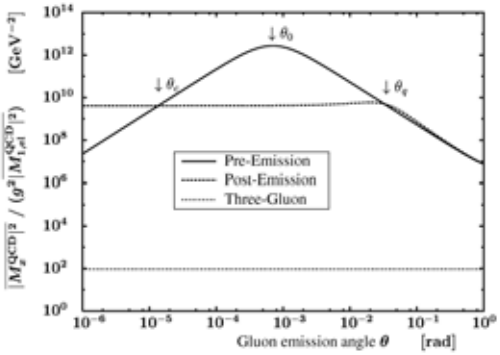


**Fig. 1** *Contributions to the radiation amplitude (normalized to elastic scattering) as a function of the gluon emission angle. The incidence energy of the quark with mass of 7 MeV is 10 GeV. The emitted gluon has an energy of $\omega = 1$ MeV.*

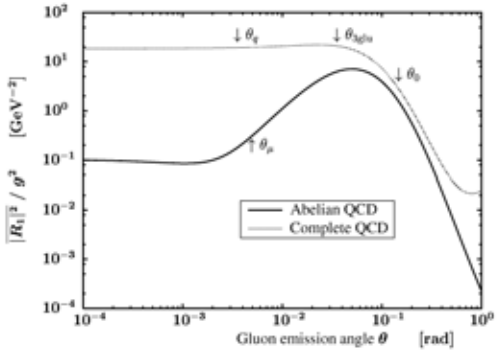


**Fig. 2** *Radiation amplitudes (normalized by the coupling strength $g^2$) of a heavy quark with mass of 1.5 GeV and incidence energy of 10 GeV as a function of the gluon emission angle. The energy of the emitted gluon is 1 GeV.*

[1] K. Gallmeister, B. Kämpfer, O.P. Pavlenko, Nucl. Phys. A 715 (2003) 705c
[2] K. Gallmeister, B. Kämpfer, O.P. Pavlenko, Phys. Rev. C 57 (1998) 3276
[3] K. Gallmeister, B. Kämpfer, O.P. Pavlenko, Phys. Rev. C 66 (2002) 014908
[4] B. Kämpfer, O.P. Pavalenko, Phys. Lett. B 477 (2000) 171
[5] R. Thomas, Diploma Thesis, TU Dresden 2003

[1] *Institut für Theoretische Physik, TU Dresden*

# Two-Proton Intensity Interferometry in Central Ca + Ca Collisions [B,G]

R. Kotte for the FOPI Collaboration

Previous studies [1, 2] of intensity interferometry with light charged particles have been resumed aiming at systematic investigations of the two-proton correlation function in central heavy-ion collisions. Here, we report on the excitation function of such small-angle pp correlations measured in central $^{40}$Ca + $^{40}$Ca reactions at beam energies between 400 and 1500 $A$MeV. The data are taken with the FOPI detector system [3] at the heavy-ion synchrotron SIS at GSI Darmstadt. A similar excitation function is available for central $^{197}$Au + $^{197}$Au collisions. Together with the results of formerly measured $^{58}$Ni + $^{58}$Ni and $^{96}$Ru/Zr + $^{96}$Ru/Zr systems at selected projectile energies [4] and with the output of a recent experiment performed with all target/projectile/beam-energy combinations of $^{58}$Ni and $^{208}$Pb nuclei at 400, 800, and 1200 $A$·MeV, respectively, the data should allow for extensive studies of system-size and beam-energy dependences. Additionally, the system $^{12}$C + $^{12}$C measured by the HADES collaboration at 1 and 2 $A$·GeV might be included.

Let $Y_{12}(\mathbf{p}_1, \mathbf{p}_2)$ be the coincidence yield of pairs of particles having momenta $\mathbf{p}_1$ and $\mathbf{p}_2$. Then the two-particle correlation function is defined as

$$1 + \mathrm{R}(\mathbf{p}_1, \mathbf{p}_2) = \mathcal{N} \frac{\sum_{events,pairs} Y_{12}(\mathbf{p}_1, \mathbf{p}_2)}{\sum_{events,pairs} Y_{12,mix}(\mathbf{p}_1, \mathbf{p}_2)} \ . \quad (1)$$

The sum runs over all events fulfilling cuts on high charged-particle multiplicities, hence allowing for the selection of the most central 10 % - 15 % events, and over all pairs satisfying certain conditions. Event mixing, denoted by the subscript "mix", means to take particle 1 and particle 2 from different events. $\mathcal{N}$ is a normalization factor fixed by the requirement to have the same number of true and mixed pairs. Artificial correlations arising from the mixing of differently azimuthally oriented events are strongly reduced by rotating all events into a unique reaction plane. The correlation function (1) is then projected onto the relative momentum $\mathbf{q}$,

$$\mathbf{q} = \mu \mathbf{v}_{12} = \mu(\mathbf{v}_1^{cm} - \mathbf{v}_2^{cm}). \quad (2)$$

Here, $\mathbf{v}_i^{cm}$ are the particle velocities calculated in the c.m. system of the colliding nuclei and $\mu = (m_1 m_2)/(m_1 + m_2)$ is the reduced mass of the pair. Velocity vectors and nuclear charges of the light reaction products are derived from the time-of-flight, energy loss and position informations measured with FOPI's outer plastic wall (PlaWa) whereas particle identification (i.e. mass selection) is done by combining the PlaWa velocity and the momentum derived from the curvature of the charged-particle tracks measured with the forward drift chamber Helitron.

Figure 1 shows the experimental results (symbols) of pp-correlation functions at small relative momenta for central Ca + Ca reactions at five beam energies from 400 to 1500 $A$MeV. At $q \simeq 20$ MeV/c a strong peak is visible for all energies. This "$^2$He"-resonance is the result of the common action of the enhancement due to the attractive nucleonic potential and the suppression due to both the mutual Coulomb repulsion and the antisymmetrization of the pp wave function. A clear beam-energy dependence is observed with a steady increase of the correlation peak with increasing projectile energy.

The data are confronted to simulations performed with a final-state-interaction (FSI) model [2] for zero lifetime but varying the Gaussian radius parameter in order to reproduce the shape of the correlation-peak. Clearly, the increase of the peak translates into a reduction of the apparent source radius $R_0^* = \sqrt{\langle r^2 \rangle / 3}$ with increasing beam energy. This observation is supposed to be the result of both the faster proton emission off the source and the stronger correlation of momentum and coordinate space during the collective expansion of the participant zone formed in central heavy-ion collisions. Further investigations are in progress.

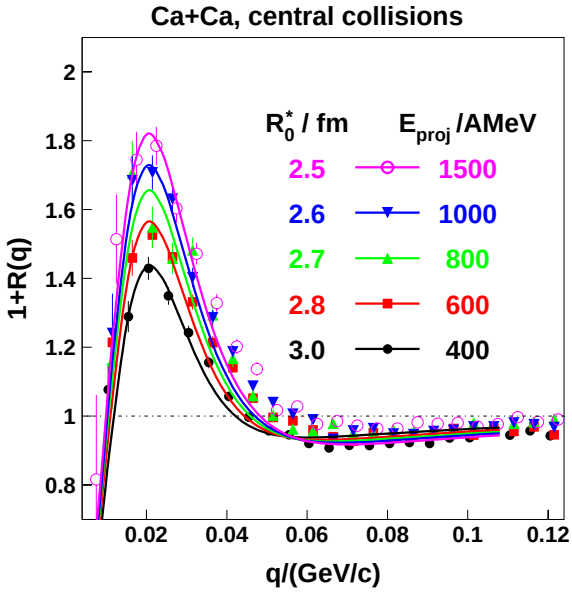


**Fig. 1** *The projectile-energy dependence of the two-proton correlation function at small relative momenta in central Ca+Ca collisions. Symbols: experimental data, full lines: FSI-model simulations for zero lifetime and different values of the Gaussian radius parameter $R_0^*$ as indicated. The simulated correlation functions are folded with the experimental q resolution of 4 MeV.*


[1] R. Kotte et al. (FOPI collaboration), Z. Phys. A 359 (1997) 47

[2] R. Kotte, H.W. Barz et al. (FOPI collaboration), Eur. Phys. J. A 6 (1999) 185

[3] A. Gobbi et al. (FOPI collaboration), Nucl. Instr. Meth. A 325 (1993) 156; J. Ritman for the FOPI collaboration, Nucl. Phys. (Proc. Suppl.) B 44 (1995) 708

[4] R. Kotte for the FOPI collaboration, Measuring the size of things in the universe: HBT inter-ferometry and heavy ion physics, Proceedings of CRIS'98, 2nd Catania Relativistic Ion Studies, Acicastello, Italy, June 8-12 1998, World Scientific, p. 299

# Life Sciences:

## Biostructures and Radiation

*The basis of biomedical research in the Institute of Nuclear and Hadron Physics is its competence for the generation, handling and detection of electromagnetic radiation in a wide photon energy range. Thus about 50 % of the resources of the institute are devoted to this field of research. The work is focussed on three main topics*
*(i) Studies on structural dynamics of biomolecules by means of infrared light,*
*(ii) Radiation biology with soft, quasi-monochromatic X-rays,*
*(iii) In-beam positron emission tomography (PET) for quality assurance of charged hadron therapy.*

*Structural dynamics of biomolecules: The function of biomolecules is based on their structural properties. Experimental approaches for the detection of protein-conformational changes are of particularly interest to understand the complex regulation of biomolecular reactions as well as the modulation of physico-chemical properties of biomolecules of potential use in technical applications. Infrared spectroscopy is the major tool used to characterize the conformation of proteins. One focus of our work is the elucidation of structural changes in G protein-coupled receptors using the bovine photoreceptor rhodopsin as a model system. Membrane proteins of this class transmit a large variety of cellular signals relevant to pharmacological applications. We have identified the interdependence of transmembrane structure and surface-conformational changes that determine receptor stability and interaction with the G protein. These data have direct implications for the molecular mechanisms of receptor activation in other class-I receptors.*
*Another system under study is the outer surface layer of bacteria. We are interested in determining their protein-structural features because no crystal structure is available. Our main goal is to understand the basis for the metal-binding ability of this protein class. Unexpectedly, our IR experiments demonstrate a distinct increase of protein stability in metal-bound S-layer protein. This result is of importance for the technological application of these proteins in biocatalysis or bioremediation, where heavy metals may be sequestered through binding to S-layers.*
*The IR-spectral investigation has provided new insight into structure function relations in these two protein classes. The identified spectral windows may be exploited to study structural dynamics by pulsed IR-radiation, that will be available from the ELBE-FEL. Corresponding calculations on undulators have been performed that address the tuning to different spectral regions relevant to biomolecules. In addition, experimental approaches have been advanced which exploit the high average power of the FEL IR-radiation as is the case for photothermal beam deflection and near-field microscopy. These techniques allow to combine spectral and spatial information on biomolecular samples.*

*Cell radiobiology: This activity is devoted to the determination of the relative biological effectiveness (RBE) of X-rays with photon energy in the range 10 to 100 keV for different cell types and biological endpoints. Since such photon radiation is widely used in diagnostic and therapeutic radiology, a precise knowledge of RBE values and moreover of the RBE dependence on photon energy is highly desirable. For this, intensive quasi-monochromatic X-rays of variable energy will be produced at the ELBE superconducting electron accelerator by channeling of the electrons in crystals. The beamline of the channeling source was put into operation and first measurements of channeling radiation produced in diamond crystals have confirmed the prediction of channeling photon intensity. In preparation of cell irradiations at the ELBE beam, a new laboratory with a conventional highly stable X-ray tube has been established in the ELBE building and will be used for reference irradiations. The dosimetric techniques have been refined and applied for precise dosimetrical characterization of the reference X-ray tube. This also involves the development of adapted algorithms for the Monte Carlo program AMOS, which will be applied for exact photon*

*and electron transport simulations down to cellular dimensions. Furthermore, the cell irradiation studies at conventional low-energy X-ray tubes have been continued. The results of these experiments revealed a strong RBE dependence on biological endpoint. RBE values obtained for different tube voltages indicate a RBE dependence on photon energy which has to be further investigated.*

*In-beam PET for quality assurance of charged hadron therapy: During the three therapy beam times of the year 2003 45 patients have been treated by means of intensity modulated carbon ion portals at the German Heavy Ion Therapy Facility. Meanwhile carbon ion therapy is offered and accepted as routine treatment for chordomas and low-grade chondrosarcomas of the skull base. Locally advanced adenoid cystic carcinomas and sacral or spinal chordomas and low-grade chondrosarcomas were treated in clinical phase I/II studies. All these treatments have been monitored by means of in-beam PET. Due to refined algorithms and the installation of state-of-the-art computing hardware the results of an in-beam PET-scan usually become available in less than half an hour after finishing the therapeutic irradiation. If inconsistencies to the treatment plan are observed, the application of our algorithm for a PET-data based calculation of local deviations from the prescribed dose provides essential information to the radiooncologists for their decision on an optimal continuation of the fractionated irradiation. Besides the clinical in-beam PET extensive work on the further development of the method in preparation of its introduction in clinical hadron therapy has been performed: (i) It has been experimentally shown that novel PET detectors consisting of the inorganic scintillator lutetium oxyorthosilicate and avalanche photodiode arrays can be operated in-beam without degradation of their imaging properties. (ii) A comprehensive experimental study on the feasibility of in-beam PET for quality assurance of proton therapy has been completed with promising results. (iii) A software tool on the basis of the simulation code FLUKA for predicting the positron emitter distribution from the treatment plan for all therapeutically relevant ions with atomic number $1 \leq Z \leq 8$ is being developed. (iv) A Monte Carlo study on the potential of in-beam PET for the quality assurance in photon therapy indicated that for electron linacs with beam energy above 20 MeV such a technique is feasible.*

*Structural Dynamics of Biomolecules*

- *Rockefeller University, New York*
- *Universität Orenburg*
- *Universität Nürnberg-Erlangen*
- *MPI für Zellbiologie und Genetik, Dresden*
- *ISAS, Berlin, FU Berlin*
- *ENEA, Frascati (Italien)*
- *CLIO, Paris (Frankreich)*

*Cell radiobiology*

- *Klinik für Strahlentherapie und Radioonkologie, TU Dresden*
- *Institut für Kern- und Teilchenphysik, TU Dresden*
- *Medizinische Fakultät, Universität Göttingen*
- *Institut für Bioanorganische und Radiopharmazeuthische Chemie (FZ Rossendorf)*

*In-beam PET for quality assurance of charged hadron therapy*

- *GSI Darmstadt*
- *Radiologische Klinik der Universität Heidelberg*
- *Deutsches Krebsforschungszentrum Heidelberg*
- *Institut für Bioanorganische und Radiopharmazeutische Chemie (FZ Rossendorf)*
- *Soltan Institute for Nuclear Studies, Otwock-Swierk, Poland*
- *National Institute of Radiological Sciences, Chiba, Japan*

# Structural Stability and Reactivity with Heavy Metal Ions of S-Layer Protein from *Bacillus sphaericus*

O. Savchuk, K. Pollmann[1], J. Raff[1], J. Philipp, S. Selenska-Pobell[1], K. Fahmy

S-Layers are two-dimensional protein arrays that form the outer surface of a variety of bacteria. They have attracted attention by their ability to bind heavy metal ions and to allow metal nanocluster formation with potential applications in bioremidiation and nanoelectronics, respectively (see e. g ref. [1]). A strain of *Bacillus sphaericus* (JGA-12) isolated from an uranium-mining waste site in Johanngeorgenstadt, Germany, has been shown to accumulate a large variety of heavy metals from drain waters. XAFS-studies have shown that phosphate groups are likely to coordinate uranium (VI) [2]. We have studied by Fourier transform infrared (FTIR)-spectroscopy the structural stability and mode of protein Pd interactions, of the S-Layer of *B. sphaericus* strain JGA-12. This method is particularly suited to observe in real time the proton exchange reations between the titratable carboxylic acid groups of asp and glu residues and the bulk solution. The IR absorption allows to correlate pH and protein secondary structure.

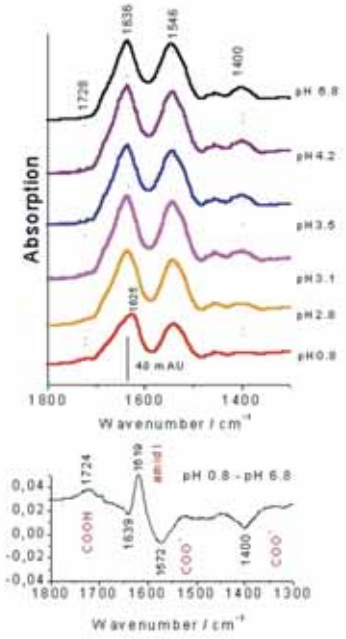


**Fig. 1** *pH-dependent IR-absorption spectra of S-Layers in suspension prepared from B. sphaericus strain JGA-12. The changes were induced by dialysis against phosphate buffers of the indicated pH using attenuated total reflection spectroscopy.*

FTIR-difference spectra where recorded with a Vector 22 BRUKER spectrophotometer using dialysis-coupled ATR-FTIR-difference spectroscopy[3]. pH changes where induced by buffer exchange in the upper compartment of the ATR-cell. Figure 1 shows the reduction of absorption by the symmetric and antisymmetric $COO^-$ stretches at 1400 and 1572 $cm^{-1}$, respectively, and the corresponding increase of the absorption of the C=O stretch of the protonated carboxylic acids upon lowering the pH. Half of the initial $COO^-$ absorption observed at neutral pH is abolished between pH 2.8 and 3.1, demonstrating a remarkably acidic average $pK_a$ of about 3. At pH 0.8, the denaturation of the S-layer protein is evidenced by the downshift of the amide I frequency.

Figure 2 shows that metallization with Pd prevents the pH-induced IR-spectral changes. The absorption of the $COO^-$ groups is almost lacking already at neutral pH and at acidic pH almost no protonation of carboxylic acids occurs. Interestingly, at pH 0.8, the protein structure does not show the changes observed in the absence of metal ions, indicating an increased stability of the metallized S-layer.

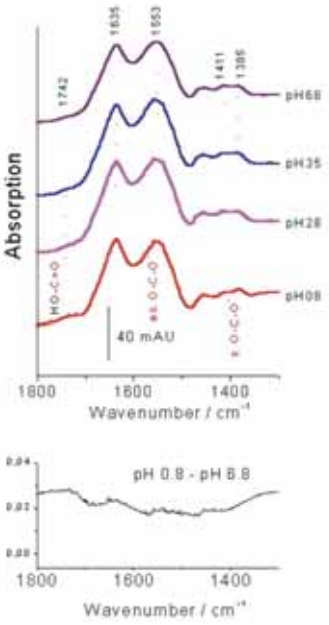


**Fig. 2** *pH-dependent IR-absorption spectra of Pd-metallized S-Layers in suspension prepared from B. sphaericus strain JGA-12.*

The data suggest that in the presence of Pd, carboxylic acid groups become blocked for protonation and may thus be involved in complexing heavy metal ions. Carboxyl-mediated metal protein interactions apparently stabilize the S-layer structure. An arrangement that is in agreement with the FTIR-spectral analysis is shown in Fig. 3.

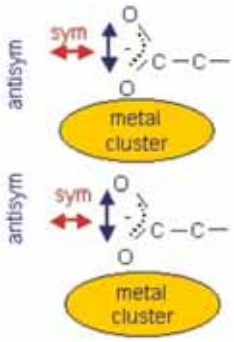


**Fig. 3** *Model, which shows different orientation of the transition moments of the two $COO^-$ modes relative to neighboring metal clusters. The symmetric $COO^-$ stretch is dipole-forbidden, the anti-symmetric is surface-enhanced.*

[1] M. Sara, U.B. Sleytr, J. Bacteriol. 182 (2000) 859-868
[2] C. Hennig, P.J. Panak, T. Reich, A. Roßberg, J. Raff, S. Selenska-Pobell, W. Matz, J.J. Bucher, G. Bernhard and H. Nitsche, Radiochim. Acta 89 (2001) 625-631
[3] K. Fahmy, Recent Res. Devel. Biophys. Chem. 2 (2001) 1-17

[1]FZR, Institute of Radiochemistry

# Involvement of the Extreme C-Terminus of Rhodopsin in Coupling Transmembrane Conformational Changes to the Cytosolic Surface

Nicole Lehmann and Karim Fahmy

G protein-coupled receptors (GPCRs) reside in the plasma membrane of virtually all eucaryotic cells. They couple extracellular signals such as hormones, neurotransmitters, and physical stimuli to cellular responses. Understanding the molecular basis of signal perception and the ensuing activation of cytoplasic G-proteins, which trigger cell-specific enzyme cascades, is of fundamental interest in molecular pharmacology. GPCRs mediate signals for growth, differentiation, and neuronal activity and are thus prime targets for the majority of current pharmacotherapeutics. Light perception by the visual photoreceptor rhodopsin follows the general principle of G protein-coupled signal transduction and is an intensively studied model system for the elucidation of GPCR structure function relations. Rhodopsin is the only GPCR for which crystal structures have been determined which allows a structural interpretation of biochemical and spectroscopic data. In rhodopsin, it is the photoisomerization of the covalently bound chromophore 11-*cis*-retinal which induces a conformational change in the heptahelical transmembrane domain of rhodopsin. This structural alteration can be followed by Fourier-Transform-Inrared (FTIR) difference spectroscopy. The functionally important transmission of transmembrane sterical strain to conformational changes on the receptor surface, where coupling to the G protein occurs cannot be deduced solely from the crystal structure of the dark state of rhodopsin. In addition, part of the cytosolic surface is not resolved. We have studied by FTIR difference spectroscopy the influence of limited proteolysis at the cytosolic surface of rhodopsin on the transmembrane structure during relaxation of the photoactivated metarhodopsin II state. We found that removal of the extreme C-terminus of rhodopsin by trypsin cleavage uncouples surface-confromational changes from the transmembrane domain around the Schiff base linkage between the chromophore and the protein. In the absence of the nine C-terminal amino acids the C=O stretching frequencies of protonated carboxylic acids in the vicinity of the Schiff base become stabilized in the seconds to minutes time range, whereas surface-conformational changes become accelerated. The stable C=O stretching mode at 1750 $cm^{-1}$ evidences a stable H-bond particularly to $Asp^{83}$. The FTIR results indicate that a H-bond network along helix 2 connects the transmembrane domain with the extreme C-terminus at the cytosolic face. Comparison with the spectral changes evoked by chymotrypsin and papain cleavage suggests that the extreme C-terminus interacts with the second cytosolic loop in MII by crossing the cytosolic end of helix 2. This interaction stabilizes the MII structure and can be disrupted either by cleavage in the second cytosolic loop or by removal of the C-terminus. The C-terminally mediated packing of the cytosolic surface is not only required for a stable MII structure but also for binding of the G protein. In the absence of the C-terminus, binding of a peptide sequence derived from the 11 C-terminal residues of the $G_{t\alpha}$ subunit destabilizes the transmembrane conformation of rhodopsin, whereas a local surface structure absorbing at 1643 $cm^{-1}$ is stabilized by the peptide. This contrasts the general stabilization of MII structural features by the peptide when bound to the intact receptor. In summary, the light activation generates a transmembrane receptor structure that does not fully determine the cytosolic conformation. The intrinsic packing properties of the cytosolic loops appear to have an important influence on the formation of the G protein-activating receptor surface.

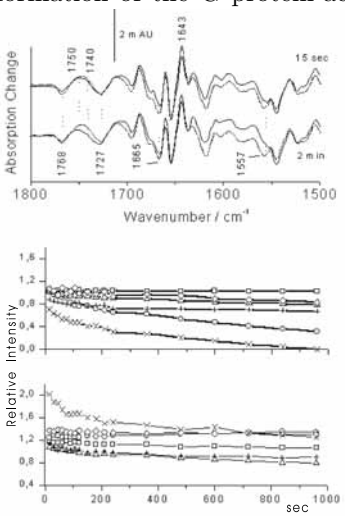


**Fig. 1** *Upper panel: Attenuated total reflection-FTIR difference spectra taken 15 sec and 2 min after photoactivation of rhodopsin in urea-stripped disk membranes (which are free of peripheral membrane proteins) attached on an ATR crystal in a bulk buffer phase (10 mM $NaH_2PO_4$, pH 4.8, 100 mM NaCl, 0° C). Positive bands belong to the photoproduct state metarhodopsin II, negative bands to the dark state of rhodopsin. Shown are spectra in the absence (solid lines) and presence of 50 % glycerol (broken lines).*

*Middle panel: Reformation of the 1557 $cm^{-1}$ absorption of the dark state over time (decrease of negative band intensity between 1560 and 1570 $cm^{-1}$, crosses) is accelerated versus normal disk membranes, whereas the C=O stretching modes of internal carboxylic acids between 1700 and 1800 $cm^{-1}$ is little affected by urea-stripping. It is mainly the C=O stretch of $Asp^{83}$ on helix 2 in the MII state which shows a decrease over time (time course of band intensity between 1761 and 1750 $cm^{-1}$, open circles). Glycerol stabilizes these bands (spectra in upper pannel) showing that surface-conformational changes are coupled to the transmembrane domain as monitored by the 1768/1750 $cm^{-1}$ difference band of $Asp^{83}$.*

*Lower panel: Upon removal of the extreme C-terminus (nine amino acids) by trypsin, the surface-conformational change causing the 1557 $cm^{-1}$ absorption is further accelerated, whereas the decay of the C=O stretching modes of all internal carboxylic acids is stabilized (band intensity of $Asp^{83}$ between 1761 and 1750, and of $Glu^{122}$ between 1745 and 1735, open circles, open triangles, respectively). This shows that the extreme C-terminus is required for the coupling of internal conformational changes to those on the cytosolic face of rhodopsin that is recognized by the G protein.*

# A Scanning Near Field Infrared Microscope Using Etched Chalcogenide Glass Fibers

M. Sczepan, J. Martin[1] K. Fahmy

Infrared microscopy is a powerful tool for the investigation of biological samples. In contrast to visible light microscopy the absorbance of the samples is high in the infrared spectral region eliminating the need for staining or fluorescence techniques. Moreover using infrared light gives direct access to chemical information i. e. the distribution of proteins, lipids and other biochemical components in the sample.

In conventional microscopy the resolution of the instrument is limited by the wavelength of the light and the numerical aperture of the microscope objective. Since the interesting absorbance bands for most biomolecules are in the 5 - 10 $\mu$m region and the numerical aperture of the reflective microscope objectives is about 0.5 in most cases a conventional infrared microscope will not be able to resolve objects in the 5 - 10 $\mu$m range such as single cells.

One way to overcome the resolution limits of classical microscopy is to employ near field techniques using small apertures of sub-wavelength size. In this case the resolution only depends on the size of the aperture. Since only a very small part of the light will be transmitted through such a sub-wavelength aperture and the efficiency of light coupling is strongly dependent of the distance between sample and aperture it is vital to have an intense light source and an effective control system for the aperture sample distance. Intense light is provided by an infrared laser source while distance is controlled by using an atomic force microscopy technique [1].

A near field microscopy setup using the fiber tip illumination scheme has been set up in our laboratory. Light from a laser source ($CO_2$-Laser, FEL or fs-OPA) is coupled into a 100 $\mu$m core diameter chalcogenide glass fiber. A fine tip at the end of the fiber which was generated using an etching process [2] serves as a sub-wavelength aperture. The distance between fiber tip and sample is controlled using an atomic force microscopic technique. In a shear force detection scheme the influence of the surface-tip adhesion forces on the frequency and phase of the transversal vibration of the tip (generated by a piezo crystal) is used for distance control. The sample is mounted on a xyz-translation stage for scanning and distance variation. A home built refractive infrared microscope objective (ZnSe lenses, focal length 20 mm) collects the light from the sample and transports it to an off-axis paraboloid mirror which focuses the light onto the detector. A liquid nitrogen cooled Mercury Cadmium Telluride (MCT) detector is used to measure the signal.

First tests of the microscopic system have been performed on various test samples such as narrow metal strips on glass substrate and liposomes dried on a glass substrate. Liposomes are widely used as a model for cell membranes. With infrared near field microscopy the distribution of membrane proteins and other biologically important components in the membrane could be studied.

The fiber coupling and collection optics have been tested. First infrared microscopic tests will be performed with a $CO_2$-laser as a light source.

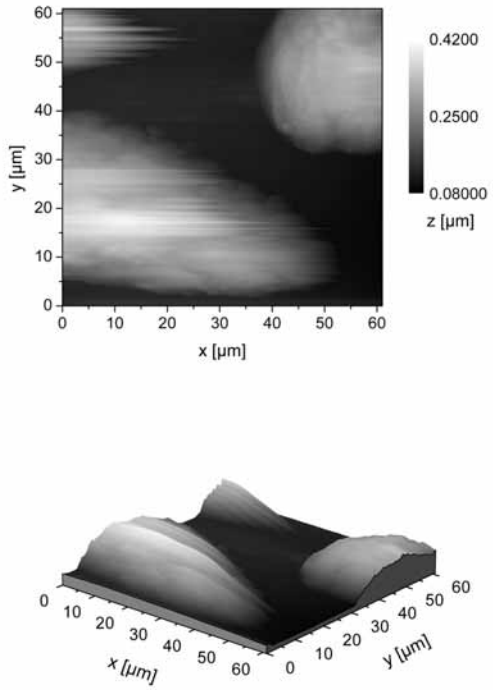


**Fig. 1** *Topographic (atomic-force-microscopic) image of a test sample (dried liposomes on a glass substrate) - instead of the expected uniform layer the liposomes form islands on the substrate after drying.*

[1] H. Yoshikawa, H. Masuhara, J. Photobiol. Photochem. C: Reviews 1 (2000) 57-78

[2] M.A. Unger, D.A. Kossakovski, R. Kongovi, J.L. Beauchamp, D.V. Palanker, Rev. Sci. Instr. 69(8) (1998) 2988-2993

[1] *TU Chemnitz, Institut für Physik*

# Exploring the Spatial Resolution of the Photothermal Beam Deflection Technique in the Infrared Region

H. Foerstendorf[1], W. Seidel, J.M. Ortega[2], F. Glotin[2], R. Prazeres[2]

Photothermal spectroscopy using an infrared pulsed pump source provides spatial information of a sample surface. In this model investigation we obtained a spatial resolution of approximately 25 $\mu$m using a strongly focused probe beam in a reflecting scheme.
In photothermal beam deflection spectroscopy (PTBD) generating and detection of a thermal wave occur normally in the sub-millimeter length scale. Therefore, PTBD can potentially provide spatial information about the surface of the sample and permits imaging and/or microspectrometry. This will possibly lead to a useful tool for investigation of adsorbed species on mineral surfaces.

In PTBD the thermal wave is generated by intermittent laser heating and is detected by a probe laser beam (e.g. a HeNe laser) which is reflected from the surface of the sample next to the spot of the incident pump beam (FEL). Depending on the modulated intensity of the FEL a thermoelastic deformation of the surface is induced which results in periodically, photoinduced displacement of the probe beam [1]. Thus, a different reflection angle is observed which is monitored by the use of a high resolution position detector placed at a suitable distance from the illuminated sample (Fig. 1).

As a model compound we investigated the border range between an $O^+$-implanted and an untreated region of a Ge-substrate by recording time curves of the deflection signal at distinct positions of the surface of the substrate using a constant FEL wavelength (11.6 $\mu$m). The recording of the time curves is synchronized to the FEL pulses. The deflection signal shows up after a short delay time (7 $\mu$s) while the thermal wave propagates from the incident FEL beam to the probe beam spot. Due to the different absorption coefficients the deflection signal decreases from the $O^+$-doped region to the nearly transparent pure germanium. Synchronization of sample micropositioning and data acquisition provides the recording of mapping plots of the sample's surface (see Fig. 2, inset).
In a first approach the spatial resolution obtained was about 50 $\mu$m [2]. In the present study we improved the spatial resolution by focusing the HeNe laser probe beam in front of the surface of the sample extensively. The diameter of the laser spot was about 15 $\mu$m at the surface of the sample. It was found that the spatial resolution of the profile is very sensitive to the focusing of the probe beam. The deflection signal can also be increased by focusing the pump beam which, however, becomes crucial with respect to the high laser power.
The set of the recorded time curves of the deflection signal at distinct sample positions is shown in the inset of Fig. 2. The step width between the distinct sample position was 5 $\mu$m. The absorption profile in Fig. 2 was extracted from the set of the time curves near the maximum of the amplitude at 10.6 $\mu$s. The transition between the $O^+$-doped and the untreated region of the substrate can be seen around 1.65 mm relative position within a range of about 25 $\mu$m. In the next series of experiments we will continue to enhance the spatial resolution to a few microns by utilizing more sophisticated focusing components. Simultaneously, this requires more complex samples showing well-defined patterns of doped regions on the germanium substrates.

Acknowledgements
The cooperation with the staff of the implanter is gratefully acknowledged.

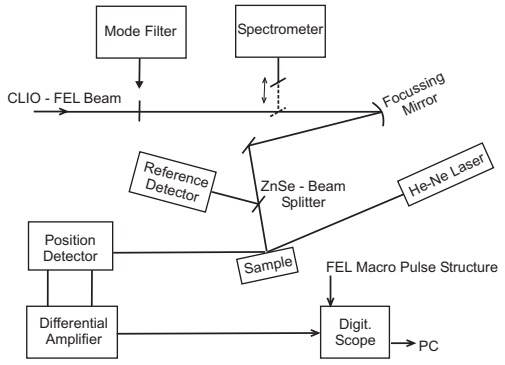


**Fig. 1** *Schematic diagram of the thermal deflection experiment setup.*

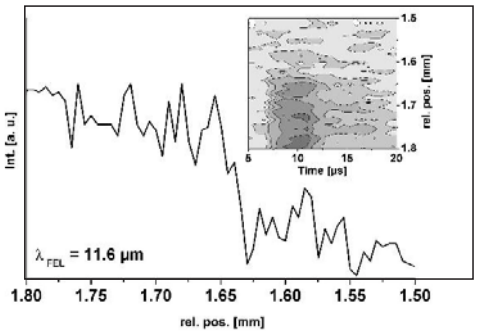


**Fig. 2** *Absorption profile of the border range between $O^+$-doped and pure germanium (extracted from inset; t = 10.6 $\mu$s). Inset: mapping plot of the set of time curves of the deflection signal.*

[1] M.A. Olmstead et al., Appl. Phys. A 32, (1983) 141-154

[2] W. Seidel, et al., Wiss.-Tech. Ber. FZR-373 (2003) 51

[1] *FZR, Institute of Radiochemistry* [2] *LURE, Université de Paris-Sud, Orsay, France*

# The Optical Resonator of the IR-FEL at ELBE

W. Seidel, P. Evtushenko, P. Gippner, E. Grosse, R. Jainsch, D. Oepts[1], M. Sobiella, D. Wohlfarth, A. Wolf, U. Wolf, R. Wünsch and B. Wustmann

Intense infrared radiation in the 5 - 30 $\mu$m range will be produced in the undulator U27 [1]. In the following we outline the actual state of the appropriate resonator and its main control elements. The optical resonator for this ELBE FEL has been mounted completely. All mechanical equipment and optical components (alignment system, interferometer for length stabilization, mirror wheels and chambers, temperature stabilization of the mirrors) have been checked thoroughly and tested for long-term stability. All components, including the undulator and both mirror chambers, have been aligned by means of optical methods.

To optimize the extraction ratio in the whole wavelength range we use 5 mirrors with different hole sizes in the upstream mirror chamber. The Au-coated Cu-mirrors are mounted on a revolvable holder (wheel), which is fixed to a high-precision rotational stage. A similar construction with 3 mirrors is used in the downstream chamber.

To ensure the stability of the resonator at wavelengths down to 3 $\mu$m the mirror angular adjustment requires a stability in the order of 6 $\mu$rad. For the initial alignment of the mirror angles an accuracy in the order of 20 $\mu$rad is required. To achieve this accuracy we built up an alignment system consisting of two collinear He-Ne lasers. It uses two wall markers and 11 moveable adjustment apertures inside the cavity.

A Hewlett-Packard interferometer system is used for monitoring and stabilizing the resonator length (Fig. 1). The interferometer beam is split in two beams (70 % and 30 %). The high intensity beam passes through the same

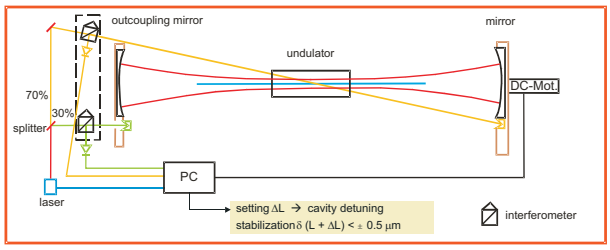


**Fig. 1** *Schematic view of the resonator length control system. Its time constant is one Hz and hence fast in comparison to the thermal time constant of the resonator.*

resonator chamber as the main laser and the electron beam. The laser passes diagonally from one side of the upstream cavity mirror to a retroreflector on the other side of the downstream mirror. The low intensity beam is directed to one of the five retroreflectors on the front side of the mirror wheel close to the working outcoupling mirror. The control electronics for the two interferometer arms include a servo system to control and stabilize the relative distance between the two cavity mirrors using the motorized micrometer drive on the translation stage of the downstream chamber. There is no active tilt stabilization.

We have estimated the maximum intracavity laser power that can be expected for the ELBE beam when using the smallest outcoupling hole. Despite their high reflectivity of more than 99 % up to 15 W (cw regime) can be absorbed in the mirrors. The entire construction is heated and the resonator adjustment (length and angle) may be disturbed by thermal expansion. Moreover that heat load may affect the precision mechanics. At a movable precision construction in ultra-high vacuum a temperature stabilized system based on water cooling is difficult to be realized. Therefore we introduced special heat isolation between the high-precision rotation stage and the mirror wheel. The wheel is also made from Cu to reduce mechanical tension between the mirrors and the surrounding material. Furthermore, the heat exchange is improved by a more flexible heat dissipation to the outside of the vacuum chamber (Peltier element or air cooling) rather than by thermal radiation only.

To stabilize the mirror wheel temperature we installed a heater in the center of the wheel. Independently of whether the laser is working or not all components are at the same equilibrium saturation temperature slightly above the saturation temperature.

The temperature behavior of the construction has been studied in vacuum by simulating the laser power by a 15 W heater at one of the mirrors. After 22 hours the saturation temperature of 54 °C was achieved at the mirror. The wheel was 4 °C colder than the heated mirror. Fig. 2 illustrates the temperature stabilization. The remaining variation of the mirror temperature (3.5 °C) changes the resonator length by not more than 1 $\mu$m which is much less than one optical wavelength in general. The interferometer system will correct this change.

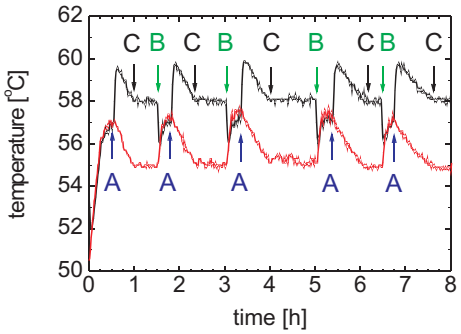


**Fig. 2** *Measured temperature behavior of the mirror (upper curve) and the wheel (lower curve) during a simulation of a working regime of a FEL for the out coupling mirror wheel (see text; arrows A : laser switched on, arrows B: laser switched off, arrows C: heating of the mirror wheel switched on).*

[1] http://www.fz-rossendorf.de/ELBE

[1] *FOM Institute for Plasma Physics Rijnhuizen, P.O. Box 1207, 3430 BE Nieuwegein, The Netherlands*

# Effects of Undulator-Field Irregularities

P. Gippner, W. Seidel, D. Wohlfarth, A. Wolf, U. Wolf, R. Wünsch and C.A.J. van der Geer[1]

In 2000 the magnetic fields of either section of the U27 undulator were scanned and analyzed at DESY using a hall-probe setup [1]. These measurements have been used to calculate the path of a reference electron (20 MeV) through the undulator (fig. 1a). After transporting the undulator to Rossendorf and installing the stainless steel vacuum chamber necessary for the electron beam the magnetic field has been rechecked by means of the pulsed wire method [2]. We found significant deviations from the field measured at DESY (fig. 1b). We suppose a displacement of certain magnets since inhomogeneities in the chamber material could not be detected by a low-$\mu$ permeability indicator. To remove the remarkable displacement of the average electron path we have shimmed some of the undulator magnets. The results are shown in figs. 1c and d for different gaps.

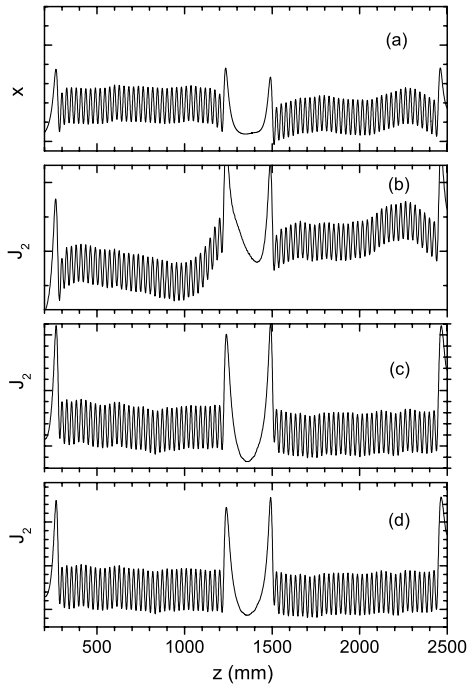


**Fig. 1** *Path $x(z)$ of a 20 MeV reference electron through the two units of the U27 undulator (gap $g = 15$ mm) calculated on the basis of a Hall-probe measurement (a) and second field integrals $J_2(z)$ determined by means of the pulsed-wire method before (b) and after (c) shimming several undulator magnets. Fig. (d) shows the field integral measured for the smaller gap $g = 13.5$ mm with the same shimmed magnets.*

Irregularities in the electron path as seen in fig. 1 affect the lasing process. If the electrons are displaced from the optical axis on a part of their path through the undulator they experience a lower optical field and the laser gain is reduced. Moreover the resonance wavelength is shifted to longer values since an additional small fraction of kinetic energy is moved from the longitudinal to the transversal motion. Altogether the interaction of the electrons with the optical wave depends in a crucial way on their path and can not be described by a simple formula in the general case. That is why we have studied the influence of irregularities in the electron path on laser gain and wavelength by means of the 3-dimensional simulation code GPT [1]. Fig. 2 shows an example where one undulator unit has been studied and the field strength of 4 magnets has been manipulated such that a part of the electron oscillations is shifted away from the axis.

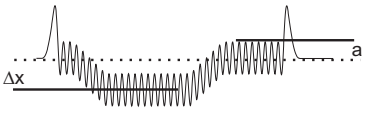


**Fig. 2** *Electron path with irregularities*

The results of such a shift are illustrated in fig. 3. Independently of the electron energy we can conclude that a significant reduction of the gain or a shift in wavelength is only caused if the electron is displaced by more than twice the amplitude of the regular oscillation in the undulator. Irregularities as observed in fig. 1 can easily be tolerated by the FEL.

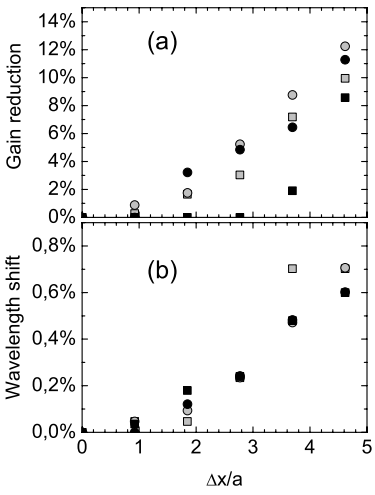


**Fig. 3** *Gain reduction (a) and wavelength shift (b) as a function of the ratio $\Delta x/a$ (defined in fig. 2) calculated for a 20 MeV (open symbols) and 40 MeV (full symbols) electron pulse. The squares and circles, respectively, represent a calculation without and with beam emittance (15 mm×mrad, 50 ps×keV) taking into account.*

[1] P. Gippner et al.; Proc. of the 23rd Int. Free Electron Laser Conference, II-55, Darmstadt, Germany, August 20-24, 2001; P. Gippner et al., Wiss.-Tech. Ber. FZR-319 (2001) 24; FZR-341 (2002) 27

[2] P. Gippner, A. Schamlott, U. Wolf; http://www.fz-rossendorf.de/ELBE/en/fel/pos.html

[3] M. J. de Loos, C. A. J. van der Geer, S. B. van der Geer, 3D Multi-Frequency FEL Simulations with the General Particle Tracer Code, EPAC 2002, Paris, France, p. 849; S. B. van der Geer, M. J. de Loos, The General Particle Tracer Code, Thesis TU Eindhoven 2002, ISBN 90-386-1739-9; Pulsar Physics, General Particle Tracer, http://www.pulsar.nl

[1] *Pulsar Physics, The Netherlands*

# The Role of Resonator Detuning for FEL Gain and Power

R. Wünsch and C. A. J. van der Geer[1]

In a free-electron laser kinetic energy of a relativistic bunch of electrons is transferred into electromagnetic field energy of a copropagating light pulse. The high-frequency accelerator of ELBE produces electron bunches, roughly half a millimeter long (in the lab frame), with the repetition rate of $\nu_r = 13\,\mathrm{MHz}$. To obtain a sufficiently strong electromagnetic field, the light pulses circulate in a resonator. To transfer energy from the electron beam to the optical field both pulses have to overlap in the undulator in a proper way. The length $L_R$ of the resonator determines the position of the optical pulse with respect to the subsequent electron bunch. The nominal resonator length $L_R = c/(2\nu_r)$ guarantees that the reflected optical pulse enters the undulator simultaneously with the subsequent electron bunch and overlaps with it when moving through the undulator.

It has turned out that the overlap between electron bunch and optical pulse is not optimal for the energy transfer to the optical pulse when both pulses enter the undulator simultaneously. By changing the resonator length by a small amount $\delta L_R$ the optical pulse can be shifted with respect to the subsequent electron bunches and their overlap can be optimized. This procedure is denoted as resonator detuning or desynchronization. There exists an optimal value of the resonator detuning for which the gain is at maximum. This optimal value depends on the electron and undulator parameters. It is negative and of the order of the wavelength of the produced light.

Resonator detuning controls the spatial and the spectral shape of the produced light pulse and influences the saturation effect. The latter determines the asymptotic value of the optical power reached after sufficiently many (a few hundreds or thousands) passes of the light through the undulator. At optimal detuning the gain is at maximum but the saturation leads to a small asymptotic power. Decreasing the detuning the gain decreases but the asymptotic power increases. Its maximum is reached closely to the nominal resonator length where the gain is just about to compensate the optical losses.

Using the code GPT [1, 2] we have simulated the effect of resonator detuning for one and for two units of the U27 undulator of the radiation source ELBE. The electron bunches are 0.7 ps long (rms) in all cases. Fig. 1 shows the evolution of the optical power for several cases of detuning using only one undulator unit. We should mention that the calculated build-up time is not realistically reproduced by our model. First the spontaneous emission, which is the origin of the amplified radiation, is artificially suppressed in order to overcome the problem of exaggerated spontaneous emission in FEL simulations. To compensate the suppressed spontaneous emission at the beginning of the lasing process and to speed up the computation time we introduce an additional seed particle. Both measures distort the power increase at the

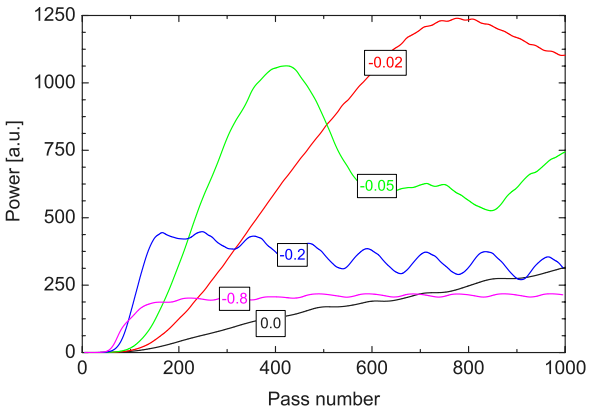


**Fig. 1** *Optical power distribution as a function of the number of passes calculated for various values of resonator detuning $\delta L_R$ (in units of the light wavelength $\lambda$). Calculation for one undulator unit (34 periods).*

beginning but do not affect the process when the contribution from spontaneous emission is negligible.
Fig. 1 shows the evaluation of the optical power for various values of resonator detuning. With the nominal resonator length ($\delta L_R = 0$) the gain is small and the power develops rather slowly. If the gain is smaller than

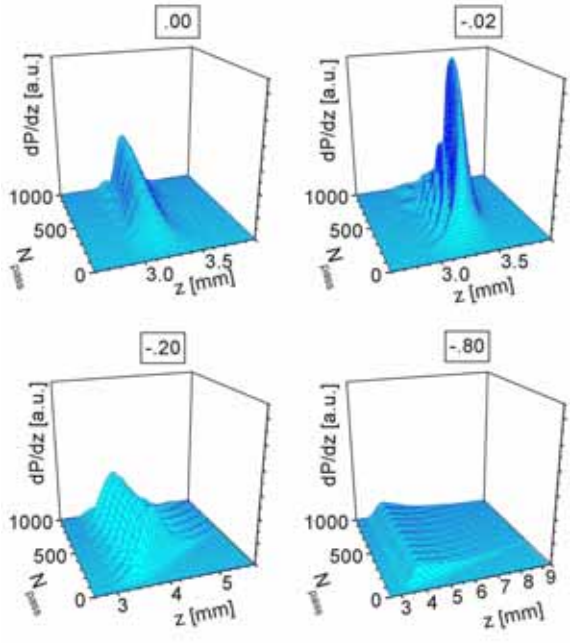


**Fig. 2** *Longitudinal distribution $dP/dz$ of the optical pulse power as a function of the pass number $N_{pass}$ calculated for various values of the resonator detuning $\delta L_R$, which is given in the boxes in units of the light wavelength $\lambda$. Calculation for one undulator unit.*

the optical losses the laser does not start. In the calculation we assumed 5 % losses including the outcoupled

[1] *Pulsar Physics, The Netherlands*

fraction. Shortening the resonator increases the gain. The power grows to a large asymptotic value. Further increasing the resonator detuning increases the gain even more but decreases the asymptotic power which is by far not constant but oscillates with a quite large amplitude. Amplitude and frequency of this oscillations decrease when increasing $\delta L_R$. These power fluctuations are denoted as limit-cycle oscillations and have been considered in ref. [3] Their frequency is determined by the ratio between cavity detuning $\delta L_R$ and electron bunch length $\sigma_z$ and can roughly be estimated by $\nu_{\rm osc} \approx \frac{\delta L_R}{1.5\,\sigma_z}\,\nu_r$. Increasing $\delta L_R$ above an optimal value, which is around $-0.8\,\lambda$ in the case of fig. 1, both gain and asymptotic power decrease. This way the resonator detuning turns out to be a proper parameter to control important laser parameters, power and spectrum without changing any of the beam or undulator parameters.

The reason for the power oscillations is elucidated in Figs. 2 - 4. Without resonator detuning (upper left panels) the power increases from pass to pass mainly in the center of the optical pulse and the pulse remains quite narrow. Accordingly the frequency spectrum is rather broad (Fig. 3). If the resonator is shortened the optical pulse moves forward relatively to the electron bunch while it grows continuously (upper right panels). This process continues until the front edge of the optical pulse moves out of the electron bunch and decays. On the other hand the back edge of the optical pulse comes into contact with the electrons and starts growing so that the optical energy swaps from the front end of the optical pulse to its rear end. Further increasing the resonator detuning (lower left panels) accelerates the process described above (higher power oscillation frequency) while the total power is smoothed. Figs. 2 and 4 show that growth at one end of the optical pulse and reduction at the other do not completely compensate each other but may result in oscillations in the total optical power observed in fig. 1. In the frequency spectra (Fig. 3), side peaks appear, while the main peak narrows. At $\delta L_R = -0.8\lambda$ (lower right panels) the side peaks have vanished and the spectrum is quite narrow. In this way the resonator detuning can be used to select either a particularly short optical pulse, a high optical power or a small spectral width.

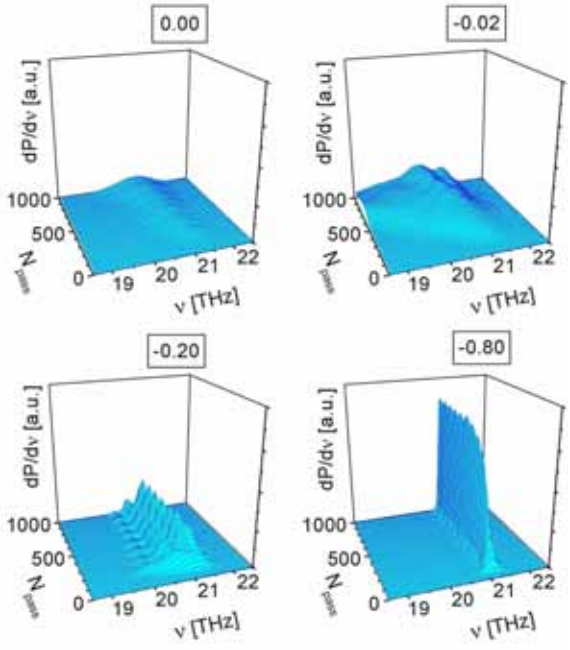


**Fig. 3** *Frequency distribution $dP/d\nu$ of the optical pulses shown in Fig. 2.*

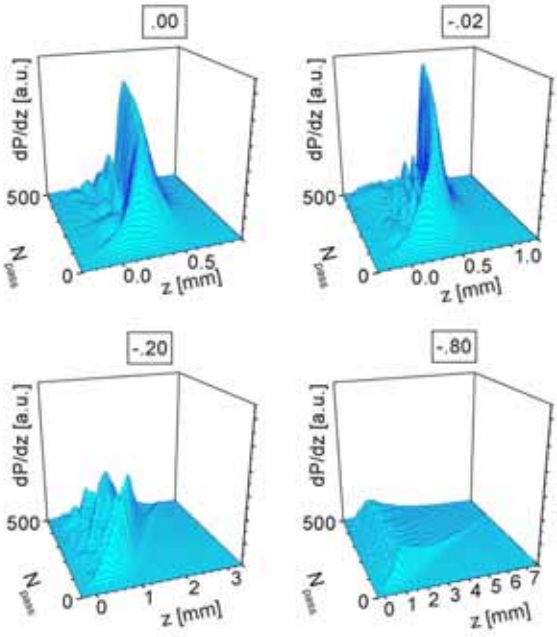


**Fig. 4** *The same as in Fig. 2 for two undulator units (68 periods).*

Increasing the number of undulator periods (two undulator units, 68 periods) increases the single-pass gain. The laser starts faster. The asymmetry between front and rear end of the optical pulses is more pronounced (Fig. 4). The main features of resonator detuning, however, are the same a for the shorter undulator.


[1] M.J. de Loos, C.A.J. van der Geer, S.B. van der Geer, 3D Multi-Frequency FEL Simulations with the General Particle Tracer Code, EPAC 2002, Paris, France, pp.849; S.B. van der Geer, M.J. de Loos, The General Particle Tracer Code, Thesis TU Eindhoven 2002, ISBN 90-386-1739-9; Pulsar Physics, General Particle Tracer, http://www.pulsar.nl

[2] R. Wünsch, C.A.J. van der Geer, S.B. van der Geer, M.J. de Loos, FZ-Rossendorf, Wiss.-Tech. Ber. FZR-372 (2003) 59

[3] R. Wünsch, C.A.J. van der Geer, S.B. van der Geer, M.J. de Loos, FZ-Rossendorf, Wiss.-Tech. Ber. FZR-372 (2003) 61

# Design of an Electromagnetic Undulator for a Far Infrared FEL at ELBE

Th. Dekorsy, K. Fahmy, E. Grosse, R. Wünsch

While the U27 undulator will soon produce light in the mid-infrared region ($5\,\mu m \leq \lambda \leq 25\,\mu m$) a new undulator for longer wavelengths ($25\,\mu m \leq \lambda \leq 150\,\mu m$) is envisaged at the radiation source ELBE.
Within this region the FEL constitutes a unique radiation source. Radiation quanta of this energy (10 - 50 meV, 2 - 10 THz) are appropriate for spectroscopy of low energy elementary and collective excitations. Such excitations are observed in solid state quantum structures and in complex biomolecules as well. Their study establishes the basis for understanding complex phenomena in solids and liquids and for elucidating processes in biological material. Technological and medical innovations are the long-term output of such investigation.
To produce radiation in the THz region by means of the ELBE beam (12 - 40 MeV) an undulator with a period $\lambda_u$ of several centimeters is needed. We propose an electromagnetic undulator with $\lambda_u = 9$ cm, 25 undulator periods and an undulator parameter up to $K_{rms} = 1.8$.

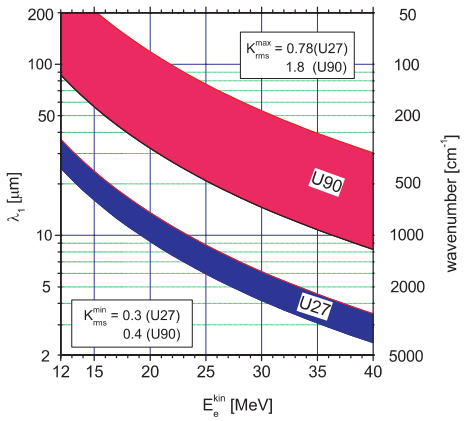


**Fig. 1** *Wavelength $\lambda_1$ (first harmonic) specified for the two undulators of ELBE as a function of the kinetic electron energy $E_e^{kin}$.*

This undulator got the preliminary name **U90**. Fig. 1 shows the wavelength region covered by such an FEL. It adjoins to the wavelength of the U27 undulator and allows to produce light up to 300 $\mu$m. Waves longer than 150 $\mu$m are subject to considerable diffraction losses in the presently designed beamline to the user laboratories. Above 200 $\mu$m the transport losses exceed 50 %.
The diffraction of the light in the resonator increases the beam radius and reduces the overlap with the electron beam. Big resonator mirrors, large diffraction losses and a small laser gain are the result. Approximately above 40 - 50 $\mu$m the losses exceed the gain. These drawbacks can be reduced by means of a waveguide compressing the optical beam. Two parallel plates are able to guide a particular optical mode without attenuating it noticeably. To avoid a bulky construction we propose a waveguide which is restricted to the interior of the undulator. It is 240 cm long, 4 cm wide and 1 cm high. To minimize the mode conversion losses at the ends of the waveguide we need bifocal resonator mirrors. The horizontal radius $R_h$ of curvature, is solely determined by the selected Rayleigh range of 1 m. The optimal vertical radius of curvature $R_v$ depends on the wavelength in general. Calculations using the code GLAD [2] have shown that a radius equal to the distance between resonator mirror and waveguide exit minimizes the mode conversion losses at $\lambda > 70\,\mu$m. Here, the losses per resonator pass do not exceed 1 %. At shorter wavelengths the losses grow up to 10 % per pass at 25 $\mu$m. Using a slightly larger radius of curvature the losses can be reduced to 7 %. At short pulses ($\sigma_t \approx 0.7$ ps) the gain is about 15 %.
Since the number of periods is smaller than in the case of U27 the spectral width and the average laser ower of U90 are expected to be larger approximately by a factor of two. The average outcoupled laser power could reach up to 100 W.
The main parameters of the proposed undulator for far-infrared radiation are summarized in the table below. Details can be found in the internet [1].

| | | |
|---|---|---|
| Undulator | Field period | 9 cm |
| | Number of periods | 25 |
| | Undulator parameter | 0.4 - 1.8 |
| Resonator | Length | 1153 cm |
| | Mirror radius of curvature | $R_h$ : 594 cm |
| | | $R_v$ : 457 cm |
| Waveguide | Length | 240 cm |
| | Height | 10 mm |
| | Width | 40 mm |

**Table 1** *Main parameters of the proposed U90 undulator including optical resonator and partial waveguide.*

The beam will be outcoupled by a 6 mm diameter hole in the center of the upstream resonator mirror and then transported to the diagnostic table in the neighboring cave, as from where it will be delivered to the user laboratories using a transport system in common with the mid-infrared beam from the U27 undulator.

[1] https://www.fz-rossendorf.de/pls/rois/Cms?pNid=471
[2] GLAD, Applied Optics Research, Woodland, WA 98674, USA

# Measurement of Channeling Radiation at ELBE

W. Wagner, A. Panteleeva, J. Pawelke, W. Enghardt

The beamline for Radiation Physics at ELBE was put into operation in October 2003.
Research work on the production of channeling radiation (CR) has been started in view of its feasibility for application as a non-conventional quasi-monochromatic X-ray source to be used for biomedical investigations [1].

The experimental setup consisted in a 42.5 $\mu$m thick diamond IIa crystal fixed on a 3-axes goniometer. This device was constructed by FMB Berlin and especially designed to meet the rather strong demands for handling it under the extremely clean UHV conditions in line with the superconducting electron accelerator.
Spectrometry of the CR observed has been carried out using Si-pin-diodes as well as CdZnTe detectors. For shielding against the intense background radiation the detectors were housed inside a 10 cm thick Pb collimator with a diaphragm of 5 mm diameter which was positioned under zero degrees with respect to the beam direction at a distance of 3.2 m from the target crystal. To avoid a high energy threshold due to the attenuation of radiation in air an evacuated (2 mbar) auxiliary pipe was mounted between the Be-window (127.5 $\mu$m) of the UHV electron beamline and the detector station.

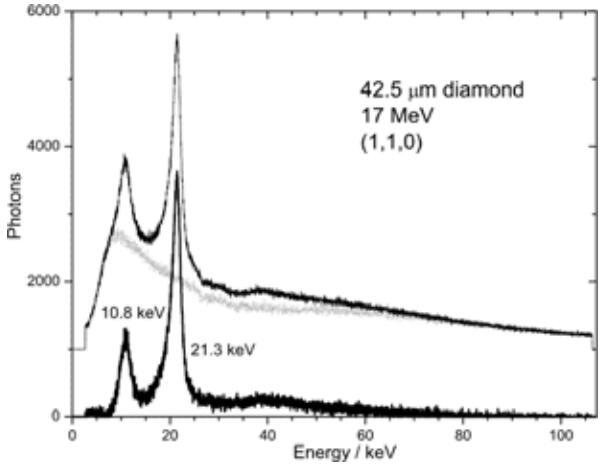


**Fig. 1** *Energy spectrum (lower one) of (110) planar CR at an electron energy of 17 MeV. For clearness, the spectra measured at aligned and random (grey) crystal orientation are shifted on the ordinate scale by +1000.*

Measurements of planar and axial CR spectra have been performed for the zone of the crystal axis [110] at electron energies ($E_e$) of 14.5 and 17 MeV. For illustration, the spectrum measured for the (110) plane at 17 MeV is given in Fig. 1 together with the related spectrum of bremsstrahlung which has been registered at slightly non-aligned crystal orientation and was normalized to the (110) spectrum at its high-energy tail.
The spectral distribution of CR (also shown in Fig. 1) is then obtained as the difference of both these spectra. The measured energy values ($E_x$) of some prominent CR lines are listed in Tab. 1.

**Tab. 1** *Energies of prominent CR lines.*

| $E_e$/MeV | Index | Transition | $E_x$/keV |
|---|---|---|---|
| 14.5 | (110) | 1–0 | 15.8 |
| | (111) | 2–1 | 11.0 |
| 17.0 | (100) | 1–0 | 13.3 |
| | (110) | 1–0 | 21.3 |
| | | 2–1 | 10.8 |
| | (111) | 2–1 | 13.7 |
| | | 3–2 | 10.8 |
| | | 1–0 | 8.5 |
| | (113) | | 11.2 |
| 17.0 | [110] | 2p–1s | 68.6 |
| | | 3d–2p | 44.0 |
| | | 3p–2s | 28.2 |

During the first run absolute monitoring of the electron beam current which typically amounted to about 1 nA was not yet available. The installation of a secondary electron monitor (SEM) [2] directly behind the source crystal to avoid electron losses due to the scattering in the target is still in progress.
Some very rough estimation of the CR yield, however, could be carried out by calculating the number of electrons from the output of bremsstrahlung registered simultaneously with CR. Partial integration of the measured spectrum has been performed at an energy larger than 70 keV where possible coherent contributions from free-to-bound transitions are negligible.
The resulting yield for the 1–0 transition of planar CR at 17 MeV (Fig. 1) amounts to 0.088 photons/sr $e^-$. Although the uncertainty of this estimation is rather high (about 70 %) and systematic errors for the time being ignored may lead to a substantial underestimation of the CR yield, this value converts into a CR rate of $1.6\times10^{10}$ photons/s 10 % BW if one assumes an average beam current of 100 $\mu$A. By the order of magnitude, such CR rate meets the requirements for investigation of RBE values of soft X-rays on living cells [3].

[1] W. Neubert, W. Enghardt, U. Lehnert, E. Müller, B. Naumann, A. Panteleeva, J. Pawelke, Proc. Conf. Monte Carlo 2000, Lisbon 2000, Eds. A. Kling, F. Barão, M. Nakagawa, L. Távora, P. Vaz, Springer-Verlag Berlin-Heidelberg-New York 2001, p. 123
[2] V.V. Morokhovskyi, PhD-Thesis D17, TU-Darmstadt, 1998
[3] A. Panteleeva et al., FZ Rossendorf, Wiss.-Tech. Ber. FZR-271 (1999) 95

# Establishment of a Laboratory for X-Ray Experiments at ELBE

J. Pawelke, S. Eckert[1], W. Enghardt

At the ELBE facility intensive quasi-monochromatic X-rays are produced by channeling of the ELBE electron beam in diamond crystals [1] in the radiation physics cave (room 112, cf. Fig. 1). The channeling X-ray source ($E_\gamma \approx 10-100$ keV) is planned to be used for radiobiological experiments by the Radiation Physics Division [2] and for imaging of phase transition and flow phenomena in liquid metals by the Magnetohydrodynamics Department of the Institute of Safety Research [3].

For the preparation of the experiments including the necessary detector tests without requiring ELBE beam time and not occupying the irradiation site in the radiation physics cave, a separate X-ray laboratory with two conventional X-ray tubes (see Table 1) has been established in the ELBE building (room 112a, cf. Fig. 1). The high stability constant potential X-ray tube ISOVOLT 320 HS (Röntgen Seifert, Ahrensburg) is very well suited for dosimetrical experiments and will be used as a reference X-ray source for the radiobiological studies, whereas the X-ray unit XS225D OEM (Phoenix X-ray Systems, Wunstorf) meets the requirements of feature recognition down to $\mu$m spatial resolution.

Important features of the laboratory are: circulating air cooling, argon gas and cooling water (20 l/min, 30°C) supply as well as access control system. The front wall stands back from the adjacent rooms giving place for the X-ray tube control units (Fig. 2). For radiation shielding, the laboratory steel structure has intermediate lead panels (thickness in the front wall of 28 mm and in the side wall toward the positron laboratory of 100 mm).

Perspectively, the use of the quasi-monochromatic X-ray beam from the radiation physics cave in the X-ray laboratory is possible.

**Tab. 1** *Main parameters of the two X-ray tubes.*

| | Isovolt 320 HS | XS225D OEM |
|---|---|---|
| Tube voltage [kV] | 5 to 320 | 10 to 225 |
| Tube current [mA] | 0.1 to 45 | 0.005 to 3 |
| Maximum anode dissipation [VA] | 4200 | 1400 |
| Beam angle [°] | 40 | 25 |
| Anode material | W | W, Cu |
| Focal spot size | 4.0 / 1.5 mm | $\geq 3$ $\mu$m |
| Inherent filtering | 7 mm Be | 0.5 mm Be |
| Minimum focus-object-distance | 13 cm | 4.5 mm |

**Fig. 2** *Control unit of the Isovolt X-ray tube in front of the laboratory.*

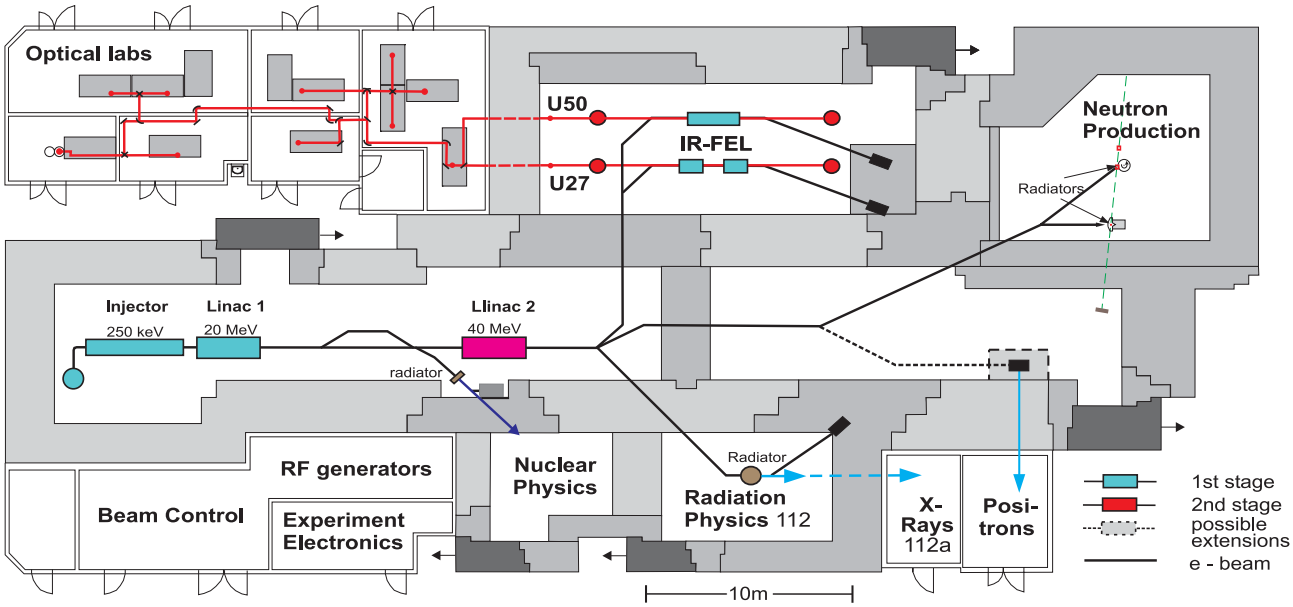


**Fig. 1** *General layout of the radiation source ELBE with the radiation physics cave (112) and the X-ray laboratory (112a).*

[1] W. Wagner et al., Measurement of channeling radiation at ELBE, This Report, p. 56
[2] W. Neubert et al., Proc. Conf. Monte Carlo 2000, Lisbon, Eds.: A. Kling et al., Springer-Verlag (2001) 123
[3] S. Eckert et al., FZ Rossendorf, Wiss.-Tech. Ber. FZR-341 (2002) 96

[1] *FZR, Institute of Safety Research*

# Dosimetric and Spectral Characterization of an ISOVOLT 320/13 X-ray Tube

J. Pawelke, T. Mikuletz[1], A. Panteleeva

One area of research at the new ELBE facility is devoted to radiobiological studies by means of cell irradiation with low energy photons. For this, the soft X-rays are produced by channeling of the ELBE electron beam in diamond crystals [1] in the radiation physics cave. Reference irradiations with a conventional tungsten anode X-ray tube ISOVOLT 320/13 HS will be performed in a nearby laboratory at ELBE [2].

Absorbed dose will be measured by standard dosimetric technique with air filled ionisation chambers (IC), optimised with respect to dose and energy dependence of response. In order to cover the wide range of photon radiation at ELBE (from several keV channeling X-rays up to 40 MeV bremsstrahlung) three different IC (Table 1), connected to an UNIDOS electrometer (PTW Freiburg), are used for high precision dose measurements. Altogether two identical systems (3 IC + UNIDOS) are used for measurements in both the radiation physics cave and the X-ray tube laboratory.

The dose response of all IC has been measured for the same conditions of X-ray tube irradiation changing the tube voltage $U_H$ from 5 to 320 kV. In agreement with the recommended energy range of the IC given in Table 1, the correct dose is obtained by the Farmer IC for the whole tube voltage range, whereas the soft X-ray IC and the rigid stem IC show correct values only for $U_H \lesssim 100$ kV and $U_H \gtrsim 200$ kV, respectively (Fig. 1). For each chamber type the dose response of both systems was compared, revealing a 10 % dose underestimation for one Farmer chamber due to lack of recent calibration. Therefore, radioactive control devices will be used in future in order to control the necessity of IC recalibration. The error contribution to the measured dose was determined to be less than 0.5 % from the charge (or current) measurement with the electrometer, 2 % to 5 % from the calibration data depending on the IC, 0.1 % to 1.5 % due to air density correction depending on experimental conditions and 0.25 % (at 1.75 m distance) to 1.6 % (at 0.25 m distance) due to positioning the IC at a given distance from the X-ray tube.

The homogeneity of beam intensity was measured for different beam filtering and tube voltages. A maximum dose difference of 4.5 % was measured within the irradiation field if anisotropic beam scattering in the environment (wall, experimental setup) is minimised by the use of appropriate aperture.

Spectral dose distribution was calculated on the base of spectral photon flux measurement [3] with a high resolution $3 \times 3 \times 1$ mm$^3$ cadmium telluride diode XR-100T-CdTe (Amptek, Bedford, USA). In order to achieve the necessary flux reduction, the detector was positioned at a distance of 8 m from the X-ray tube in the radiation physics cave and the tube was operated at the minimum tube current in order to achieve the necessary flux reduction. Consideration of detector geometry as well as detector dead time and efficiency correction results in a reasonable agreement between dose rate directly measured with rather high precision by IC with the less accurate dose rate calculated on the base of photon flux measurement (Table 2). However, the dose calculated in this way is useful in determining a precise spectral dose distribution if the flux is limited to $\lesssim 15000$ ph/s.

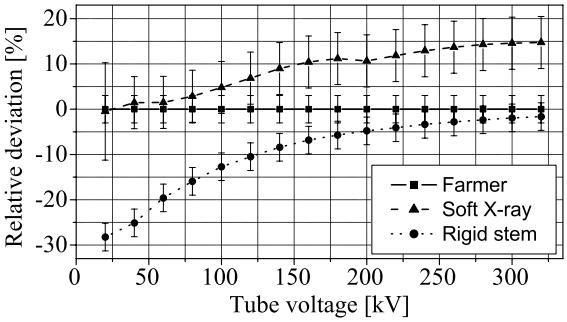


**Fig. 1** *Dose deviation of the soft X-ray and the rigid stem IC with respect to the response of the Farmer chamber.*

**Tab. 2** *Photon flux $I_\gamma$ measured with the detector at 0.1 mA tube current and corresponding dose rate $\dot{D}$ scaled to 10 mA for comparison with IC measurement.*

| Tube parameters | | $I_\gamma$ | $\dot{D}$ $[mGy/min]$ | |
|---|---|---|---|---|
| $U_H[kV]$ | Filter | [ph/s] | Detector | IC |
| 90 kV | no | 19500 | 0.9±0.7 | 1.1±0.1 |
| 100 kV | 50 $\mu$m Mo | 15500 | 0.6±0.5 | 0.8±0.1 |
| 160 kV | 0.5 mm Cu | 27500 | 1.1±1.1 | 1.8±0.1 |
| 200 kV | 0.5 mm Cu | 41300 | 2.0±1.8 | 3.2±0.1 |
| 160 kV | 2.0 mm Cu | 7500 | 0.4±0.5 | 0.7±0.1 |
| 200 kV | 2.0 mm Cu | 13300 | 0.7±1.0 | 1.5±0.1 |

**Tab. 1** *Main parameters of the ionisation chamber types (PTW Freiburg) used for photon dosimetry.*

| Chamber type | Soft X-ray, M23342 | Farmer, M30001 | Rigid stem, M23332 |
|---|---|---|---|
| Sensitive volume | 0.02 cm$^3$ | 0.6 cm$^3$ | 0.3 cm$^3$ |
| Response | $1{\cdot}10^{-9}$ C/Gy | $2{\cdot}10^{-8}$ C/Gy | $1{\cdot}10^{-8}$ C/Gy |
| Energy range | 7.5 keV – 70 keV | 30 keV – 50 MeV | 140 keV – 50 MeV |
| Dose range | 3 mGy – 30 Gy | 100 $\mu$Gy – 1 Gy | 200 $\mu$Gy – 2 Gy |
| Dose rate range | 20 mGy/min – 84 kGy/min | 0.6 mGy/min – 2.8 kGy/min | 1.3 mGy/min – 5.6 kGy/min |

[1] W. Wagner et al., Measurement of channeling radiation at ELBE, This Report, p. 56
[2] J. Pawelke et al., Establishment of a laboratory for X-ray experiments at ELBE, This Report, p. 57
[3] J. Pawelke et al., FZ Rossendorf, Wiss.-Tech. Ber. FZR-341 (2002) 92

[1] *Hochschule Mittweida (University of Applied Sciences)*

# RBE of Soft X-Rays for Cell Survival in a Human and a Rodent Cell Line

A. Panteleeva, W. Dörr[1], E. Lessmann, J. Pawelke

Recently, the energy dependence of the relative biological effectiveness (RBE) of X-rays has become a topic of intensive discussion. In order to draw definite conclusions, data for different biological objects and endpoints in a wide energy range are necessary. An RBE of 25 kV X-rays in the range 1.1 - 1.3 has been previously found for one human and two rodent cell lines by clonogenic survival [1]. Since the X-rays in the energy range below $\sim$ 30 keV are applied in diagnostic radiology, and especially in mammography, the study was extended to the human mammary epithelial cell line MCF-12A. As a further step towards investigation of the RBE dependence on photon energy, the clonogenic survival after irradiation with 10 kV X-rays was studied for MCF-12A cells as well as for the well-established mouse fibroblast cell line NIH/3T3. The culture conditions have already been presented for the NIH/3T3 cells [2] and for MCF-12A [3]. The study was performed at the Medical Faculty of TU Dresden, where the reference source was a tungsten anode X-ray tube, operated at 200 kV with 0.5 mm Cu filtration, resulting in a dose rate of 1.2 Gy/min. The irradiations with soft X-rays were performed using a tungsten anode X-ray tube. For the 10 kV X-rays irradiation, no filtration was used and the dose rate was 0.53 Gy/min, whereas for the 25 kV irradiation, a 0.3 mm Al filter was used, resulting in a dose rate of 1.9 Gy/min. For the clonogenic assay, exponentially growing cells were irradiated in polystyrene culture flasks and afterwards seeded at low densities. After an incubation period of about 2 weeks, the formed colonies were stained and scored. In order to avoid additional attenuation in the cell medium, the flasks for the irradiation with 10 kV and 25 kV X-rays were placed upside down in the holder. Since the longest irradiation time did not exceed 15 min, no effects of medium depletion should be expected. The dose dependences of the clonogenic survival for the used radiation qualities together with the fitted survival curves according to the linear-quadratic model $S = exp(-\alpha D - \beta D^2)$ are presented in Fig. 1. From the resulting coefficients for both cell lines, presented in Table 1, $RBE_{0.1}$ at the 10% survival level of 10 kV and 25 kV X-rays of 1.1 - 1.3 is obtained, where for both cell lines 10 kV X-rays are slightly more effective in cell killing. The resulting RBE is in good agreement with the data for other cell lines and with the expected photon energy dependence. We further investigated the RBE dependence on the survival level. Considering a 95% confidence interval (CI), the RBE of 10 kV X-rays was found to be significantly higher than 1 for surviving fractions in the range 0.03 - 0.6, increasing with increasing survival, or, equivalently, decreasing dose. The effectiveness of 25 kV X-rays was found to be significantly higher than 1 in the surviving fraction range 0.03 - 0.2, but decreasing with increasing survival for both cell lines.

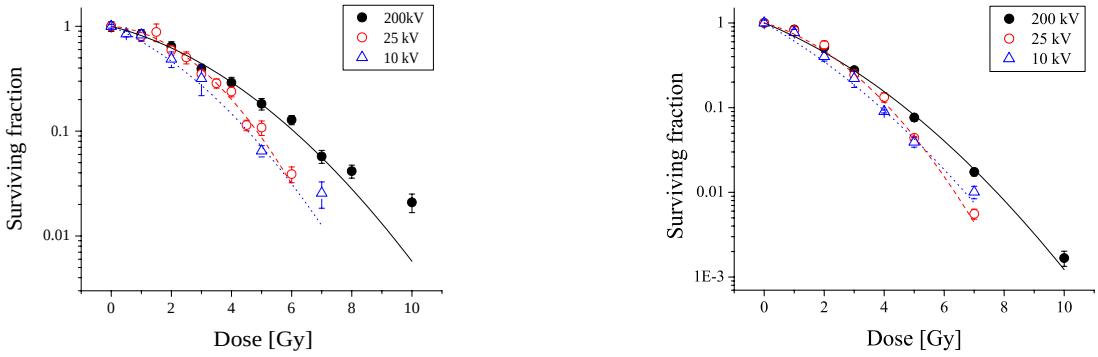


**Fig. 1** *Mean values for survival and standard errors of the mean of NIH/3T3 (left) and MCF-12A (right) after irradiation with 10 kV (open triangles, dotted lines), 25 kV (open circles, dashed lines) and 200 kV X-rays (filled circles, solid lines).*

**Tab. 1** *Coefficients (± standard error) of the linear-quadratic model and the $RBE_{0.1}$ at the 10% survival level (± 95% CI) for survival after irradiation with 10 kV, 25 kV and 200 kV X-rays. Also presented are the coefficients of determination $R^2$.*

| Cell line | Radiation quality | $\alpha$ [$Gy^{-1}$] | $\beta$ [$Gy^{-2}$] | $R^2$ | $RBE_{0.1}$ |
|---|---|---|---|---|---|
| NIH/3T3 | 10 kV X-rays | 0.288 ± 0.082 | 0.048 ± 0.017 | 0.994 | 1.34 ± 0.12 |
| | 25 kV X-rays | 0.050 ± 0.048 | 0.088 ± 0.017 | 0.978 | 1.25 ± 0.14 |
| | 200 kV X-rays | 0.169 ± 0.022 | 0.035 ± 0.006 | 0.996 | |
| MCF-12A | 10 kV X-rays | 0.460 ± 0.061 | 0.034 ± 0.014 | 0.986 | 1.21 ± 0.06 |
| | 25 kV X-rays | 0.226 ± 0.055 | 0.078 ± 0.011 | 0.992 | 1.13 ± 0.06 |
| | 200 kV X-rays | 0.331 ± 0.037 | 0.034 ± 0.006 | 0.993 | |

[1] A. Panteleeva et al., Radiat. Environ. Biophys. 42 (2003) 95
[2] A. Panteleeva et al., FZ Rossendorf, Wiss.-Tech. Ber. FZR-319 (2001) 103
[3] A. Panteleeva et al., FZ Rossendorf, Wiss.-Tech. Ber. FZR-372 (2003) 64

[1] *Dept. of Radiotherapy, Medical Faculty, Technical University of Dresden*

# RBE of Soft X-Rays for Micronuclei Induction in a Human and a Rodent Cell Line

A. Panteleeva, W. Dörr[1], E. Lessmann, J. Pawelke

The cytokinesis-blocking micronucleus assay is a well-known alternative of the more laborious chromosomal aberrations test. The relative biological effectiveness (RBE) of 25 kV X-rays has been previously determined for micronuclei induction in two human and one rodent cell lines, resulting in an RBE value of $\sim$ 1.3 [1]. These studies have been extended by the human mammary epithelial cell line MCF-12A, since it presents a model system for risk estimation from mammography, which is performed with X-rays below $\sim$ 30 keV. On the other hand, in order to investigate the dependence of the RBE on the photon energy, the RBE of 10 kV X-rays was determined for one of the previously studied cell lines, NIH/3T3 mouse fibroblasts. The details of the cell culture have been previously described for NIH/3T3 [2] and for MCF-12A [3]. The X-ray tube irradiations were performed at the Medical Faculty of TU Dresden. A tungsten anode X-ray tube, operated at 200 kV with a 0.5 mm Cu filter, was used as a reference source. The tungsten anode soft X-ray tube was operated at 25 kV with 0.3 mm Al filtration or at 10 kV with no filtration. The dose rates were 1.2 Gy/min, 1.5 Gy/min and $\sim$ 0.58 Gy/min for the 200 kV X-rays, 25 kV X-rays and 10 kV X-rays, respectively. For the micronucleus test, the cells were irradiated in Petri dishes (3 replications per dose point), incubated with cytochalasin B for 24 h (NIH/3T3) or 48 h (MCF-12A), fixed and stained with Giemsa. The fraction of binucleated cells (BNC), fraction of binucleated cells with micronuclei (BNC+MN) and the number of micronuclei per binucleated cell (MN/BNC) were determined. The resulting dose dependence for the effect $S$ was fitted to the linear-quadratic model $S = c + \alpha D + \beta D^2$.

For the RBE of 25 kV X-rays determination, the irradiation of MCF-12A was performed on the same passage parallelly for both radiation qualities. The dose dependence of BNC+MN is presented in Fig. 1 together with the linear-quadratic model fit, where the response at zero dose was fixed to the control level. A value of 1.4 was found for the RBE, which is in a good agreement with the previously published values for other cell lines [1]. The irradiation of NIH/3T3 with 10 kV X-rays was performed in Petri dishes, placed upside down in a holder. Thus the X-ray attenuation was minimised, since only the dish wall had to be penetrated by the beam and the cells were not covered with the liquid medium during irradiation. However, variation in the dish thickness could still lead to variation in the absorbed dose. Therefore, after cell staining, the thickness of the dishes was measured and the absorbed dose for each dish was calculated from the measured thickness dependence of dose rate. The resulting data were pooled and fitted to the linear-quadratic model, where the $\beta$ coefficient was set to 0 and the response at zero dose was fixed to the control level. Since the application of high doses resulted in saturation of the response, the values for 4 and 5 Gy of 200 kV X-rays and 2.69 Gy of 10 kV X-rays were not included in the fit. The scatter of the dish thicknesses was found to be sufficiently small to present the data by the corresponding means and standard error of the mean (SEM) from the 5 experiments, together with the mean dose values and the corresponding dose SEM (see Fig. 2). The RBE of 10 kV X-rays for micronuclei induction in NIH/3T3 was calculated to be in the range 1.1 - 1.2. This values are smaller than expected from the assumed RBE photon energy dependence. Therefore, determination of RBE of 10 kV X-rays for micronuclei induction in other cell lines is planned.

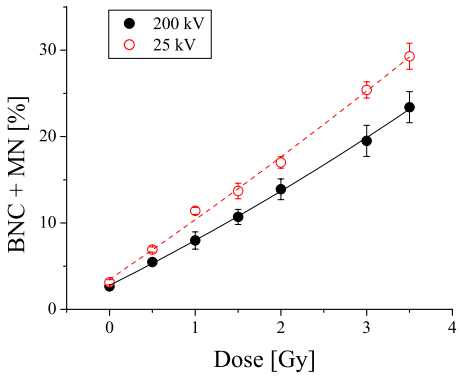


**Fig. 1** *Dose response of micronuclei induction in MCF-12A cells, irradiated with 25 kV X-rays (open circles, dashed line) and 200 kV X-rays (closed circles, solid line). The mean values and the SEM from 6 experiments are shown.*

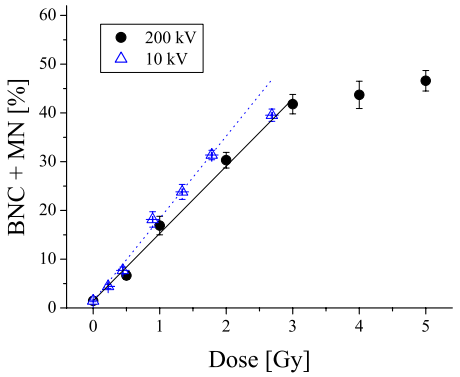


**Fig. 2** *Dose response of micronuclei induction in NIH/3T3 cells, irradiated with 10 kV X-rays (open triangles, dashed line) and 200 kV X-rays (closed circles, solid line).*

[1] D. Slonina et. al., Radiat. Environ. Biophys. 42 (2003) 55
[2] A. Panteleeva et. al., FZ Rossendorf, Wiss.-Tech. Ber. FZR-319 (2001) 103
[3] A. Panteleeva et. al., FZ Rossendorf, Wiss.-Tech. Ber. FZR-372 (2003) 64

[1] *Dept. of Radiotherapy, Medical Faculty, Technical University of Dresden*

# Determination of RBE of 25 kV X-Rays for Chromosomal Aberrations in MCF-12A Human Mammary Epithelial Cells

A. Panteleeva, E. Wolfring[1], E. Lessmann, J. Pawelke, W. Dörr[2]

The relative biological effectiveness (RBE) of soft X-rays has been recently determined by clonogenic survival [1] and micronucleus test [2] for the human mammary epithelial cell line MCF-12A. For 25 kV X-rays, the RBE was found to be endpoint-dependent, resulting in a larger value when studied at the level of chromosomal damage than for cell kill. The micronuclei are formed by a certain kind of chromosomal aberrations (CA) - the chromosome fragments without spindle attachment organelles (acentric fragments). During the cell division, some of these fragments are excluded from the daughter nuclei and form the micronuclei, either on their own, or in conjunction with other fragments within the cytoplasm of the daughter cells. In order to resolve the chromosomal changes caused by soft X-ray irradiation, the RBE of 25 kV X-rays was determined by CA analysis.

The culture conditions of the MCF-12A cell line have been described elsewhere [3]. The irradiation of synchronised cells (confluent cultures were maintained for several days), was performed in polystyrene culture flasks at the Medical Faculty of TU Dresden. As a reference source, a tungsten anode X-ray tube, operated at 200 kV with a 0.5 mm Cu filter, at dose rate of 1.2 Gy/min, was used. The irradiation with 25 kV X-rays was performed with a tungsten anode X-ray tube with 0.3 mm Al filtering at dose rate of 1.9 Gy/min, and the flasks were placed upside down in the holder. Immediately after irradiation, the cells were transported to the cell laboratory in FZ Rossendorf for further processing. In order to inhibit repair processes which could bias the final results, the culture flasks were kept on ice. The cells were splitted at low density and incubated for 39 h, where for the last 3 h of incubation, colcemid at concentration 0.3 $\mu$g/ml was added to the medium in order to arrest the cells in the metaphase. Parallelly, control of the number of cell cycles passed after the irradiation was performed by incubation of cells (controls or irradiated with 5 Gy) with BrdU. A metaphase suspension was obtained by scraping the cells from the flask surface. After treatment in a hypotonic solution of 10 mM trisodium cytrate dihydrate and 32 mM KCl, the cells were fixed in a 3:1 methanol/acetic acid solution and dropped onto grease-free, cold, wet slides. The metaphase slides were stained in Giemsa and observed with magnification of 1000. The acentric fragments, dicentric chromosomes and centric rings in up to 500 cells per dose point were scored, where the dicentrics and centric rings were united in one CA group of exchange aberrations, one acentric fragment being associated with each exchange aberration. The dose response curves for the excess acentric fragments and for dicentrics and centric rings were fitted to the linear-quadratic model $N = c + \alpha D + \beta D^2$, where the response at zero dose was fixed to the control level. From the results, presented in Fig. 1, $RBE_M = \alpha_{25\,kV}/\alpha_{200\,kV}$ was calculated, resulting in a value of $4.4 \pm 2.6$ for the number of excess fragments, whereas for the exchange aberrations an $\mathrm{RBE}_M$ of $0.55 \pm 0.56$. These results, although indicating a high effectiveness of 25 kV X-rays, do not allow definite conclusions about the RBE and will be repeated with better statistics.

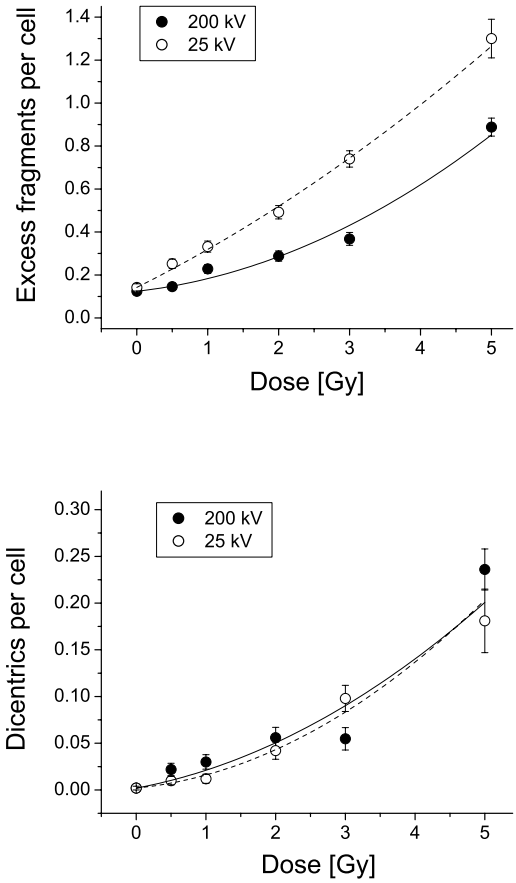


**Fig. 1** *Dose dependence of excessive fragments (upper plot) and exchange aberrations (lower plot) induction in MCF-12A cells, irradiated with 25 kV X-rays (open circles, dashed line) and 200 kV X-rays (closed circles, solid line).*

[1] A. Panteleeva et. al., This Report, p. 59
[2] A. Panteleeva et. al., This Report, p. 60
[3] A. Panteleeva et. al., FZ Rossendorf, Wiss.-Tech. Ber. FZR-372 (2003) 64

[1] *Freiberg University of Mining and Technology*
[2] *Dept. of Radiotherapy, Medical Faculty, Technical University of Dresden*

# Monte Carlo Methods for Electron Transport by Single Scattering Modells

U. Reichelt, J. Henniger[1], W. Enghardt

For the investigation of biological effects by irradiating cells with photons and electrons the spatial and spectral distribution of primary and secondary electrons, which are the main reason for damage production, have to be well known. Therefore, exact electron transport simulations down to subcellular dimensions are necessary.

Only single scattering models can be used in order to avoid uncertainties as they occur using pure multiple scattering models in small dimensions and thin layers. Adapted algorithms for ionisation and elastic scattering were developed for the Monte Carlo (MC) program AMOS [2], which are efficient enough to handle the large number of interactions ($\approx 10^6$ for a 100 keV electron).

If an atomic shell is ionised by electron impact, the secondary electron spectrum is symmetric as shown in Fig. 1. This results from the indistinguishability of both electrons and the dependence of their energy values. Only one half of the spectrum is required to describe the ionisation completely.

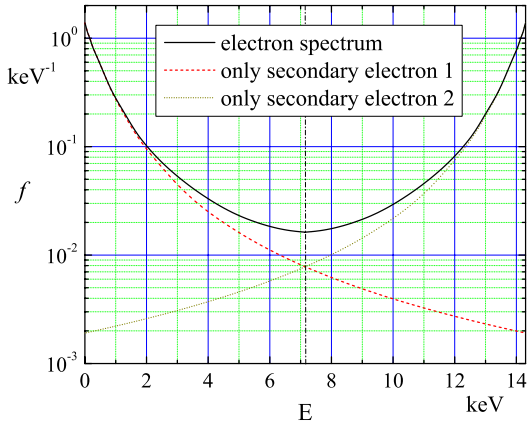


**Fig. 1** *Recoil spectrum by ionisation of the aluminium K shell for an incidence energy of 16 keV*

To interpolate spectra for various primary electron energy values $E_0$, the total recoil spectra have to be separated into the ones of the single electrons. Therefore a power extrapolation is used. Its parameters are determined by using the data points with highest energy values $E$. After the interpolation to the requested energy value $E_0$ the resulting single electron distribution is summed with the same but mirrored one to the secondary electron spectra. Of course the influence of this summation is only important in the middle of the spectrum. But also these quite rare events significantly contribute to the slowing down of an electron concerning the relatively high energy loss.

Further on an algorithm to handle the elastic scattering of electrons was developed. The scattering angle distributions of electrons are extremely anisotropic. The probability density $f$ of the example shown in Fig. 2 varies over eight orders of magnitude. With increasing energy the forward scattering dominates more and more. That leads to the lateral broadening of e. g. an electron needle beam. But also the very rare hard scattering events are of importance for problems like backscattering at material interfaces and in very small dimensions, as there are at cell irradiation experiments. Fig. 2 shows the exact reproduction of the angle distribution by AMOS.

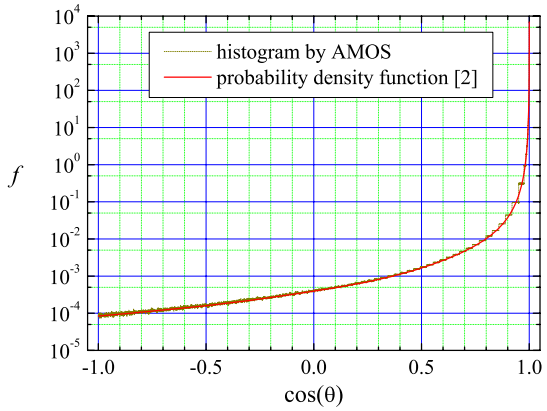


**Fig. 2** *Distribution of elastic scattering angle $\theta$ for 64 keV electrons in aluminium*

To verify the developed MC algorithm it is compared with experimental and simulated data from the literature. Fig. 3 shows transmission spectra for two aluminium layers of different thickness. The results of both simulations, AMOS and PENELOPE [3], fit very well. But in AMOS a much smaller binning could be used because of its high processing speed. The discrepancies to the data by Thomas [3] are conjectured to have their reason in less well known experimental conditions.

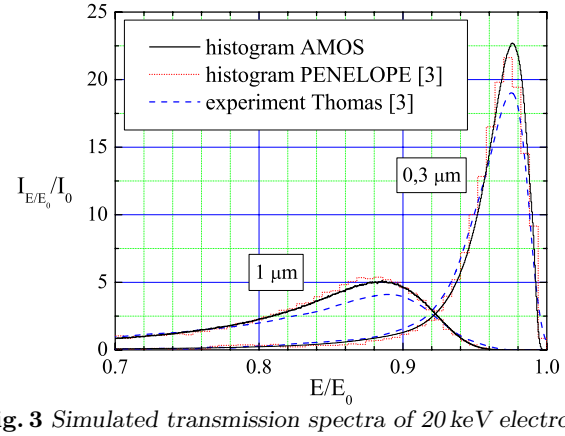


**Fig. 3** *Simulated transmission spectra of 20 keV electrons at 1 µm and 0.3 µm in comparison with results by experiment and the MC program PENELOPE*

[1] Henniger J., AMOS - ein multivalent nutzbares Programmsystem zur Beschreibung von Strahlungstransportproblemen, Strahlenschutz: Physik und Messtechnik, Band 1, Verlag TÜV Rheinland (1994) 145-150

[2] Perkins S. T. et. al., Evaluated Electron Data Library, Lawrence Livermore National Laboratory

[3] Salvat et. al., PENELOPE: An algorithm for Monte Carlo simulation of the penetration and energy loss of electrons and positrons in matter, Nucl. Instr. and Meth. B 100 (1995) 31-46

[1] *Department for Radiation Protection Physics, Institute for Nuclear and Particle Physics, TU Dresden*

# Calculation of Fluence Kerma Conversion Factors for Arbitrary Compounds

U. Reichelt, J. Henniger[1]

Estimating energy dose distributions of photon radiation fields is a common task in radiation protection and radiobiology. Often this can be done by estimating the kerma $K$. It is defined as the sum of kinetic energies of all secondary particles per unit of mass, if the secondary particle equilibrium is fulfilled.
Thereby, the spectral fluence $\Phi_E$ or flux density $\varphi_E$ is often known from radiation transport simulations or experiments. If the effect of interest $I$ (e.g. dose or kerma) is independent on the angle of incidence, it is possible to use fluence conversion factors $f^{\Phi\to I}$ to calculate $I$ from

$$I(\vec{r}) = \int \Phi_E(\vec{r}, E) f^{\Phi\to I}(E)\, dE. \tag{1}$$

This is an adequate assumption in photon dosimetry and the dose can be derived by

$$f^{\Phi\to D} = f^{\Phi\to K}(1-\eta_{br}) \tag{2}$$

with the fluence kerma conversion factor $f^{\Phi\to K}$. At lower photon energies the fraction of energy loss induced by bremsstrahlung production of secondary particles $\eta_{br}$ can be neglected. Thus the dose distribution is described by the kerma distribution. The fluence kerma conversion factor can be calculated from

$$f^{\Phi\to K}(E) = \frac{1}{\rho\cdot\Lambda(E)}\overline{W} \tag{3}$$

using the mean free path length $\Lambda$, mean energy loss per interaction $\overline{W}$ and density of the material $\rho$.
If the material consists of a single element, the mean energy loss per interaction

$$\overline{W} = \sum_x P_x \cdot \overline{W}_x \tag{4}$$

is calculated by adding up the products of the conditional probability $P_x$ and the corresponding mean kinetic energy loss $\overline{W}_x$ for each interaction $x$. For photon radiation with photo effect ($e$), pair production ($p$), coherent (no energy loss) and incoherent scattering ($i$) this results in

$$\overline{W} = P_e\cdot E(1-\eta_x) + P_i\cdot\langle W_i(\mu)\rangle + P_p\cdot(E-2m_ec^2). \tag{5}$$

Therein $\mu$ denotes the cosine of the incoherent scattering angle. For materials of low atomic number the X-ray loss $\eta_x$ is negligible. The expectation value of the inelastic scattering energy loss can be calculated from

$$\langle W_i(\mu)\rangle = \int_{-1}^{+1} f(\mu)\, E(\mu)\, d\mu \tag{6}$$

containing the probability density function (pdf) $f(\mu)$ and

$$E(\mu) = \frac{E^2}{m_ec^2(1-\mu)^{-1}+E}\,. \tag{7}$$

If the material consists of a mixture of $n_s$ elements with molar amounts $\nu^{(s)}$, and if binding effects are small, the conditional probabilities are expanded to

$$P_x = \sum_{s=1}^{n_s} P_x^{(s)} \tag{8}$$

with

$$P_x^{(s)} = \frac{\nu^{(s)}}{\sum_{l=1}^{n_s}\nu^{(l)}}\cdot\frac{\sigma_x^{(s)}}{\sum_k\sigma_k^{(s)}}. \tag{9}$$

Consequently (6) is changing to

$$\langle W_i(\mu)\rangle = \sum_{s=1}^{n_s}\left[\frac{P_i^{(s)}}{P_i}\cdot\int_{-1}^{+1}\frac{f(\mu)\cdot E^2\cdot(1-\mu)}{m_ec^2+E(1-\mu)}d\mu\right]. \tag{10}$$

Using equation (3), (8) and (9) it is possible to determine the fluence kerma conversion factors also for not tabulated elemental compounds. The necessary data for mean free path, interaction probability and pdf of the inelastic scattering angle can be calculated from several data libraries, here the EPDL [1] is used.
Fig. 1 shows the achieved fluence kerma conversion factors of water in comparison with values retrieved from ICRU 44 [2] and NISTIR 5632 [3]. The calculated graph fits very well with the data in the literature except a discrepancy at energy values above 20 MeV. It is the consequence of bremsstrahlung emission by the secondary particles of the increasing pair production.
Combined with fluence detectors in Monte-Carlo simulations the fluence kerma conversion factors are very useful estimating dose distributions with high spatial resolution.

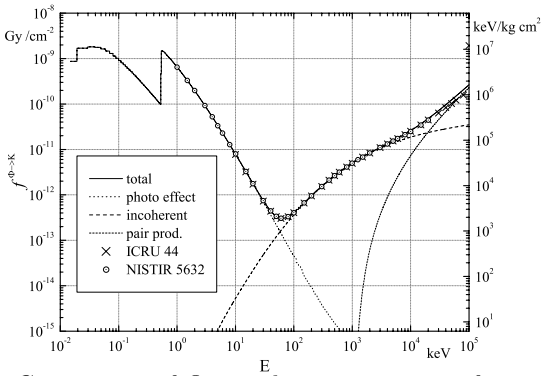


**Fig. 1** *Comparison of fluence kerma conversion factors for water; plots - self calculated, symbols - data from literature*

[1] D.E. Cullen et al., Evaluated Photon Data Library, UCRL–50400, Vol. 6, Rev. 5 (1997)
[2] ICRU Report 44, Tissue Substitutes in Radiation Dosimetry and Measurement (1989)
[3] Technical Report NISTIR 5632, NIST, Gaithersburg, MD 20899 (1995)

[1] *Department for Radiation Protection Physics, Institute for Nuclear and Particle Physics, TU Dresden*

# An Efficent Monte Carlo Detector for Fluence and Dose Estimations for Uncharged Particles

U. Reichelt, J. Henniger[1]

For treatment planning in brachytherapy the dose distribution around a radioactive source has to be exactly known. Calculating this by means of Monte Carlo (MC) methods requires an adequate number of photon histories.

Some possible models are based on adding up all energy depositions in the detector elements. The low number of interactions in the lifetime of photons makes these approaches less effective.

Another possibility is to use a fluence detector. In doing so each crossed detector element at the photon path contributes to the detector response. If dose estimations are requested, this fluence can be transformed by fluence dose conversion factors.

The main problem in this detector type is to avoid the calculation of interface passages, because this requires numerical instable or complex algorithms. This is achieved by means of the developed MC detector, which is based on the fact that radiation transport is a Markov chain. This means that the interaction probabilities are independent from all former events as long as the distribution parameters stay unchanged. At the way between two interaction points this is fulfilled. Thus the energy dependent mean free path length $\Lambda(E)$ can be reduced to an arbitrary value $\Lambda_{min}(E)$ if after each allotted step length a random number $\xi \in (0; 1]$ is compared with the interaction probability

$$P_i(E) = \frac{\Lambda_{min}(E)}{\Lambda(E)}. \quad (1)$$

Only if $\xi < P_i(E)$ is satisfied, a physical interaction is processed. Otherwise the photon is moving on without any changes (ongoing Markov chain).

The end points of all resulting steps are used for the fluence estimation. Thereby, the particle weights $n_{wgt}$ are added up to the detector element according to the discretised spatial position $(i, j, k)$

$$M_{ijk} \Rightarrow M_{ijk} + \frac{n_{wgt}}{\Lambda_{min}(E)}. \quad (2)$$

Nevertheless, also the time and energy dependence can be treated in a uniform manner. If the dose distribution is requested, the energy dependent conversion factors have to be taken into account by

$$M_{ijk} \Rightarrow M_{ijk} + \frac{n_{wgt} \cdot f^{\Phi \to D}(E)}{\Lambda_{min}(E)}. \quad (3)$$

At the end of the photon transport simulation each detector element must be normalized to the number of simulated photon histories and its specific volume.

Furthermore, the handling of material interface passages in particle transport can be simplified if $\Lambda_{min}(E)$ is defined to be equal to or less than the smallest mean free path of all occurring materials in the geometry [1]. So, there are no error-prone calculations of intercept points when sampling the interaction length.

As an example the calculation for an $^{125}$I brachytherapy source by means of AMOS [2] is presented. For its application in radiotherapy of prostate cancer the dose distribution has to be well known with uncertainties less than 8%. Therefore, an annular detector of an axial symmetric stack of 1000 x 1000 hollow cylinders was used to determine the dose in the surrounding water. The stack has a radius of 5 cm and a length 10 cm. This results in an axial and radial binning of 0.005 cm using the mirror symmetry of the source. $^{125}$I emits photons of discrete energy values in the range of 27.2 keV to 35.5 keV. Thus the energy loss by bremsstrahlung can be neglected, and the kerma is equivalent to the dose. Hence, the fluence kerma conversion factors obtained by [3] could be used. The simulation was done with a common personal computer.

Figure 1 shows the dose distribution per emitted photon. The lower dose area on top of the brachy source originates from self-shielding. Normally the distribution in a distance up to 5 cm is of therapeutic interest. In radial direction results with statistical uncertainties below 5% are achievable up to 25 cm. Along this distance the dose rate varies over nine orders of magnitude.

This example proves the ability of the presented algorithm to simulate MC detectors of high spatial resolution. The efficiency enables small statistical error margins in simulations on state of the art personal computers. This is required or at least advantageous for many applications in medicine and radiobiology.

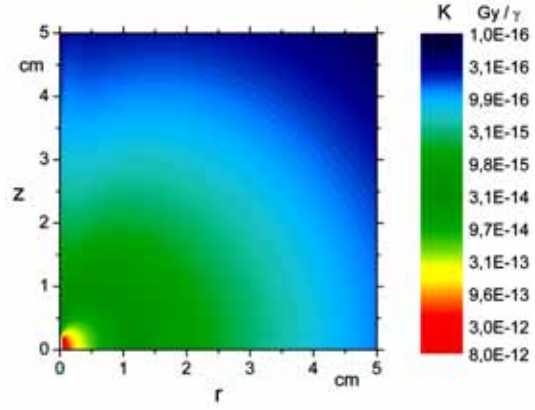


**Fig. 1** *Dose distribution in water induced by an $^{125}I$ brachytherapy source*

[1] I. Lux, Monte Carlo particle transport methods: neutron and photon calculation, CRC Press, Boca Raton (1991)

[2] J. Henniger, AMOS - ein multivalent nutzbares Programmsystem zur Berechnung von Strahlungstransportproblemen, Strahlenschutz: Physik und Messtechnik, Band 1, Verlag TÜV Rheinland (1994) 145-150

[3] U. Reichelt, J. Henniger, Calculation of Fluence Kerma Conversion Factors, This Report p. 63

[1] *Department for Radiation Protection Physics, Institute for Nuclear and Particle Physics, TU Dresden*

# In-Beam PET Imaging with LSO/APD-Array Detectors: First Results [B,G,S]

P. Crespo, M. Kapusta[1], J. Pawelke, M. Moszyński[1] W. Enghardt

The promising clinical results achieved at the heavy ion tumor therapy project in GSI Darmstadt [1] prompted the construction of a hospital-based facility at the Heidelberg University Clinics. Here, delicate therapeutic situations are expected to be treated with a rotating beam delivery (gantry) equipped with a dedicated in-beam PET system. The detectors of such a PET system should cover a large solid angle, be of small volume and minimal weight and insensitive to magnetic fields due to the proximity to the beam bending magnets. The combination of crystals of cerium-doped lutetium oxyorthosilicate (LSO) and avalanche photodiode arrays (APDA) could solve this problem. While similar detectors have shown their applicability to tracer imaging [2], their performance for in-beam PET is unknown up to now. Thus, they have to be experimentally studied before the final design of the in-beam PET scanner for the Heidelberg therapy facility. Therefore, we have investigated the performance and in-beam imaging capabilities of two position sensitive $\gamma$-ray detectors consisting of Hamamatsu avalanche photodiode arrays (S8550) individually coupled to crystals of cerium-doped lutetium oxyorthosilicate (LSO). The two detectors were operated in coincidence at the GSI medical beam line.

In a first set of experiments their imaging performance was tested before, during and after the irradiation of phantoms of polymethylmethacrylate (PMMA) with carbon ion beams with fluences equivalent to 1000 typical daily therapeutic fractions. The detectors were positioned at relatively small forward or backward angles ($\sim 30°$) relative to the incoming radiation in order to simulate the geometry of the detectors positioned at the edges of the tomograph planned for Heidelberg [3]. A $^{68}$Ge line source placed vertically between the detectors was imaged, with the source slightly shifted (14 mm) towards one of the detectors in order not to be hit by the beam or by the flux of light particles leaving the phantom that stopped the beam. Only minor energy, time and spatial resolution deterioration was observed in the measurements performed under beam irradiation (Table 1 and Fig. 1), with the initial values being recovered after stopping the irradiation. The mean energy resolution obtained both with a line source ($^{68}$Ge) and a point source ($^{22}$Na) for the 64 channels is $15.5 \pm 0.4$ % FWHM, and the coincidence time resolution is $6.2 \pm 0.2$ ns FWHM. Both values are in agreement with our previous results [4] of $14.6 \pm 0.5$ % FWHM (energy) and $3.0 \pm 0.2$ ns (time, extrapolated from measurement against $BaF_2$) obtained for one single pixel. The slightly worse performance arises from the longer LSO crystals used (15 mm vs. 10 mm in [4]) and, more importantly, from the increased number of channels introducing a higher time spread.

A second set of experiments successfully imaged the depth distribution of positron emitter radionuclides created in a phantom that stopped the high energy carbon ion beam (Fig. 2). This set of imaging experiment is of importance since it simulates the application of such detectors for monitoring the $^{12}$C patient tumour irradiations. It checks furthermore the imaging capability of the detectors after being exposed to the back and forward cones of light particles resulting from high fluences of $^{12}$C delivered to PMMA phantoms.

The obtained results show that LSO is a suitable material for in-beam PET and that its coupling with avalanche photodiode arrays is feasible for a PET system dedicated to in-beam monitoring of ion therapy.

**Table 1** *Performance of the LSO/APDA detectors.*

| Experiment | Before irradiation | Detectors up-beam | Detectors down-beam | After irradiation |
|---|---|---|---|---|
| $^{12}$C beam ($A$M$e$V) | No | 342.0 | 342.0 | No |
| Phantom | No | Yes | Yes | No |
| $\Delta E/E$ (fwhm, %) | $15.5 \pm 0.5$ | $15.5 \pm 0.3$ | $16.4 \pm 0.6$ | $15.5 \pm 0.3$ |
| $\Delta t$ (fwhm, ns) | $6.2 \pm 0.2$ | $6.1 \pm 0.2$ | $6.3 \pm 0.2$ | $6.2 \pm 0.2$ |

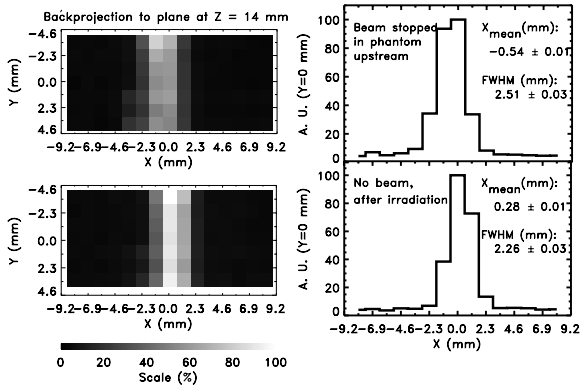


**Fig. 1** *Imaging a $^{68}$Ge line source under several irradiation conditions.*

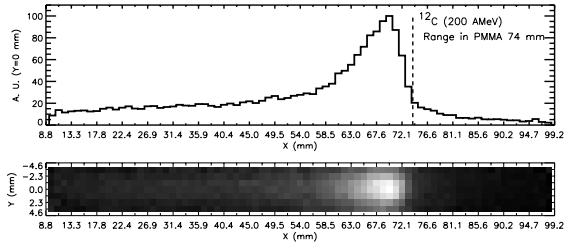


**Fig. 2** *Positron emitter distribution generated by stopping the carbon beam in a phantom. Imaged with the LSO/APDA detectors. Intensity scale as in Fig. 1.*

[1] D. Schulz-Ertner et al., Int. J. Radiation Oncology Biol. Phys., 53 (2002) 36
[2] B.J. Pichler et al., IEEE Trans. Nucl. Sci., 48 (2001) 1291
[3] P. Crespo et al., IEEE Trans. Nucl. Sci., submitted for publication
[4] M. Kapusta et al., Nucl. Inst. and Meth. A, 504 (2003) 139

[1] *Andrzej Soltan Institute for Nuclear Studies, 05-400 Otwock-Świerk, Poland.*

# Experimental Investigations on In-Beam PET for Proton Therapy [G, E]

K. Parodi, F. Pönisch, W. Enghardt

Following the promising results of [1], further phantom experiments have been performed at GSI in order to address the feasibility and accuracy of in-beam positron emission tomography (PET) for proton therapy. For the most challenging issue of range monitoring it has been demonstrated for mono-energetic as well as for spread-out Bragg peak (SOBP) irradiation that range differences of about 0.9 mm can be resolved (Fig. 1). The activation study of an inhomogenous phantom also supported the usefulness of PET for assessment of local tissue modifications or field misalignments leading to strong density gradients in the beam path during fractionated therapy. Despite the limitations of the presently used calculation model for other materials than lucite [1] [2], a fairly good correspondence especially with respect to the range spike after the lateral density gradient polyethylene/lung was observed in measured and predicted images (Fig. 2). Finally, the value of PET for lateral position verification was assessed by irradiation of a specially designed lucite phantom allowing insertion of radiographic films for the simultaneous measurement of the lateral dose distribution (Fig. 3). All these results, more deeply addressed in [2], strongly support the value of in-beam PET for proton therapy. However, the extension of such millimetre precision to real clinical cases at least in low perfused tissues requires a detailed description of all reaction channels leading to

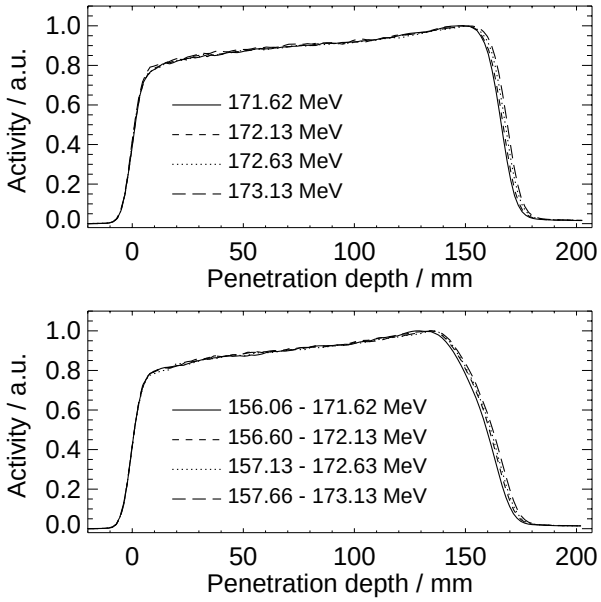


**Fig. 3** *Measured depth profiles of $\beta^+$-activity induced by mono-energetic and SOBP (formed by 11 equally spaced energy steps) irradiation stopped in lucite at maximum depths differing less than 1 mm.*

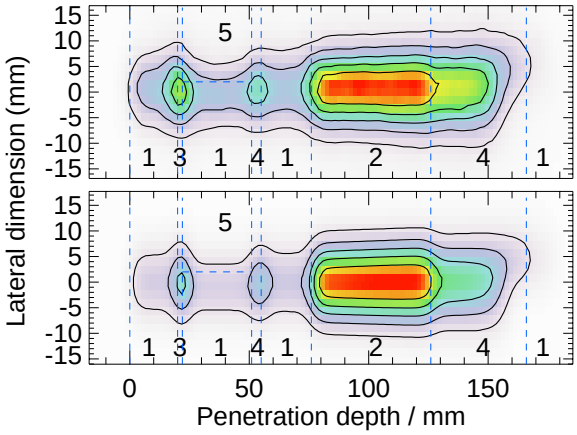


**Fig. 2** *Measured (top) and predicted (bottom) PET images induced by a 156.06 MeV pencil-like proton beam in a target with inserts of polyethylene (1), lucite (2) and bone (3), muscle (4) and lung (5) equivalent materials. The different regions are marked by the dashed lines.*

$\beta^+$-emitters in combination with an accurate knowledge of the tissue stoichiometry for a realistic prediction to be compared with the PET measurement. Investigations on the influence of the $^{11}C/^{15}O$ ratio reported in [2] indicate also the sensitivity of the $\beta^+$-activity distal edge to the time course of the irradiation and PET acquisition. Hence, an optimal irradiation strategy in combination with proper off-line analysis should be considered in order to achieve the required accuracy for range monitoring. In perspective of the clinical implementation at the ion beam facility at Heidelberg, the extension of the modeling to include more reaction channels in combination with further PET experiments in pure phantom for validation of the available cross-section data is planned.

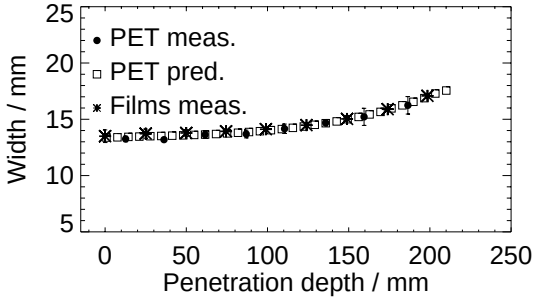


**Fig. 3** *Lateral broadening (FWHM) of the measured (points) and predicted (squares) $\beta^+$-activity in comparison to the optical density of the exposed films (stars) for a 190.37 MeV proton irradiation. A vertical offset was introduced in order to adjust the distributions to the same average FWHM of the PET response.*

[1] K. Parodi et al., Phys. Med. Biol. 47 (2002) 21
[2] K. Parodi, Ph.D. Thesis, *in preparation* (2004)

# A New Computer System for In-Beam PET Data Evaluation [G]

F. Pönisch, W. Enghardt

The reconstruction of in-beam PET data acquired during the therapeutic irradiation with heavy ions at GSI Darmstadt requires high computational power since the PET images have to be available as shortly as possible after finishing a fractionated irradiation, however, at the latest before applying the next daily dose fraction. Furthermore, the number of patients treated per day (up to 15) increases steadily and more sophisticated and thus time consuming reconstruction techniques as e.g. the scatter correction introduced recently [1] and new data evaluation tools [2] are applied. Therefore, we have adapted our data processing software to a state-of-the-art computer system (Hewlett-Packard Linux cluster located at the computing centre of FZR). The cluster consists of 40 CPU, from which up to 4 can be exclusively occupied for in-beam PET purposes and it has been working for the routine PET data processing for heavy ion therapy since 2002. However, there remain two drawbacks: (*i*) The data transfer of the raw PET-data from the GSI to FZR and the retransfer of the reconstructed images to GSI requires a reliable long-distance data transmission. (*ii*) The effectiveness of the PET data evaluation correlates with the load of the local network which is of course not as efficient like a direct connection to a PC.

These disadvantages can be overcome by means of an on-site computer system placed at the therapy facility of GSI Darmstadt. Such a system provides a better in-time data evaluation [2] since it simplifies the data handling and it fastens the interactive calculation of deviations between planned and applied dose. Thus, in 2003 we have installed a new dual processor workstation (Fujitsu Siemens Celsius R610) with Intel Xeon processors of 3.06 GHz equipped with 4 GB DDR-SDRAM memory and a fast redundant SCSI RAID-1 storage disk array with a capacity of 122 GB that is sufficient to store data for future beam-times (each $\approx 5$ GB). The workstation is connected via a Gigabit Ethernet LAN network device to the intranet of the therapy facility and it is protected against hacker attacks from outside using the GSI-firewall. The Linux operating system has been installed since it provides a high level of transparency and compatibility to the existing source codes and the shell scripts. Furthermore, the maintenance is rather easy and no additional license costs are expected for the future. Consequently, we have installed the SUSE Linux 8.2 with kernel 2.4.22, the IDL software package and the Intel C-Compiler. The benchmark tests below base on the comparison of the C-code implementation of the maximum likelihood tomographic reconstruction with scatter correction [1] for PET data acquired during the carbon ion irradiation of a patient with a rather large PET image ($118 \times 100 \times 116$ voxels) and a large number of valid registered coincidences (156800) according to the patient in [3]. Moreover, the influence of the different computer systems, compilers and the reconstruction parameters on the run-time has been also studied. An example for a reconstruction parameter of the scatter correction algorithm (single scatter simulation) affecting the run-time is the lattice parameter (mean distance of the scatter points). Our first estimation assumes a lattice parameters of 10 mm. Later investigations [4] showed that a size up to 15 mm results in similar PET images. However, in order to compare previous run-time tests with the recent calculations, the smaller grid size is also presented. The results of the benchmark test are shown in Table 1 and may summarized as follows: State-of-the-art high-end PC deliver the performance for a time efficient processing of sophisticated problems in scientific computing on a low cost level. The run-time is strongly dependent on the applied C-compiler. The performance of the Intel compiler on a Xeon CPU is about 1.5 times higher than that of the GNU compiler. The reconstruction code runs faster on the Intel Xeon processor (3.06 GHz) than on the tested workstation from IBM. Even the latest IBM machine (1.45 GHz Power4+CPU), whose clock cycle is by a factor of 4 higher than that of the processor shown in Table 1 is inferior to the new 3.06 GHz Xeon system. The measured run-time of 21 min for the reconstruction of a typical PET image on the new Xeon workstation is less than the time needed for the treatment itself. Therefore, the two CPUs of a standard low cost workstation are sufficient to complete the data processing of the measured and simulated PET data within less than 1/2 hour.

| Processor | Clock cycle /GHz | L2-Cache /kB | Reconstruction Time /min | | |
|---|---|---|---|---|---|
| | | | Intel Compiler | | GNU Compiler |
| | | | grid 10 mm | grid 15 mm | grid 15 mm |
| Intel Xeon | 2.0 | 256 | 97[I] | 45[I] | 71[III] |
| Intel Xeon | 3.06 | 512 | 39[II] | **21**[II] | 28[IV] |
| IBM Power3 | 0.375 | 8192 | 161[V] | 81[V] | - |

**Tab. 1** *Comparison of the reconstruction time on different computers, reconstruction parameters and compilers;* [I] *Version 6.0 with options: -O3 -tpp7 -xW,* [II] *V7.1: -O3 -tpp7 -xW -ipo,* [III] *V2.95.2: -O3,* [IV] *V3.3: -march=pentium4,* [V] *V3.6.6: -O4.*

[1] F. Pönisch, W. Enghardt, K. Lauckner, Phys. Med. Biol. 48 (2003) 2419
[2] K. Parodi, W. Enghardt, Wiss.-Tech. Ber. FZR-372 (2002) 98
[3] F. Pönisch, W. Enghardt, M. Schlett, Wiss.-Tech. Ber. FZR-372 (2002) 100
[4] F. Pönisch, Wiss.-Tech. Ber. FZR-378 (2003) 61

# In-Beam PET for Radiotherapy with Helium Beams: Model Predictions [E, G]

F. Fiedler, K. Parodi, W. Enghardt

For a first estimation on the amount and spatial distribution of $\beta^+$-emitters produced by helium beams in tissue the approach of [1] was used. The experimental cross sections from references [2-7] (Fig. 1) were combined with the particle fluences calculated by the FLUKA-Simulation code [1], [2] to get the number of $\beta^+$-emitters produced in a PMMA-target. For the reactions $^{16}$O($^3$He,$^3$He$\,n$)$^{15}$O and $^{16}$O$(\alpha,\alpha\,n)^{15}$O the cross sections were estimated from the ratio corresponding reactions with $^{12}$C and the $^{12}$C$(p,p\,n)^{11}$C/$^{16}$O$(p,p\,n)^{15}$O, because there is a lack of experimental data. The predicted $\beta^+$-activity distributions resulting from the most important positron emitters $^{11}$C and $^{15}$O produced in a $9\times9\times20$ cm$^3$ PMMA-target by a $^3$He and $^4$He beam are shown in Figs. 3 and 4. The calculations were made for $10^6$ particles and the distributions are convolved with the spatial resolution of the imaging system (FWHM = 5 mm).

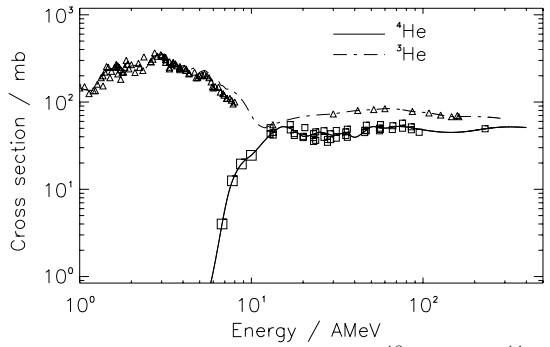


**Fig. 1** *Cross sections for the reactions $^{12}C(\alpha,\alpha\,n)^{11}C$ resp. $^{12}C(^3He,^3He\,n)^{11}C$ and $^{12}C(^3He,a)^{11}C$, the symbols mark the data given in refs. [2-7].*

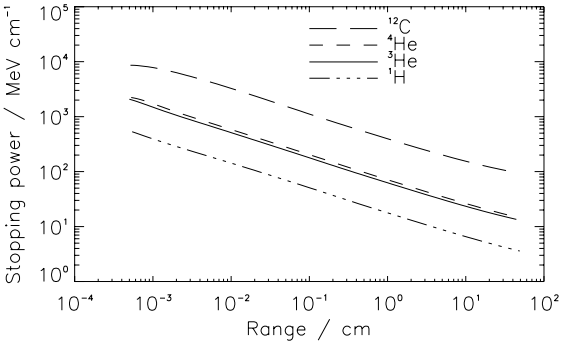


**Fig. 2** *Stopping power of different ions in dependence on the residual range in water.*

For getting the same physical dose at the same particle range with protons a 20 times higher particle fluence than in the carbon case is required. Since the $\beta^+$-emitter production rate per proton is about ten percent of the $^{12}$C induced reactions and from this ratio an increase of the activity signal up to a factor of 2 was expected [10]. Comparing the stopping power for carbon and helium (Fig. 2) we need a particle fluence about 6 times larger than in the carbon case to get the same physical dose. The number of $\beta^+$-emitters produced per incident particle is about 10 times less than for carbon ions. Thus a signal approximately half as intense as for a carbon beam is expected if the same physical dose is applied. If comparing to the same biologically equivalent dose [11] a further increase of the helium induced signal up to a maximum of about 3 can be expected because of the higher relative biological effectivness of carbon ions.

| Ion | $E$/AM$e$V | Range/cm | $^{15}$O | $^{11}$C |
|---|---|---|---|---|
| $^1$H | 140 | $\sim$ 12.0 | 12300 | 26650 |
| $^{12}$C | 270.55 | $\sim$ 12.2 | 100400 | 266100 |
| $^3$He | 166 | $\sim$ 12.2 | 10672 | 31022 |
| $^4$He | 140 | $\sim$ 12.1 | 6976 | 20361 |

**Tab. 1** *Prediction on the number of $\beta^+$- emitters produced in a $9\times9\times20$ $cm^3$ PMMA-target by helium beams with a particle fluence of $10^6$ for therapeutic energies in comparison with the confirmed predictions for protons [10] and carbon ions [10].*

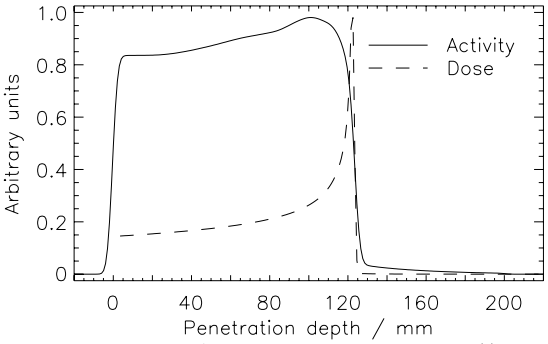


**Fig. 3** *Prediction of $\beta^+$-emitter distribution for $^{11}C$ and $^{15}O$ in case of a $^3$He-beam with E = 166 AMeV in a $9\times9\times20$ $cm^3$ PMMA-target.*

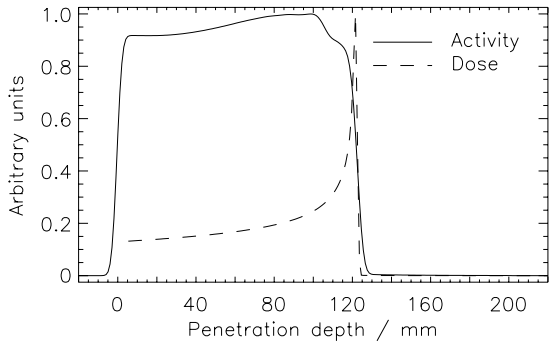


**Fig. 4** *Prediction of $\beta^+$-emitter distribution for $^{11}C$ and $^{15}O$ in case of an alpha beam with E = 140 AMeV in a $9\times9\times20$ $cm^3$ PMMA-target.*

[1] K. Parodi et al., Phys. Med. Biol. 47 (2002) 21
[2] M. Lindner, R.N. Osborne, Phys. Rev. 91 (1953) 1501
[3] W.E. Crandall et al., Phys. Rev. 101 (1956) 329
[4] D.R.F. Cochran, J.D. Knight, Phys. Rev. 128 (1962) 1281
[5] J. Radin, Phys. Rev. C 2 (1970) 793
[6] R.L. Hahn, E. Ricci, Phys. Rev 146 (1966) 650
[7] S.D. Cirilov et al., Nucl. Phys. 77 (1966) 472
[8] A. Fassò et al., Proc. Monte Carlo 2000 Conference, Lisbon, October 23-26 2000 (2001) 159
[9] A. Fassò et al., Proc. Monte Carlo 2000 Conference, Lisbon, October 23-26 2000 (2001) 955
[10] K. Parodi et al., Phys. Med. Biol. 45 (2000) N151
[11] M. Belli et al., Int. J. Rad. Biol. 76 (2000) 1095

# The Prediction of the $\beta^+$-Activity Distribution on the Basis of the Treatment Planning CT Using the FLUKA Simulation Code [B, E, G]

F. Fiedler, K. Parodi, A. Ferrari[1], W. Enghardt

The in-beam PET technique for quality assurance of $^{12}$C therapy is based on the comparison of $\beta^+$-activity distributions measured during therapeutic irradiations with those predicted from the treatment plan. The generalisation of this method to all species of therapeutically relevant ions requires a precise description of both the stopping process and the nuclear interactions of the projectiles in tissue. The FLUKA radiation transport simulation code [1], [2] may meet these requirements since the implementation of suitable models for describing light ion nuclear interactions is in progress. Furthermore, it has been demonstrated that measurements of proton beam induced $\beta^+$-activity distributions can be rather well reproduced by calculations based on the FLUKA code [3]. The approach developed for the proton case may be feasible for other ion species: In a first step the spatial distribution of the flux of primary and secondary particles $\phi(E, A, Z, \mathbf{r})$ is calculated on the basis of the FLUKA internal models of nuclear reactions. In a second step a realistic description of the production of positron emitters is obtained by combining these results with measured or semi-empirical cross sections [3].

The $\beta^+$-activity produced via target fragmentation strongly depends on the stoichiometric tissue composition, especially on the $^{16}$O/$^{12}$C ratio, which varies between 0.22 for adipose tissue and 4.05 for muscle. This ratio determines the relative abundances of $^{15}$O ($T_{1/2}$ = 2.03 min) and $^{11}$C ($T_{1/2}$ = 20.38 min) as the dominating $\beta^+$-active reaction products, and because of the different half-lives the activity in different tissue types. Especially for projectiles with $Z < 5$, where $\beta^+$-emitter can only be produced via target fragmentation, taking into account the tissue stoichiometry is unavoidable for a correct description but also for heavier projectiles as e.g. $^{12}$C a refinement of the prediction of the $\beta^+$-activity

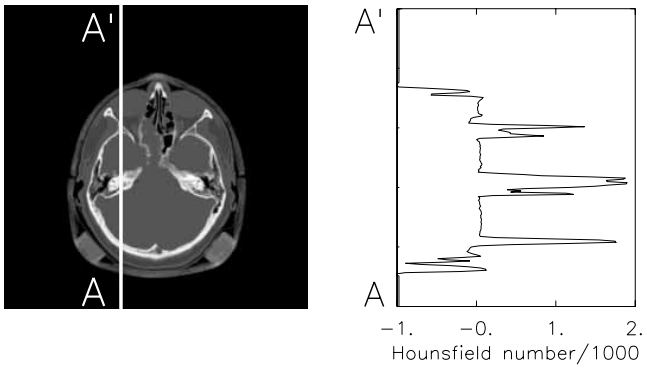


**Fig. 1** *left: Patient CT, right: Profile of Hounsfield units along the section* $\overline{AA'}$.

distribution from the treatment plan is expected. In a typical patient CT the Hounsfield numbers range from −1024 to 3071 representing different densities and different chemical compositions of tissue (Fig. 1). The CT numbers are converted by a Fortran code into a file which is adopted by FLUKA as geometrical input. For deriving the stoichiometric information we use the conversion of CT numbers to elemental weights established by [4],

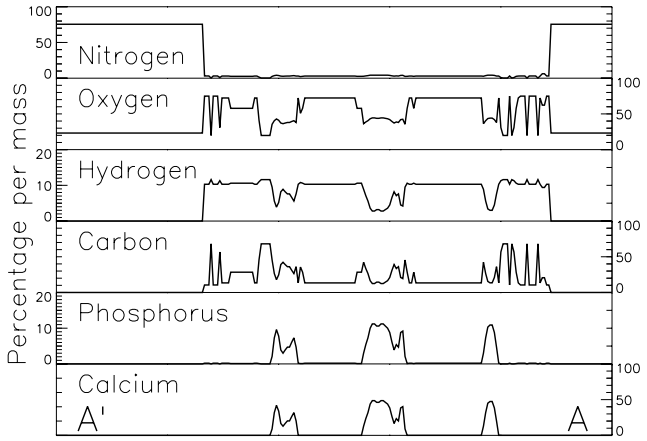


**Fig. 2** *Chemical composition of the tissue along the section* $\overline{AA'}$ *in Fig. 1 referring to the segmentation described in the text. Abundances below 1.5 % (Na, Mg, S, Ar, K) are not displayed in this figure.*

which gives the chemical composition for Hounsfield numbers between −1000 and 1600. Hounsfield units lower than −950 are set to the composition of air, between −120 and −950 the composition of lung is assigned, in the range of soft tissue between −120 and 200 a finer raster is applied and in the region above 200 a grid of 100 Hounsfield units is used. For Hounsfield units larger than 1600 the chemical composition has been extrapolated with the step width of 100 Hounsfield units up to 3000, the Hounsfield numbers larger than 3000 are treated as titanium. This segmentation leads to 39 different tissue compositions (Fig. 2). For each portal the distribution of position emitters can be calculated for each pencil beam using a file containing general information for the patient as well as the beam energy, focus and position as well as the number of particles for all points to be irradiated. This can be done before the treatment starts, after the fractionated irradiation these results can be combined with the time protocol of the irradiation and give for each positron emitter the time when it was created. Then all processes from $\beta^+$-decay to the detection of $\gamma$-rays can be done as described in [5].

[1] A. Fassò et al., Proc. Monte Carlo 2000 Conference, Lisbon, October 23-26 2000 (2001) 159
[2] A. Fassò et al., Proc. Monte Carlo 2000 Conference, Lisbon, October 23-26 2000 (2001) 955
[3] K. Parodi et al., Phys. Med. Biol. 47 (2002) 21
[4] W. Schneider et al., Phys. Med. Biol. 45 (2000) 459
[5] F. Pönisch, Wiss.-Tech. Ber. FZR-378 (2003)

[1] *CERN, Geneva, Switzerland*

# Monte Carlo Simulations on In-Beam PET Imaging of Photon Radiotherapy: Target Activation via Photonuclear Reactions

H. Müller, W. Enghardt

Positron emission tomography (PET) plays an increasingly important role as a diagnostic method for supporting radiation therapy [1]. Applying appropriate radiotracers PET is capable of quantifying the metabolic activity of tissue and provides, therefore, information for a precise target definition during radiotherapeutic treatment planning and for monitoring the tumor response during and after the treatment. Furthermore, the combination of PET with radiotherapeutic treatment units (in-beam PET) offers a unique possibility of a three dimensional in situ and non-invasive dose delivery monitoring, which allows the irradiation field position to be controlled and local dose deviations from the treatment plan to be quantified [2]. This technique has been developed for ion beam therapy [2, 3], but is expected to have a considerable potential for improving the precision of therapy with hard photon beams [1].

In this contribution the yield of positron emitters via the $(\gamma, n)$ reaction in various organic materials under the irradiation with bremsstrahlung is simulated using GEANT4 [4]. Calculations are carried out for electron beams of 15, 18, 21 and 50 MeV, which hit a layer of 1 mm tungsten and produce thus bremsstrahlung. The electrons are then absorbed in 5 cm iron. A parallel photon beam is formed by randomly sampling the starting points of the photons within an area of $4 \times 4\,\mathrm{cm}^2$. This beam impinges centrally on targets of $9 \times 9 \times 20\,\mathrm{cm}^3$ consisting of various materials. The resulting dose $D$ and activity $A$ depth profiles as well as the ratio $\alpha = A/D$ are shown in Fig. 1 for the case of 50 MeV electrons and target material PMMA. Here, the activity is derived from the number of produced $^{11}$C and $^{15}$O nuclei by taking into account their half lives of $T_{1/2} = 20.38\,\mathrm{m}$ and $T_{1/2} = 2.03\,\mathrm{m}$, respectively. The dose distribution shows a broad maximum around 50 mm depth, while the activity drops down continuously with increasing depth. It should be noted that like in the case of ion therapy the activity distribution is not proportional to the dose distribution. This concerns, however, mainly the entrance region with its low dose delivery before reaching the secondary electron equilibrium. From a certain depth on the ration $\alpha$ of activity to dose remains nearly constant.

The ratio $\alpha$ averaged over the target region irradiated by the 4 cm × 4 cm photon beam is gathered in Table 1 for all energies and materials considered.

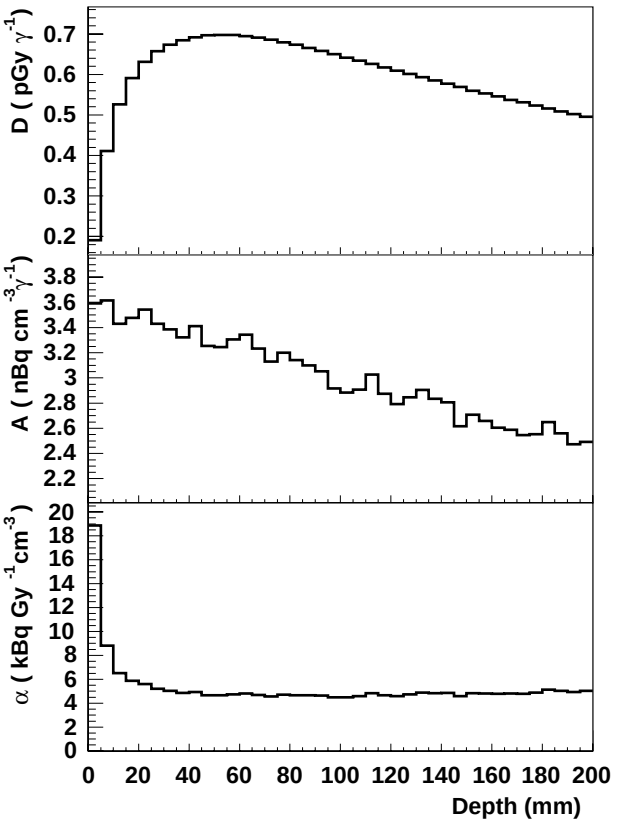


**Fig. 1** *Depth profile of dose $D$ (upper panel), distribution of activity $A$ (middle panel) and the ratio $\alpha = A/D$ (lower panel) in PMMA for* 50 MeV *photon beam.*

**Table 1** *The ratio $\alpha\,(\mathrm{Bq\,Gy^{-1}\,cm^{-3}})$ of activity to dose for various electron beam energies and target materials.*

| Energy(MeV) | 15 | 18 | 21 | 50 |
|---|---|---|---|---|
| PMMA | 21 | 113 | 359 | 5327 |
| Adipose | 15 | 89 | 244 | 4177 |
| Bone | 166 | 406 | 988 | 6163 |
| Muscle | 37 | 155 | 443 | 3631 |

The strong increase of $\alpha$ with energy for all materials makes the higher energies the better candidates for in-beam PET imaging. Comparing to the clinically applied $^{12}$C and p beams where ratios of $\alpha \approx 200\,\mathrm{Bq\,Gy^{-1}\,cm^{-3}}$ and $\alpha \approx 600\,\mathrm{Bq\,Gy^{-1}\,cm^{-3}}$, respectively, were found we get for photons produced with electron energies above 20 MeV an even higher activity per dose.

[1] A. Brahme, Acta Oncol. 42 (2003) 123
[2] W. Enghardt et al., Nucl. Instr. and Meth. A (in press)
[3] E. Urakabe et al., Jpn. J. Appl. Phys. 40 (2001) 2540
[4] S. Agostinelli et al., Nucl. Instr. and Meth. A506 (2003) 250

# Monte Carlo Simulation on In-Beam PET Imaging of Photon Radiotherapy: Pair Production

H. Müller, W. Enghardt

In the previous contribution [1] we have discussed the use of the positron emitters $^{11}$C and $^{15}$O produced by bremsstrahlung during therapy for imaging on the basis of positron emission tomography (PET). In this contribution we discuss the possibility of the direct use of the annihilation radiation following $e^+e^-$-pair production during photon therapy for PET imaging simultaneously to therapeutic irradiations.

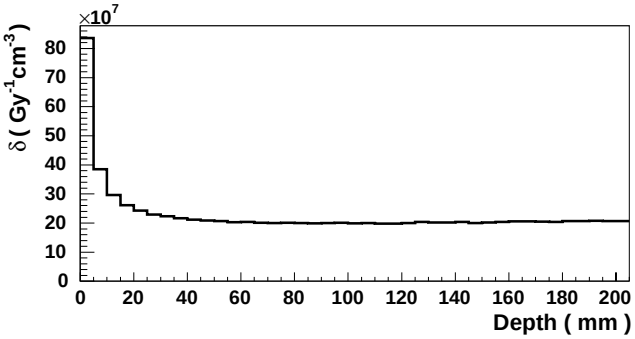


**Fig. 1** *The ratio $\delta$ of the number of pair production positrons to dose in PMMA for 50 MeV photon beam.*

In Fig. 1 the distribution of the ratio of the number of produced positrons to the dose is depicted. As in the previous contribution the proportionality to dose delivery is strongly violated in the entrance region of the target.

A second problem concerns the question whether it is possible to image anatomic structures by measuring positrons from pair production in a positron camera to get a method for controlling the positioning of the patients. Since these positrons have high initial energies they may travel appreciable distances before they annihilate at rest. This effect degrades the resolution of the image. The distances between the space points of positron creation and annihilation for the case of a bremsstrahlung spectrum created by 50 MeV electrons under conditions described in [1] are shown in Fig. 2. Since the positrons are mainly produced in forward direction, we distinguish between the projections parallel and transverse to the direction of the incoming beam.

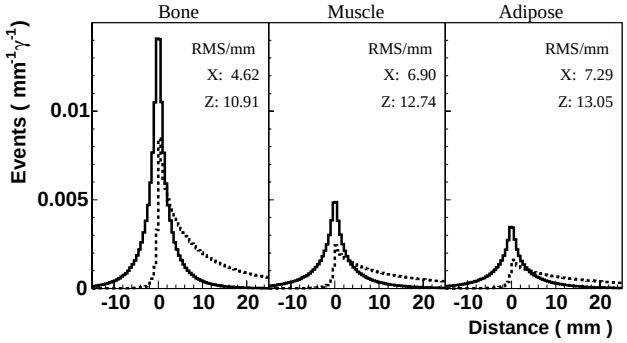


**Fig. 2** *Distance between production and annihilation transverse -X- (full histograms) and longitudinal -Z- (dashed histograms) to the beam direction for various types of tissue indicated in the figure for 50 MeV photon beam.*

As expected the transverse distribution is symmetric to zero and much smaller than the longitudinal distribution, which shows a strong asymmetry.

In Fig. 3 the distribution of annihilation points of positrons in a target filled with water is shown. In its centre a cube of 1 cm side length is located containing different kinds of tissue. From the different density of annihilation points in the various materials can be concluded that, in spite of the broad distributions of Fig. 2, an imaging on the basis of PET should be possible. Especially perpendicular to the beam direction the position of steep density gradients can be localized.

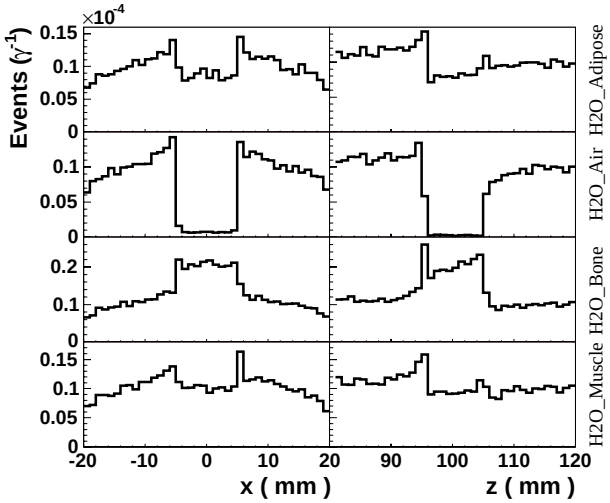


**Fig. 3** *Distribution of annihilation points in a water phantom of $9 \times 9 \times 20$ cm$^3$ containing in its center a cube of 1 cm side length filled with different types of tissue as indicated in the figure for 50 MeV photon beam.*

The production rate of positrons is estimated according to the following assumptions:

- The number density of positrons per dose produced in PMMA amounts to about $\delta \approx 2 \times 10^8\,\mathrm{Gy}^{-1}\mathrm{cm}^{-3}$ (see Fig. 1).
- For the volume the whole target is taken $V = 4 \times 4 \times 20$ cm$^3$ $= 320$ cm$^3$.
- A dose of $D = 1$ Gy is delivered in $t = 100$ $s$.
- For the duty cycle a value of $f = 10^{-3}$ is taken typical for medical linear accelerators.
- This results in an annihilation $\gamma$-ray flux of $\dot{N}_\gamma = 2\,\delta\,V D/(f\,t) \approx 12 \times 10^{11} s^{-1}$ and a total $\gamma$-ray number of $12 \times 10^{10}$.
- For a single detector of area $A = 4 \times 4$ mm$^2$ placed in a distance of $R = 400$ mm we get a counting rate of $\dot{N}_A = \dot{N}_\gamma\ A\ /\ (4\pi\ R^2) \approx 10^7\ s^{-1}$ during the macro pulse of the electron beam.

PET imaging of annihilation $\gamma$-rays following pair production is thus not feasible because of overloading the PET detectors during the beam macro pulses of medical accelerators, whereas target activation should be measurable during the pauses between the macro pulses.

[1] H. Müller, W. Enghardt, This Report, p. 70

## Publications and Talks

## Teaching Activities

## Ph.D. Theses and Meetings

# Publications[1]

**Measurement of the $\eta$ production in proton-proton collisions with the COSY time-of-flight spectrometer**
Eur. Phys. J. A 16, 127 (2003)
Abdel-Bary, M.; Abdel-Samad, S.; Bilger, R.; Brinkmann, K.-Th.; Clement, H.; Dshemuchadse, S.; Dorochkevitch, E.; Dutz, H.; Eyrich, W.; Erhardt, A.; Filges, D.; Filippi, A.; Freiesleben, H.; Fritsch, M.; Geyer, R.; Gillitzer, A.; Hesselbarth, D.; Jakob, B.; Karsch, L.; Kilian, K.; Koch, H.; Kreß, J.; Kuhlmann, E.; Marcello, S.; Marwinski, S.; Mauro, S.; Meyer, W.; Michel, P.; **Möller, K.**; Morsch, H. P.; **Naumann, L.**; Paul, N.; Richter, M.; Roderburg, E.; Rogge, M.; Schamlott, A.; Schmitz, M.; Schönmeier, P.; Schulte-Wissermann, M.; Schroeder, W.; Sefzik, T.; Stinzing, F.; Sun, G. Y.; Wagner, G. J.; Wagner, M.; Wilms, A.; Wintz, P.; Wirth, S.; Zupranski, P.

Abstract: The reaction pp $\rightarrow$ pp$\eta$ was measured at excess energies of 15 and 41 MeV at an external target of the Jülich Cooler Synchrotron COSY with the time-of-flight spectrometer. About 25000 events were measured for the excess energy of 15 MeV and about 8000 for 41 MeV. Both protons of the process pp$\eta$ were detected with an acceptance of nearly 100 % and the $\eta$ was reconstructed by the missing-mass technique. For both excess energies the angular distributions are found to be nearly isotropic. In the invariant-mass distributions strong derivations from the pure phase space distributions are seen.

**Study of the reaction pp $\rightarrow$ pp$\pi^0$ within 10 MeV above the threshold**
Eur. Phys. J. A 17, 595 (2003)
Abdel-Samad, S.; Bilger, R.; Böhm, A.; Brinkmann, K.-Th.; Clement, H.; Dshemuchadse, S.; Eyrich, W.; Filges, D.; Freiesleben, H.; Fritsch, M.; Geyer, R.; Hesselbarth, D.; Jakob, B.; Kilian, K.; Koch, H.; Karsch, L.; Kress, J.; Kuhlmann, E.; Marwinski, S.; Michel, P.; **Möller, K.**; Morsch, H. P.; **Naumann, L.**; Richter, M.; Roderburg, E.; Rogge, M.; Schamlott, A.; Schmitz, M.; Schönmeier, P.; Schroeder, M.; Schulte-Wissermann, M.; Sun, G. Y.; Steinke, M.; Stinzing, F.; Wagner, G. J.; Wagner, M.; Wilms, A.; Wirth, S.

Abstract: Kinematically complete measurements of the pp $\rightarrow$ pp$\pi^0$ reaction were performed for beam energies in the range 292 - 298 MeV. By detecting both protons in coincidence with the large acceptance COSY-TOF spectrometer set up at an external beam line of the proton synchrotron COSY-Jülich, total and differential cross sections and energy distributions were obtained. A strong enhancement is observed in the Dalitz plots resulting from the final state interaction between the outgoing proton pair; the data are well reproduced by Monte Carlo simulations with standard parameters for scattering lengths $a_0 = 7.83$ fm and effective range $r_0 = 2.8$ fm. The total cross sections exceed the ones measured recently in internal target experiments at IUCF and CELSIUS by roughly 50 %. Arguments are presented which link this discrepancy with the effect of the final state interaction pushing yield into the very small-angle region and the near-impossibility of an internal target experiment to cover just this range.

**Cranked relativistic Hartree-Bogoliubov theory: probing the gateway to superheavy nuclei**
Phys. Rev. C 67, 024309 (2003)
Afanasjev, A. V.; Khoo, T. L.; **Frauendorf, S. G.**; Lalazissis, G. A.; Ahmad, I.

Abstract: The cranked relativistic Hartree-Bogoliubov theory has been applied for a systematic study of the nuclei around $^{254}$No, the heaviest element for which detailed spectroscopic data are available. The deformation, rotational response, pairing correlations, quasiparticles and other properties of these nuclei have been studied with different parametrizations for the effective mean-field Lagrangian. Pairing correlations are taken into account by a finite range two-body force of Gogny type. While the deformation properties are well reproduced, the calculations reveal some deficiencies of the effective forces both in the particle-hole and particle-particle channels. For the first time, the quasiparticle spectra of odd deformed nuclei have been calculated in a fully self-consistent way within the framework of the relativistic mean field (RMF) theory. The energies of the spherical subshells, from which active deformed states of these nuclei emerge, are described with an accuracy better than 0.5 MeV

[1]From the authors printed in **bold** further information can be obtained

for most of the subshells with the NL1 and NL3 parametrizations. However, for a few subshells the discrepancies reach 0.7961 MeV. In very heavy systems, where the level density is high, this level of accuracy is not sufficient for reliable predictions of the location of relatively small deformed shell gaps. The calculated moments of inertia reveal only small sensitivity to the RMF parametrization and, thus, to differences in the single-particle structure. However, in contrast to lighter systems, it is necessary to decrease the strength of the D1S Gogny force in the pairing channel in order to reproduce the moments of inertia.

**Quadrupole correlations and inertial properties of rotating nuclei**
J. Phys. G: Nucl. Part. Phys. 29, 1 (2003)
Almehed, D.; **Dönau, F.**; Nazmitdinov, R. G.

Abstract: The contribution of quantum shape fluctuations to inertial properties of rotating nuclei has been analysed for QQ nuclear interaction using the random phase approximation (RPA). The different recipes to treat the cranking mean field plus RPA problem are considered. The effects of the dN = 2 quadrupole matrix elements and the role of the volume conservation condition are discussed.

**Directed flow in Au+Au, Xe+CsI and Ni+Ni collisions and the nuclear equation of state**
Phys. Rev. C 67, 034907 (2003)
Andronic, A.; Reisdorf, W.; Herrmann, N.; Crochet, P.; Barret, V.; Basrak, Z.; Bastid, N.; Berek, G.; Caplar, R.; Devismes, A.; Dupieux, P.; Dzelalija, M.; Finck, C.; Fodor, Z.; Gobbi, A.; Grishkin, Yu.; Hartmann, O. N.; Hildenbrand, K. D.; Hong, B.; Kecskemeti, J.; Kim, Y. J.; Kirejczyk, M.; Koczon, P.; Korolija, M.; **Kotte, R.**; Kress, T.; Lebedev, A.; Lee, K. S.; Leifels, Y.; Lopez, X.; Merschmeyer, M.; **Neubert, W.**; Pelte, D.; Petrovici, M.; Rami, F.; Schauenburg, B. de; Schuettauf, A.; Seres, Z.; Sikora, B.; Sim, K. S.; Simion, V.; Siwek-Wilczynska, K.; Smolyankin, V.; Stockmeier, M.; Stoicea, G.; Tyminski, Z.; Wagner, P.; Wisniewski, K.; **Wohlfarth, D.**; Yushmanov, I.; Zhilin, A.

Abstract: We present new experimental data on directed flow in collisions of Au+Au, Xe+CsI and Ni+Ni at incident energies from 90 to 400 AMeV. We study the centrality and system dependence of integral and differential directed flow for particles selected according to charge. All the features of the experimental data are compared with Isospin Quantum Molecular Dymnamics (IQMD) model calculations in an attempt to extract information about the nuclear matter equation of state (EoS). We show that the combination of rapidity and transverse momentum analysis of directed flow allows to disentangle various parametrizations in the model. At 400 AMeV, a soft EoS with momentum dependent interactions is best suited to explain the experimental data in Au+Au and Xe+CsI, but in case of Ni+Ni the model underpredicts flow for any EoS. At 90 AMeV beam energy, none of the IQMD parametrizations studied is able to consistently explain the experimental data.

**Contribution of the nucleon-hyperon reaction channels to $K^-$ production in proton-nucleus collisions**
Phys. Rev. C 68, 041901(R) (2003)
**Barz, H. W.; Naumann, L.**

Abstract: The cross section for producing $K^-$ mesons in nucleon-hyperon collisions is estimated using the experimentally known pion-hyperon cross sections. The results are implemented in a transport model which is applied to calculation of proton-nucleus collisions. Contrarily to earlier estimates in heavy-ion collisions the inclusion of the nucleon-hyperon cross section roughly doubles the $K^-$ production in near-threshold proton-nucleus collisions.

**Isomerism in $^{96}$Ag and non-yrast levels in $^{96}$Pd and $^{95}$Rh studied in $\beta$ decay**
Nucl. Phys. A 720, 245 (2003)
Batist, L.; Döring, J.; Mukha, I.; Plettner, C.; Bingham, C. R.; Borcea, R.; Gierlik, M.; Grawe, H.; Hauschild, K.; Janas, Z.; Johnstone, I. P.; Karny, M.; Kavatsyuk, M.; Kirchner, R.; La Commara, M.; Mazzocchi, C.; Moroz, F.; Pavan, J.; Plochocki, a.; Roeckl, E.; Salvachúa, B.; Schmidt, K.; **Schwengner, R.**; Skouras, L. D.; Tabor, S. L.; Wiedeking, M.

Abstract: The $\beta$ decay of $^{96}$Ag ($Z$ = 47, $N$ = 49) was investigated by measuring positrons, X rays as well as $\beta$-delayed protons and $\gamma$ rays. The $\gamma$ radiation was studied by means of germanium detectors and a NaI

total-absorption spectrometer. Two $\beta$-decaying isomers in $^{96}$Ag were established with half-lives of 4.40(6) and 6.9(6)s and tentative spin-parity assignments of (8+) and (2+), respectively. For both isomers, the intensities of $\beta$ transitions to low-lying levels of $^{96}$Pd (Z = 46, N = 50) and $\beta$-delayed proton decays to levels in $^{95}$Rh (Z = 45, N = 50) were measured. Several new $^{96}$Pd levels were firmly established. The level energies, their $\gamma$ decays and the Gamow-Teller decay of $^{96}$Ag are compared to shell-model predictions. A new low-lying level in $^{95}$Rh was found at 680 keV excitation energy. Through a comparison with low-lying states of N = 50 isotones, this level is interpreted as the first excited 7/2+ state built on the proton 9/2+ ground state. The assignments of further excited states in $^{95}$Rh are discussed.

**Towards strangeness saturation in central heavy ion collisions at high-energies**
Nucl. Phys. A 715, 553 (2003)
Cleymans, J.; **Kämpfer, B.**; Wheaton, S.

Abstract: Analyses of the centrality binned identified hadron multiplicities at SPS ($\sqrt{}$s = 17 AGeV) and RHIC ($\sqrt{}$s = 130 AGeV) within the statistical-thermal model point to strangeness saturation with increasing centrality and energy.

**A transport and diagnostic system for the IR beam of ELBE**
Nucl. Instr. Meth. A 507, II-35 (2003)
Dekorsy, Th.; **Grosse, E.**; Helm, M.; **Seidel, W.**; **Wohlfarth, D.**; Wolf, A.; **Wünsch, R.**

Abstract: We outline the diagnostic and transport system of the infrared beam produced by the two free-electron lasers of the ELBE facility.

**Infrared-phonon-polariton resonance of the nonlinear susceptibility in GaAs**
Phys. Rev. Lett. 90, 055508 (2003)
Dekorsy, T.; Yakovlev, V. A.; **Seidel, W.**; Helm, W.; Keilmann, F.

Abstract: Nonlinear probing of the fundamental lattice vibration of polar crystals is shown to reveal insight into higher-order cohesive lattice forces. With a free-electron laser tunable in the far infrared we experimentally investigate the dispersion of the second-order susceptibility due to the phonon resonance in GaAs. We observe a strong resonance enhancement of second harmonic light generation at half the optical phonon frequency, and in addition a minimum at a higher frequency below the phonon frequency. Measuring this frequency and comparison to a theoretical model allows the determination of competing higher-order lattice forces.

**Identification of isomers in the $N = Z + 1$ nucleus $^{95}$Ag**
Phys. Rev. C 68, 034306 (2003)
Döring, J.; Grawe, K.; Schmidt, K.; Borcea, R.; Galanopoulos, S.; Gorska, M.; Harissopulos, S.; Hellström, M.; Janas, Z.; Kirchner, R.; La Commara, M.; Mazzocchi, C.; Roeckl, E.; **Schwengner, R.**

Abstract: Three $\gamma$-decaying isomers in the $N = Z + 1$ nucleus $^{95}$Ag have been identified for the first time. The $^{95}$Ag nuclei were produced via the $^{58}$Ni($^{40}$Ca,$p2n$) reaction and separated by using the GSI on-line mass separator. The emitted g rays were measured with a multi-Ge detector setup in anticoincidence with positrons. Three individual $\gamma$-decay cascades have been identified and assigned to $^{95}$Ag, representing the depopulation of isomers at 344, 2531, and 4859 keV excitation energy with tentative spin-parity assignments of $(1/2^-)$, $(23/2^+)$, and $(37/2^+)$, respectively. The spin and parity assignments are based on a comparison with shell-model predictions employing empirical interactions.

**Hyperon–nucleon bound states and electroproduction of strangeness on $^{3,4}$He**
Prog. Part. Nucl. Phys. 50, 587 (2003)
**Dohrmann, F.**; Abbott, D.; Ahmidouch, A.; Ambrozewicz, P.; Armstrong, C. S.; Arrington, J.; Asaturyan, R.; Assamagan, K.; Avery, S.; Bailey, K.; Baker, O. K.; Beedoe, S.; Bitao, H.; Breuer, H.; Brown, D. S.; Carlini, R.; Cha, J.; Chant, N.; Christy, E.; Cochran, A.; Cole, L.; Collins, G.; Cothran, C.; Crowder, J.; Cummings, W. J.; Danagoulian, S.; Duncan, F.; Dunne, J.; Dutta, D.; Eden, T.; Elaasar, M.; Ent, R.; Ewell, L.; Fenker, H.; Fortune, H. T.; Fujii, Y.; Gan, L.; Gao, H.; Garrow, K.; Geesaman, D. F.; Gueye, P.; Gustafsson, K.; Hafidi,

K.; Hansen, J. O.; Hinton, W.; Jackson, H. E.; Juengst, H.; Keppel, C.; Klein, A.; Koltenuk, D.; Liang, Y.; Liu, J. H.; Lung, A.; Mack, D.; Madey, R.; Markowitz, P.; Martoff, C. J.; Meekins, D.; Mitchell, J.; Miyoshi, T.; Mkrtchyan, H.; Mohring, R.; Mtingwa, S. K.; Mueller, B.; O'Neill, T. J.; Niculescu, G.; Niculescu, I.; Potterveld, D. H.; Price, J. W.; Raue, B. A.; Reimer, P. E.; Reinhold, J.; Roche, J.; Roos, P.; Sarsour, M.; Sato, Y.; Savage, G.; Sawafta, R.; Segel, R. E.; Semenov, A. Yu.; Stepanyan, S.; Tadevosian, V.; Tajima, S.; Tang, L.; Terburg, B.; Uzzle, A.; Wood, S.; Yamaguchi, H.; Yan-1, C.; Yan-2, C.; Yuan, L.; Zeier, M.; Zeidman, B.; Zihlmann, B.

The A(e, e'K+)YX reaction has been investigated in Hall C at Jefferson Lab. Data were taken for $Q^2 \approx 0.35$ and 0.5 GeV$^2$ at a beam energy of 3.245 GeV for $^3$He, $^4$He. The missing mass spectra are fitted with Monte Carlo simulations including $\Lambda, \Sigma^0, \Sigma^-$ hyperon production. Models for quasifree production are compared to the data, excess yields close to threshold are attributed to FSI. Evidence for Λ-hypernuclear bound states is seen for $^{3,4}$He targets.

**Nuclear transparency with the $\gamma\ n \to \pi^- p$ process in $^4$He**
Phys. Rev. C 68, 021001 (2003)
Dutta, D.; Xiong, F.; Zhu, L. Y.; Arrington, J.; Averett, T.; Beise, E.; Calarco, J.; Chang, T.; Chen, J. P.; Chudakov, E.; Coman, M.; Clasie, B.; Crawford, C.; Dieterich, S.; **Dohrmann, F.**; Fissum, K.; Frullani, S.; Gao, H.; Gilman, R.; Glashauser, C.; Gomez, J.; Hafidi, K.; Hansen, O.; Higinbotham, D. W.; Holt, R. J.; deJager, C. W.; Jiang, X.; Kinney, E.; Kramer, K.; Kumbartzki, G.; LeRose, J.; Liyanage, N.; Mack, D.; Markowitz, P.; McCormick, K.; Meziani, Z.-E.; Michaels, R.; Mitchell, J.; Nanda, S.; Potterveld, D.; Ransome, R.; Reimer, P. E.; Reitz, B.; Saha, A.; Schulte, E. C.; Seely, J.; Sirca, S.; Strauch, S.; Sulkosky, V.; Vlahovic, B.; Weinstein, L. B.; Wijesooriya, K.; Williamson, C.; Wojtsekhowski, B.; Xiang, H.; Xu, W.; Zeng, J.; Zheng, X.

Abstract: We have measured the nuclear transparency of the fundamental process $\gamma n \to \pi^- p n^4$He. These measurements were performed at Jefferson Lab in the photon energy range of 1.6 to 4.5 GeV and at $\theta^\pi_{cm} = 70$ und 90. These measurements are the first of their kind in the study of nuclear transparency in photoreactions. They also provide a benchmark test of Glauber calculations based on traditional models of nuclear physics. The transparency results suggest deviations from the traditional nuclear physics picture. The momentum transfer dependence of the measured nuclear transparency is consistent with Glauber calculations which include the quantum chromodynamics phenomenon of color transparency.

**Nuclear resonance fluorescence experiments on $^{204,206,207,208}$Pb up to 6.75 MeV**
Nucl. Phys. A 724, 243 (2003)
Enders, J.; Brentano, P. von; Eberth, J.; Fitzler, A.; Fransen, C.; Herzberg, R.-D.; Kaiser, H.; **Käubler, L.**; Neumann-Cosel, P. von; Pietralla, N.; Ponomarev, V. Yu.; Richter, A.; **Schwengner, R.**; Wiedenhöver, I.

Abstract: Dipole and electric quadrupole excitations in $^{204,206,207,208}$Pb have been measured up to 6.75 MeV in resonant photon scattering experiments at the superconducting Darmstadt electron linear accelerator S-DALINAC using two Euroball-Cluster detector modules. In $^{208}$Pb, 14 excited states have been populated; in $^{206}$Pb, the decays of 41 states have been detected. Information about 45 heretofore unknown excited states in $^{204}$Pb could be measured as well as eleven known levels in $^{207}$Pb. The extracted dipole strength distributions are discussed within phenomenological ("pygmy resonance") and microscopic models (quasiparticle-phonon model). A strong fragmentation and a small shift of the detected E1 strength towards higher energies is observed with the opening of the neutron shell closure.

**Energy loss of quarks in deconfined matter at RHIC: Photon tagged jets, single electron and dilepton spectra from open charm**
Nucl. Phys. A 715, 705 (2003)
Gallmeister, K.; **Kämpfer, B.**, Pavlenko, O.P.

Abstract: We report a first attempt (i) to derive constraints on the energy loss of charm quarks in a deconfined medium from the recent PHENIX single-electron transverse momentum spectra and (ii) to estimate the resulting suppression of dileptons from correlated semileptonic decays of open charmed mesons. The momentum imbalance of photon-tagged light-quark jets is also considered.

**Properties and planned use of the intense THz radiation from ELBE at Dresden-Rossendorf**
J. Biol. Phys. 29, 303 (2003)
**Fahmy, K.; Furlinski, G.; Gippner, P.; Grosse, E.; Seidel, W.; Sczepan, M.; Wohlfahrt, D.; Wolf, A.; Wünsch, R.**

Abstract: The radiation source ELBE at Dresden-Rossendorf is centered around a superconducting **EL**ectron accelerator of high **B**rilliance and low **E**mittance (ELBE) which produces electron beams up to 40 MeV. This new facility delivers secondary radiation of different kinds. Special emphasis will be given to the production of intense THz radiation from its Free-Electron Lasers (FEL). This radiation will be used for various research activities including the life sciences. Two additional femtosecond Ti:sapphire laser systems allow to exploit different methods of THz generation for such investigations.

**First evidence for different freezeout conditions for kaons and anti-kaons observed in heavy ion collisions**
Phys. Rev. Lett. 91, 152301 (2003)
Förster, A.; Uhlig, F.; Boettcher, I., Debowski, M.; **Dohrmann, F.; Grosse, E.**; Koczon, P.; Kohlmeyer, B.; Laue, F.; Menzel, M.; **Naumann, L.**; Oeschler, H.; **Scheinast, W.**; Schwab, E.; Senger, P.; Shin, Y.; Ströbele, H.; Sturm, C.; Surowka, G.; **Wagner, A.**; Walus, W.

Abstract: Differential production cross sections of $K^-$ and $K^+$ mesons have been measured in Ni + Ni and Au + Au collisions at a beam energy of 1.5 AGeV. The $K^-/K^+$ ratio is found to be nearly constant as a function of the collisions centrality and system size. The spectral slopes and the polar emission pattern differ for $K^-$ and $K^+$ mesons. These observations indicate that $K^+$ mesons decouple earlier from the fireball than $K^-$ mesons.

**Temperature-induced pair correlations in cluster and nuclei**
Phys. Rev. B 68, 024518 (2003)
**Frauendorf, S.**; Kuzmenko, N. K.; Mikhajlov, V. M.; Sheikh, J. A.

Abstract: The pair correlations in mesoscopic systems such as nanometer-size superconducting clusters and nuclei are studied at a finite temperature for the canonical ensemble of fermions in model spaces with a fixed particle number: (i) a degenerate spherical shell (strong-coupling limit), (ii) an equidistantly spaced deformed shell (weak coupling limit). It is shown that after the destruction of the pair correlations at T = 0 by a strong magnetic field or rapid rotation, heating can bring them back. This phenomenon is a consequence of the fixed number of fermions in the canonical ensemble.

**Lifetime study of particle-hole excitations in the semimagic nucleus $^{93}$Tc**
Phys. Rev. C 68, 024309 (2003)
Hausmann, M.; Jungclaus, A.; Galindo, E.; Lieb, K. P.; Yordanov, O.; Johnstone, I. P.; **Schwengner, R.**; Dewald, A.; Fitzler, A.; Möller, O.; Angelis, G. de; Gadea, A.; Martinez, T.; Napoli, D.R.; Ur, C.

Abstract: The recoil-distance Doppler-shift technique was employed for determining lifetimes of high-spin states in the semimagic nucleus $^{93}$Tc. The nuclei were populated using the reaction $^{64}Zn(^{35}\mathrm{Cl},\alpha 2\mathrm{p})$ at a beam energy of 135 MeV, and the $\gamma$ radiation from their decay was detected in the GASP spectrometer. A total of 26 reduced transition probabilities and limits for 19 further transitions were extracted and compared to large scale shell model calculations, considering different configuration spaces and residual interactions. The information deduced about transition strengths turned out to be essential for the correct assignment of the calculated to the experimental excited states.

**Electromagnetic-induced fission of $^{238}$U projectile fragments, a test case for the production of spherical super-heavy nuclei**
Nucl. Phys. A 713, 3 (2003)
Heinz, A.; Schmidt, K.-H.; **Junghans, A.R.**; Armbruster, P.; Benlliure, J.; Böckstiegel, C.; Clerc, H.-G.; Grewe, A.; de Jong, M.; Müller, J.; Pfützner, M.; Steinhäuser, S.; Voss, B.

Abstract: Isotopic series of 58 neutron-deficient secondary projectiles ($^{205,206}$At, $^{205-209}$Rn, $^{208-212,217,218}$Fr, $^{211-223}$Ra, $^{215-226}$Ac, $^{221-229}$Th, $^{226-231}$Pa, $^{231-234}$U) were produced by projectile fragmentation using a 1 A

GeV $^{238}$U beam. Cross sections of fission induced by nuclear and electromagnetic interactions in a secondary lead target were measured. They were found to vary smoothly as a function of proton and neutron number of the fissioning system, also for nuclei with large ground-state shell effects near the 126-neutron shell. No stabilization against fission was observed for these nuclei at low excitation energies. Consequences for the expectations on the production cross sections of super-heavy nuclei are discussed.

**Precise measurement of the $^7$Be (p, $\gamma$) $^8$B S factor**
**Junghans, A.R.**; Mohrmann, E.C.; Snover, K.A.; Steiger, T.D.; Adelberger, E.G.; Casandjian, J.M.; Swanson, H.E.; Buchmann, L.; Park, S.H.; Zyuzin, A.; Laird, A.M.
Phys. Rev. C 68, 065803 (2003)

Abstract: We present new measurements of the $^7$Be(p,$\gamma$)$^8$B cross section from $E_{c.m.}$ = 116 to 2460 keV (where c.m. means center-of-mass), which incorporate several improvements over our previously published experiment, also discussed here. Our new measurements lead to $S_{17}(0)$ = 22.1±0.6(expt)±0.6(theor) eV b based on data from $E_{c.m.}$ = 116 to 362 keV, where the central value is based on the theory of Descouvemont and Baye. The theoretical error estimate is based on the fit of 12 different theories to our low-energy data. We compare our results to other $S_{17}(0)$ values extracted from both direct [$^7$Be(p,$\gamma$)$^8$B] and indirect (Coulomb-dissociation and heavy-ion reaction) measurements, and show that the results of these three types of experiments are not mutually compatible. We recommend a "best" value, $S_{17}(0)$ = 21.4±0.5(expt)±0.6(theor) eV b, based on the mean of all modern direct measurements below the 1$^+$ resonance. We also present S factors at 20 keV which is near the center of the Gamow window: the result of our measurements is S17(20) = 21.4±0.6(expt)±0.6(theor) eV b, and the recommended value is S17(20) = 20.6±0.5(expt)±0.6(theor) eV b.

**Probing the strange quark condensate by dielectrons from $\phi$-meson decays in heavy ion collision at SIS energies**
Eur. Phys. J. A 17, 83 (2003)
**Kämpfer, B.**; Pavlenko, O.P.; **Zschocke, S.**

Abstract: QCD sum rules predict that the change of the strange quark condensate d¥ss¢ in hadron matter at finite baryon density causes a shift of the peak position of the di-electron spectra from $\phi$-meson decays. Due to the expansion of hadron matter in heavy-ion collisions, the peak suffers a smearing governed by the interval of density in the expanding fireball, which appears as an effective broadening of the di-electron spectrum in the region. The emerging broadening is sensitive to the in-medium change of d¥ss¢. This allows to probe directly in-medium modifications of d¥ss¢ via di-electron spectra in heavy-ion collisions at SIS energies with HADES.

**Baryon resonance dynamics in $\pi$ N $\to$ N V reactions near threshold**
Nucl. Phys. A 721, 583 (2003)
**Kämpfer, B.**; Titov, A.I.; Reznik, B.L.

Abstract: The $\phi - \omega$ interference in the exclusive reaction $\pi N \to N' e^+ e^-$ is studied within a schematic model including the established baryon resonances up to 1720 MeV. Near threshold the interference can be used to separate the isoscalar part of the electromagnetic current. The role of various baryon resonances is highlighted.

**Thermal parameters in heavy ion collisions at SPS and RHIC: centrality dependence**
Heavy Ion Phys. 18, 1 (2003)
**Kämpfer, B.**; Cleymans, J.; Gallmeister, K.; Wheaton, S.M.

Abstract: The centrality dependence of thermal parameters describing hadron multiplicities and intermediate-mass dilepton spectra in heavy-ion collisions at SPS and RHIC is analyzed. From experimental hadron multiplicities we deduce evidence for strangeness saturation at high energy and maximum centrality. The observed dilepton spectra can be parameterized by a centrality independent temperature.

**Exclusive charge exchange reaction pD $\to$ N(pp) within the Bethe-Salpeter formalism**
Eur. Phys. J. A 17, 119 (2003)
Kaptari, L.P.; **Kämpfer, B.**; Semikh, S.S.; Dorkin, S.M.

Abstract: The exclusive charge exchange reaction $pDN \rightarrow (pp)$ at intermediate and high energies is studied within the Bethe-Salpeter formalism. The final-state interaction in the detected pp pair at nearly zero excitation energy is described by the 1So component of the Bethe-Salpeter amplitude. Results of numerical calculations of polarization observables and differential cross-section persuade that, as in the non-relativistic case, this reaction i) can be utilized as a "relativistic deuteron polarimeter" and ii) delivers further information about the elementary nucleon-nucleon charge exchange amplitude.

**Hamamatsu S8550 APD arrays for high-resolution scintillator matrices readout**
Nucl. Instr. Meth. A 504, 139 (2003)
Kapusta, M.; **Crespo, P.**; Wolski, D.; Moszynski, M.; **Enghardt, W.**

Abstract: The performance of Hamamatsu S8550 avalanche photodiode (APD) arrays for scintillator matrices readout has been evaluated. The S8550 device is a monolithic 8 x 4 pixels structure with an active area of 2.56 $mm^2$ for each pixel. The device allows stable operation at gains up to 74, with a detection efficiency of about 60 % for photons of 420 nm wavelength. It is characterized by a low noise equal to 27 electrons equivalent noise charge at room temperature. The energy resolution of 14.6%, for the 511 keV peak from $^{22}$Na source has been recorded with a 2 x 2 x 10 $mm^3$ LSO crystal coupled to one pixel. The number of electron-hole pairs produced by the 511 keV photopeak absorbed in LSO is equal to $4830 \pm 240\, e-h/MeV$. Coupling LSO scintillator crystals to individual pixels of the APD array a coincidence timing resolution of 3.0 $\pm$ 0.2 ns FWHM has been measured for the 511 keV $\gamma$-rays from a $^{22}$Na source. Finally, we compared the characteristics and readout performance of the Hamamatsu array with the results measured earlier under the same conditions for the quadrant large area avalanche photodiodes of Advanced Photonics Inc.

**Platinmetall-Führung der Ni-Cu Sulfidmineralisationen im Bereich der Lausitzer Antiklinalzone**
Z. Angew. Geol. 43 (2/2003)
Kindermann, A.; **Fiedler, F.**; Seifert, T.; Uhlig, S.

Abstract: The PGE content of liqid magmatic NI-Cu(-PGE) sulfide mineralization in the Lusatian anticline has been known since the early 20th century. The mineralization occurs only in vein- or stock-like intrusive bodies of gabbroic, dioritic or noritic composition. Mineralization consisting mainly of pyrrhotite, pentlandite and chalcopyrite probably results from gravity segregation of an exsolved sulfide melt. Sulfides occur in general near the contacts of the intrusions. Different types of ore textures can be distinguished. Besides extensive field work at numerous exposures, microscopic, geochemical, and semiquantitative microanalysis was carried out to charackterize the sulfide mineralization and the PGE phases. These contain, beside Pt and Pd, remarkable amounts of Sb, Te, Hg and As. The Lusatian Ni-Cu(-PGE) mineralization is genetically similar to Norilsk-Talnakh-type ore deposits.

**Change of the dipole strength distributions between the neighboring Gamma-soft nuclei $^{194}$Pt and $^{196}$Pt**
Phys. Lett. B 554, 15 (2003)
Linnemann, A.; Brentano, P. von; Eberth, J.; Enders, J.; Fitzler, A.; Fransen, C.; Guliyev, E.; Herzberg, R.-D.; **Käubler, L.**; Kuliev, A. A.; Neumann-Cosel, P. von; Pietralla, N.; Prade, H.; Richter, A.; **Schwengner, R.**; Thomas, H. G.; Weisshaar, D.; Wiedenhöver, I.

Abstract: A nuclear resonance fluorescence experiment with two highly efficient EUROBALL Cluster detectors has been performed on the Gamma-soft nucleus $^{194}$Pt. Dipole excitations were observed between 2 and 4 MeV excitation energy. They are tentatively interpreted as the main fragments of the scissors mode based on the measured excitation strengths and a comparison to microscopic calculations in the framework of the quasiparticle random phase approximation (QRPA). The data indicate large differences to the neighbouring isotope $^{196}$Pt: a doubling of the observed dipole strength and a shift of the energy centroid by about 600 keV. None of the currently available models is able to reproduce these features consistently in both nuclei.

**3D particle tracking technique for FEL start-up and saturation effects**
Nucl. Instr. Meth. A 507, 97 (2003)
de Loos, M. J.; van der Geer, C. A. J.; van der Geer, S. G.; van der Meer, A. F. G.; Oepts, D.; **Wünsch, R.**

Abstract: Self-consistent simulation of a LINAC-driven FEL by time-domain particle tracking can give very detailed results on both the produced radiation and the evolution of the electron bunch. We show that when special subsets are tracked, instead of individual macro-particles, only a few of these subsets are required to obtain converging results. The subsets used are short longitudinal arrays of macro-particles, of the order of a few ponderomotive waves, distributed longitudinally in such a way that they are almost only sensitive to stimulated emission. This new approach has been carried out with the 3D General Particle Tracer code and a set of axisymmetric Gaussian waves propagating in free space. Due to the first-principles approach, it can be used for a variety of radiation problems, including studies of FEL start-up and saturation effects. The model and two applications will be presented.

**Subthreshold $\phi$-meson yield in central $^{58}$Ni + $^{58}$Ni collisions at 1.93 AGeV**
Nucl. Phys. A 714, 89 (2003)
Mangiarotti, A.; Herrmann, N.; Maurenzig, P. R.; Gobbi, A.; **Kotte, R.**; Keczkemeti, J.; Leifels, Y.; Alard, J. P.; Andronic, A.; Averbeck, R.; Barret, V.; Basrak, Z.; Bastid, N.; Belyaev, I.; Bendarag, A.; Berek, G.; Caplar, R.; Crochet, P.; Devismes, A.; Dupieux, P.; Dzelalija, M.; Finck, Ch.; Fodor, Z.; Grishkin, Y.; Hartmann, O.; Hildenbrand, K. D.; Hong, B.; Kim, Y. J.; Kirejczyk, M.; Koczon, P.; Korolija, M.; Kress, T.; Kutsche, R.; Lebedev, A.; Lee, K. S.; Manko, V.; Merschmeyer, M.; Moisa, D.; Nianine, A.; **Neubert, W.**; Pelte, D.; Petrovici, M.; Plettner, C.; Rami, F.; Reisdorf, W.; Schauenburg, B. de; Schüll, D.; Seres, Z.; Sikora, B.; Sim, K. S.; Simion, V.; Siwek-Wilczynska, K.; Smolyankin, V.; Stockmeier, M.; Stoicea, G.; Vasiliev, M.; Wagner, P.; Wisniewski, K.; **Wohlfarth, D.**; Yang, J. T.; Yushmanov, I.; Zhilin, A.

Abstract: The $\phi$-meson production cross section is measured for the first time at a sub-threshold energy of 1.93 AGeV in $^{58}$Ni+$^{58}$Ni collisions. The $\phi$ data were obtained within the acceptance of the CDC/Barrel subsystem of the FOPI detector. For a sample of $4.7 \cdot 10^6$ central events, after background subtraction, 23 $\phi$ candidates were observed. Extensive simulation calculations of the detector performance are shown in a detailed comparison to the data, aiming at a good understanding of the apparatus response and at a reliable determination of the efficiencies, production probability and possible systematic errors. A filter procedure is elaborated, which is meant to facilitate the comparison of any theoretical calculation with the data in the detector acceptance. How to extrapolate the result to a $\phi$-meson cross section in $4\pi$ is also discussed. This first result on pseudo-vector mesons can now be compared to existing data for the same reaction at the same incident energy for various outgoing channels, $K^+$ and $K^-$ included. It suggests that a significant fraction (at least 20 %) of the $K^-$-mesons is originating in the decay of the $\phi$ showing that the two channels are strongly correlated. A first comparison to existing model calculations indicates the possible role of the $\rho$-meson channels in $\phi$ production.

**Washout measurement of radioisotope implanted by radioactive beams in the rabbit**
Phys. Med. Biol. 48, 2269 (2003)
Mizuno, H.; Tomitani, T.; Kanazawa, M.; Kitagawa, A.; **Pawelke, J.**; Iseki, Y.; Urakabe, E.; Suda, M.; Kawano, A.; Iritani, R.; Matsushita, S.; Inaniwa, T.; Nishio, T.; Furukawa, S.; Ando, K.; Nakamura, Y. K.; Kanai, T.; Ishii, K.

Abstract: Washout of $^{10}$C and $^{11}$C implanted by radioactive beams in brain and thigh muscle of rabbits was studied. The biological washout effect in a living body is important in the range verification system or three-dimensional volume imaging in heavy ion therapy. Positron emitter beams were implanted in the rabbit and the annihilation gamma-rays were measured by an in-situ positron camera which consisted of a pair of scintillation cameras set on either side of the target. The ROI (region of interest) was set as a two-dimensional position distribution and the time-activity curve of the ROI was measured. Experiments were done under two conditions: live and dead. By comparing the two sets of measurement data, it was deduced that there are at least three components in the washout process. Time-activity curves of both brain and thigh muscle were clearly explained by the three-component model analysis. The three components ratios (and washout half-lives) were 35 % (2.0 s), 30 % (140 s) and 35 % (10191 s) for brain and 30 % (10 s), 19 % (195 s) and 52 % (3175 s) for thigh muscle. The washout effect must be taken into account for the verification of treatment plans by means of positron camera measurements.

**Limits of complete equilibration of fragments produced in central Au on Au collisions at intermediate energies**
Eur. Phys. J. A 17, 559 (2003)
**Neubert, W.**; Botvina, A. S.

Abstract: Experimental data related to fragment production in central Au on Au collisions were analysed in the framework of a modified statistical model which considers cluster production both prior and at the equilibrated stage. The analysis provides limits to the number of nucleons and to the temperature of the equilibrated source. The rather moderate temperatures obtained from experimental double-yield ratios of d, t, $^3$He and $^4$He are in agreement with the model calculations. A phenomenological relation was established between the collective flow and the chemical temperature in these reactions. It is shown that dynamical mechanisms of fragment production, e.g. coalescence, dominate at high energies. It is demonstrated that coalescence may be consistent with chemical equilibrium between the produced fragments. The different meaning of chemical and kinetic temperatures is discussed.

**Evidence for isovector neutron-proton pairing from high-spin states in N = Z $^{74}$Rb**
Phys. Rev. C 67, 021301(R) (2003)
O´Leary, C. D.; Svensson, C. E.; **Frauendorf, S. G.**; Afanasjev, A. V.; Appelbe, D. E.; Austin, R. A. E.; Ball, G. C.; Cameron, J. A.; Clark, R. M.; Cromaz, M.; Fallon, P.; Hodgson, D. F.; Kelsall, N. S.; Macciavelli, A. O.; Ragnarsson, I.; Sarantites, D.; Waddington, J. C.; Wadsworth, R.

Abstract: High-spin states in the odd-odd $N = Z$ nucleus $^{74}_{37}$Rb were studied using the $^{40}$Ca($^{40}$Ca,$\alpha np$) reaction. A previously observed odd-spin T = 0 band has been extended to $I^\pi = (31^+)$ and an even-spin T = 0 band has been observed for the first time to $I^\pi = (22^+)$; both have a $\pi(g_{9/2}) \otimes \nu(g_{9/2})$ structure. A strongly coupled low-spin $T = 0$, $K = 3$ band has been interpreted as being based upon a $\pi[312]\frac{3}{2} \otimes \nu[312]\frac{3}{2}$ configuration. Cranked relativistic Hartree-Bogoliubov calculations, which are corrected for the $T = 1$ $np$-pair field by restoring isospin symmetry, reproduce the observed spectrum. These new results provide evidence for the existence of an isovector pair field that contains a neutron-proton component with the proper strength for ensuring isospin conservation.

**Clonogenic survival of human keratinocytes and rodent fibroblasts after irraditaion with 25 kV X-rays**
Radiation and Environmental Biophys. 42, 95 (2003)
**Panteleeva, A.**; Slonina, D.; Brankovic, K.; Spekl, K.; **Pawelke, J.**; Hoinkis, C.; Dörr, W.

Abstract: Low energy X-rays ($E_{ph}$ $<$50 keV) are widely used in diagnostic radiology and radiotherapy. However, data on their relative biological effectiveness (RBE) are scarce. Of particular importance for risk estimation are the RBE value of X-rays in the range which is commonly used in mammography (10 - 30 keV). In the present study we have determined clonogenic survival after low-energy X-ray irradiation for 3 cell lines: primary human epidermal keratinocytes (HEKn), mouse fibroblasts (NIH/3T3) and Chinese hamster fibroblasts (V79). Experiments were performed with a 25 kV X-ray tube and compared to 200 kV X-rays as a reference. Compared to the effect of 200 kV X-rays, irradiation with 25 kV X-rays resulted in a decreased survival rate in the murine fibroblasts but not the human epithelial cell line. RBE value was calculated for 10 % surviving fraction. For HEKn cells, RBE was 1.33 ± 0.27, for NIH/3T3 cells 1.25 ± 0.07 and for V79 cells 1.10 ± 0.09. In conclusion, no consistently increased RBE was observed in the various cell lines. Nevertheless, a potential of increased cytogenetic changes has to be considered for risk estimation of low-energy X-rays.

**Multiphonon vibrations at high angular momentum in $^{182}$Os**
Phys. Rev. Lett. 91, 182501 (2003)
Pattison, L. K.; Cullen, D. M.;Smith, J. F.; Fletcher, A. M.; Walker, P. M.; El-Masri, H. M.; Podolyák, Zs.; Wood, R. J.; Scholey, C.; Wheldon, C.; Mukherjee, G.; Balabanski, D.; Djongolov, M.; Dalsgaard, Th.; Thisgaard, H; Sletten, G.; Kondev, F.; Jenkins,D.; Lane, G.J.; Lee, I.-Y.; Macchiavelli, A.O.; **Frauendorf, S.**, Almehed, D.

Abstract: Evidence is presented for multiphonon excitations based on a high-spin ($25\hbar$) intrinsic state in the deformed nucleus $^{182}$Os. Angular momentum generation by this mode competes with collective rotation. The experimental data are compared with tilted-axis cranking calculations, supporting the vibrational interpretation. However, the lower experimental energies provide evidence that more complex interactions of states are playing a

role.

**Attenuation and scatter correction for in-beam PET monitoring of tumour irradiations with heavy ions**
Phys. Med. Biol. 48, 2419 (2003)
**Pönisch, F.; Enghardt, W.**; Lauckner, K.

Abstract: An in-beam dual head positron camera is used to monitor the dose application in situ during the tumour irradiation with carbon ion beams at the experimental heavy ion therapy facility at GSI Darmstadt. Therefore, a positron emission tomograph has been mounted directly at the treatment site. A fully 3D reconstruction algorithm based on the Maximum Likelihood Expectation Maximisation (MLEM) algorithm has been developed and adapted to this spatially varying imaging situation. The scatter and attenuation correction is included into the forward projection step of the Maximum Likelihood image reconstruction. This requires an attenuation map containing the information on the material composition and densities. This information is derived from the X-ray computed tomograms of the patient and the patient fixation system including the head-rest. The normalisation of scattered events relative to the unscattered events is done by a global scatter fraction factor which is estimated by means of a Monte Carlo simulation. The feasibility of the proposed algorithm is shown by means of computer simulations, phantom measurements as well as patient data.

**Infrared charakterization of environmental samples by pulsed photothermal spectroscopy**
Eur. Phys. J. Appl. Phys. 25, 39 (2004)
**Seidel, W.**; Förstendorf, H.; Heise, K. H.; Nicolai, R.; Schamlott, A.; Ortega, J. M.; Glotin, F.; Prazeres, R.

Abstract: Low concentration of toxic radioactive metals in environmental samples often limits the interpretation of results of infrared studies investigating the interaction processes between the metal ions and environmental compartments. For the first time, we show that photothermal infrared spectroscopy performed with a pulsed free electron laser can provide reliable infrared spectra throughout a distinct spectral range of interest. In this model investigation, we provide vibrational absorption spectra of a rare earth metal salt dissolved in a KBr matrix and a natural calcite sample obtained by thermal beam deflection technique and FT-IR spectroscopy, respectively. General agreement was found between all spectra of the different recording techniques. Spectral deviations were observed with samples containing low concentration of the rare earth metal salt indicating a lower detection limit of the photothermal method compared to conventional FT-IR spectroscopy.

**Evidence for a new type of shears mechanism in $^{106}$Cd**
Phys. Rev. Lett., 91, 16, 162501 (2003)
Simons, A. J.; Wadsworth, R.; Jenkins, D. G.; Clark, R. M.; Cromaz, M.; Deleplanque, M. A.; Diamond, R. M.; Fallon, P.; Lane, G. J.; Lee, I. Y.; Macchiavelli, A. O.; Stephens, F. S.; Svensson, C. E.; Vetter, K.; Ward, D.; **Frauendorf, S.**

Abstract: Lifetimes of states in the lowest lying positive parity band in $^{106}$Cd have been measured using the Doppler shift attenuation method. The deduced $D(E2)$ transition rates show a marked decrease with increasing spin. Cranking and semiclassical model calculation suggest that the structure has the character of a shears-type band resulting from the coupling of $g_{9/2}$ proton holes to aligned pairs of $h_{11/2}$ and $g_{7/2}$ neutron particles. This is the first clear evidence for the phenomenon of "antimagnetic" rotation in nuclei.

**Induction of micronuclei in human fibroblasts and keratinocytes by 25 kV x-rays**
Radiation and Environmental Biophys. 42, 55 (2003)
Slonina, D.; Spekl, K.; **Panteleeva, A.**; Brankovic, K.; Hoinkis, C.; Dörr, W.

Abstract: A relative biological effectiveness (RBE) not much larger than unity is usually assumed for soft x-rays (up to 50 keV) that are applied in diagnostic radiology such as mammography, in conventional radiotherapy and in novel radiotherapy approaches such as x-ray phototherapy. On the other hand, there have been recent claims of an RBE of more than 3 for mammography and respective conventional x-rays. Detailed data on the RBE of soft x-rays, however, are scarce. The aim of the present study was to determine the effect of low-energy x-rays on chromosomal damage in vitro, interms of micronucleus induction. Experiments were performed with 25 kV x-rays and a 200 kV x-ray reference source. The studies were carried out on primary human epidermal keratinocytes (HEKn), human fibroblasts (HFIB) and NIH/3T3 mouse fibroblasts. Micronucleus (MN) induction

was assayed after in vitro irradiation with doses ranging from 1 to 5.2 Gy. Compared to the effect of 200 kV x-rays, 25 kV x-rays resulted in moderately increased chromosomal damage in all cell lines studied. This increase was observed for the percentage of binucleated (BN) cells with micronuclei as well as for the number of micronuclei per BN cell. Moreover, the increased number of micronuclei per micronucleated BN cell in human keratinocytes and 3T3 mouse fibroblasts suggests that soft x-rays induce a different quality of damage. For all cell lines studied the analysis of micronucleus induction by 25 kV soft x-rays compared to 200 kV x-rays resulted in an RBE value of about 1.3. This indicates a somewhat enhanced potential of soft x-rays for induction of genetic effects.

**Four-quasiparticle alignments in $^{66}$Ge**
Phys. Rev. C 67, 054319 (2003)
Stefanova, E. A.; Stefanescu, I.; Angelis, G. de; Curien, D.; Eberth, J.; Farnea, E.; Gadea, A.; Gersch, G.; Jungclaus, A.; Lieb, K. P.; Martinez, T.; **Schwengner, R.**; Steinhardt, T.; Thelen, O.; Weisshaar, D.; Wyss, R.

Abstract: The neutron-deficient nucleus $^{66}$Ge was populated at high spin in two experiments using the reaction $^{40}$Ca($^{32}$S, $\alpha 2p$) at beam energies of 105 and 95 MeV. In the first experiment, a self supporting $^{40}$Ca target was used, while a gold-backed target of similar thickness was used in the second experiment. $\gamma$-rays were detected with the EUROBALL array, combined with the charged-particle detector array EUCLIDES and the Neutron Wall. The level scheme of $^{66}$Ge was extended up to $E = 18$ MeV and $I = 23^-$. Above angular momentum $10^+$, we found two sequences, connected by energetically staggered $I = 1$ M1 transitions. The total Routhian surface calculations describe $^{66}$Ge at lower spins as a $\gamma$-soft nucleus a having moderate deformation of $\beta_2 = 0.23$, while a triaxial deformation is predicted for the band structures above $I_\pi = 10^+$. To our knowledge, this is the first observation of staggered M1 transitions in a deformed four-quasiparticle $\pi(g_{9/2})\,\nu(g_{9/2}S)$ structure.

**Washout studies of $^{11}$C in rabbit thigh muscle implanted by secondary beams of HIMAC.**
Phys. Med. Bio. 48, 875 (2003)
Tomitani, T.; **Pawelke, J.**; Kanazawa, M.; Yoshikawa, K.; Yoshida, K.; Sato, M.; Takami, T.; Koga, M.; Futami, Y.; Kitagawa, A.; Urakabe, E.; Suda, M.; Mizuno, H.; Kanai, T.; Matsuura, H.; Shinoda, I.; Takizawa, S.

Abstract: Heavy ion therapy has two definite advantages: good dose localization and higher biological effect. Range calculation of the heavy ions is an important factor in treatment planning. X-ray CT numbers are used to estimate the heavy ion range by looking up values in a conversion table which relates empirically photon attenuation in tissues to particle stopping power; this is one source of uncertainty in the treatment planning. Use of positron emitting radioactive beams along with a positron emission tomograph or a positron camera gives range information and may be used as a means of checking in heavy ion treatment planning. However, the metabolism of the implanted positron emitters in a living object is unpredictable because the chemical forms of these emitters are unknown and the metabolism is dependent on the organ species and may be influenced by many factors such as blood flow rate and fluid components present. In this paper, the washout rate of $^{11}$C activity implanted by injecting energetic $^{11}$C beams into thigh muscle of a rear leg of a rabbit is presented. The washout was found to consist of two components, the shorter one was about 4.2 $\pm$ 1.1 min and the longer one ranged from 91 to 124 min. About one third of the implanted positron activity can be used for imaging and the rest was washed out of the target area.

**Cross section measurement of charged pion photoproduction from hydrogen and deuterium**
Phys. Rev. Lett. 91, 022003 (2003)
Zhu, L.Y.; Arrington, J.; Averett, T.; Beise, E.; Calarco, J.; Chang, T.; Chen, J.P.; Chudakov; E.; Coman, M.; Clasie, B.; Crawford, C.; Dieterich, S.; **Dohrmann, F.**; Dutta, D.; Fissum, K.; Frullani, S.; Gao, H.; Gilman, R.; Glashauser, C.; Gomez, J.; Hafidi, K.; Hansen, J.-O.; Hignbotham, D. W.; Holt, R.J.; de Jager, C.W.; Jiang, X.; Kinney, E.; Kramer, K.; Kumbartzki, G.; LeRose, J.; Liyanage, N.; Mack D.; Markowitz, P.; McCormick, K.; Meekins, D.; Meziani, Z.-E.; Michaels, R.; Mitchell, J.; Nanda, S.; Potterveld, D.; Ransome, R.; Reimer, P.E.; Reitz, B.; Saha, A.; Schulte, E.C.; Seely, J.; Sirca, S.; Strauch, S. Sulkosky, V.; Vlahovic, B., Weinstein, L. B.; Wijesoriya, K.; Williamson, C. F.; Wojtsekhowski, B; Xiang, H.; Xiong, F.; Xu, W.; Zeng, J.; Zheng, Y.

Abstract: We have measured the differential cross section for the $\gamma n \to \pi^- p$ and $\gamma p \to \pi^+$reactions at center of mass angle 90 degree in the photon energy range from 1.1 to 5.5 GeV at Jefferson Lab (Jlab). The data at photon energies greater than 3.3 GeV exhibit a global scaling behavior for both $\pi^-$ and $\pi^+$ photoproduction, consistent with the constituent counting rule and the existing $\pi^+$ photoproduction data. Possible oscillations around the scaling value are suggested by these new data. The data show enhancement in the scaled cross section

at a center-of-mass energy near 2.2 GeV. The cross section ratio of exclusive $\pi^-$ to $\pi^+$ photoproduction at high energy is consistent with the prediction based on one-hard-gluon-exchange diagrams.

**A composite chiral pair of rotational bands in the odd-A nucleus $^{135}Nd$**
Phys. Rev. Lett., 91, 132501 (2003)
Zhu, S.; Garg, U.; Nayak, B. K.; Ghugre, S. S.; Pattabiraman, N.; Fossan, D. B.; Koike, D. B.; Starosta, K.; Vaman, C.; Janssens, R. V. F.; Chakrawarthy, R. S.; Whitehead, M.; Macchiavelli, A. O.; **Frauendorf, S.**

Abstract: High-spin states in $^{135}$Nd were populated with the $^{110}$Pd($^{30}$Si, $5n$)$^{135}$Nd reaction at a $^{30}$Si bombarding energy of 133 MeV. Two dI = 1 bands with close excitation energies and the same parity were observed. These bands are directly linked by d$I$ = 1 and d$I$ = 2 transitions. The chiral nature of these two bands is confirmed by comparison with three-dimensional tilted axis cranking calculations. This is the first observation of a three-quasiparticle chiral structure and establishes the primary geometric nature of this phenomenon.

**In-medium spectral change of omega meson as a probe of QCD four-quark condensate**
Phys. Lett. B 562, 57 (2003)
**Zschocke, S.**; Pavlenko, O. P.; **Kämpfer, B.**

Abstract: Within QCD sum rules at finite baryon density we show the crucial role of four-quark condensates, such as $\langle(\overline{q}\gamma_\mu\lambda^a q)^2\rangle_n$, for the in-medium modification of the $\omega$ meson spectral function. In particular, such a global property as the sign of the in-medium $\omega$ meson mass shift is found to be governed by a parameter which describes the strength of the density dependence of the four-quark condensate beyond mean-field approximation. To study self-consistently the broadening of the $\omega$ meson resonance we employ a hadron spectral function based on the $\omega$ meson propagator delivered by an effective chiral Lagrangian. Measurements of the $\omega$ meson spectral change in heavy-ion collisions with the HADES detector can reveal the yet unknown density dependence of the four-quark condensate.

# Proceedings and Reports

Afanasjev, A. V.; Khoo, T. L.; **Frauendorf, S.**; Lalazissis, G. A.; Ahmad, I.
Probing the gateway to superheavy nuclei in cranked relativistic Hartree-Bogoliubov theory
Proceedings of the Conference on Frontiers of Nuclear Structure, Berkeley, California, 2002,
UC Berkeley, Clark Kerr Campus, p. 379 (2003)

Beckert, C.; Freiesleben, H.; **Grosse, E.**; Naumann, B.; Weiß, F.-P.
Particle flux Calculations for a pulsed photoneutron source at the radiation source ELBE
Jahrestagung Kerntechnik 2003, Berlin, 20.-22. Mai 2003,
Tagungsbericht S. 47

**Crespo, P.**; Kapusta, M.; **Pawelke, J.**; Moszynski, M.; **Enghardt, W.**
First in-beam PET imaging with LSO/APD-array detectors.
IEEE Nuclear Science Symposium and Medical Imaging Conference, Conference Reports, Portland, USA, Oct. 19-25, 2003

Deleplanque, M. A.; **Frauendorf, S.**; Pashkevich, V.V.; Chu, S.Y.; Unzhakova, A.
Gross shell structure of moments of inertia
Proceedings of the Conference on Frontiers of Nuclear Structure, Berkeley, California, 2002,
UC Berkeley, Clark Kerr Campus, p. 105 (2003)

Dimitrov, V.I.; **Frauendorf, S.**
Chirality of rotating nuclei
Proceedings of the third International Conference on Fission and Properties of Neutron-Rich Nuclei, Sanibel Island, Florida, 2002, World Science Pub. p. 93 (2003)

Dimitrov, V.; **Dönau, F.; Frauendorf**, S.; Zhang, J.
Left-handed nuclei
Proceedings of the Conference on Frontiers of Nuclear Structures, Berkeley, California, 2002,
UC Berkeley, Clark Kerr Campus, p. 151 (2003)

**Dohrmann, F.**; Abbott, D.; Ahmidouch, A.; Ambrozewicz, P.; Armstrong, C. S.; Arrington, J.; Asaturyan, R.; Assamagan, K.; Avery, S.; Bailey, K.; Baker, O. K.; Beedoe, S.; Bitao, H.; Breuer, H.; Brown, D. S.; Carlini, R.; Cha, J.; Chant, N.; Christy, E.; Cochran, A.; Cole, L.; Collins, G.; Cothran, C.; Crowder, J.; Cummings, W. J.; Danagoulian, S.; Duncan, F.; Dunne, J.; Dutta, D.; Eden, T.; Elaasar, M.; Ent, R.; Ewell, L.; Fenker, H.; Fortune, H. T.; Fujii, Y.; Gan, L.; Gao, H.; Garrow, K.; Geesaman, D. F.; Gueye, P.; Gustafsson, K.; Hafidi, K.; Hansen, J. O.; Hinton, W.; Jackson, H. E.; Juengst, H.; Keppel, C.; Klein, A.; Koltenuk, D.; Liang, Y.; Liu, J. H.; Lung, A.; Mack, D.; Madey, R.; Markowitz, P.; Martoff, C. J.; Meekins, D.; Mitchell, J.; Miyoshi, T.; Mkrtchyan, H.; Mohring, R.; Mtingwa, S. K.; Müller, B.; O'Neill, T. J.; Niculescu, G.; Niculescu, I.; Potterveld, D. H.; Price, J. W.; Raue, B. A.; Reimer, P. E.; Reinhold, J.; Roche, J.; Roos, P.; Sarsour, M.; Sato, Y.; Savage, G.; Sawafta, R.; Segel, R. E.; Semenov, A. Yu.; Stepanyan, S.; Tadevosian, V.; Tajima, S.; Tang, L.; Terburg, B.; Uzzle, A.; Wood, S.; Yamaguchi, H.; Yan-1, C.; Yan-2, C.; Yuan, L.; Zeier, M.; Zeidman, B.; Zihlmann, B.
Electroproduction of strangeness on light nuclei
Proceedings of the 9th International Conference on the Structure of Baryons, Baryons 2002, March 3-8 2002, Jefferson Lab, Newport News, VA, USA
World Scientific, New Jersey, 2003 , p. 585, B.A. Mecking and C.E. Carlson (eds.)

**Dohrmann, F.**; Abbott, D.; Ahmidouch, A.; Ambrozewicz, P.; Armstrong, C. S.; Arrington, J.; Asaturyan, R.; Assamagan, K.; Avery, S.; Bailey, K.; Baker, O. K.; Beedoe, S.; Bitao, H.; Breuer, H.; Brown, D. S.; Carlini, R.; Cha, J.; Chant, N.; Christy, E.; Cochran, A.; Cole, L.; Collins, G.; Cothran, C.; Crowder, J.; Cummings, W. J.; Danagoulian, S.; Duncan, F.; Dunne, J.; Dutta, D.; Eden, T.; Elaasar, M.; Ent, R.; Ewell, L.; Fenker, H.; Fortune, H. T.; Fujii, Y.; Gan, L.; Gao, H.; Garrow, K.; Geesaman, D. F.; Gueye, P.; Gustafsson, K.; Hafidi, K.; Hansen, J. O.; Hinton, W.; Jackson, H. E.; Juengst, H.; Keppel, C.; Klein, A.; Koltenuk, D.; Liang, Y.; Liu, J. H.; Lung, A.; Mack, D.; Madey, R.; Markowitz, P.; Martoff, C. J.; Meekins, D.; Mitchell, J.; Miyoshi, T.; Mkrtchyan, H.; Mohring, R.; Mtingwa, S. K.; Müller, B.; O'Neill, T. J.; Niculescu, G.; Niculescu, I.; Potterveld, D. H.; Price, J. W.; Raue, B. A.; Reimer, P. E.; Reinhold, J.; Roche, J.; Roos, P.; Sarsour, M.; Sato, Y.; Savage, G.; Sawafta, R.; Segel, R. E.; Semenov, A. Yu.; Stepanyan, S.; Tadevosian, V.; Tajima, S.; Tang, L.; Terburg, B.; Uzzle, A.; Wood, S.; Yamaguchi, H.; Yan-1, C.; Yan-2, C.; Yuan, L.; Zeier, M.; Zeidman, B.; Zihlmann, B.
Hyperon-nucleon bound states and electroproduction of strangeness on light nuclei
MESON 2002: 7th International Conference on Meson Production, Properties and Interaction of Mesons, Crakow, Poland, May 24-28 2002,
World Scientific, New Jersey, 2003, p. 427

**Enghardt, W., Crespo, P.; Fiedler, F.; Parodi, K.; Pawelke, J.; Pönisch, F.**
Dose quantification from in-beam PET
9th Workshop on Heavy Charged Particles in Biology and Medicine, Lyon, France, Extended Abstracts 45 (2003)

Förstendorf, H.; **Seidel, W.**; Heise, K.-H.; Ortega, J.-M.; Glotin, F.; Prazeres, R.
Photothermal beam deflection using a free electron laser for infrared characterization of environmental samples
Poster: The 2nd International Conference on Advanced Vibrational Spectroscopy (ICAVS-2), August 24-29, 2003, Nottingham, U.K.

Kanazawa, M.; Kitagawa, A.; Kanai, T.; Murakami, T.; Noda, K.; Suda, M.; Tomitani, T.; Torikoshi, M.; Urakabe, E; Sato, S.; Mizuno, H.; **Pawelke, J.**; Hanawa, K.; Iseki, Y.; Sato, K.
Radioactive beams
9th Workshop on Heavy Charged Particles in Biology and Medicine, Lyon, France,
Extended Abstracts 45 (2003)

**Kämpfer, B.**; Peshier, A.; Soff, G.
Quasi-particle model for deconfined matter
Quark Confinement and the Hadron Spectrum, Proceedings of the 5th International Conference, Sept. 10-14, 2002, Gargano, Italy
(Eds.) N. Brambilla, G.M. Prosperi, World Scientific, New Jersey, p. 448 (2003)

**Kämpfer, B.**; Cleymans, J.; Wheaton, S.; Steinberg, P.
Strangeness Saturation: Dependence on system-size, centrality and energy
Proc. of the 19th Winter Workshop on Nuclear Dynamics, Feb. 8-15 2003, Breckenridge, CO, USA
(Eds.) W. Bauer, R. Bellwied, J.W. Harris, G.D. Westfall; EP Systema, Debrecen, Hungary, p. 103 (2003)

Kapusta, M.; **Crespo, P.**; Wolski, D.; **Heidel, K.; Heinrich, L.; Hutsch, J.; Pawelke, J.; Sobiella, M.**; Trzcinska, A.; Moszynski, M.; **Enghardt, W.**
The LSO/APD array as a possible detector for in-beam PET in hadron therapy
IEEE Nuclear Science Symposium and Medical Imaging Conference, Conference Reports, Portland, USA, Oct. 19-25, 2003

Kelsall, N. S.; Svensson, C. E.; Fisher, S.; Appelbe, D. E.; Austin, R. A. E.; Balamuth, D. P.; Ball, G. C.; Cameron, J. A.; Carpenter, M. P.; Clark, R. M.; Cromaz, M.; Deleplanque, M. A.; Diamond, R. M.; Durell, J. L.; Fallon, P.; Freeman, S. J.; Hausladen, P. A.; Hodgson, D. F.; Janssens, R. V. F.; Jenkins, D. G.; Lane, G. J.; Leddy, M. J.; Lister, C. J.; Macchiavelli, A. O.; O'Leary, C. D.; Sarantites, D. G.; Stephens, F. S.; Schmidt, D. C.; Seweryniak, D.; Varley, B. J.; Vincent, S.; Vetter, K.; Waddington, J. C.; Warsworth, R.; Ward, D.; Wilson,

A. N.; Afanasjev, A. V.; **Frauendorf, S. G.**; Ragnarsson, I.; Wyss, R.
High-spin studies of $N \rightarrow Z$ Nuclei in the mass 70 region
Proceedings of the Conference on Frontiers of Nuclear Structure, Berkeley, California, 2002,
UC Berkeley, Clark Kerr Campus, p. 261 (2003)

Park, S.H., **Junghans, A.R.**, Mohrmann, E.C., Snover, K.A., Steiger, T.D., Adelberger, E.G., Cajandian, J.M., Swanson, H.E., Buchmann, L., Zyuzin, A., Laird, A.
A new measurement of $^{7}$Be(p,$\gamma$)$^{8}$B cross section and its astrophysical meaning
Nucl. Phys. A 718, 113c-116c (2003),
7th International Symposium on Nuclei in the Cosmos (NIC7), Tokyo, May 25-June 1st, 2002

**Pönisch, F.**
Optimierung der Positronen-Emissions-Tomographie bei der Schwerionentherapie auf der Basis von Röntgentomogrammen
Wiss.-Tech. Ber./ FZ Rossendorf; FZR-378, Mai 2003

**Seidel, W.**; Förstendorf, H.; Heise, K. H.; Nicolai, R.; Dekorsy, T.; Ortega, J. M.; Glotin, F.; Prazeres, R.
Infrared characterization of environmental samples by pulsed photothermal spectroscopy
Poster: International Workshop on Infrared Microscopy and Spectroscopy with Accelerator Based Sources, July 8-11, 2003, Lake Tahoe, CA, USA

## Talks at Conferences and other Institutes

**Barz, H.W.**
Einfluss der Lebensdauer von $\phi$-Mesonen auf ihre Erzeugung in pA-Stößen
Frühjahrstagung der Deutschen Physikalischen Gesellschaft, Tübingen,
17-21 März 2003

**Barz, H.W.**
The role of three-body collisions in subthreshold meson production processes in nucleus-nucleus collisions
International workshop on "Off-shell effects in quantum transport", Max-Planck-Institut, Dresden,
May 05-16, 2003

**Barz, H.W.**
Rossendorf results on the home work problems and the role of the nucleon-hyperon channel in K- production
International Workshop on "Transport Theories for Heavy-Ion Reactions", Trento, Italy,
May 19-24, 2003

**Dönau, F.**
Lectures on Nuclear Theory
Nuclear Physics Summer School, St.Andrews, Scotland,
Sept. 2003

**Dönau, F.**
Collective Excitations in Nuclei
Graduierten-Colleg Basel -Tübingen, Tübingen ,
Dec. 11, 2003

**Dönau, F.**
Die Welt der Quantenphysik
Studium Generale, TU Dresden,
Dez. 19, 2003

**Dohrmann, F.**
Second year of operation for the HADES drift chambers MDC III at SIS
Frühjahrstagung der Deutschen Physikalischen Gesellschaft, Tübingen,
März 17-21, 2003

**Dohrmann, F.**
Hypernuclear bound states and electroproduction of strangeness on light nuclei
Frühjahrstagung der Deutschen Physikalischen Gesellschaft, Tübingen,
März 17-21, 2003

**Dohrmann, F.**
Seltsame Mesonen aus Proton-Kern-Stössen
Frühjahrstagung der Deutschen Physikalischen Gesellschaft, Tübingen,
März 17-21, 2003

**Dohrmann, F.**
Electroproduction of strangeness on light nuclei
SENDAI 03, International Symposium on Electrophoto-production of Strangeness on Nucleons and Nuclei, Sendai, Japan,
June 16-18, 2003

**Dohrmann, F.**
Electroproduction of strangeness on $^{3,4}$He
VIII International Conference on Hypernuclear & Strange Particle Physics, Jefferson Lab, Newport News, Virginia, USA,
Oct. 14-18, 2003

**Dohrmann, F.**
The HADES Tracking System: First in-beam experiences with operation and aging
IEEE Nuclear Science Symposium and Medical Imaging Conference, Portland, Oregon, USA,
Oct. 19-25, 2003

**Dohrmann, F.**
The special role of strange quarks in nuclei and nuclear matter
Seminaire de la Division de Recherche, Institut de Physique Nucléaire, Orsay, France,
Nov. 3, 2003

**Enghardt, W.**
Tumour therapy with ion beams
Seminar at the University of Genova,
March 26, 2003

**Enghardt, W.**
Krebstherapie mit Schwerionenstrahlen
Dresdner Seniorenakademie, Dresden,
April 24, 2003

**Enghardt, W.**
Charged hadron tumour therapy monitoring by means of in-beam PET
Imaging 2003, Stockholm, Sweden,
June, 2003

**Enghardt, W.**
Instrumentation for in-beam PET charged hadron therapy monitoring
2nd meeting of the ENLIGHT Workpackage 5: In-situ monitoring with positron emission tomography, Lyon, France,
June 30 - July 1, 2003

**Enghardt, W.**
Medical physics experience in Dresden
Workshop on Perspectives of Medical Physics in Oncology, Dresden,
Sept. 18, 2003

**Enghardt, W.**
Tier-PET: Erfahrungen und Perspektiven; Einführung zum Rundtisch-Gespräch
11. Treffen der Arbeitsgemeinschaft Radiochemie/Radiopharmazie, Brehna,
Sept. 18-20, 2003

**Enghardt, W.**
Dose quantification from in-beam PET
HCPBM 2003, Lyon, France,
Oct. 2-5, 2003

**Enghardt, W.**
Real time imaging of dose distributions
ESTRO Conference on Advances in Radiation Oncology: Harnessing Modern Biology and New Technology, Dresden,
Nov. 21-22, 2003

**Fiedler, F.**
Strategies for predicting positron radioactivity distributions from the treatment plan for different projectiles
Instrumentations and Monte Carlo Methods for Dedicated PET Systems, Dresden,
Jan. 30 - Feb. 1, 2003

**Frauendorf, S.**
Tidal waves
Gordon Research Conference on Nuclear Chemistry, New London, USA,
June 15-20, 2003

**Frauendorf, S.**
Axial vector deformations
Workshop on "Nuclear Mean Field Symmetries and Spontaneous Symmetry Breaking", ETC, Trento, Italy,
Sept. 15-20, 2003

**Frauendorf, S.**
Chirality on nuclear rotation
Technical University Dresden,
Oct. 9, 2003

**Frauendorf, S.**
Theoretical aspects of triaxiality
Workshop on "Shape coexistence in nuclei at high angular momentum", ECT, Trento, Italy,
Nov. 25-27, 2003

**Frauendorf, S.**
How do nuclei rotate?
Marie Curie Doctoral Training Program, ECT, Trento, Italy, 5 lectures,
Aug. 8 to Dec. 12, 2003

**Junghans, A.R.**
Präzise Bestimmung des S-Faktors der Reaktion $^{7}$Be(p,$\gamma$)$^{8}$B aus direkten Messungen
DPG Frühjahrstagung Tübingen
17. - 21. März 2003

**Junghans, A.R.**
The new Seattle-TRIUMF $^{7}$Be(p,$\gamma$)$^{8}$B S-factor determination
Eighth International Workshop On Topics In Astroparticle and Underground Physics (TAUP 2003),
University of Washington, Seattle, Washington

September 5 - 9, 2003

**Junghans, A.R.**
Precise Measurement of the $^7$Be(p,$\gamma$)$^8$B S-factor
INPA journal club seminar at Berkeley (Institute for Nuclear and Particle Astrophysics, Nuclear Science Division, Lawrence Berkeley Laboratory, Berkeley)
15 September

**Junghans, A.R.**
New determination of the $^7$Be(p,$\gamma$)$^8$B S-factor
The sixth international conference on radioactive nuclear beams (RNB6), Argonne, Illinois, USA
22-26 September 2003

**Kämpfer, B.**
Strangeness saturation: energy- and system-size dependence
Nuclear Dynamics 19, Breckenridge, USA,
Feb. 9-14, 2003

**Kämpfer, B.**
Wege zur chiralen Symmetrie-Restauration
Plenarvortrag auf der Frühjahrstagung der Deutschen Physikalischen Gesellschaft, Tübingen,
März 17-21, 2003

**Kämpfer, B.**
Chiral symmetry restoration and vector-meson mass shift
HADES-Kollaborationsmeeting, GSI, Darmstadt,
May 7-10, 2003

**Kämpfer, B.**
Quasiparticle model for deconfinement matter
International Workshop "Off-Shell Effects in Quantum Transport", Max-Planck-Institut, Dresden,
May 5-16, 2003

**Kämpfer, B.**
$\phi$-meson production
International Workshop on "Transport Theories for Heavy-Ion Reactions", Trento, Italy,
May 19-24, 2003

**Kämpfer, B.**
QCD sum rules for $\rho,\ \omega,\ \phi$ mesons
Theorieseminar, GSI, Darmstadt,
July 8, 2003

**Kämpfer, B.**
Dileptons at HADES: Predictions by QCD Sum Rules and Transport Models
International School of Nuclear Physics, Erice, Italy,
Sep. 16-24, 2003

**Kämpfer, B.**
QCD sum rules for $\rho, \omega, \phi$ mesons with finite widths
Europäisches Graduiertenkolleg, Giessen,
Oct. 30, 2003

**Kämpfer, B.**
Unser Universum - Vergangenheit und Zukunft
Studium generale - Ringvorlesung, TU Dresden,
Nov. 6, 2003

**Kanaki, K.**
Dileptons at HADES
Arbeitstreffen "Hadronen und Kerne", Meissen,
Sep. 8-11, 2003

**Kanaki, K.**
Investigation of MDC behaviour
HADES collaboration meeting, Nicolosi, Italy,
Dec. 3-6, 2003

**Kanaki, K.**
Report of repair work on Rossendorf chambers
HADES-Collaboration meeting XII at GSI, Darmstadt,
May 7-10, 2003

**Kotte, R.**
Sub-Schwellen-Produktion von $\phi$-Mesonen in zentralen Stössen von Ni+Ni bei 1.93 AGeV
IKTP-Seminar, TU Dresden,
Jan. 16, 2003

**Kotte, R.**
Status of Outer Plastic Wall calibrations for experiments S261 (Jan. 03) and S263 (Feb. 03)
FOPI collaboration meeting, Darmstadt,
May 12-13, 2003

**Kotte, R.**
Excitation function of pp correlations in central Ca+Ca and Au+Au collisions
FOPI collaboration meeting, Darmstadt,
Nov. 14-15, 2003

**Kotte, R.**
Is it feasible to analyse HADES C+C data with respect to *pp* correlations?
HADES collaboration meeting, Nicolosi, Italy,
Dec. 3, 2003

**Naumann, L.**
Inclusive $K^{\pm}$ and $\pi^{\pm}$ production in proton-nucleus collisions at SIS energies
XXVIII Mazurian Lakes Conference on Physics, Krzyze, Poland,
Aug. 31- Sept. 7, 2003

**Parodi, K.**
Positron Emission Tomography for the monitoring of proton therapy
Specialization in Medical Physics, University of Genova, Italy,
March 26, 2003

**Parodi, K.**
Data processing techniques for in-beam PET therapy monitoring
2nd ENLIGHT Workshop "In-situ monitoring with Positron Emission Tomography, Lyon, France,
July 1, 2003

**Parodi, K.**
Investigations of the applicability of PET quality assurance to proton therapy
IKTP Seminar, TU Dresden,
July 3, 2003

**Parodi, K.**
Instrumentation requirements for in-beam PET
Nordic meeting on light ion and advanced radiation therapy, Stockholm, Sweden,
Aug. 23, 2003

**Pawelke, J.**
The FZR Engagement to the Integrated Project SynBioMed
Working Meeting, European Synchrotron Facility, Grenoble, Switzerland,
Feb. 24, 2004

**Panteleeva, A.**
RBE of soft X-rays determined by survival and chromosomal damage in human and rodent cell lines
Seminar, IKTP, TU Dresden,
Nov. 13, 2003

**Rusev, G.**
Nuclear-Resonance-Fluorescence Experiments on $^{98}$Mo and $^{100}$Mo
Frühjahrstagung der Deutschen Physikalischen Gesellschaft, Tübingen,
März 17-21, 2003

**Rusev, G.**
Photon-Scattering Experiments on $^{98}$Mo and $^{100}$Mo
Dynamitron Tag, Institut für Strahlenphysik, Universität Stuttgart,
Juli 04, 2003

**Rusev, G.**
The Bremsstrahlung Facility at the ELBE accelerator
XV International School on Nuclear Physics, Neutron Physics and Nuclear Energy, Varna, Bulgaria
September 9-13, 2003

**Sadovsky, A.**
A general tool for post-analysis of QA-output
HADES collaboration meeting XII at GSI, Darmstadt,
May 7-10, 2003

**Sadovsky, A.**
Search for $K^+$ mesons in C+C Collisions at 2 AGeV
HADES collaboration meeting, Catania, Italy
Dec. 2-7,2003

**Sadovsky, A.**
High momentum resolution 3MDC kickplane vs. 2 MDC kickplane using Nov. 01 data
HADES internal Analysis meeting, GSI, Darmstadt
Aug. 26, 2003

**Schilling, K.D.**
Planned photofission experiments at the new ELBE accelerator in Rossendorf
Seminar on Fission, Pont d'Oye V, Habay-la-neuve, Belgium
September 16-19, 2003

**Zschocke, S.**
Das $\omega$-Meson in baryonischer Materie
Frühjahrstagung der Deutschen Physikalischen Gesellschaft, Tübingen,
März 17-21, 2003

# Talks of Visitors

**Backe, H.**, Institut für Kernphysik der Universiät Mainz:
Die vielen Facetten der Interferenz von Übergangsstrahlung im Röntgenbereich, March 28, 2003

**Fujita, Y.**, Lab. of Nuclear Studies, Fac. of Science Osaka Univ., Japan:
Comparison of analogous Gamow-Teller and M1 transitions,
Oct. 2, 2003

**Haque, A.M.I.**, Department of Radiation Oncology, Royal Prince Alfred Hospital, Sydney:
A National Proton Therapy Facility for Australia,
Aug. 27, 2003

**Harissopulos, S. V.**, Institute of Nuclear Physics, National Centre for Scientific Research, Greece:
Nuclear data needs for the modelling of the astrophysical p-process: Status and perspectives,
Nov. 26, 2003

**Kamanin, V.**, VIK Dubna, Flerov Laboratorium für Kernreaktionen:
Photospaltung und Transmutation - interessante Anwendungen niederenergetischer Elektronenstrahlen,
April 14, 2003

**Nankov, N.**, Institute for Nuclear Research and Nuclear Energy, Sofia, Bulgaria:
Deceleration of heavy ions in matter in the energy range 40 - 400 MeV/u,
Oct. 29, 2003

**Nazmitdinov R.**, JINR Dubna and Univ. de les Illes Balears:
Symmetry breaking and random phase approximation in quantum dots and nuclei,
April 24, 2003

**Oelert, W.**, FZ Jülich:
Beobachtungen zur Produktion von Antiwasserstoff
June 20, 2003

**Reinhardt, H.**, Universität Tübingen:
Was die Welt im Innersten zusammenhält,
Nov. 7, 2003

**Schmid, K.W.**, Universität Tübingen:
Variational approach to the nuclear many body problem,
June 12, 2003

**Spohr, K.**, University of Paisley, UK:
Neutron rich nuclei - an experimental and theoretical challenge,
Oct. 20, 2003

**Wolf, G.**, KFKI Budapest, Hungary:
Transport calculation of dileptons for HADES-experiments,
April 25, 2003

**Zétényi, M.**, KFKI Budapest, Hungary:
New results on $\phi$ meson production in p+A collisions,
June 20, 2003

# Teaching Activities

**Barz, H.W.**
Streutheorie für Elementarteilchen
TU Dresden, Sommersemester 2003

**Dohrmann, F.**
Ausgewählte Experimente der Kern- und Teilchenphysik
TU Dresden, Wintersemester 2002/2003

**Enghardt, W.**
Schwerionentherapie
Lecture course, Institut für Biomedizinische Technik, TU Dresden, Mai 27, 2003

**Frauendorf, S.**
Electromagnetic Waves
University of Notre Dame, USA, Frülingssem. 2003

**Frauendorf, S.**
Electricity and Magnetism
University of Notre Dame, USA, Herbstsem. 2003

**Grosse, E., K. Fahmy**
Infrarot-Spektroskopie und ihre Anwendung in den Biowissenschaften
TU Dresden, Wintersemester 2003/2004

**Grosse, E., Kämpfer, B.**, Spaan, B., et al.
Kosmologie
TU Dresden Sommersemester 2003

**Kämpfer, B.**
Lecture course "Gauge Field Theory"
TU Dresden, Wintersemester 2002/2003

**Wagner, A.**
Nukleare Astrophysik
TU Dresden, Sommersemester 2003

# Ph.D. Theses

**Falk Pönisch**
Optimierung der Positronen-Emissions-Therapie bei der Schwerionentherapie auf der Basis von Röntgentomogrammen
TU Dresden, April 2003

# Meetings organized by the IKH

| Topic | Period | Number of Participants |
|---|---|---|
| Workshop at Dresden-Rossendorf "Instrumentation and Monte Carlo Methods for Dedicated PET Systems" | Jan. 31 - Febr. 01, 2003 | 24 |
| Workshop at Dresden-Rossendorf "HADES Simulation and Analysis Meeting" | February 17-20, 2003 | 40 |
| Workshop at Meißen near Dresden "Hadronen und Kerne" | September 08-11, 2003 | 100 |
| Workshop* at Dresden "Lebensqualität für ausländische Wissenschaftler in Dresden" | September 15, 2003 | 30 |
| Workshop* at Dresden "Perspectives of Medical Physics in Oncologie & Ausbildung von Medizinphysik-Experten" | September 18-19, 2003 | 100 |

* During application for funding the ZIK OncoRay organized together with Technische Universiät Dresden and Universitätsklinikum "Carl Gustav Carus" Dresden

## Departments of the IKH